

A coronal loop in a box: From energy generation to coronal emission

Dissertation

zur Erlangung des mathematisch-naturwissenschaftlichen Doktorgrades

“Doctor rerum naturalium”

der Georg-August-Universität Göttingen

im Promotionsstudiengang Physik

der Georg-August University School of Science (GAUSS)

vorgelegt von

Cosima Alexandra Breu

aus Frankfurt am Main

Göttingen, 2022

Betreuungsausschuss

Prof. Dr. Hardi Peter

Max-Planck-Institut für Sonnensystemforschung, Göttingen, Germany

Dr. Robert Cameron

Max-Planck-Institut für Sonnensystemforschung, Göttingen, Germany

Prof. Dr. Wolfgang Glatzel

Institut für Astrophysik, Georg-August-Universität Göttingen, Germany

Mitglieder der Prüfungskommission

Referent: Prof. Dr. Hardi Peter

Max-Planck-Institut für Sonnensystemforschung, Göttingen, Germany

Korreferent: Prof. Dr. Laurent Gizon

Institut für Astrophysik, Georg-August-Universität Göttingen, Germany

Max-Planck-Institut für Sonnensystemforschung, Göttingen, Germany

Weitere Mitglieder der Prüfungskommission:

Prof. Dr. Sami K. Solanki

Max-Planck-Institut für Sonnensystemforschung, Göttingen, Germany

Prof. Dr. Wolfram Kollatschny

Institut für Astrophysik, Georg-August-Universität Göttingen, Germany

Prof. Dr. Andreas Tilgner

Institut für Astrophysik, Georg-August-Universität Göttingen, Germany

Prof. Dr. Ariane Frey

Physikalisches Institut, Georg-August-Universität Göttingen, Germany

Tag der mündlichen Prüfung: 31.03.2022

© Cosima Alexandra Breu



This work is distributed under a
Creative Commons Attribution 4.0 License

Printed in Germany

Contents

1	Introduction	13
1.1	The solar atmosphere	13
1.1.1	The coronal heating problem	14
1.2	Magnetohydrodynamics	15
1.2.1	Assumptions	15
1.2.2	Equations	16
1.2.3	The energy equation	20
1.3	Magnetic reconnection	24
1.3.1	2D magnetic reconnection	25
1.3.2	3D magnetic reconnection	25
1.4	Coronal heating mechanisms	25
1.4.1	DC heating	26
1.4.2	AC heating	28
1.4.3	MHD turbulence	30
1.4.4	Flux cancellation	31
1.4.5	Swirls	31
1.5	Coronal loops	32
1.5.1	The RTV scaling laws	33
1.5.2	1D loop models	34
1.5.3	3D coronal loop models	34
1.6	Motivation of this work	36
2	Numerical and analysis methods	39
2.1	The MURaM code	39
2.1.1	Numerical scheme	40
2.1.2	Radiative losses	41
2.1.3	Optically thick radiative losses	42
2.1.4	Boundary conditions	43
2.1.5	The computational timestep	44
2.1.6	Hyperbolic heat conduction	44
2.1.7	Boris correction	45
2.1.8	Numerical diffusivities	46
2.1.9	Model setup	48
2.2	Structure of the solar atmosphere	50
2.3	Numerical diffusivity	51
2.4	Analysis methods	52

2.4.1	Field line tracing	52
2.4.2	Vortex detection: Swirling strength	54
2.4.3	Synthetic spectral profiles	56
3	A solar coronal loop in a box: Energy generation and heating	61
3.1	Introduction	62
3.2	Coronal loop model	64
3.2.1	Equations and loop model	64
3.2.2	Loop geometry	67
3.3	Initial conditions	68
3.3.1	Magnetoconvection in the bottom layers	69
3.3.2	Synthetic emission	70
3.4	Results	70
3.4.1	Overall behavior	71
3.4.2	Poynting flux and heating	74
3.4.3	Loop structure	78
3.4.4	Synthesized emission	84
3.5	Discussion	86
3.5.1	Poynting flux and heating	86
3.5.2	Current sheets	87
3.5.3	Atmospheric coupling	88
3.5.4	Emission	89
3.6	Conclusions	89
4	Swirls in the solar corona	91
4.1	Introduction	91
4.2	Methods	93
4.2.1	Numerical setup	93
4.2.2	Vortex detection	95
4.3	Results	95
4.3.1	Atmospheric coupling	95
4.3.2	Swirl properties	101
4.3.3	Additional events	102
4.4	Discussion	103
4.4.1	Atmospheric coupling	103
4.4.2	Swirl properties	107
4.4.3	Implications for coronal heating	109
4.5	Conclusion	110
5	Nonthermal broadening of coronal lines in a 3D MHD loop model	111
5.1	Introduction	112
5.2	Methods	114
5.2.1	The loop model	114
5.2.2	Synthesizing line profiles	114
5.2.3	Nonthermal velocities	114
5.3	Results	115

5.3.1	Nonthermal broadening perpendicular to guide field	115
5.3.2	Nonthermal broadening parallel to guide field	119
5.3.3	Nonthermal broadening and heating	122
5.3.4	Line profiles	130
5.3.5	Dependence on resolution	134
5.4	Discussion	135
5.4.1	Perpendicular and parallel broadening	135
5.4.2	Line profiles	136
5.4.3	Heating	137
5.4.4	Dependence on resolution	138
5.5	Conclusion	139
6	Discussion and conclusions	141
7	Outlook	143
	Bibliography	145
A	Timescales of the energy transport	157
B	Is there a turbulent cascade in the coronal loop?	159
B.1	Aim	159
B.2	Methods	159
B.3	Results	160
B.3.1	Transfer Functions	160
B.3.2	Convection zone	160
B.3.3	Chromosphere and corona	160
B.4	Discussion	161
B.5	Conclusion	162

Abstract

The corona is the outer atmosphere of the Sun. It contains an abundance of bright arcs that consist of hot plasma trapped by the magnetic field. These coronal loops are heated to temperatures far surpassing the solar surface temperature. The heating of this hot coronal plasma is one of the major open problems in stellar astrophysics. Several mechanisms have been proposed, which can be divided roughly into models based on the slow braiding of magnetic field lines and subsequent impulsive energy release in the corona, the dissipation of magnetohydrodynamic waves, and flux emergence and cancellation and reconnection at the loop footpoints.

We conduct 3D radiative magnetohydrodynamic simulations with the MURaM code to study the generation and transport of energy and observable signatures of heating. To combine the computational efficiency of idealized loop models with the more realistic driving of coronal heating and mass flows in simulations that include part of the convection zone, we model the coronal loop as a "straightened-out" magnetic flux tube in a Cartesian box connected to a shallow convection zone layer at each footpoint. This way, our model is driven self-consistently by magnetoconvection, while the structure across the loop cross-section is well resolved. Gray radiative transfer in the photosphere and chromosphere, optically thin losses in the corona and field-aligned Spitzer heat conduction are taken into account in the model.

The interaction of granulation with the magnetic field leads to a Poynting flux into the atmosphere. The model reproduces the bursty heating found in previous coronal simulations. In response to the energy input, the coronal loop develops a complex structure of small-scale current sheets and flows. The emission synthesized from the loop model shows substructure reproducing observed strand widths.

In the next step, we have a closer look at the magnetic coupling between the photosphere and the corona. Vortex motions are abundant within magnetic concentrations in the photosphere and have been found to contribute to chromospheric heating. We find that some of these vortex tubes reach coronal heights and carry a strong Poynting flux beyond the transition region. Regions with enhanced swirling strength show increased Poynting flux and heating rates. The influence of vortex flows on the atmospheric structure is largest in the chromosphere and low corona, where vortices are overdense and twisted magnetic field lines lead to an upwards directed Lorentz force. With increasing height, vortex flows get deformed until the original rotational motion is not discernible anymore. The relation between vortices and coronal emission is complex. While the rotational motion can lead to gradients in the magnetic and velocity field that show increased viscous and resistive dissipation and lead to brightening of the plasma, coronal emission depends both on temperature and density, which is not significantly increased in vortices in the coronal part of the plasma. Therefore, there is no one-to-one correspondence between vortex tubes and

coronal strands.

Eventually, we calculate synthetic spectral line profiles of coronal emission lines to study the response of coronal emission to heating and plasma motions. We find values for the nonthermal line broadening close to observational values both perpendicular and parallel to the loop axis. Despite being on the same order of magnitude, nonthermal line broadening parallel and perpendicular to the line of sight attributed to different processes. Perpendicular to the magnetic guide field, the velocity field is governed by small-scale twisting and shearing motions. For a line of sight parallel to the magnetic field, evaporation in response to heating events causes an increase in nonthermal broadening. For a line of sight perpendicular to the magnetic guide field, we reproduce the independence of the nonthermal line broadening of the resolution of the observing instrument.

This model provides a new comprehensive view of processes governing the structure and evolution of coronal loops. In particular, the complex magnetic structure drives the energy flux into the upper atmosphere. Small vortex structures extend from the photosphere into the corona and the internal turbulent-like motions lead to a fine-structuring of the loop.

Zusammenfassung

Die Korona ist die äußere Atmosphäre der Sonne. Sie enthält eine Fülle von hellen Bögen, die aus heißem Plasma bestehen, das durch das Magnetfeld eingeschlossen wird. Diese koronalen Bögen werden auf Temperaturen aufgeheizt, die weit über der Temperatur der Sonnenoberfläche liegen. Die Heizung dieses heißen koronalen Plasmas ist eines der größten offenen Probleme der stellaren Astrophysik. Es wurden mehrere Mechanismen vorgeschlagen, die sich grob unterteilen lassen in Modelle, die auf der langsamen Verflechtung von Magnetfeldlinien und anschließender impulsiver Energiefreisetzung in der Korona, der Dissipation magneto-hydrodynamischer Wellen und Aufsteigen, Auslöschung und Rekonnexion magnetischen Flusses an den Fußpunkten der koronalen Bögen beruhen.

Wir führen dreidimensionale magneto-hydrodynamische Simulationen mit dem MURaM-Code durch, um die Erzeugung und den Transport von Energie und die beobachtbaren Signaturen der Heizung zu untersuchen. Um die Effizienz von numerischen Modellen idealisierter koronaler Bögen mit dem realistischeren Antrieb der koronalen Heizung und der Massenströme in Simulationen zu kombinieren, die einen Teil der Konvektionszone einschließen, modellieren wir den koronalen Bogen als eine "begradigte" magnetische Flussröhre in einer kartesischen Box, die mit einer flachen Konvektionszonenschicht an jedem Fußpunkt verbunden ist. Auf diese Weise wird unser Modell selbstkonsistent von der Magnetokonvektion angetrieben, während die Struktur im Querschnitt des Bogens gut aufgelöst ist. "Grauer" Strahlungstransport in der Photosphäre und Chromosphäre, optisch dünne Emission in der Korona und die Spitzer-Wärmeleitung entlang des Magnetfeldes werden in dem Modell berücksichtigt. Die Wechselwirkung der Granulation mit dem Magnetfeld führt zu einem Poynting-Fluss in die Atmosphäre. Das Modell reproduziert die Heizung in kurzen Bursts, die in früheren koronalen Simulationen gefunden wurde. Als Reaktion auf den Energieeintrag entwickelt der koronale Bogen eine komplexe Struktur aus kleinskaligen elektrischen Strömen und Plasmaströmungen. Die aus dem Modell des koronalen Bogens synthetisierte Emission zeigt eine Substruktur, welche die beobachteten Breiten koronaler "Strands" reproduziert.

Im nächsten Schritt untersuchen wir die magnetische Kopplung zwischen der Photosphäre und der Korona genauer. Wirbelbewegungen sind innerhalb der magnetischen Konzentrationen in der Photosphäre reichlich vorhanden und tragen nachweislich zur Heizung der Chromosphäre bei. Wir stellen fest, dass einige dieser Vortizes koronale Höhen erreichen und einen starken Poynting-Fluss über die Übergangsregion hinaus transportieren. Regionen mit verstärkter Wirbelstärke zeigen einen erhöhten Poynting-Fluss und höhere Heizraten. Der Einfluss von Wirbelströmungen auf die atmosphärische Struktur ist in der Chromosphäre und der unteren Korona am größten. Dort weisen die Wirbel eine höhere Dichte als der Hintergrund auf und verdrehte Magnetfeldlinien führen zu einer nach oben

gerichteten Lorentzkraft. Mit zunehmender Höhe werden die Vortizes deformiert, bis die ursprüngliche Rotationsbewegung nicht mehr erkennbar ist. Die Beziehung zwischen Wirbeln und koronaler Emission ist komplex. Während die Rotationsbewegung zu Gradienten im Magnet- und Geschwindigkeitsfeld führen kann, die eine erhöhte viskose und resistive Dissipation aufweisen und zu einer Aufhellung des Plasmas führen, hängt die koronale Emission sowohl von der Temperatur als auch von der Dichte ab, die in Vortizes im koronalen Teil des Plasmas nicht wesentlich erhöht ist. Daher gibt es keine Eins-zu-Eins-Entsprechung zwischen Vortizes und koronalen "Strands".

Zum Schluss berechnen wir synthetische Spektrallinienprofile der koronalen Emissionlinien, um die Reaktion der koronalen Emission auf die Heizung und die Plasmaströmungen zu untersuchen. Wir finden Werte für die nichtthermische Linienverbreiterung, die nahe an den Beobachtungswerten liegen, sowohl senkrecht als auch parallel zur Achse des Plasmabogens. Obwohl sie in der gleichen Größenordnung liegen, sind die nichtthermische Linienverbreiterungen parallel und senkrecht zur Sichtlinie auf unterschiedliche Prozesse zurückzuführen. Senkrecht zum magnetischen Führungsfeld wird das Geschwindigkeitsfeld durch kleinskalige Verdrehungs- und Scherungsbewegungen dominiert. Bei einer Sichtlinie parallel zum Magnetfeld verursacht die durch ein Heizereignis ausgelöste Evaporation eine Zunahme der nichtthermischen Verbreiterung. Für eine Sichtlinie senkrecht zum magnetischen Führungsfeld reproduzieren wir die Unabhängigkeit der nichtthermischen Linienverbreiterung von der Auflösung des Beobachtungsinstruments.

Dieses Modell bietet eine neue, umfassende Sicht auf die Prozesse, die die Struktur und Entwicklung koronaler Bögen bestimmen. Insbesondere treibt die komplexe magnetische Struktur den Energiefluss in die obere Atmosphäre an. Kleine Wirbelstrukturen erstrecken sich von der Photosphäre in die Korona und die internen turbulenten Bewegungen führen zu einer Feinstrukturierung des koronalen Bogens.

1 Introduction

1.1 The solar atmosphere

Despite our daily existence revolving around the Sun, we only ever see a part of it. The Sun's outer atmosphere remains hidden from view most of the time because the bright disc outshines the fainter atmosphere. Only during solar eclipses, when the disc is being obscured by the moon, the structure of the Sun's outer atmosphere is revealed to the naked eye.

The energy the Sun needs to bear its own weight and to generate its tremendous output of radiation stems from thermonuclear fusion in its interior. Energy is transmitted from the furnace at the solar core to the surface by radiation and convection.

The visible surface of the Sun is the photosphere, a thin layer that is only several 100 km thick. Most of the visible light in the continuum in the optical part of the spectrum from 4000 to 8000 Å and beyond is emitted from this region, while it is opaque in most spectral lines. The photosphere is structured by granulation. Hot plasma rises from the interior, loses some of its energy by radiation, and sinks down again in the cooler and darker intergranular lanes. The magnetic field is swept into the intergranular lanes by convective motions. It is concentrated into narrow flux tubes of kilogauss strength with a diameter of about 100 km. These continuously emerging and evolving magnetic elements form the so-called magnetic carpet (Priest 2014).

The layer above the photosphere appears red during solar eclipses and was therefore named the chromosphere (Greek: chromos color). Responsible for the colorful appearance are emission lines of the Balmer series. The chromosphere is mostly optically thin in the wavelength range from near-infrared to near-ultraviolet but optically thick in strong spectral lines. The temperature is on the order of 10^4 K (Priest 2014).

After reaching a minimum at about 500 km above the photosphere, the temperature starts to rise again. It increases steeply through the narrow transition region (TR) from about 10^4 K to several million Kelvin. Since the pressure is continuous across the transition region, the density falls by several orders of magnitude. The different layers of the atmosphere are not spherical shells, but have a complex structure. The transition region is not a static layer at a constant height, instead it is comprised of a thin, highly corrugated layer of plasma between the temperatures of 3×10^4 K and 3×10^5 K that is continuously heating up and cooling down. The steep temperature gradient is concentrated over a height range of just tens of kilometers, making the transition region difficult to model in numerical experiments.

Appearing as a bright halo around the disk of the Sun during eclipses, the corona is an extended atmosphere of tenuous hot plasma extending into the solar wind. With the ex-

ception of a few spectral lines, the corona is optically thin (Priest 2014). The dynamics of the low corona is dominated by the magnetic field. The lower parts of the corona are structured by closed magnetic field lines, while farther out the field opens up to the solar wind. Before the invention of the coronagraph, the corona could only be observed during solar eclipses. A coronagraph creates an artificial eclipse by blotting out light from the bright photosphere. The corona visible in optical wavelengths consists of the K- and F-corona, which arise from the scattering of light off electrons and dust, respectively (Priest 2014). Due to the extreme temperatures in the range from 8000 K to several million Kelvin, the corona mainly emits in ultraviolet (UV), extreme ultraviolet (EUV) and X-ray wavelengths (Stix 2004). This part of the spectrum is made up from emission lines from neutral atoms up to highly ionized particle species. X-ray emission can also provide information about stellar coronae (Güdel 2004). A downside of observations in these short wavelengths is that they are absorbed by Earth's atmosphere and the telescopes therefore need to be located in space. Information about the plasma at different temperatures and thus height levels can be obtained by using filters at different wavelengths.

1.1.1 The coronal heating problem

The quest for disentangling the mystery of the corona started with the observation of the green coronal line at 530.3 nm during a solar eclipse (Peter and Dwivedi 2014). At first this observation was falsely attributed to emission lines of a new element, the hypothetical "coronium". Instead, it was found in the 1930s that these lines did not originate from a mysterious new element, but instead from the fairly mundane iron and calcium (Grotrian 1939, Edlén 1943). Under the extreme environment of the solar atmosphere, hydrogen is fully ionized and atoms of heavier elements such as iron are also stripped of most of their electrons. Forbidden spectral lines cannot be observed in the laboratory because the gas density cannot be lowered sufficiently. The identification of the observed spectral lines as emission lines of highly ionized elements such as Fe IX and Ca XIV enabled Hannes Alfvén in the 1940s to draw the conclusion that the corona must be extremely hot (Peter and Dwivedi 2014).

While the photosphere has a temperature of roughly 6000 K, the corona is significantly hotter with temperatures up to several million Kelvin. This defies the expectation that the temperature should decrease with increasing distance to a heat source. The coronal heating problem consists of the question how energy is transported from the photosphere to the corona against the temperature gradient and how it is converted into heat. The heating of the corona is a current unsolved problem in astrophysics. Direct transport of heat by thermal conduction to the outer layers of the solar atmosphere would violate the second law of thermodynamics, which states that heat can only flow from the hotter to the cooler reservoir. Since the plasma in the corona is optically thin, radiation cannot be responsible for the heating. Another process is needed to explain the energy transport and release. The only known agent that can be responsible for the transport of energy is the magnetic field. The interaction of photospheric granulation and the magnetic field leads to an energy flux into the atmosphere. The main groups of models are based on either the excitation of magnetohydrodynamic waves by turbulent motions at the surface and subsequent dissipation of these waves, or reconnection resulting from slowly built up stresses in the magnetic field depending on the timescales of the surface motions driving

the magnetic field evolution. Only cool stars have coronae, since the surface motions due to magnetoconvection are needed to drive the magnetic field. X-ray emission has also been observed from O- and B stars, but in this case, acoustic shocks in the stellar wind are the likely cause of the emission (Güdel 2004).

Due to the low density of the corona, the energy required to heat it to temperatures of several million Kelvin is just a fraction of the energy required to heat the much denser chromosphere. Coronal and chromospheric heating have to be treated together (Priest 2014).

1.2 Magnetohydrodynamics

1.2.1 Assumptions

In magnetohydrodynamics, the behavior of a collection of particles is described by continuous variables such as density, temperature and the velocity field. For this to be a sufficiently accurate description of reality, several assumptions have to be made. The first assumption is that the matter under consideration can be described as a plasma. The term plasma is only applicable if the number of particles inside a sphere with a radius of the Debye length

$$\lambda_D = \sqrt{\frac{k_B T}{4\pi n_e e^2}} \quad (1.1)$$

is large (Priest 2014). If that is the case, the plasma is quasi-neutral on length scales exceeding the Debye length.

MHD is concerned with the macroscopic behavior of a fluid. In order to be described as a continuum, variations of the thermodynamic variables have to take place over length scales much larger than internal length scales such as the ion gyroradius. The plasma has to be strongly collisional so that it can be treated as being in thermal equilibrium. This means that its state can be described by a single well-defined temperature and the velocity distribution is roughly Maxwellian. This approximation is valid if we regard only timescales larger than timescales of collisions in the fluid and the ion gyroperiod and length scales much larger than the mean free paths that the particles in the plasma can travel between collisions. This assumption could break down in the steep temperature and density gradients in the narrow transition region (Peter 2015). We assume that all relevant speeds are much smaller than the speed of light. We also neglect effects from the curvature of spacetime and therefore neglect relativistic effects.

The plasma is treated as a single fluid without differentiating between charged and neutral particles, although this assumption might be problematic in the cool and rarefied parts of the solar atmosphere. The action of the magnetic force, that is only felt by charged particles, is communicated to neutral species by collisions. These assumptions constitute the magnetohydrodynamic approximation.

1.2.2 Equations

Magnetohydrodynamics combines the Maxwell's equations with the Navier-Stokes equations describing the motion of a fluid. In this section, we introduce and briefly discuss the relevant equations for solar physics. For a detailed discussion, see Priest (2014).

1.2.2.1 Maxwell's equations

The Maxwell equations describing the interplay of time-dependent electric and magnetic fields in cgs units are:

$$\nabla \cdot \mathbf{E} = 4\pi\rho_e, \quad (1.2)$$

$$\nabla \cdot \mathbf{B} = 0, \quad (1.3)$$

$$\nabla \times \mathbf{E} = -\frac{1}{c} \frac{\partial \mathbf{B}}{\partial t}, \quad (1.4)$$

$$\nabla \times \mathbf{B} = \frac{4\pi}{c} \mathbf{j} + \frac{1}{c} \frac{\partial \mathbf{E}}{\partial t}. \quad (1.5)$$

The first equation is Gauss' law describing how a static electric field \mathbf{E} arises from a distribution of electric charges with ρ_e being the charge density. The second equation is the magnetic analogue of Gauss' law stating that the magnetic field \mathbf{B} is divergence-free, consequentially there are no magnetic monopoles. The third and fourth equations are Faraday's law of induction and Ampère's law with Maxwell's addition describing time-dependent electric and magnetic fields. Faraday's law determines how a time-varying magnetic field induces an electric field \mathbf{E} , and Ampère's law states that magnetic fields can be produced by both electric currents and an electric field varying in time, with \mathbf{j} being the current density. The second term on the right hand side is called the displacement current.

Although the plasma is usually treated as a continuous fluid in MHD, it consists of charged particles experiencing forces due to the electric and magnetic fields present in the plasma. The proportionality between the current density and the electric field strength is called Ohm's law. The proportionality constant is the electric conductivity σ . Since Ohm's law is valid in the co-moving frame of reference, charged particles moving in magnetic field \mathbf{B} and electric field \mathbf{E} experience not only an electric force due to the field \mathbf{E} as they would at rest, but also an additional electric field $\frac{1}{c}(\mathbf{v} \times \mathbf{B})$ (Priest 2014). The current density in a frame of reference moving with the plasma is then

$$\frac{1}{\sigma} \mathbf{j} = \mathbf{E} + \frac{1}{c} \mathbf{v} \times \mathbf{B}, \quad (1.6)$$

with σ being the electrical conductivity. In ideal MHD, the conductivity is assumed to be infinite due to zero resistivity. Ohm's law then reduces to

$$\mathbf{E} = -\frac{1}{c} \mathbf{v} \times \mathbf{B}. \quad (1.7)$$

In the phenomena studied in solar physics with the help of MHD, variations in the electric and magnetic fields are usually considered nonrelativistic. Under the assumption of non-

relativistic speeds, we can neglect the displacement term. With characteristic electromagnetic or plasma speeds $v_0 = l_0/t_0$, where l_0 and t_0 are typical length and time scales, we can estimate the relative importance of the displacement term (see Priest (2014)). Using Ohm's law for ideal MHD, we can approximately express $|\mathbf{E}|$ as $|\mathbf{E}| = -\frac{1}{c}|\mathbf{v} \times \mathbf{B}| \approx -\frac{v_0}{c}B$. The time derivative of \mathbf{E} can be approximated as $\frac{\partial \mathbf{E}}{\partial t} \approx \frac{E}{t_0} = \frac{-v_0 B}{t_0}$. The displacement current can then be approximately expressed as

$$\frac{1}{c} \frac{\partial \mathbf{E}}{\partial t} \approx \frac{E}{ct_0} = -\frac{v_0 B}{c^2 t_0} = -\frac{v_0^2 B}{c^2 l_0}. \quad (1.8)$$

With $|\nabla \times \mathbf{B}| \approx \frac{B}{l_0}$, the displacement term is of the order of magnitude $\frac{E}{ct_0} \approx \frac{v_0^2}{c^2} |\nabla \times \mathbf{B}|$ and can be neglected for $v_0 \ll c$.

Equation 1.5 can then be simplified to

$$\nabla \times \mathbf{B} = \frac{4\pi}{c} \mathbf{j}. \quad (1.9)$$

1.2.2.2 The frozen flux theorem

In a perfectly conducting fluid, plasma and magnetic field cannot move independently in the direction transverse to the magnetic field lines. The magnetic field lines are frozen into the plasma. The parameter plasma β , which is defined as the magnetic-to-fluid pressure ratio $\beta = \frac{P_{\text{gas}}}{P_{\text{mag}}}$, with the magnetic pressure defined as $P_{\text{mag}} = B^2/(8\pi)$, determines whether the magnetic field or the plasma motions govern the dynamics of a system. Depending on the value of plasma beta, the magnetic field lines either push the plasma or are dragged by the plasma. This follows from the induction equation, since plasma moving across magnetic field lines would lead to an infinite current density. This would require infinite energy. The assumption of the magnetic field and plasma being frozen together allows for the tracing of magnetic field lines in time by following a parcel of plasma in time and at every timestep tracing the magnetic field line connected to the moving parcel. In reality, the electric conductivity in the solar corona is not infinite and magnetic field lines can diffuse through the plasma.

1.2.2.3 The magnetic diffusivity

If the corona is assumed to be a fully ionized plasma, the conductivity is then $\sigma = n_e e^2 \tau_{ei} / m_e$. τ_{ei} is the effective electron collision time for a hydrogen plasma, while n_e and m_e are electron density and mass. The values derived by Spitzer (1962) for the electrical conductivity and magnetic diffusivity are

$$\sigma = 1.53 \times \frac{T^{3/2}}{\ln \Lambda} \text{ mho cm}^{-1} \quad (1.10)$$

$$\eta = 5.2 \times 10^{11} \ln \Lambda T^{-1.5} \text{ cm}^2 \text{ s}^{-1}. \quad (1.11)$$

The Coulomb logarithm $\ln \Lambda$ is weakly dependent on temperature and density and has typical values in the range between 5 and 20. With typical values of the coronal temperature of 2.5 MK and density of $10^{-14.8} \text{ g cm}^{-3}$ in our simulations, and a Coulomb

logarithm $\ln \Lambda = 20$ the Spitzer value for the magnetic diffusivity is $2631 \text{ cm}^2\text{s}^{-1}$ and the Spitzer viscosity is $6.9 \times 10^{14} \text{ cm}^2\text{s}^{-1}$. The value for the Spitzer resistivity lies well below diffusivities associated with magnetic Reynolds numbers currently achievable in simulations.

1.2.2.4 The induction equation

Combining Faraday's law with Ohm's law to eliminate electric fields and current yields

$$\frac{\partial \mathbf{B}}{\partial t} = -\nabla \times (-\mathbf{v} \times \mathbf{B} + c\mathbf{j}/\sigma) \quad (1.12)$$

$$= \nabla \times (\mathbf{v} \times \mathbf{B}) - \nabla \times (c\mathbf{j}/\sigma). \quad (1.13)$$

$$(1.14)$$

Using the relation between the magnetic diffusivity and the electrical conductivity $\eta = c^2/(4\pi\sigma)$ and Ampère's law $\mathbf{j} = \frac{c}{4\pi}\nabla \times \mathbf{B}$ we get the induction equation

$$\frac{\partial \mathbf{B}}{\partial t} = \nabla \times (\mathbf{v} \times \mathbf{B}) - \nabla \times (\eta \nabla \times \mathbf{B}). \quad (1.15)$$

For constant values of the magnetic diffusivity, this becomes

$$\frac{\partial \mathbf{B}}{\partial t} = \nabla \times (\mathbf{v} \times \mathbf{B}) + \eta \nabla^2 \mathbf{B}. \quad (1.16)$$

The first term on the right hand side states that material motions lead to either increase or decrease of the magnetic field by induction, while the second term describes the decay of the magnetic field due to finite magnetic diffusivity. A measure for the relative importance of induction and magnetic diffusion is the magnetic Reynolds number. The magnetic Reynolds number is defined as $R_m = \frac{uL}{\eta}$ where u is a typical velocity, L a typical length scale and η the magnetic resistivity. The evolution of the magnetic field depends on whether the magnetic Reynolds number is large or small. For large Reynolds numbers, the magnetic field and the plasma are frozen together, a plasma parcel connected to a certain field line remains connected to that field line. If the Reynolds number is small, the induction equation reduces to a diffusion equation and the magnetic field can diffuse through the plasma. The corresponding diffusion timescale is $\tau_{\text{diff}} = L^2/\eta$. Small-scale structures in the magnetic field thus diffuse faster than large-scale structures. In the ideal MHD limit, for $R_m \gg 1$, the plasma is perfectly conducting and the induction equation becomes

$$\frac{\partial \mathbf{B}}{\partial t} = \nabla \times (\mathbf{v} \times \mathbf{B}). \quad (1.17)$$

In ideal MHD, Alfvén's frozen flux theorem holds and magnetic flux, field lines and magnetic topology are conserved. If the diffusive timescale is much larger than typical timescales in the system, the frozen flux theorem can still be used as an approximation to track field lines.

1.2.2.5 Fluid equations

The MHD equations are derived from the Boltzmann moment equations and arise from the conservation of various quantities such as mass, momentum and energy. The equations governing a fluid are the continuity equation, the momentum equation and the energy equation, respectively:

$$\frac{\partial \rho}{\partial t} + \nabla \cdot (\rho \mathbf{v}) = 0, \quad (1.18)$$

$$\frac{\partial \rho \mathbf{v}}{\partial t} = -\nabla \cdot (\rho \mathbf{v} \mathbf{v}) - \nabla P + \mathbf{F}, \quad (1.19)$$

$$\frac{\partial E_{\text{tot}}}{\partial t} = -L, \quad (1.20)$$

where ρ is the mass density, \mathbf{v} the plasma velocity, P the plasma pressure and e the energy density. \mathbf{F} is the sum of external forces, E_{tot} is the total energy density $E_{\text{tot}} = \frac{1}{2}\rho v + \epsilon + B^2/8\pi$ comprised of kinetic, internal energy density ϵ and magnetic energy density in the presence of a magnetic field. L is the combination of sinks and sources for the energy density which will be discussed in detail in Sect. 1.2.3. The continuity equation states that mass is conserved since it is neither created nor annihilated. The density increases if mass flows into a cell and decreases if it flows out. With the help of the Lagrangian derivative $\frac{D}{Dt} = \frac{\partial}{\partial t} + \mathbf{v} \cdot \nabla$, the continuity equation can be expressed as

$$\frac{D\rho}{Dt} + \rho \nabla \cdot \mathbf{v} = 0. \quad (1.21)$$

The Lagrangian or material derivative yields time variation in the reference frame of a moving gas parcel.

The second equation states the conservation of momentum. The momentum of the plasma in a given grid cell changes by advection of plasma into or out of the cell or by external forces. The specific forces entering the equation depend on the problem under consideration. We use the momentum equation in the form

$$\frac{\partial \rho \mathbf{v}}{\partial t} = -\nabla \cdot (\rho \mathbf{v} \mathbf{v}) - \nabla P + \frac{1}{c} \mathbf{j} \times \mathbf{B} + \mathbf{F}_g + \mathbf{F}_{\text{visc}}. \quad (1.22)$$

The forces acting on the plasma are the force due to the pressure gradient ∇P , the Lorentz force per unit volume $\frac{1}{c} \mathbf{j} \times \mathbf{B}$ and the gravitational force $\mathbf{F}_g = -\rho \mathbf{g}$. \mathbf{g} is a vector pointing towards the center of the Sun. At the solar surface, the gravitational acceleration can be assumed to be constant and has the value $g_{\odot} = 2.74 \times 10^4 \text{ cm s}^{-2}$. In case of a nonzero viscosity, we have an additional viscous force $\mathbf{F}_{\text{visc}} = \rho \nu [\nabla^2 \mathbf{v} + \frac{1}{3} \nabla(\nabla \cdot \mathbf{v})]$, with ν being the coefficient of kinematic viscosity.

Additional forces, such as the centrifugal force and coriolis force, arise in the case of a rotating reference frame. We focus in this work on a small enough region of the Sun that the influence of rotation can be neglected.

1.2.2.6 The Lorentz force

The Lorentz force

$$\mathbf{F}_L = \frac{1}{c} \mathbf{j} \times \mathbf{B} \quad (1.23)$$

arises from the motion of charged particles across the magnetic field. For plasma motions along the magnetic field, the resulting Lorentz force is zero. The Lorentz force can therefore not accelerate plasma along the magnetic field lines. With $\mathbf{j} = \frac{c}{4\pi} \nabla \times \mathbf{B}$ this becomes

$$\mathbf{F}_L = \frac{1}{4\pi} (\nabla \times \mathbf{B}) \times \mathbf{B}. \quad (1.24)$$

The Lorentz force can be decomposed into a contribution from magnetic tension and a contribution from the magnetic pressure by making use of vector calculus identities:

$$\mathbf{F}_L = \frac{1}{4\pi} \left[(\mathbf{B} \cdot \nabla) \mathbf{B} - \frac{1}{2} \nabla (\mathbf{B} \cdot \mathbf{B}) \right] \quad (1.25)$$

$$= \frac{(\mathbf{B} \cdot \nabla) \mathbf{B}}{4\pi} - \nabla \left(\frac{B^2}{8\pi} \right). \quad (1.26)$$

The first term is a force arising from a variation in \mathbf{B} along the direction of \mathbf{B} . This is the case if the magnetic field is curved. The tension force has a non-zero component normal to \mathbf{B} and increases with decreasing radius of curvature. This tension force plays a role in the propagation of magnetohydrodynamic waves.

The second term arises in response to a gradient in the magnetic pressure $B^2/8\pi$. The magnetic pressure is a scalar quantity and therefore uniform in all directions. The magnetic tension force and the magnetic pressure force in the direction of \mathbf{B} cancel, resulting in a force normal to \mathbf{B} . Effects of the two components of the Lorentz force are to shorten magnetic field lines through the tension part and to compress plasma by magnetic pressure. The magnetic pressure inside a magnetic flux tube has to be compensated by the gas pressure in the exterior. Magnetic flux tubes therefore have a decreased gas pressure compared to their environment.

1.2.3 The energy equation

The right-hand-side of the energy equation contains all the sinks and sources of energy. The energy in a point in space can be changed by advection, work done by the Lorentz force, heat conduction, radiative gains and losses, and resistive and viscous dissipation. Additionally, other forces in the system can do work on the plasma, such as the gravitational or the viscous force. We assume an energy equation of the form

$$\begin{aligned} \frac{\partial E_{\text{HD}}}{\partial t} = & -\nabla \cdot [\mathbf{v}(E_{\text{HD}} + P)] + \rho \mathbf{v} \cdot \mathbf{g} + \mathbf{v} \cdot \mathbf{F}_L + \nabla \cdot \mathbf{q} + Q_{\text{rad}} + Q_{\text{thin}} \\ & + Q_{\text{res}} + \nabla \cdot (\boldsymbol{\tau} \cdot \mathbf{v}), \end{aligned} \quad (1.27)$$

where $E_{\text{HD}} = \frac{1}{2}\rho v^2 + \epsilon$ is the sum of kinetic and internal energy density, P is the pressure. The first term describes the transfer of energy due to the motion of fluid mass, $\rho \mathbf{v} \cdot \mathbf{g}$ the work done by the gravitational force, $\mathbf{v} \cdot \mathbf{F}_L$ the Lorentz force work, $\nabla \cdot \mathbf{q}$ the divergence of the heat flux, Q_{rad} the optically thick radiative heating or cooling, Q_{thin} the optically thin radiative losses, Q_{res} the resistive heating by Ohmic dissipation and $\nabla \cdot (\boldsymbol{\tau} \cdot \mathbf{v})$ the work done by the viscous force with $\boldsymbol{\tau}$ being the viscous stress tensor. In the following we will discuss the individual terms on the right hand side.

1.2.3.1 Heat conduction

The heat flux due to particles can be expressed as (Priest 2014)

$$\mathbf{q} = -\kappa \nabla T. \quad (1.28)$$

κ is the thermal conduction tensor. The heat flux term in eq. 1.28 can be decomposed into a contribution along and across the magnetic field:

$$\nabla \cdot \mathbf{q} = \nabla \cdot [\kappa_{\parallel} \hat{\mathbf{b}} (\hat{\mathbf{b}} \cdot \nabla) T + \kappa_{\perp} \hat{\mathbf{b}} \times (\hat{\mathbf{b}} \times \nabla) T], \quad (1.29)$$

where $\hat{\mathbf{b}}$ is the unit vector in the direction of the magnetic field and κ_{\parallel} and κ_{\perp} are the conduction coefficients parallel and perpendicular to the magnetic field, respectively. Electrons are responsible for the heat transport. The conduction coefficient parallel to the magnetic field is:

$$\kappa_{\parallel} = \kappa_0 T^{5/2} = 1.8 \times 10^{-10} \frac{T^{5/2}}{\ln \Lambda} \text{Wm}^{-1} \text{K}^{-1}, \quad (1.30)$$

In a strong magnetic field, the conduction coefficient for heat conduction parallel to the magnetic field lines is much larger than the coefficient for heat conduction across field lines.

In a strong magnetic field, the movement of the electrons perpendicular to the magnetic field is restricted, therefore heat conduction occurs mainly parallel to the magnetic field. Heat conduction perpendicular to the magnetic field is mainly due to collisions of protons. If the magnetic field is sufficiently strong, the heat flux across the magnetic field can be neglected and the heat conduction term can be approximated as

$$\nabla \cdot \mathbf{q} = \nabla \cdot (\kappa_0 T^{5/2} \hat{\mathbf{b}} (\hat{\mathbf{b}} \cdot \nabla) T). \quad (1.31)$$

The heat conduction is strongly temperature dependent and increasingly efficient at high temperatures. Under coronal conditions with temperatures of several million Kelvin, this can lead to problems with numerical simulations. This issue is further discussed in Sect. 2.1.6. The assumption behind Spitzer heat conduction is that the electron mean free path is much shorter than the temperature scale height. This assumption is problematic in the transition region due to the steep temperature gradient (Peter 2015).

1.2.3.2 Ohmic dissipation

Due to the finite resistivity in the corona, electric currents are dissipated due to collisions in the plasma. The Ohmic heating term is defined as

$$Q_{\text{res}} = \frac{\eta}{4\pi}(\nabla \times \mathbf{B})^2 = 4\pi\eta\mathbf{j}^2, \quad (1.32)$$

with η being the magnetic diffusivity.

1.2.3.3 Viscosity

The viscosity (internal friction) of a fluid influences the motion of the fluid by transport of momentum and energy. Momentum is transferred between fluid parcels both with the mass of the moving fluid and by particle collisions. The viscous stress tensor τ quantifies the latter part. The momentum is transferred from regions with larger velocity to regions with smaller velocity (Landau and Lifshitz 1987). The viscous stress tensor is defined as

$$\tau = \rho\nu(\nabla\mathbf{v} + \nabla\mathbf{v}^T - \frac{2}{3}(\nabla \cdot \mathbf{v})\mathbf{I}). \quad (1.33)$$

The kinematic viscosity ν is a function of temperature and density and generally not constant in a fluid. The viscosity associated with compression of the fluid is neglected for most fluids. The viscous force is given by the divergence of the viscous stress tensor. This force can lead to heating, but also to a change of kinetic energy density in a plasma parcel due to friction.

The kinematic viscosity according to Spitzer (1962) for a fully ionized hydrogen plasma is

$$\nu = 2.21 \times 10^{-15} \frac{T^{2.5}}{\ln \Lambda \rho} \text{cm}^2 \text{s}^{-1}. \quad (1.34)$$

In contrast to values for the resistive diffusivity in numerical simulations, the expected value for the Spitzer viscosity is even larger than numerical values that have been obtained in simulations (Rempel 2017). The scales of energy dissipation due to viscous heating should thus be captured correctly in the simulations. The ratio of viscous to magnetic diffusivities is measured by the magnetic Prandtl number: $P_m = \nu/\eta$. If the Prandtl number is sufficiently high, resistive heating can be neglected compared to viscous heating and energy is dissipated due to thermalization of reconnection outflows (Rempel 2017). The numerical viscosity then provides an adequate parametrization of the microphysics involved in viscous energy dissipation.

1.2.3.4 Radiative losses

In the optically thin regime, the radiative losses are no longer coupled to the radiation field. The optically thin radiative losses are only dependent on local particle densities and temperature:

$$Q_{\text{thin}} = -n_e n_H \Lambda(T), \quad (1.35)$$

where n_e is the electron density and n_H the density of hydrogen nuclei. In a fully ionized plasma both are equal. $\Lambda(T)$ is a temperature dependent radiative loss function. Usually a tabulated version of $\Lambda(T)$ is employed.

In the optically thick regime, the full radiative transfer equations have to be solved. The optical depth at frequency ν is

$$d\tau_v = -\kappa_v \rho dr. \quad (1.36)$$

The variation of the intensity with depth is then

$$\mu \frac{dI_v}{d\tau_v} = I_v - S_v, \quad (1.37)$$

where $\mu = \cos \theta$ is the direction along which integration takes place and the source function S_v is defined as the ratio between the emission and the absorption coefficient. Multiplying each side with $\mu^{-1} \exp -\tau_v/\mu$ and integrating from $\tau_v = 0$, which is the location of the observer, to $\tau_{0v} = \infty$ which is located deep inside the star, we obtain for the observed intensity at an angle θ (Stix 2004):

$$I_v(0, \mu) = \frac{1}{\mu} \int_0^\infty S_v(\tau_v) \exp -\tau_v/\mu d\tau_v. \quad (1.38)$$

The radiation field is coupled to the MHD equations via the term Q_{rad} . Assuming that the matter is in local thermodynamic equilibrium, the source function can be set to the Planck function $S_v(T) = B_v(T) = \frac{2h\nu^3}{c^2} \frac{1}{e^{h\nu/k_B T} - 1}$. The radiative energy flux is computed by integrating the intensity over all possible ray directions

$$\mathbf{F}_v = \int_{4\pi} I_v(\mu) \boldsymbol{\mu} d\omega. \quad (1.39)$$

The radiative source term can then be computed from the divergence of the radiative flux

$$Q_{\text{rad}} = - \int (\nabla \cdot \mathbf{F}_v) dv. \quad (1.40)$$

In the grey radiative transfer approximation, the opacity is calculated as an average over frequency. The frequency dependence is calculated from the probability of absorption or scattering for a photon of a certain energy. The Rosseland mean opacity is defined as (Stix 2004)

$$\frac{1}{\kappa} = \frac{\int_0^\infty \frac{1}{\kappa_\nu} \frac{dB_\nu}{dT} d\nu}{\int_0^\infty \frac{dB_\nu}{dT} d\nu}. \quad (1.41)$$

This is the harmonic mean. Thus more energy is transported at frequencies where the matter is more transparent. Since the temperature gradient of the radiation field is used as weight, more energy is transported at frequencies where the radiation field has a larger temperature dependence.

1.2.3.5 The Poynting theorem

The Poynting flux vector \mathbf{S} is a measure for magnitude and direction of the flux of electromagnetic energy and defined as

$$\mathbf{S} = \mathbf{E} \times \mathbf{H} = \frac{1}{4\pi} \mathbf{B} \times (\mathbf{v} \times \mathbf{B}) + \frac{\eta}{4\pi} \mathbf{j} \times \mathbf{B}. \quad (1.42)$$

The second term is ignored in ideal MHD and often neglected under the assumption of small resistivity η .

We are mainly interested in the vertical component of the Poynting flux vector, since this is the component responsible for the injection of energy into the corona. The vertical component of the Poynting flux vector in ideal MHD can be decomposed as follows (Shelyag et al. 2012):

$$\begin{aligned} S_z &= \frac{1}{4\pi}(v_z(B_x^2 + B_y^2) - B_z(v_x B_x + v_y B_y)) \\ &= S_z^v + S_z^h. \end{aligned} \quad (1.43)$$

The first term is the part of the Poynting flux generated by the vertical transport of horizontal field, for example during flux emergence, the second term is the component generated by horizontal flows acting on the vertical field.

According to Poynting's theorem, the energy flux into the atmosphere due to the Poynting flux can be written as (Priest 2014)

$$\int \frac{\mathbf{E} \times \mathbf{B}}{4\pi} \cdot d\mathbf{S} = \int \frac{j^2}{\sigma} + \mathbf{v} \cdot \mathbf{j} \times \mathbf{B} + \frac{\partial}{\partial t} \left(\frac{B^2}{8\pi} \right) dV. \quad (1.44)$$

The Poynting flux can have several effects on the upper atmosphere. The first term on the right hand side corresponds to heating of the plasma by Ohmic dissipation, the second term to work done by the Lorentz force, and the third term to a change in the magnetic energy. Not all the Poynting flux is thus necessarily converted immediately into heat. Dissipation of the injected electromagnetic energy can either occur directly through Ohmic dissipation or through ohmic or viscous dissipation of outflows or waves generated by reconnection. The treatment of dissipation is problematic in simulations because the regions of dissipation are so thin that the assumption of MHD breaks down and kinetic treatment becomes necessary.

1.3 Magnetic reconnection

Reconnection is a change in the magnetic connection of plasma elements in an almost-ideal plasma with a magnetic Reynolds number outside of current sheets much larger than unity (Priest 2014). If the resistivity is zero, according to Alfvén's frozen-in theorem magnetic field lines and plasma are frozen together and a plasma element connected to a certain field line will remain connected to the same field line. Reconnection can take place when non-ideal effects become important in a localized region, allowing a parcel of plasma to become connected to a different field line. Through magnetic reconnection, magnetic energy can be converted into heat by Ohmic dissipation, or magnetic energy might be converted into kinetic energy due to acceleration of plasma. Shock waves and turbulence can arise from reconnection. Changes in the field line connectivity redirect fluxes of particles and heat.

1.3.1 2D magnetic reconnection

A current sheet that has been formed will diffuse away. A steady state can be established if magnetic field and plasma are entering the reconnection region at the same rate as the diffusion of the magnetic field takes place. In the Sweet-Parker model, a current sheet is formed between two regions with opposite magnetic polarities. The magnetic field lines then form an intersection, a so-called X-type neutral point (Sweet 1958, Priest 2014). At the neutral point itself, the magnetic field vanishes. Plasma is accelerated at the reconnection site by reconnected magnetic field lines shortening due to the tension force caused by the curvature of the newly reconnected magnetic field lines. The reconnection rate or inflow plasma speed for the Sweet-Parker mechanism is $v_i = v_{Ai} / \sqrt{R_m}$ with v_{Ai} being the inflow Alfvén speed. The Sweet-Parker mechanism leads to slow reconnection, since the reconnection rate is slow for large Reynolds numbers.

A small Sweet-Parker current sheet forming in a region with locally enhanced magnetic diffusivity can produce shock waves which also convert magnetic energy into kinetic energy and heat. This configuration leads to fast reconnection. For reconnection to proceed at a fast rate, the magnetic diffusivity needs to be nonuniform. This mechanism is referred to as Petschek mechanism after its discoverer (Petschek 1964). Other types of 2D reconnection are possible.

1.3.2 3D magnetic reconnection

While reconnection can only occur at a null point in two dimensions, more magnetic topologies are possible in three dimensions. Reconnection can occur whenever antiparallel magnetic field components are present in a region where the plasma has a nonzero resistivity (Schindler et al. 1988). The condition for reconnection to occur is then

$$\int E_{\parallel} ds \neq 0 \quad (1.45)$$

along a magnetic field line.

In three dimensions, reconnection can occur at null points, but also at the boundary between separate flux systems, the separatrix surfaces, and in a number of additional topologies.

1.4 Coronal heating mechanisms

The two main competing models are DC (direct current) models and AC (alternating current) models. In DC models, heating arises from motions at the solar surface below the Alfvén speed. The photospheric motions lead to slowly changing currents in the higher atmosphere. In contrast to that, AC heating assumes faster changes that lead to waves travelling up into the corona. In AC models, energy is deposited in the atmosphere by dissipation of MHD waves while in the DC model impulsive reconnection events act as dissipation mechanism (Priest 2014). In addition to motions at the solar surface, waves may also result from reconnection sites and can in turn cause impulsive heating events. Heating of the corona by shocks resulting from nonlinear Alfvén waves can lead to "nanoflare-like" variations in intensity in simulations (Moriyasu et al. 2004). In the real corona, several

mechanisms could be connected and be at work at the same time (Priest 2014). A current challenge is to measure their relative importance. Different processes could be dominant in different regions on the Sun. In stellar coronae, the magnetic structures and thus also the heating mechanism could differ from the Sun depending on mass, surface gravity and rotation period (Güdel 2004).

1.4.1 DC heating

In the DC model, horizontal photospheric motions shuffle the magnetic field around and lead to tangling of the magnetic field lines (Parker 1983). The magnetic field evolves away from a potential configuration, storing energy in the process. The energy is injected at the coronal base by a Poynting flux (Klimchuk 2006)

$$\mathbf{S} = -\frac{1}{4\pi} B_v \mathbf{B}_h v_h, \quad (1.46)$$

where B_v and \mathbf{B}_h are the vertical and horizontal magnetic field components and v_h is the horizontal footpoint velocity. The Poynting flux has a second component arising from vertical transport of horizontal magnetic field, for example due to flux emergence. In the following, we will focus on the energy injection due to horizontal shuffling of the magnetic field. Typical horizontal velocities of magnetic flux tubes at the solar surface are $1 \times 10^5 \text{ cm s}^{-1}$ (Klimchuk 2006). If the horizontal and vertical magnetic field are assumed to be of similar order of magnitude, this process can lead to a sufficient Poynting flux to provide heat to the solar atmosphere. The major challenge is to explain how the injected energy is converted into heat in the solar atmosphere. Since the coronal plasma is almost ideal, magnetic reconnection can only occur in current sheets induced by the gradients in the magnetic field that build up due to motions at the solar surface. As the field geometry is becoming increasingly complicated due to braiding, the thickness of the current sheets decreases (Pontin and Hornig 2015). At some point, the current sheets become sufficiently thin for the magnetic Reynolds number to approach order unity and for magnetic reconnection to set in. This allows the magnetic field to rearrange itself into a lower energy state, releasing the stored magnetic energy in the process. The freed magnetic energy is converted either converted directly into heat or into kinetic energy that is later dissipated.

1.4.1.1 The Parker braiding model

In an infinite volume bounded by infinitely conducting planes containing a magnetic field spanning from one plate to the other and moved around by boundary motions, the magnetic field develops tangential discontinuities during the relaxation to a static equilibrium (Parker 1972). This model is illustrated in Fig. 1.1. For almost all possible boundary flows no smooth static equilibrium exists.

This hypothesis has never been formally proven or disproven (Pontin and Hornig 2020).

The tangling of field lines leads to gradients in the magnetic field and thus induces currents in the corona (Parker 1983). If the footpoint motions are sufficiently slow compared to the Alfvén wave travel time, the magnetic field evolves through a series of equilibria, storing magnetic energy in excess of the energy associated with the potential field. This

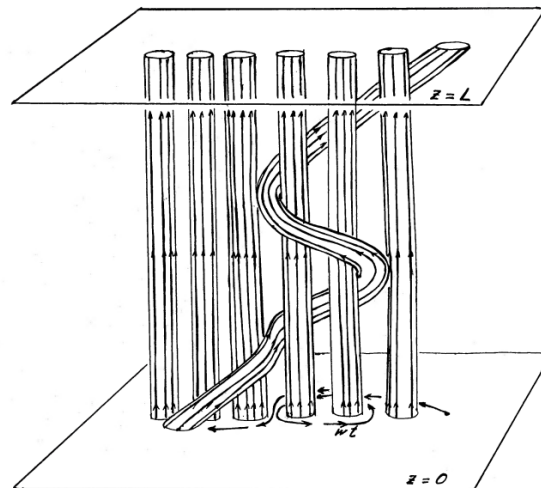


Figure 1.1: Sketch to illustrate the Parker field line braiding model. The motions at the boundaries $z = 0$ and $z = L$ braid the flux tubes around each other. Figure taken from Parker (1983). Credit: Parker, E. N.: 1983, ApJ 264, 642, DOI: 10.1086/160637, reproduced with permission © AAS

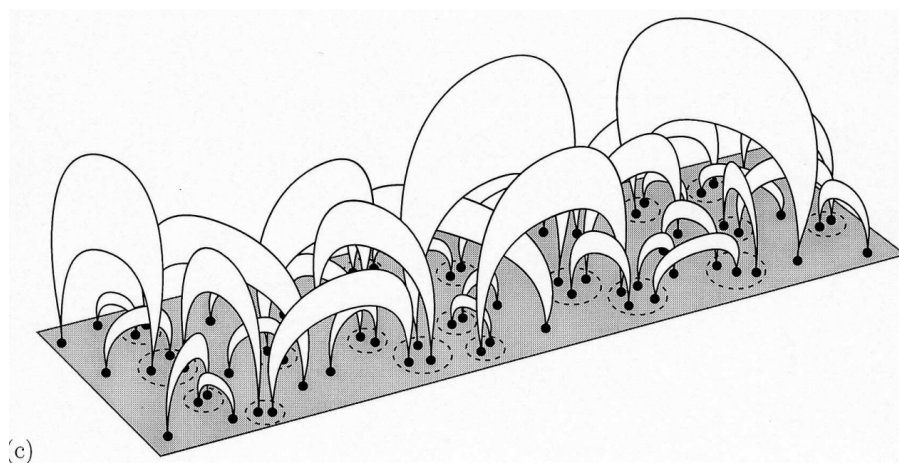


Figure 1.2: Sketch to illustrate the flux tube tectonics model. Magnetic elements at the photosphere are connected to multiple neighbors. Heating takes place at separatrix surfaces between the flux tubes. Figure taken from Priest et al. (2002). Credit: Priest, E. R., Heyvaerts, J. F., and Title, A. M.: 2002, ApJ 576(1), 533, DOI: 10.1086/341539, reproduced with permission © AAS

energy can be released by Ohmic dissipation of the currents and reconnection of braided field lines (Parker 1988), unresolved impulsive events dubbed "nanoflares".

1.4.1.2 Flux tube tectonics

Coronal loops are not isolated structures, they interact with their environment. The original braiding model did not take into account the complexity of the magnetic field on the Sun and assumed a uniform background field tangled by random motions. In the flux tube tectonics picture, the magnetic flux is assumed to be concentrated in many intense, discrete flux tubes in the photosphere, which are continuously moved around by photospheric motions. The magnetic elements are continuously emerging, fragmenting, merging and cancelling. These flux tubes have a diameter of 100 km, a magnetic field strength of 1200 G and a magnetic flux of 3×10^{17} Mx (Priest et al. 2002). In analogy to plate tectonics on Earth, this coronal heating model is called the fluxtube tectonics model. This idea is illustrated in Fig. 1.2. The boundary between separate flux systems, the separatrix surfaces, are preferred locations for the formation of current sheets. The heating occurs in current sheets formed and dissipated at separatrices and quasi-separatrix layers at boundaries between flux from different sources. Along the separatrices, the heating was found to be uniform, so the elementary flux tubes are expected to be heated uniformly. Most of the magnetic flux closes in the magnetic carpet at low heights, so from this model the heating would be expected to be strongest near the loop footpoints. The time range over which the field is replaced is 10-40 hours (Schrijver et al. 1998, Priest et al. 2002). This is also the timescale over which the process of reconnection of the large-scale magnetic field takes place. The strong magnetic elements are pushed around at the solar surface on the timescale of granulation, which is five minutes. This model does not take into account internal motions within photospheric concentrations, only the relative motion of magnetic elements. The smallest coronal loops have their footpoints in one such strong flux concentration and are bounded by current sheets, while larger loops link to several sources and can contain separatrix surfaces.

1.4.2 AC heating

The turbulent convection at the solar surface produces motions on a variety of timescales. In addition to slowly stressing the magnetic field, the photospheric motions also launch MHD waves propagating into the atmosphere (Alfvén 1947). If the driving motions cause coronal currents varying on timescales short compared to the Alfvén transit time, the nature of the heating is considered to be Alternating Current (AC) heating (Priest 2014). A variety of different wave types can exist in the solar atmosphere, such as sound waves, Alfvén waves, magnetosonic waves, or various magnetic flux tube waves (Klimchuk 2006). Through processes such as mode coupling, energy can be transferred between different wave modes so that the combination of wave modes present is a function of height. The estimated energy flux associated with waves in the low atmosphere is sufficient to heat the solar corona. It is however unclear how much of this energy flux is actually able to pass through the transition region into the corona due to the steep gradients in density and temperature. Acoustic and slow-mode magnetosonic waves will steepen into shocks and be damped, while fast magnetosonic waves undergo strong refraction and reflection. Alfvén waves are transverse and do not steepen into shocks, so they are the most promising candidates for a wave mode that reaches the corona to dispose energy (Klimchuk 2006). Alfvén waves do, however, undergo reflection at the transition region due to the

large increase in Alfvén speed. Transmission is only strong for loop resonance frequencies (Hollweg 1984). This is a problem for short loops, since the photosphere might not produce sufficient oscillatory power at high enough frequencies. Alfvén waves could also be produced in the corona itself, for example in magnetic reconnection sites. Since in this case the energy is first stored in the magnetic field stressed by slow motions, this scenario fits neither neatly in the DC nor in the AC category (Klimchuk 2006).

Similar to reconnection, energy release due to MHD waves occurs by resistive or viscous dissipation. For a long time it was thought that Alfvén waves could not be dissipated efficiently in the corona. Transverse gradients in the Alfvén velocity due to variations in density may enable the formation of small scales and the extraction of energy.

Alfvén waves have been found to be abundant in the corona (Tomczyk and McIntosh 2009). Energy fluxes inferred from nonthermal line broadening of coronal emission lines are sufficient for coronal heating, but the observed nonthermal broadening could also arise from unresolved motions such as field aligned flows produced by heating events (Patsourakos and Klimchuk 2006, Klimchuk 2006).

1.4.2.1 Alfvén waves

Alfvén waves are propagating perturbations in a magnetized plasma. The magnetic tension force acts as a restoring force (Alfvén 1942). Compressional or fast mode waves are associated with perturbations of the magnetic field and the plasma and propagate in any direction. For torsional or shear Alfvén waves the perturbations in the magnetic field and the plasma velocity are transverse to the direction of propagation and the magnetic guide field.

If the perturbations in the magnetic field are small compared to the guide field, the magnetic field can be expressed as the superposition of a strong guide field and a perturbation $\mathbf{B} = \mathbf{B}_0 + \mathbf{b}$. Assuming a homogeneous background state, a small velocity perturbation \mathbf{v}_1 and incompressibility $\nabla \cdot \mathbf{v}_1 = 0$, the system of MHD equations can be linearized. The dispersion relation for an Alfvén wave derived from linearized system is:

$$\omega^2 = v_A^2(\mathbf{k} \cdot \mathbf{e}_z), \quad (1.47)$$

$$\mathbf{v}_{\text{group}} = \frac{\partial \omega}{\partial \mathbf{k}} = v_A \mathbf{e}_z, \quad (1.48)$$

where \mathbf{e}_z is a unit vector in the direction of the magnetic guide field, \mathbf{k} is the wave vector directed in the direction of wave propagation, and v_A is the local Alfvén speed, which is defined as $v_A = B_0 / \sqrt{4\pi\rho}$. For a detailed derivation of the dispersion relation, see Priest (2014). If the wave vector and the direction of the guide field are orthogonal, the wave frequency ω is zero. The group velocity of an Alfvén wave packet is the Alfvén speed. The group velocity of a wave packet determines the velocity at which information and energy is transported. The energy is transported by an Alfvén wave packet in the direction of the guide field, while an individual Alfvén wave can travel at any inclination to the magnetic guide field except from the direction normal to the field (Priest 2014). The perturbations of velocity field \mathbf{v} and magnetic field \mathbf{b} are antiparallel if the wave propagates into the direction of the magnetic field. The perturbed velocity is orthogonal to the guide field since the Lorentz force is driving the velocity perturbation and only has a

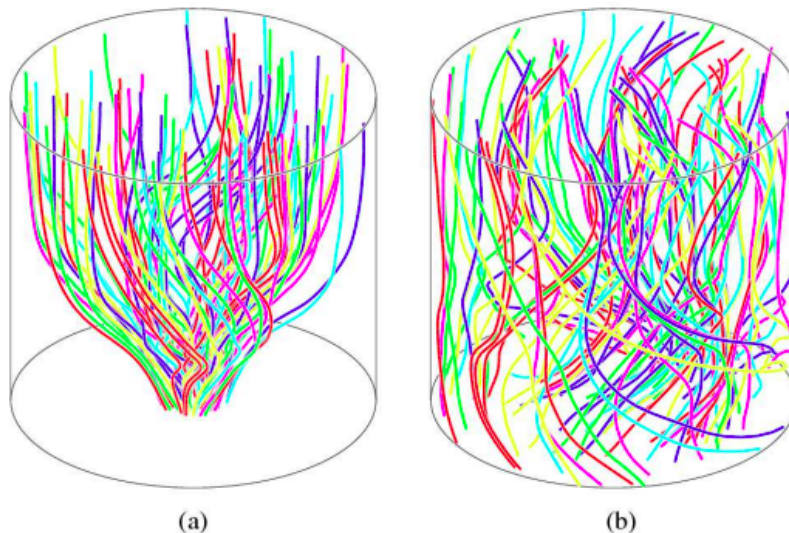


Figure 1.3: Magnetic field lines in the lower atmosphere (panel a)) and in the coronal part of the loop (panel b)) in the Alfvén wave turbulence model. Figure taken from van Ballegooijen et al. (2011). Credit: van Ballegooijen, A. A., Asgari-Targhi, M., Cranmer, S. R., and DeLuca, E. E.: 2011, *The Astrophysical Journal* 736(1), 3, DOI: 10.1088/0004-637X/736/1/3, reproduced with permission © AAS

component orthogonal to the guide field in the linear approximation. Linear Alfvén waves do not cause perturbations in the magnetic pressure since the perturbation is orthogonal to the guide field $P_m = \mathbf{b} \cdot \mathbf{B}_0 / 8\pi = 0$. The remaining part of the Lorentz force that can drive flows is the tension force.

In case of a homogeneous background medium, dissipation of the energy carried by Alfvén waves is very inefficient. The damping timescale can be shortened by processes such as resonant absorption (Ionson 1978) or phase mixing (Heyvaerts and Priest 1983). In the phase mixing scenario, different Alfvén speeds on neighboring field lines due to inhomogeneity in magnetic field and/or density causes Alfvén waves propagating along those field lines to become more and more out of phase. This leads to an energy cascade to small scales until the energy is dissipated.

1.4.3 MHD turbulence

The heating by reconnection or waves can also be described by magnetic turbulence. The observed broadening of emission lines from unresolved flows could stem from either reconnection outflows at current sheets or a superposition of Alfvén waves (Iroshnikov 1964, Kraichnan 1965). MHD turbulence can both cause and arise from magnetic reconnection and wave dissipation. In response to the winding by the footpoint motions, the corona tries to relax toward a force-free state. This can happen through an evolution through nonlinear force-free equilibria or through 3D reconnection preserving magnetic helicity (Priest 2014). Quantities conserved in the absence of dissipation are energy, magnetic helicity and cross-helicity. These invariants can undergo cascades from large to

small scales or from small to large scales (inverse cascade). According to a model by van Ballegooijen et al. (2011), the chromosphere and the corona can both be heated by turbulence generated by a superposition of Alfvén waves propagating up from the photosphere. The setup is illustrated in Fig. 1.3. Due to the steep increase in Alfvén velocity at the transition region, part of the wave energy is reflected at the boundary between chromosphere and corona and part of it is transmitted into the corona. This model, however, cannot explain the heating of the hottest loops in the center of active regions that can reach temperatures above 3 MK (Priest 2014). Furthermore, the estimated broadening of emission lines by the nonthermal motions exceed observed values (van Ballegooijen et al. 2017). The velocity amplitudes that would be necessary to heat the hot loops are therefore not compatible with observational constraints.

1.4.4 Flux cancellation

High resolution magnetograms recorded by IMAX on Sunrise as well as magnetograms from HMI onboard SDO revealed that some hot and bright active region loops with temperatures of several million Kelvin are anchored in regions with a dominant magnetic polarity and nearby smaller opposite-polarity patches (Chitta et al. 2017, 2018). The cancellation of these small opposite polarity patches could lead to reconnection in the chromosphere and subsequent heating of the loop. Coronal brightenings have been observed simultaneously with flux cancellation (Chitta et al. 2017, 2018). Evidence for reconnection at the base of active region loops was found with the Interface Region Imaging Spectrograph (IRIS) (Chitta et al. 2020). Small inverse Y-shaped plasma jets ejected from regions of flux cancellation have been observed. These jets provide a possible source of mass to the corona.

An analytical model for this cancellation nanoflare scenario was developed by Priest et al. (2018) and it was concluded that this mechanism could in principle provide sufficient energy to power the chromosphere and corona given that enough energy liberated by the flux cancellation leaks through to higher layers. Numerical models of this scenario were in good agreement with the analytical estimate (Syntelis et al. 2019).

1.4.5 Swirls

Rotating structures were found in observations of the photosphere (Brandt et al. 1988, Bonet et al. 2008, 2010) and observed as rotating rings in the chromospheric Ca II line (Wedemeyer-Böhm and Rouppe van der Voort 2009). Signatures of energy dissipation were observed in the low corona above swirls and they have been interpreted as energy channels into the low corona (Wedemeyer-Böhm et al. 2012). Vortex motions do not constitute a distinct heating mechanism, but could be responsible for channeling energy from the photosphere into the corona by twisting magnetic field lines.

In agreement with observations, abundant vortex motions have been found in simulations of solar surface magnetoconvection (Moll et al. 2011) and have been shown to carry Poynting flux into the chromosphere (Yadav et al. 2020a, 2021, Battaglia et al. 2021). They could also play a role for the formation of chromospheric jets accelerated by the upward directed Lorentz force arising from twisted magnetic field lines (Iijima and Yokoyama 2017). It was suggested that vortices in the lower atmosphere behave like

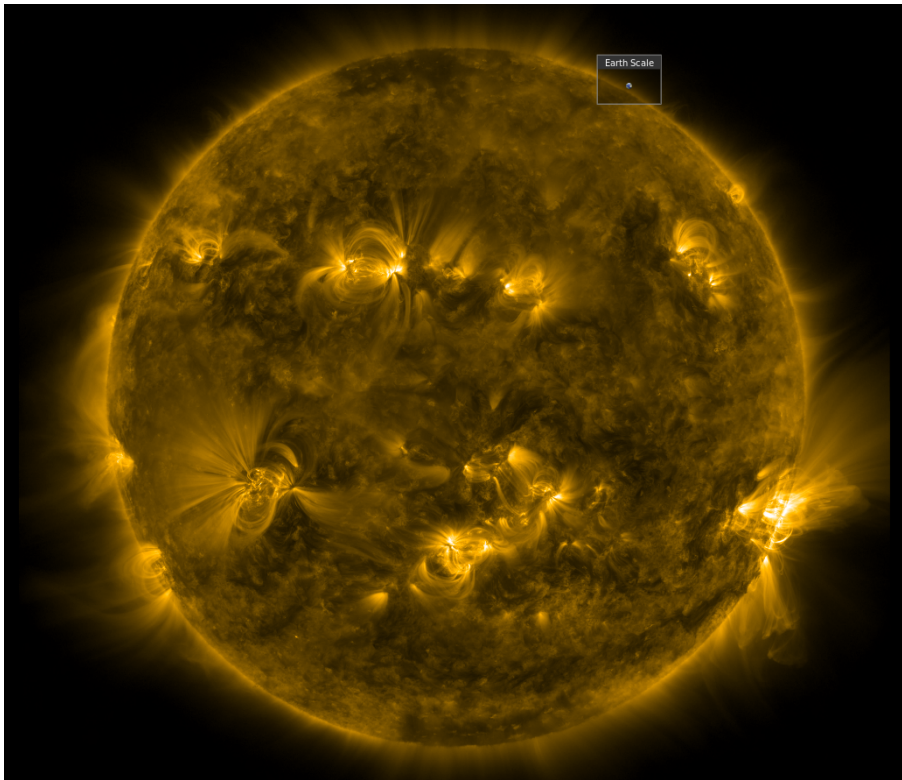


Figure 1.4: Coronal loops seen in the 171 Å band of AIA on Christmas 2021. The image was produced using helioviewer (Müller et al. 2017). Credit: SDO (NASA).

Alfvénic perturbations and could launch torsional Alfvén waves or pulses into the upper atmosphere (Fedun et al. 2011, Shelyag et al. 2013, Battaglia et al. 2021, Yadav et al. 2022).

1.5 Coronal loops

To the naked eye, the solar disk appears homogeneous. Zooming into a small region, a multitude of structures is manifesting itself. The structure of the solar atmosphere is determined by gravitational stratification and the geometry of the magnetic field. Coronal loops are bright magnetically closed structures of dense plasma confined by the magnetic field connecting different polarities at the solar surface, observable in X-ray and EUV light by EUV imagers such as SoHO/EIT, TRACE and SDO/AIA (Reale 2014). The magnetic field determines the loop structure, stores energy and directs the heat flow. Due to the high electric conductivity of the corona, the frozen-in condition holds and particles cannot move across the magnetic field. Since the magnetic field traps the plasma, coronal loops outline arches of magnetic field lines. The plasma temperatures in the coronal loops range from 1 to 10 MK. The heating mechanism that sustains coronal loops is subject to active discussions, as discussed above.

Loops appear to consist of many thin strands. Heat is conducted much more efficiently along than across the magnetic field, so that regions with different magnetic connectivity

are effectively thermally insulated from each other. Loop brightenings have also been observed to last longer than the loop cooling timescale, so it is likely that the loop consists of multithermal strands. The heat released in the corona is conducted along the field lines down to the chromosphere. The colder and denser chromospheric plasma is heated and expands into the atmosphere, filling the loop with hot and dense plasma. The density is then determined by the temperature of the plasma that is magnetically connected. When the loop fills with plasma, it brightens and can be detected in EUV or X-ray emission. After the heating event, the plasma cools down by conduction and radiation and drains from the loop. With decreasing density and temperature, the loop dims.

In thermal equilibrium, the time-dependent terms in the energy equation vanish. Assuming the coronal loop is static and $\mathbf{v} = 0$, the energy balance for a coronal loop is

$$H - Q_{\text{rad}} - \nabla \cdot \mathbf{q} = 0, \quad (1.49)$$

where H is the heating rate, Q_{rad} are the radiative losses and $\nabla \cdot \mathbf{q}$ is the divergence of the downward conductive heat flux $\mathbf{q} = -\kappa_0 T^{5/2} \nabla T$. In the chromosphere, heating rate and radiative losses are large and the conductive losses are small. The radiative losses reach a maximum in the lower transition region that far exceeds the local heating rate (Priest 2014). This leads to a steep increase in the temperature gradient. The heat conducted downwards from the corona is then radiated away in the transition region. This energy balance allow for the derivation of scaling relations for static coronal loop models.

1.5.1 The RTV scaling laws

Under the assumption of hydrostatic equilibrium, coronal loops can be described by an analytical relation of loop temperature, pressure and size. Such scaling laws depending on heating rate and loop length were derived by Rosner et al. (1978) and were named Rosner-Tucker-Vaiana (RTV) scaling laws after the authors. The assumption behind the derivation of the scaling laws is that the conductive heat flux and the heating rate are in balance, while the radiative losses in the corona itself are negligible since the energy conducted downward is radiated away at the footpoints.

The relation between the apex temperature and heating rate and the loop length is

$$T_{\text{max}} \approx 1.4 \times 10^3 (PL/2)^{1/3} \text{ K}, \quad (1.50)$$

$$H_{\text{max}} \approx 9.8 \times 10^4 P^{7/6} (L/2)^{-5/6} \text{ erg s}^{-1} \text{ cm}^{-3}. \quad (1.51)$$

Alternatively, temperature and pressure can be expressed as a function of heating rate:

$$p \propto H^{6/7} L^{5/7}, \quad (1.52)$$

$$T \propto H^{2/7} L^{4/7}. \quad (1.53)$$

The scaling relation for the density follows from the relations for temperature and pressure using the ideal gas law $p = 2n_e k_B T$ as

$$\rho \propto \frac{1}{2k_B} H^{4/7} L^{1/7}. \quad (1.54)$$

A modification of the RTV scaling laws for nonconstant heating rates was derived by Serio et al. (1981).

1.5.2 1D loop models

In 1D loop models, the equations of hydrodynamic equilibrium are solved along a magnetic field line. In contrast to scaling laws, 1D models treat time-dependent problems. 1D models have been used to study the response of the plasma to various spatial and temporal distributions of heating events (Boris and Mariska 1982, Mariska and Boris 1983, Hansteen 1993). 1D models allow for a very high resolution at low computational cost. This allows to better resolve the steep temperature and density gradients at the transition region. At some point, however, the small grid spacings can get smaller than the electron mean free path and the MHD approximation stops being valid (Peter 2015). 1D models can reproduce flows parallel to the magnetic guide field and spectral line broadening (Patsourakos and Klimchuk 2006). While the effects of expansion of magnetic field with height can be incorporated in this model, the interactions of magnetic field lines cannot (Mikić et al. 2013). One of the drawbacks of 1D models is that most coronal heating mechanisms cannot be modelled in a self-consistent way since they require the reconnection of magnetic field lines or motions transverse to the magnetic field, thus they require a parameterized heating rate as input.

1.5.3 3D coronal loop models

In order to self-consistently reproduce the coronal heating mechanism, 3D models are needed. Due to computational cost, these models are limited to lower resolutions than the 1D models. Several variations of 3D coronal models have been studied with varying degrees of realism.

1.5.3.1 Coronal loop models in a Cartesian geometry

In the original braiding model by Parker, a uniform field is braided by boundary motions that are applied on the perfectly conducting plates. Various versions of this scenario have been studied in numerical simulations.

Coronal loops have been modelled in the framework of reduced MHD as long and thin magnetic flux tubes with a strong, time-independent uniform background field. Reduced MHD models allow for a high resolution at a low computational cost. The reduced MHD formalism was first developed to describe the behavior of plasma enclosed in the strong magnetic field of a tokamak (Strauss 1976). Only perturbations in the velocity field and the magnetic field transverse to the background magnetic field are evolved. The background field and density are assumed to be constant. These models have been used mainly for the study of the simplified braiding model of Parker and resulting MHD turbulence (Rappazzo et al. 2007, Rappazzo et al. 2008, 2010, Rappazzo et al. 2017) and Alfvén waves (van Ballegooijen et al. 2011, van Ballegooijen et al. 2014, 2017). The effect of specific photospheric motions has been studied, such as different configurations of vortex motions at the photosphere (Rappazzo et al. 2019).

A drawback of reduced MHD models is that the plasma response cannot accurately be modelled, the large scale evolution of the magnetic field is neglected and the coupling to the lower atmosphere is not incorporated. The driving velocity field has to be prescribed at the boundaries in order to provide the necessary energy input to heat the loops. Furthermore, it is assumed in the framework of reduced MHD that the deviations from the background magnetic field are small and can be treated as perturbations. In the real corona this is not necessarily the case.

Coronal loops approximated as straightened flux tubes driven at the boundaries have also been studied in ideal MHD for the limit of vanishing gas pressure (Mikic et al. 1989). Mikic et al. (1990) investigated the time evolution and development of the kink instability of a twisted magnetic flux tube due to photospheric vortex motions at the boundaries in ideal MHD. Heating of the corona by braided magnetic flux tubes in a stretched loop geometry was studied numerically in full MHD by Galsgaard and Nordlund (1996). Reconnection between magnetic field braided by large-scale boundary motions was found sufficient to heat the solar corona, with the injected Poynting flux being a function of parameters such as the driving timescale and the loop length. Gravitational stratification has been added in Galsgaard and Rousev (2002) for the 2D case.

In addition to studying the influence of various types of driving motions, this setup has also been used to investigate the relaxation of an already braided flux tube and the resulting turbulence. Instead of braided magnetic fields being built up by boundary motions, a magnetic braid is used as an initial condition and then evolved in an ideal MHD simulation (Wilmot-Smith et al. 2009a,b) until a force-free state is reached. The final state is then evolved in a resistive MHD simulation (Wilmot-Smith et al. 2010, Pontin et al. 2011, Wilmot-Smith et al. 2011). These studies circumvent the problem that numerical simulations are more diffusive than the real solar atmosphere and magnetic reconnection sets in before complex structures can form in the magnetic field.

Reconnection can not only arise from a complex braided field, but also from instabilities occurring in an ordered magnetic field. Instabilities that occur in one flux tube can destabilize neighboring structures. This can lead to a chain reaction, causing a series of bursty coronal energy releases. Cellular automata have been used to describe these avalanches leading to coronal heating. Models based on the concept of avalanches were studied by Hood et al. (2016), Reid et al. (2018). Reid et al. (2018) perform a full 3D MHD simulation of a magnetic avalanche. They model a coronal loop as an assortment of magnetic flux tubes driven by photospheric motions. After the kink instability occurs in one of the threads, the previously stable threads are disrupted in the ensuing chain reaction. This demonstrates that a large-scale energy release can be triggered by a local instability.

1.5.3.2 Full 3D active region models

Models solving the full MHD problem for an active region either have a velocity driver mimicking granulation, or contain part of the convection zone in the simulation box. An important goal of these models is to model synthetic coronal emission. An observed magnetogram can be used as a boundary driver to study the evolution of the magnetic field. This allows the modelling of a complete active region without having to properly resolve the near-surface convection. Alternatively, a shallow convection zone can be included at the bottom boundary so that the model is self-consistently heated. These types of models

allow for heating by horizontal shuffling of magnetic field as well as for flux emergence and also allow the magnetic field to expand, leading to a drop of the heating rate in response to the stratification which is not incorporated in simplified models assuming a strong uniform field.

The achievable Reynolds numbers in these comprehensive simulations are lower than what can be achieved in lower dimensional setups and reduced MHD. They do, however, produce values for coronal quantities such as density and temperature consistent with observations. They include the dynamical response of the plasma to heating and allow for the forward modelling of coronal emission that can be directly compared to observations. The first model of a full active region was studied by Gudiksen and Nordlund (2002, 2005b,a) by extrapolating the magnetic field from the magnetogram of an active region and including a photospheric driver mimicking granulation. The Ohmic heating due to currents arising from braiding of the magnetic field was found to be sufficient to heat the plasma in the simulation domain to coronal temperatures. A similar concept was employed by Bingert and Peter (2011), who found both continuous heating and heating events strongly intermittent in space and time, thus supporting the nanoflare picture. The energy distribution in this model was found to be consistent with nanoflares (Bingert and Peter 2013). Bourdin et al. (2013) found that a coronal model driven by observed magnetic and velocity fields reproduces coronal loops and their dynamics in active regions. Instead of using an observed magnetogram, Chen et al. (2014) coupled a coronal part to the photospheric magnetic field produced by a large-scale flux emergence simulation as the lower boundary to study the formation of a coronal loop with a realistic curved geometry driven by motions of the magnetic field at the solar surface. They found that the coronal loop was energized by converging flows advecting small magnetic patches into the emerging sunspot. A visualization of the active region loop forming in their model is shown in Fig. 1.5. The loop forms between the outskirts of the two sunspots.

Models self-consistently including the convection zone were done, among others, by Gudiksen et al. (2011), Hansteen et al. (2015) with the BIFROST code and by Rempel (2017), who implemented a coronal extension to the MURaM code. The energy input due to braiding was studied by Hansteen et al. (2015). They find that, consistent with the braiding model, the convective motions at the solar surface lead to the buildup of gradients in the magnetic field in the atmosphere with strong Joule heating.

Simulations in a realistic setup have been extended to the emergence of a full active region (Chen et al. 2021) and large-scale flares (Cheung et al. 2019).

1.6 Motivation of this work

The aim of our study is to investigate the self-consistent exchange of energy between atmospheric layers and the resulting internal structure of a coronal loop. In this work, we follow a mixed approach for the modelling of large-scale coronal systems. We study a coronal loop modelled as a straightened-out magnetic flux tube in a Cartesian geometry that we couple to a shallow convection zone layer.

Coronal loop models based on a straightened-out magnetic flux tube and an empirically prescribed velocity driver at the base of the corona do not capture the complexity of the magnetic field in the solar atmosphere and the exchange of material and energy be-

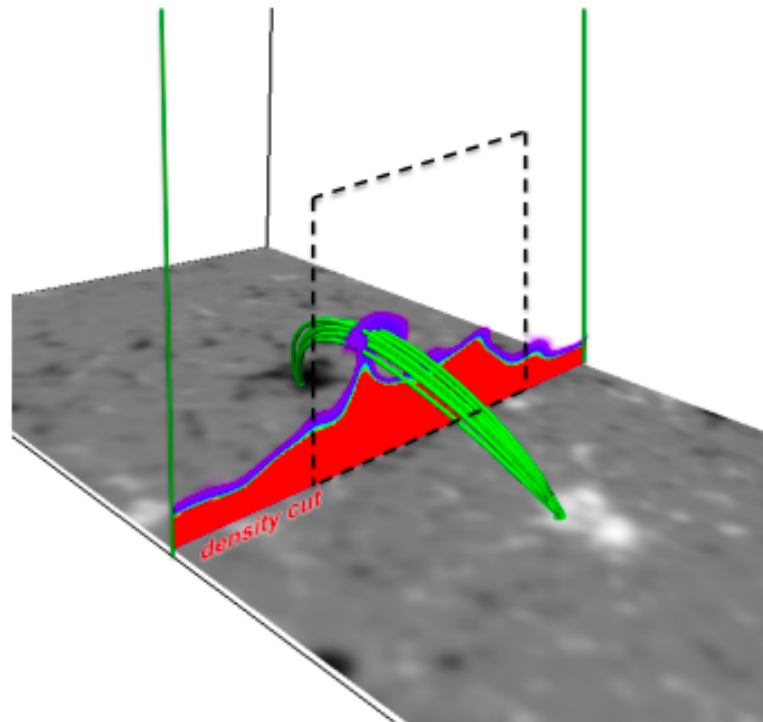


Figure 1.5: Visualization of a 3D simulation of an active region loop driven by a simulation of emerging magnetic flux. Reproduced from Chen et al. (2014). Credit: Chen, F.; Peter, H.; Bingert, S.; Cheung, M.C.M, *A&A*, 564, A12, 2014, DOI: 10.1051/0004-6361/201322859, reproduced with permission © ESO

tween different atmospheric layers. Simulations including both magnetoconvection and the corona that allow for forward modelling of "realistic" coronal structures are costly and typically the resistivity is too high to resolve the fast small-scale motions that could contribute to energy transfer into the corona and to observable fine structure. Models based on observed magnetograms are limited by the finite available resolution of observing instruments and the lack of information about the horizontal magnetic field components and twist in the magnetic field. Small-scale motions within magnetic flux concentrations are not well captured and thus these models are biased towards DC-processes caused by relative motions of magnetic patches at the photosphere for heating. While smaller coronal structures such as bright points can be modelled in high resolution, typical grid resolutions in active region models are of the order of several hundred kilometers, which is also the order of magnitude of the diameter of observed loop strands. Coronal loop strands are therefore only resolved by a few gridpoints in these models, if at all.

By coupling a coronal loop modelled as a straightened-out magnetic flux tube to a convection zone layer, the energy required to heat the loop to coronal temperatures is injected in a self-consistent way by the interaction of surface convection with magnetic concentrations. We have both a realistic lower atmosphere that serves as an energy and mass reservoir and a high resolution of the loop cross-section. This way, we can study the

magnetic coupling of different atmospheric layers, capturing both small-scale motions of the velocity field driving the magnetic field evolution and the fine structure that develops in the atmosphere as a response.

The structure of this thesis is as follows. In **chapter 2**, we give an introduction to the MURaM code and describe analysis methods that we have employed in this work and the numerical setup that we have used. In **chapter 3**, we discuss the initial low resolution run we performed in the new setup. We describe the general behavior of the coronal loop and identify structures in the loop cross section related to energy injection and heating. We find abundant vortex motions present from the photosphere to the corona. In **chapter 4**, we investigate small-scale vortices in the high resolution run and the role they play as an energy channel into the corona. Eventually, in **chapter 5** we synthesize spectral lines and study the impact of the loop structure and resolution on the synthetic emission. We summarize our findings and present conclusions in **chapter 6**. In **chapter 7** I discuss further applications of the loop model presented in this thesis.

2 Numerical and analysis methods

In this chapter, we give an introduction to the MURaM code that has been employed to conduct the 3D MHD simulations studied in this work, briefly discuss the changes that have been made to the code for the setup used in this study, and describe the initial conditions. We also present some of the analysis methods used, such as magnetic field line tracing and vortex identification using the swirling strength criterion.

2.1 The MURaM code

We use the MURaM code to conduct radiative magnetohydrodynamic simulations. The MURaM code solves the full system of compressible MHD equations coupled with radiative transfer. The code was originally developed to simulate magnetoconvection in the photosphere. For a more in-depth description of the MURaM code see Vögler (2003) and Vögler et al. (2005).

In order to include the corona in the simulation domain, several changes have been implemented into the MURaM code by Rempel (2017). This includes field-aligned Spitzer heat conduction, a limiter for the Alfvén speed and an approximate treatment for the heat flux to limit the thermal conduction speed, and optically thin radiative losses. Imposing a limit on the Alfvén speed and the thermal conduction speed is done to prevent the timestep from becoming too small and increase the computational cost of the simulations. The coronal extension is described in detail in Rempel (2017).

The system of equations as they are used in the code is:

$$\frac{\partial \rho}{\partial t} = -\nabla \cdot (\rho \mathbf{v}), \quad (2.1)$$

$$\begin{aligned} \frac{\partial \rho \mathbf{v}}{\partial t} &= -\nabla \cdot (\rho \mathbf{v} \mathbf{v}) - \nabla P + \rho g_s(z) \hat{\mathbf{z}} + \mathbf{F}_L + \mathbf{D}_{\text{num,visc}} \\ &+ \mathbf{F}_{\text{SR}}, \end{aligned} \quad (2.2)$$

$$\begin{aligned} \frac{\partial E_{\text{HD}}}{\partial t} &= -\nabla \cdot [\mathbf{v}(E_{\text{HD}} + P + q\mathbf{B}/|\mathbf{B}|)] + \rho \mathbf{v} \cdot (g_s(z) \hat{\mathbf{z}}) \\ &+ \mathbf{v} \cdot \mathbf{F}_L + \mathbf{v} \cdot \mathbf{F}_{\text{SR}} + Q_{\text{rad}} + Q_{\text{thin}} \\ &+ Q_{\text{num,res}} + \nabla \cdot (\boldsymbol{\tau} \cdot \mathbf{v}), \end{aligned} \quad (2.3)$$

$$\frac{\partial \mathbf{B}}{\partial t} = \nabla \times (\mathbf{v} \times \mathbf{B}) + \mathbf{D}_{\text{num,res}}, \quad (2.4)$$

$$\frac{\partial q}{\partial t} = \frac{1}{\tau_{\text{cond}}} (-f_{\text{Sat}} \sigma T^{5/2} \mathbf{B}/|\mathbf{B}| \cdot \nabla T - q). \quad (2.5)$$

ρ , \mathbf{v} , P and \mathbf{B} are mass density, velocity, pressure, and magnetic field, respectively. $g_s(z)$ is the gravitational acceleration depending on the position on the loop axis. \mathbf{F}_L is the Lorentz force, E_{HD} is the sum of kinetic and internal energy density, q is the magnitude of the heat flux, Q_{rad} and Q_{thin} are the optically thick and optically thin radiative heating/cooling terms, $Q_{\text{num, res}}$ is the resistive heating term and $\mathbf{D}_{\text{num, res}}$ is the diffusive part of the induction equation arising from numerical resistivity, while $\mathbf{D}_{\text{num, visc}}$ is the viscous force arising from the numerical viscosity. The viscous heating term is taken care of implicitly since the numerical scheme is conservative for the sum of kinetic and internal energy density. $\nabla \cdot (\boldsymbol{\tau} \cdot \mathbf{v})$ is an energy flux due to viscosity. This energy flux is here taken care of implicitly by numerical diffusivities.

The energy equation is solved for the kinetic and internal energy density, excluding the magnetic energy density. This is done to avoid numerical errors in low beta regions where the magnetic energy density is dominating at the expense of a scheme that is conservative for the total energy density. The system of equations contains additional terms compared to the system of MHD equations listed in Sect. 1.2.2. The momentum and energy equations contain a semi-relativistic correction term \mathbf{F}_{SR} that arises from limiting the Alfvén speed in the simulation domain in order to avoid strong constraints on the numerical timestep. This so-called Boris correction will be discussed in Sect. 2.1.7. The heat conduction equation for the heat flux q contains a factor τ_{cond} governing the maximum wave speed in the hyperbolic heat conduction treatment and a factor f_{sat} accounting for the saturation of the heat flux. The treatment of the heat flux is described in Sect. 2.1.6. The code does not use explicit diffusivities, instead the code makes use of the inherent diffusivity of numerical schemes due to finite resolution. The numerical diffusion terms in the energy and momentum equations are discussed in Sect. 2.1.8.

The condition $\nabla \cdot \mathbf{B} = 0$ is not strictly preserved in a numerical simulation due to the finite resolution. In order to avoid spurious magnetic monopoles, a divergence cleaning scheme following Dedner et al. (2002) is employed. Essentially, a wave equation is solved for the $\nabla \cdot \mathbf{B}$ error. Monopoles are propagated out of the simulation domain while at the same time the $\nabla \cdot \mathbf{B}$ error is damped.

To close the system of MHD equations, a relation between temperature, pressure and density is needed. The MURaM code uses the OPAL equation of state (Rogers and Iglesias 1996) in regions with large densities joined to an equation of state based on the Uppsala Opacity Package (Gustafsson et al. 1975) for densities below $10^{-6} \text{ g cm}^{-3}$. The code accesses the equations of state in the form of a merged lookup table. In the corona, temperatures can exceed the table bounds. For regions of the simulation domain exceeding the upper temperature bounds, an ideal equation of state is used with an adiabatic index of $\gamma = 1.65$ and a mean molecular weight of $\mu = 0.62 m_p$. The equation of state tables include effects of partial ionization and are based on the assumption that the LTE approximation is valid throughout the entire simulation domain including the chromosphere.

2.1.1 Numerical scheme

The equations are solved on a three dimensional Cartesian grid. The spatial derivatives in the equations are discretized using a fourth-order centered difference scheme on a five-point stencil. For a partial differential equation corresponding to a conservation law such

as the system of MHD equations, this is equivalent to solving the equations in conservative form using a finite volume scheme (Vögler 2003). The primary variables are ρ , \mathbf{v} , \mathbf{B} , and specific internal energy density ε . Temperature and pressure are obtained via table inversion.

An explicit fourth-order Runge-Kutta-like scheme is employed for the time integration (Jameson 2017).

The code is parallelized with MPI using a domain-decomposition scheme. In order to compute partial derivatives at the domain boundaries using a five-point stencil, two layers of ghost cells are attached to each subdomain in every grid direction.

2.1.2 Radiative losses

We include LTE radiative transfer in the optically thick regime and a radiative loss function in the optically thin regime in order to model the heating and cooling due to the interaction of matter and radiation. The radiative source term is obtained from solving the radiative transfer equation for a number of directions in the optically thick regime and from a density- and temperature dependent loss function in the optically thin part of the simulation domain. The matter is supposed to be in local thermal equilibrium (LTE) in the whole simulation domain, including the chromosphere.

2.1.2.1 Optically thin radiative losses

In the optically thin limit, the mean free path of photons is much larger than the dimensions of the system. The radiative transfer switches off once the transition region is reached. The location of the transition region is determined on a column-by-column basis using a threshold value of $T=20000$ K (Rempel 2017). For an optical depth below 10^{-8} , the radiative losses are calculated using the optically thin radiative loss function

$$Q_{\text{thin}} = -n_e n_H \Lambda(T), \quad (2.6)$$

where n_e is the electron density and n_H the density of hydrogen nuclei. Assuming a mixture of hydrogen and helium with a hydrogen fraction of 0.7, the densities are given by

$$n_e = \frac{\rho}{m_p} \cdot 0.85, \quad (2.7)$$

$$n_H = \frac{\rho}{m_p} \cdot 0.7. \quad (2.8)$$

$\Lambda(T)$ is a tabulated, temperature-dependent radiative loss function taken from the CHIANTI 7 atomic database and m_p is the mass of a proton. The abundances used are from Landi et al. (2012). The radiative loss function has a weak dependence on density, but here we use a density-averaged version (Rempel 2017).

An issue that arises when calculating the radiative losses is the insufficient resolution of the transition region in realistic 3D MHD simulations. A resolution of just a few

kilometers or even spatial scales below a kilometer would be necessary to resolve the transition region (Bradshaw and Cargill 2013). Even if such high spatial resolutions would be reached in 3D MHD simulations, the grid spacing would reach the order of the electron mean free path and the MHD assumption breaks down (Peter 2015). If a lower numerical resolution is used, the radiative losses from the transition region are either over- or underestimated, depending on the temperature variation in the grid cells. If the temperature in a grid cell corresponds to transition region temperatures, the radiative loss would be overestimated, since the grid cell is wider than the real transition region. If the transition region falls between two grid cells, the radiative losses would be underestimated. If the heat flux from the corona is radiated away in the chromosphere instead of heating transition region plasma that subsequently evaporates into the corona, the density in the loop can be underestimated by a factor of two or more (Bradshaw and Cargill 2013). To ameliorate this problem, MURaM oversamples density and temperature between grid points for the radiative loss calculation. The logarithm of density and temperature is assumed to vary linearly between grid points. A detailed description of the implementation of the optically thin radiative losses can be found in Rempel (2017).

2.1.3 Optically thick radiative losses

In the optically thick part of the simulation domain radiative transfer calculations in the grey approximation are performed. To calculate the radiative source term, a short characteristics formal solver is employed (Kunasz and Auer 1988, Vögler 2003). The equation of radiative transfer (1.38) is discretized and solved along a ray segment. To compute the intensity at a certain grid point for a certain direction and frequency, the radiative transfer equation is solved along a ray segment between the grid point and the nearest upwind intersection of the ray with a cell boundary. A staggered grid is used for the radiative transfer. Temperature, density and pressure are interpolated onto the cell corners of the MHD grid. The density, opacity, and source function are assumed to vary linearly along the ray segment. The integration proceeds in the downwind direction. The correct initial values for the intensity on the upwind boundary of a subdomain are unknown unless the boundary is the global top or bottom boundary of the simulation domain. Therefore, the procedure must be iterated until convergence on the boundaries is achieved. The values at the top and bottom boundary have to be explicitly specified. If the atmosphere is optically thin at the top boundary of the box, it can be assumed that the incoming radiation is negligible and the intensity at the top can be set to zero. At the bottom boundary, which is usually in the convection zone, the plasma is optically thick and the mean free path of photons is much smaller than the scale of the modelled system. Interaction of radiation and matter are assumed to be local since an emitted photon is absorbed almost instantaneously and does not leave the grid cell under consideration. In this case the diffusion approximation for radiation is valid and the incoming radiation can be set to the local value of the source function, which is the Planck function:

$$I_\nu(\boldsymbol{\mu}, \mathbf{x})|_{\text{bot}} = B_\nu(\mathbf{x}). \quad (2.9)$$

We use here the grey radiative transfer approximation and neglect the frequency dependency in the calculation of Q_{rad} . The Planck function is replaced by its frequency-integrated version. To obtain the mean intensity J and the radiation flux F_{rad} , the inten-

sity is integrated over all discrete ray directions. For a detailed description of the radiative transfer module in MURaM, see Vögler (2003).

In the framework of my thesis, I modified the radiative transfer scheme for the straightened loop setup. MURaM is designed for a box-in-a-star setup consisting of a convection zone layer and an optional atmosphere on top. In this setup, the radiation exits the computational box at the top boundary. In the straightened-loop setup that we use, the top boundary is replaced by another convection zone layer that constitutes the second loop footpoint. The radiation from one loop footpoint would thus arrive at the second footpoint, and heat the chromosphere at the opposite end of the loop. This is not realistic since in reality the radiation would not travel along the loop axis and reach the second footpoint. In order to prevent both loop footpoints heating each other, the radiation in both the up- and downward direction is set to zero at the loop midplane. Since the midplane is located in the optically thin part of the computational box, the radiation is not coupled to the plasma and does not enter the energy equation apart from the optically thin radiative loss function, which is calculated on a local basis.

The boundary values for the intensity calculation also need to be modified. For the straightened loop setup, the "top" boundary is identical to the bottom boundary. The value for the incoming intensity at both the global top and bottom boundary is set to the local value of the frequency-integrated Planck function.

Additionally, the calculation of the optical depth needs to be adjusted for the new setup. The optical depth integration is carried out in the z -direction according to eq. 1.36. Originally, the integration starts at the top boundary and proceeds towards the bottom boundary of the box. In our case, this is the axial direction along the loop. The optical depth calculation needs to be modified so that for each footpoint, the integration starts in the optically thin part of the loop and is carried out towards the interior of the convection zone, in this case from the loop midplane towards the top and bottom boundaries. The optical depth calculation cannot be carried out locally since it depends on the path length.

MURaM uses a Cartesian geometry for the distribution of the subdomains of the global simulation domain onto different processes. For the integration of the optical depth, a separate MPI communicator is employed for each column of grid cells. The integrated values for the optical depth τ at the boundary of each subdomain need to be communicated to the adjacent computational subdomain in the z -direction. To adjust the calculation to the new setup, each MPI column communicator is split into two separate subcommunicators for the lower and upper half of the simulation domain. The direction of integration depends on whether the respective subdomain is located in the upper or lower half of the computational box and is always directed towards the interior of the Sun, which is the top- or bottom boundary depending on whether the subdomain in question is located in the upper or lower half of the global simulation domain.

2.1.4 Boundary conditions

We use open boundaries for the hydrodynamic variables that allow flows across the boundary in order to mimick the coupling to the deeper layers of the convection zone. Symmetric boundary conditions are applied in the ghost cells for all three components of mass flux and magnetic field at the bottom boundary, so that the gradient of velocity and magnetic fields is zero at the boundary (Rempel 2014). The heat flux is set to zero at the bottom

boundary (Rempel 2017). The gas pressure is decomposed into the mean pressure and a fluctuation component. The mean pressure component is extrapolated into the ghost cells assuming a fixed value of pressure taken from the standard solar model at the boundary, while the fluctuation component is damped (Rempel 2014).

The entropy is set to a value specified by the standard solar model in the upflow regions at the bottom boundary. In downflow regions, it is assumed to be symmetrical across the boundary. The values for the density and the hydrodynamic energy density in the ghost cells are then determined by the equation of state.

For the runs without a corona on top we use a vertical boundary condition for the magnetic field at the top boundary.

For the straightened loop setup, the "top" boundary is located at the second loop footpoint and behaves like another bottom boundary. The original top boundary conditions used by MURaM are therefore replaced by the bottom boundary conditions with sign changes for the upflow and downflow regions. All quantities are periodic in the horizontal directions.

2.1.5 The computational timestep

The numerical domain of dependence has to include the physical domain of dependence. This means that a signal propagating in the domain should not be able to traverse more than one grid cell in a single timestep. This so-called Courant-Friedrichs-Lewy (CFL) condition imposes a limit on the timestep

$$f_{\text{CFL}} = c_{\text{max}} \frac{\Delta t}{\Delta x}, \quad (2.10)$$

where c_{max} is the maximum wave speed in the simulation. A condition for numerical stability is that $f_{\text{CFL}} < 1$.

2.1.6 Hyperbolic heat conduction

The heat conduction along magnetic field lines is much more efficient than the heat conduction across field lines. In the MURaM code, only the field-aligned component of heat conduction is taken into account and the heat conduction across magnetic field lines is neglected. The inclusion of field-aligned heat conduction poses a severe limit on the timestep. This is mitigated by using a hyperbolic diffusion equation instead of the original heat conduction equation. This approach was originally used in Snodin et al. (2006). The method was implemented in MURaM by Rempel (2017). For hyperbolic equations, there exists a maximum signal propagation speed.

Limiting the signal speed is accomplished by introducing an additional term $\tau \frac{\partial q}{\partial t}$ into the equation for the heat flux. This yields a modified evolution equation for the temperature:

$$\frac{\partial T}{\partial t^2} + \frac{1}{\tau} \frac{\partial T}{\partial t} - c^2 \frac{\partial^2 T}{\partial t^2} = 0 \quad (2.11)$$

with the finite wave speed $c = \sqrt{\frac{\kappa}{\tau}}$. For a value of $\tau > 0$ the heat conduction equation has the form of a wave equation for the temperature. τ is chosen so that the maximum signal propagation speed is of the order of the Alfvén speed in the simulation

$$\tau = \frac{\Delta t^2 \kappa}{f_{\text{CFL}}^2 \Delta x^2}, \quad (2.12)$$

with Δt being the timestep, Δx the grid spacing and f_{CFL} the CFL factor. τ is then determined by the grid spacing. τ has to be smaller than timescale of interest. In order to avoid violations of the CFL conditions in regions where heat is transported by both conduction and advection of material, the maximum propagation velocity of the heat front is set to $f_{\text{CFL}} \frac{\Delta x_{\text{min}}}{\Delta t} - |v|$. The equation for the evolution of the heat flux q then takes the following form:

$$\frac{\partial q}{\partial t} = \frac{1}{\tau} (-f_{\text{sat}} \sigma T^{\frac{5}{2}} (\hat{\mathbf{b}} \cdot \nabla) T - q), \quad (2.13)$$

$$\tau = \left(f_{\text{CFL}} \frac{\Delta x_{\text{min}}}{\Delta t} - |v| \right)^{-2} \frac{f_{\text{sat}} \sigma T^{\frac{7}{2}}}{E_{\text{int}}}. \quad (2.14)$$

σ is the Spitzer heat conductivity and $\hat{\mathbf{b}}$ is the unit vector in the direction of the field. In the original form, the temperature gradient and thus the heat flux can be arbitrarily large. In reality, this is not possible. Heat is mainly transported by electrons, and when all electrons are moving in the same direction at the electron thermal speed, the heat flux saturates (Fisher et al. 1985, Meyer et al. 2012). Spitzer heat conduction assumes that the electron mean free path is shorter than the temperature scale height. If the mean free path is equal or greater to the temperature scale height, Spitzer's formulation is no longer valid (Cowie and McKee 1977). The saturation of the heat flux is taken into account by the pre-factor

$$f_{\text{sat}} = \left(1 + \frac{|\sigma T^{\frac{5}{2}} (\hat{\mathbf{b}} \cdot \nabla) T|}{1.5 \rho C_s^3} \right)^{-1}, \quad (2.15)$$

where C_s is the speed of sound.

2.1.7 Boris correction

The Alfvén speed can reach very large values in the tenuous corona and thus severely limit the simulation timestep. If the nonrelativistic version of the MHD equations are used, it can even exceed the speed of light. To overcome this problem, the MURaM code solves a modified semi-relativistic momentum equation imposing a reduced speed of light. This is the so-called Boris correction introduced by (?). The implementation in the MURaM code follows Gombosi et al. (2002). If we do not neglect the displacement current in eq. (1.5), the Lorentz force becomes

$$\frac{1}{c} \mathbf{j} \times \mathbf{B} = \frac{1}{4\pi} (\nabla \times \mathbf{B}) \times \mathbf{B} + \frac{1}{4\pi c} \mathbf{B} \times \frac{\partial \mathbf{E}}{\partial t}. \quad (2.16)$$

Inserting the modified Lorentz force into the momentum equation, using the relation $\mathbf{E} = -\frac{1}{c} \mathbf{v} \times \mathbf{B}$ and neglecting terms of the order of $\frac{v^2}{v_A^2}$ under the assumption that the plasma velocities are much smaller than the real Alfvén speed, that yields the modified momentum equation

$$\frac{\partial}{\partial t} \left(\frac{\mathbf{E} \times \mathbf{B}}{4\pi c} + \rho \mathbf{v} \right) + \nabla \cdot (\rho \mathbf{v} \mathbf{v} + IP) = \rho \mathbf{g} + \frac{1}{4\pi} (\nabla \times \mathbf{B}) \times \mathbf{B} + \frac{1}{4\pi} (\nabla \times \mathbf{E}) \times \mathbf{E}. \quad (2.17)$$

Inserting the expression for \mathbf{E} leads to a modified momentum equation

$$\frac{\partial \rho \mathbf{v}}{\partial t} + \nabla \cdot (\rho \mathbf{v} \mathbf{v} + IP) = \rho \mathbf{g} + \frac{1}{4\pi} (\nabla \times \mathbf{B}) \times \mathbf{B} + \mathbf{F}_{\text{SR}} \quad (2.18)$$

with the semi-relativistic correction term \mathbf{F}_{SR}

$$\mathbf{F}_{\text{SR}} = -(1 - f_A) [I - \hat{\mathbf{b}} \hat{\mathbf{b}}] \left(-\rho (\mathbf{v} \cdot \nabla) \mathbf{v} - \nabla P + \rho \mathbf{g} + \frac{1}{4\pi} (\nabla \times \mathbf{B}) \times \mathbf{B} \right), \quad (2.19)$$

where f_A is an approximate limiting factor chosen as $f_A = \frac{1}{\sqrt{1 + (\frac{v_A}{c})^4}}$. The Alfvén velocity then becomes $\frac{v_A^2}{\sqrt{1 + (\frac{v_A}{c})^4}}$.

The main effect of the Boris correction is to limit the Alfvén speed to the reduced speed of light by increasing the inertia perpendicular to the field lines. The Boris correction does not violate the conservation of energy. The work done by the correction term in the momentum equation stores energy in the electric energy reservoir. For details on the implementation of the Boris correction see the appendix of Rempel (2017).

2.1.8 Numerical diffusivities

Currently it is not known which processes exactly are responsible for the dissipation of energy in the corona. These mechanisms likely operate on length scales of centimeters. These small scales cannot be resolved by coronal simulations, furthermore the MHD approximation breaks down at those scales. Every large-scale simulation of the solar atmosphere is therefore necessarily a large-eddy simulation. This means that some kind of parameterization is needed to account for the dissipation of energy.

In order to avoid the buildup of energy on the grid scale and maintain numerical stability, we need to introduce artificial diffusivities (Rempel 2014). To this end, MURaM uses a slope-limited diffusion scheme. The MURaM code only uses numerical diffusivities. We do not use explicit resistivity and viscosity in our simulations.

Variables at the cell interfaces are reconstructed using a piecewise linear reconstruction (Rempel 2014):

$$u_l = u_i + 0.5 \Delta u_l, \quad (2.20)$$

$$u_r = u_r + 0.5 \Delta u_r, \quad (2.21)$$

with u_l and u_r being the extrapolated values at the cell interfaces and Δu_l and Δu_r the respective reconstruction slopes. The reconstruction slopes are calculated using a monotonized central difference limiter:

$$\Delta u_i = \text{minmod}([(u_{i+1} - u_{i-1})/2, 2(u_{i+1} - u_i), 2(u_i - u_{i-1}))]). \quad (2.22)$$

This is a combination of the minmod and the Superbee limiter. The numerical diffusive fluxes at the cell interfaces are calculated as

$$f_{i+\frac{1}{2}} = -\frac{1}{2}c_{i+\frac{1}{2}}\Phi_h(u_r - u_l, u_{i+1} - u_i) \cdot (u_r - u_l), \quad (2.23)$$

where $c_{i+\frac{1}{2}}$ is a characteristic velocity at the cell interface and Φ_h is a function controlling the hyperdiffusivity of the scheme. The characteristic velocity is given by a combination of the Alfvén velocity, the sound speed and the speed of the fluid flow $c_{i+\frac{1}{2}} = |\mathbf{v}| + \sqrt{\max(c_s^2, f_A \cdot (c_s^2 + v_A^2))}$, where f_A is the limiting factor for the Alfvén speed. The function Φ_h is given by

$$\Phi_h = \begin{cases} \max\left[0, 1 + h\left(\frac{u_r - u_l}{u_{i+1} - u_i}\right)\right] & \text{for } (u_r - u_l) \cdot (u_{i+1} - u_i) > 0 \\ 0 & \text{for } (u_r - u_l) \cdot (u_{i+1} - u_i) \leq 0 \end{cases} \quad (2.24)$$

The term $(u_r - u_l) \cdot (u_{i+1} - u_i)$ becomes smaller than zero if the difference between reconstructed values at the cell interfaces has the opposite sign of the difference between the non-reconstructed values. This would lead to a diffusive flux from a grid cell with a lower magnitude of the variable in question to a grid cell with a higher value. The choice to set the function Φ_h to zero in this case therefore ensures that there is no antidiffusion.

If the parameter h is chosen to be zero, the numerical scheme reduces to a second order Lax-Friedrichs scheme. A choice of $h > 0$ leads to a reduction of diffusion in smooth regions, while for $h > 1$ the diffusivity is completely disabled for sufficiently smooth regions with well-resolved features. The diffusivity is only applied in regions with monotonicity changes or features that are just resolved by a few gridpoints. The diffusion scheme is applied to the variables $\log(\rho)$, ε , \mathbf{v} , \mathbf{B} , with $\varepsilon = \frac{E_{\text{int}}}{\rho}$ being the specific internal energy density. Different diffusivities are chosen for different variables and in different regions. The diffusive mass flux is assumed to also transport momentum and internal energy, therefore a term depending on the diffusive mass flux is added to the momentum equation and to the energy equation.

The numerical diffusion terms in the momentum and induction equation lead to a change in kinetic and magnetic energy and thus do work (Rempel 2018):

$$\mathbf{v} \cdot \mathbf{D}_{\text{num,vis}} = -\nabla \cdot \mathbf{F}_{\text{visc}} - Q_{\text{vis}} \quad (2.25)$$

$$\frac{1}{4\pi} \mathbf{B} \cdot \mathbf{D}_{\text{num,res}} = -\nabla \cdot \mathbf{F}_{\text{res}} - Q_{\text{res}}, \quad (2.26)$$

where \mathbf{F}_{visc} and \mathbf{F}_{res} are energy fluxes that are small compared to the other energy fluxes in the simulation and $Q_{\text{num,vis}}$ and $Q_{\text{num,res}}$ are the viscous and resistive heating rate, respectively. The numerical resistive and viscous heating rates at each gridpoint are computed from the gradient of the magnetic and velocity field and the numerical fluxes of the respective quantities:

$$(Q_{\text{vis,num}})_i = \frac{1}{2}\rho_i \sum_{m=1}^3 \left((f_v^{\text{num}})_{i-\frac{1}{2}}^m \frac{v_i^m - v_{i-1}^m}{\Delta x} + (f_v^{\text{num}})_{i+\frac{1}{2}}^m \frac{v_{i+1}^m - v_i^m}{\Delta x} \right), \quad (2.27)$$

$$(Q_{\text{res,num}})_i = \frac{1}{8\pi} \sum_{m=1}^3 \left((f_B^{\text{num}})_{i-\frac{1}{2}}^m \frac{B_i^m - B_{i-1}^m}{\Delta x} + (f_B^{\text{num}})_{i+\frac{1}{2}}^m \frac{B_{i+1}^m - B_i^m}{\Delta x} \right). \quad (2.28)$$

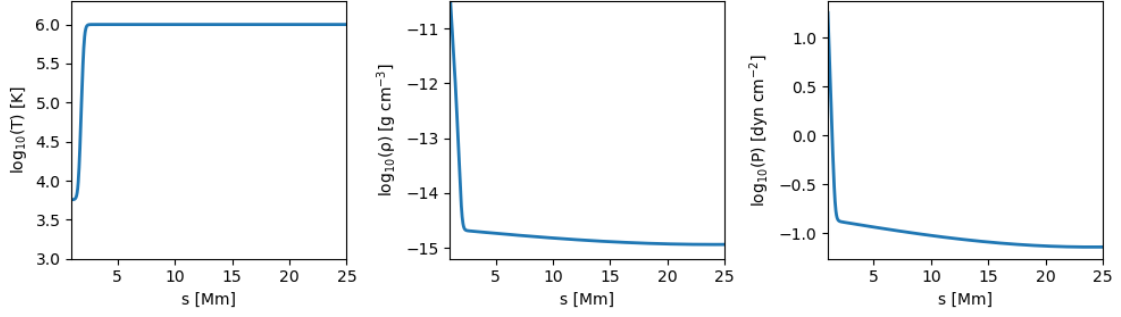


Figure 2.1: Initial horizontally averaged profiles of thermodynamic quantities in the coronal part of the simulation domain as a function of arclength. From left to right: Temperature, density and pressure.

The components in the different spatial directions are added sequentially. Since the magnetic diffusivity is not uniform in the simulation domain but instead enhanced at the location of gradients in the magnetic field, this could be seen as a parameterization of anomalous resistivity. Effective numerical diffusivities can be computed from averages of the resistive heating terms and the explicit expressions following Rempel (2018)

$$v_{\text{eff}} = \frac{\langle Q_{\text{vis,num}} \rangle}{\langle \rho \sum_{i,k} \frac{\partial v_i}{\partial x_k} \left[\frac{\partial v_i}{\partial x_k} + \frac{\partial v_k}{\partial x_i} - \frac{2}{3} \delta_{ik} \nabla \cdot \mathbf{v} \right] \rangle}, \quad (2.29)$$

$$\eta_{\text{eff}} = 4\pi \frac{\langle Q_{\text{res,num}} \rangle}{\langle |\nabla \times \mathbf{B}|^2 \rangle}. \quad (2.30)$$

The correlation between the Spitzer resistivity and the effective numerical resistivity, however, was found to be weak (Rempel 2017).

2.1.9 Model setup

2.1.9.1 Initial conditions

To build the coronal loop model, we start with a shallow computational box that extends up to one Mm above the solar surface. For the initial profiles of temperature, density and pressure in the shallow box the standard solar model (SSM) is employed. The thermodynamic quantities are interpolated from tabulated values. Above the SSM an isothermal, constant pressure scale height extrapolation is used with the atmosphere supposed to be in hydrostatic equilibrium:

$$0 = -\frac{\partial P}{\partial z} - \rho g_{\odot}, \quad (2.31)$$

where P is the gas pressure and g_{\odot} is the gravitational acceleration at the solar surface. The box is evolved for several hours to reach a steady state. We add a uniform magnetic field and evolve the box for another hour.

In the last step, we add the coronal part. In order to avoid numerical transients arising from a corona that is initially at chromospheric temperatures and would immediately drain from

the loop, we impose an initial temperature profile of the form

$$T(s) = T_0 + \frac{(T_{\text{cor}} - T_0)}{2} \left(1 + \tanh \left(\frac{\sin \frac{\pi s}{2L} \cdot R - z_{\text{cor}}}{z_{\text{width}}} \right) \right), \quad (2.32)$$

where T_0 is the mean temperature at the upper boundary of the shallow simulation box, T_{cor} is the temperature at the loop apex, z_{cor} is the extent of the original shallow box above the photosphere, s is the distance along the loop axis, L is the half-length of the loop and z_{width} is a parameter determining the thickness of the transition region, which we set to $z_{\text{width}} = 0.18$. In addition to an initial state for the temperature, an initial profile for the density and the pressure in the loop leg is required. In order to determine pressure and density from the temperature profile, we assume that the atmosphere is initially in hydrostatic equilibrium.

In order to compute the initial profiles of temperature, density and pressure, we need to take into account that the component of the gravitational force directed along the loop axis changes with height due to the loop curvature. We assume that the loop has a semicircular shape above the solar surface. In the shallow convection zone layer below the solar surface, the gravitational acceleration should be equal to the full gravitational acceleration at the solar surface, but needs to have the opposite sign at both footpoints. The variation of the gravitational acceleration starts only above the height of the photosphere. A new parameter h_{photo} was introduced that specifies the depth of the shallow convection zone of the initial snapshot. The gravitational acceleration is modified as follows:

$$g(s) = \begin{cases} -g_{\odot} & \text{for } s < h_{\text{photo}} \\ g_{\odot} & \text{for } s > 2L - h_{\text{photo}} \\ -g_{\odot} \cdot \cos \left(\pi \frac{s - h_{\text{photo}}}{2(L - h_{\text{photo}})} \right) & \text{otherwise,} \end{cases} \quad (2.33)$$

where $g_{\odot} = 2.74 \times 10^4 \text{ cm s}^{-2}$ is the gravitational acceleration at the solar surface. We set the parameter h_{photo} to 3.5 Mm so that we have a convection zone layer with a depth of several megameters. In order to calculate initial profiles for the coronal part of the loop, we plug the modified gravity into the equations of hydrostatic equilibrium. The gravitational acceleration is also modified in the energy equation in the MURaM code.

With the modified gravitational acceleration, the local pressure scale height becomes

$$H(s) = \frac{k_B T(s)}{m g_{\odot} \cos \left(\frac{s - h_{\text{photo}}}{2(L - h_{\text{photo}})} \right)}. \quad (2.34)$$

With the imposed temperature profile, profiles for the density and pressure are determined by hydrostatic equilibrium:

$$\rho(s) = \rho_0 \cdot \frac{T_0}{T(s)} \exp \left(- \int_0^s \frac{ds}{H(s)} \right), \quad (2.35)$$

$$P(s) = P_0 \cdot \exp \left(- \int_0^s \frac{ds}{H(s)} \right). \quad (2.36)$$

Here ρ_0 and P_0 are the mean values of density and pressure at the top of the shallow simulation box. The equations are integrated numerically using the Euler method to determine

the initial profiles. The initial profiles for temperature, density and pressure for the values $T_0 = 5700$ K, $\rho_0 = 5 \times 10^{-11}$ g cm⁻³ and $P_0 = 18$ dyn cm⁻² are shown in Fig. 2.1. The internal energy density is calculated from the temperature profile with the help of the EOS table.

A uniform vertical magnetic field is chosen as an initial condition for the coronal magnetic field. To ensure a smooth transition between the coronal magnetic field and the magnetic field in the original shallow box, a vertical boundary condition is imposed for the magnetic field at the top of the shallow box. The magnetic field extension is then calculated on a column-by-column basis from the value of the vertical magnetic field at the top boundary of the original box. The x- and y- component of the magnetic field are set to zero. All velocity components in the coronal part are originally set to zero.

The box is now extended to the loop apex. To obtain the full loop, the box is duplicated, flipped and stitched together at the midplane. A small random velocity is added to one footpoint to ensure that the two footpoints evolve independently. The field-aligned Spitzer heat conduction and optically thin losses are now switched on and the box is evolved for another hour. The maximum velocity is initially limited to 100 km s⁻¹ to avoid large initial transients. The velocity limit for the plasma velocity is subsequently increased to 1000 km s⁻¹.

We conducted runs in low resolution with different magnetic field strengths. A shortcoming of our model is that the magnetic field does not expand in the corona. The magnetic field strength therefore has to be chosen so that it is strong enough to heat the corona to several million Kelvin, but is not unrealistically high for coronal heights. Field strengths in the corona have been measured using coronal seismology, where the magnetic field strength is inferred from oscillations of the loop. Field strengths measured using this method lie between roughly 10 and 100 G (Nakariakov and Ofman 2001, Guo et al. 2015, Tian et al. 2012, Verwichte et al. 2013). An initial low resolution run with a field strength of 30 G is described in detail in chapter 3. To better resolve the internal loop dynamics, we conduct simulations in higher resolution. We performed low resolution simulations for field strengths of 30 G and 60 G. The runs with increased resolution start from an interpolated snapshot of the low resolution run. A higher magnetic field strength leads to an increase in Poynting flux injected into the loop and thus to higher loop temperatures. For the runs with increased resolution, we chose a field strength of 60 G since this run produced average coronal temperatures exceeding 2 MK, reaching temperatures also found in active regions. After the interpolation, the simulation is run for half an hour to let initial transients subside.

The limit on the Alfvén velocity (see Sect. 2.1.7) was chosen dependent on the magnetic field strength and set to 3000 km s⁻¹ and 6000 km s⁻¹, for the 30 G run and the 60 G runs, respectively.

2.2 Structure of the solar atmosphere

We choose a simulation domain of $6 \times 6 \times 57$ Mm. With an average convection zone depth of 3.5 Mm, this leads to an effective loop length of 50 Mm. We run simulations for three different resolutions, 60 km, 24 km and 12 km. Temperature, heating rate, density

and rms velocities for all three different resolutions are shown in Fig. 2.2. The medium and high resolution runs show slightly higher heating rates and temperatures than the run with the lowest resolution.

A stronger difference can be seen in the rms-velocities, which show an increase with resolution. In the high resolution run, more small-scale current sheets form that could serve as sites for energy dissipation. In a steady state, however, all the energy that cannot be stored by a system has to be dissipated, the heating rate should therefore become independent of the diffusivity. Since in the high resolution magnetic elements at the photosphere are better resolved, the high resolution run could have a higher energy injection. The high resolution rate The Poynting flux at a height of 2 Mm above the $\langle \tau \rangle = 1$ surface averaged over half an hour for both footpoints is $1.2 \times 10^7 \text{ erg s}^{-1} \text{ cm}^{-2}$ for the low resolution simulation, $1.7 \times 10^7 \text{ erg s}^{-1} \text{ cm}^{-2}$ for the medium resolution simulation and $3.2 \times 10^7 \text{ erg s}^{-1} \text{ cm}^{-2}$ for the high resolution simulation. the Poynting flux is strongly variable in time. Runtimes of several hours would be necessary for a rigorous analysis of the dependence of the atmospheric bulk quantities on resolution, which is computationally expensive for the high resolution run.

The energy balance for the high resolution run is presented in Fig. 2.3. In the coronal part of the simulation domain, the energy input is dominated by the work done by the Lorentz force. The energy input through viscous and resistive dissipation is balanced by the conductive heat flux. The heat conducted downward to the transition region and chromosphere is then radiated away. The advective energy flux can add or remove energy from the corona depending on the direction of flows in the loop. The contributions from the work done by the gravitational force, the work done by the semi-relativistic correction term and the numerical diffusion are small compared to the other terms in the energy equation.

2.3 Numerical diffusivity

In order to determine the diffusivity of the numerical scheme for different quantities and thus the effective numerical Prandtl number, the parameter h discussed in Sect. 2.1.8 needs to be chosen. Different values for h are employed in the layers of the solar atmosphere. Following Rempel (2017), a value of $h = 2$ is used in the convection zone and photosphere. In low density regions with $\rho < 10^{-11} \text{ g cm}^{-3}$ a value of $h = 1.25$ is chosen for mass, momentum and energy and $h = 5$ for the magnetic field. This choice of h emulates a high Prandtl number setting with a higher viscous than resistive diffusivity in the coronal part. To study the dependence of the simulation on the choice of h for different quantities, we perform a test run with switched settings, a value of $h = 5$ is used for the velocity field and a value of $h = 1.25$ for the magnetic field. This choice of parameters leads to lower temperatures and densities of the loop, as shown in Fig. 2.4. While in the high Prandtl number setting the viscous heating dominates over the resistive heating in the corona, this behavior is reversed in the low Prandtl number run. The resistive heating rate in the low Prandtl number run is only slightly larger than in the high Prandtl run, while the viscous heating rate is significantly reduced, leading to less overall heating. The diffusivities in the convection zone and photosphere were not changed, therefore the Poynting

flux generated by photospheric motions should be the same. The Poynting flux entering the corona, however, is reduced compared to the high Prandtl number run. The Poynting flux must therefore be dissipated in the chromospheric layer due to the high numerical resistivity before it can even reach the corona. The transverse magnetic field components are reduced, while the rms-velocity is increased since the damping of the velocity fluctuations is less strong. Switching the values of h for the velocity field and the magnetic field, however, does not mean that the effective values for the numerical resistivity and viscosity are simply switched. The numerical diffusivities depend on the gradients of the respective quantities they are applied to, a more complex velocity or magnetic field thus leads to a higher numerical diffusivity. Due to the low value of plasma beta in the corona, the magnetic field is generally smoother than the velocity field.

We estimate the effective estimated numerical diffusivities in the coronal part of the simulation domain for the three different resolutions considered (60, 24 and 12 km) by using eq. (2.29) and (2.30) To calculate the expected Spitzer value of the magnetic and viscous diffusivities, a coronal temperature of 2.5 MK, a density of $\rho = 10^{-14.8} \text{ g cm}^{-3}$, and a value of $\ln \Lambda = 20$ for the Coulomb logarithm were assumed.

	60 km	24 km	12 km	Spitzer value
$\eta_{\text{eff}} [\text{cm}^2 \text{ s}^{-1}]$	1.8×10^{11}	4.5×10^{10}	2.2×10^{10}	2631
$\nu_{\text{eff}} [\text{cm}^2 \text{ s}^{-1}]$	3.1×10^{13}	6.9×10^{12}	1.7×10^{12}	6.9×10^{14}
$P_{\text{m,eff}}$	172.2	153.3	77.3	2.6×10^8

For the setup used in this study, increasing the resolution by a factor of five reduced the effective magnetic diffusivity by roughly a factor of eight and the effective viscous diffusivity by a factor of 18. In a realistic Prandtl number regime, the resistive diffusivity would be negligible compared to the viscous diffusivity.

Numerical resistive and viscous heating rates are strongly intermittent in space and time and not necessarily well-correlated with current structures and strain rate for a single timestep (Rempel 2017), therefore effective viscous and resistive diffusivities are not well defined.

2.4 Analysis methods

2.4.1 Field line tracing

In order to trace magnetic field lines, we follow the magnetic field vector in three dimensions. A Runge-Kutta-Fehlberg algorithm with an adaptive stepsize was used to integrate the equations

$$\frac{\partial x}{\partial s} = B_x, \quad (2.37)$$

$$\frac{\partial y}{\partial s} = B_y, \quad (2.38)$$

$$\frac{\partial z}{\partial s} = B_z. \quad (2.39)$$

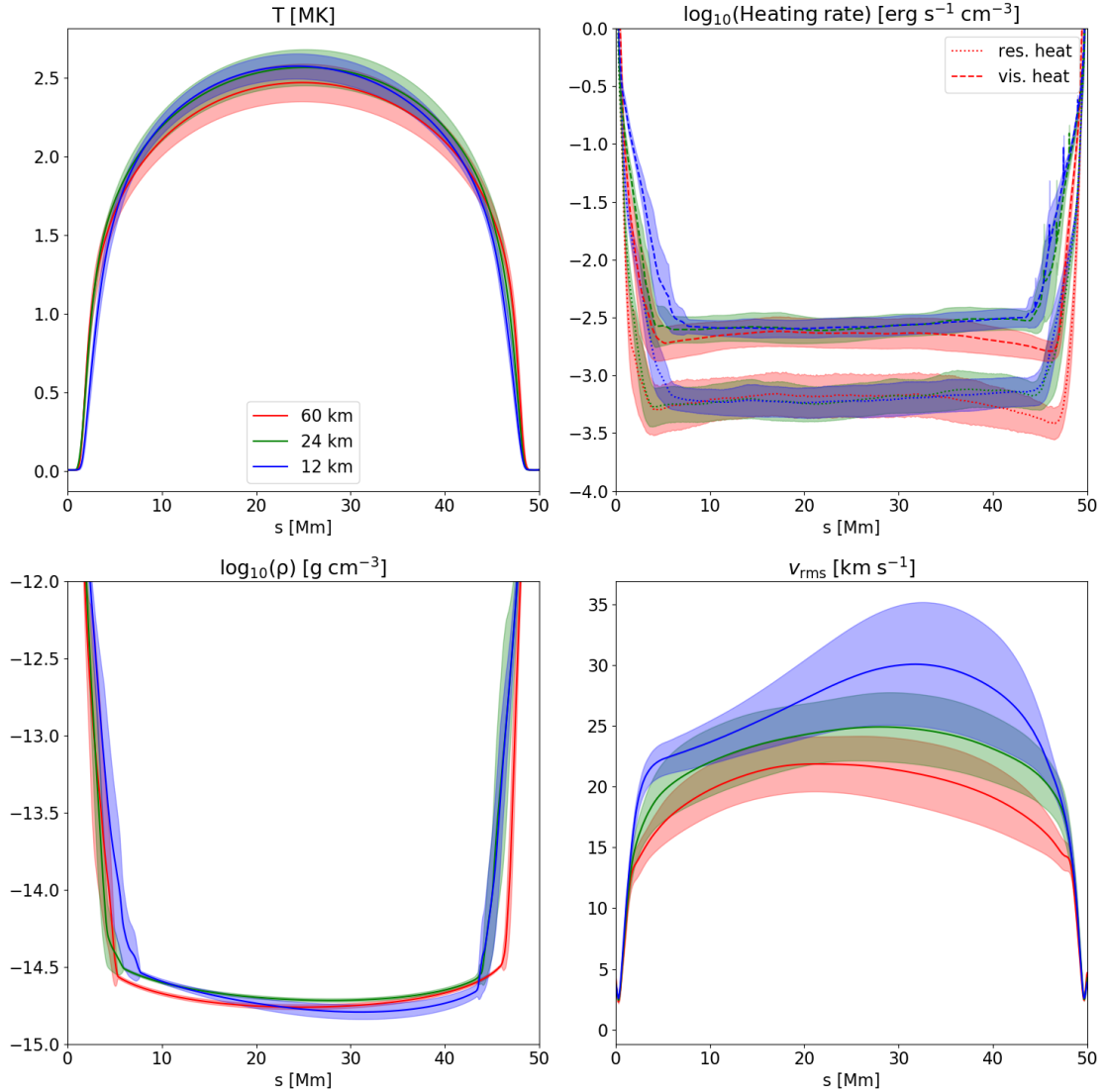


Figure 2.2: Horizontally averaged temperature, viscous (dashed line) and resistive (dotted line) heating rate, density and rms velocity for the three runs with a resolution of 60 km (red), 24 km (green) and 12 km (blue) and a uniform magnetic field of 60 G as a function of arclength s . The quantities have been averaged over half an hour of solar time. The shaded areas refer to the standard deviation due to the variation in time of the horizontally averaged quantities.

The seed points from which the magnetic field lines are traced are passively advected with the fluid. The position \mathbf{x}_i of a seed point evolves as

$$\frac{\partial \mathbf{x}_i}{\partial t} = \mathbf{v}_i, \quad (2.40)$$

where \mathbf{v}_i is the plasma velocity at the location of the seed point. The position of the seed particles is evolved in time using a 4th-order Runge-Kutta-algorithm with a fixed stepsize. The data cubes are interpolated between timesteps using linear interpolation. Tracking is

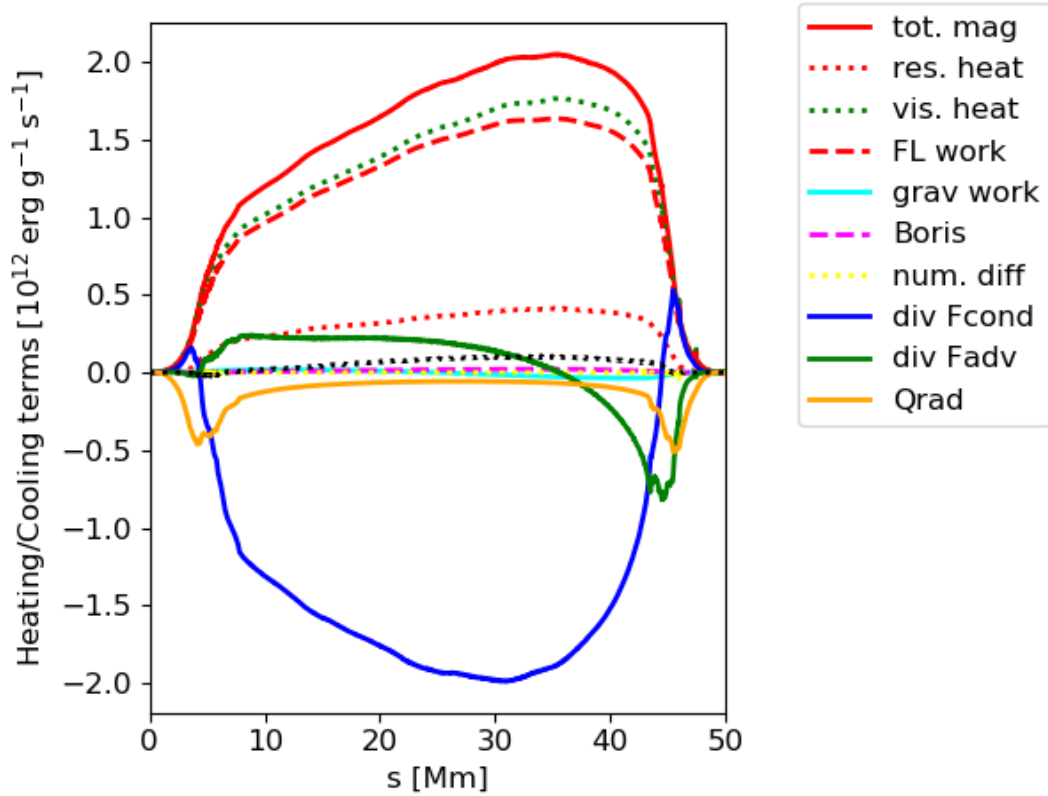


Figure 2.3: Energy balance for the high resolution run as a function of arclength. Depicted are the total magnetic energy input (solid red line), a combination of the work done by the Lorentz force (red, dashed), the Ohmic heating rate (red, dotted), the advective energy flux (green, solid), the viscous heating rate (green, dotted), radiative losses (orange, solid), heat conduction (blue, solid), work done by the gravitational force (light blue), the semi-relativistic correction term in the energy equation (magenta, dashed), and the numerical diffusion term (dashed, yellow). The dotted black line marks the sum of all the different terms in the energy equation. The quantities were averaged over half an hour of solar time. The volumetric energy fluxes are divided by the horizontally averaged density.

possible forwards and backwards in time. All quantities including the magnetic field are assumed to be periodic in the horizontal directions, therefore a field line that exits the simulation domain through the side boundaries re-enters the domain at the opposite side boundary. I implemented the field line tracing algorithm in Python based on an existing analysis script.

2.4.2 Vortex detection: Swirling strength

The concept of a vortex is a tube-like structure coherently rotating about its spine (Zhou et al. 1999). Several techniques have been employed to identify vortices, but despite the intuitive definition of a vortex, there is no unambiguous detection criterion. Potential vortex identification criteria include enhanced vorticity $\omega = |\nabla \times \mathbf{v}|$ or Instantaneous Vorticity

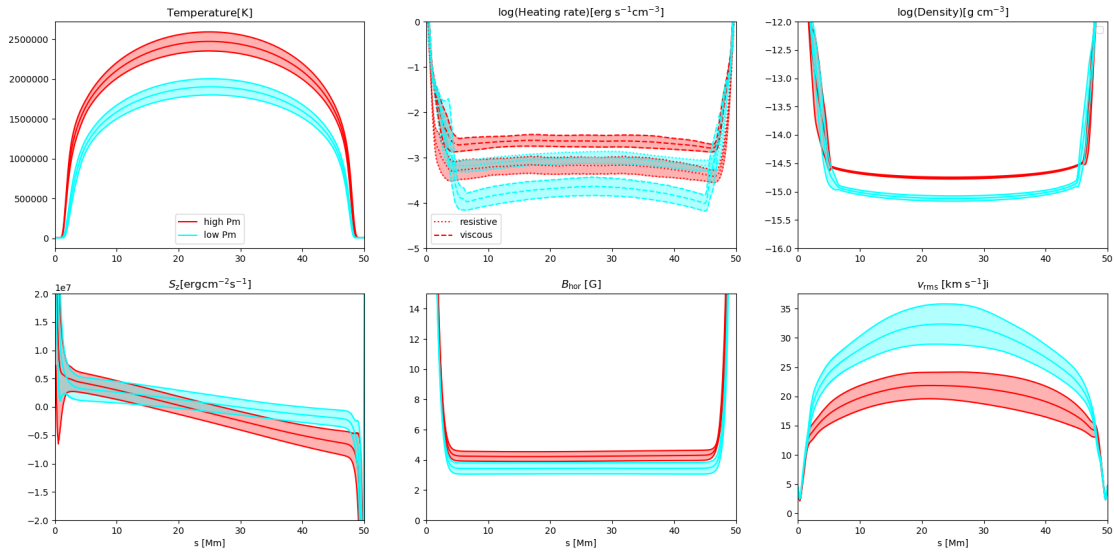


Figure 2.4: Comparison of the high and low Prandtl number regime. Top row: Horizontally averaged temperature, viscous (dashed line) and resistive (dotted line) heating rates and density above the photosphere as a function of arclength. Bottom row: Axial component of the Poynting flux, transverse magnetic field and rms velocities. The high Prandtl number run is shown in red and the low magnetic Prandtl number run in blue. The shaded areas refer to the standard deviation of the profiles due to temporal variation. The quantities have been averaged over half an hour.

Deviation (IVD) (Silva et al. 2020).

The vorticity as a criterion for vortex detection is problematic since a nonzero vorticity $\omega = |\nabla \times \mathbf{v}|$ can also arise from a shear flow without rotation (Moll et al. 2011). Here we make use of the swirling strength criterion. To find grid cells that are part of a rotating fluid structure, the eigenvalues of the velocity gradient tensor $\mathfrak{U}_{ij} = (\partial_j v_i)$ are examined (Zhou et al. 1999). When the discriminant of the characteristic equation for the velocity gradient tensor is positive, the tensor can either have three real eigenvalues or a real eigenvalue and a pair of complex conjugated eigenvalues. The velocity gradient tensor can be locally diagonalized as (Zhou et al. 1999, Canivete Cuissa and Steiner 2020)

$$\mathfrak{U} = [\mathbf{u}_r, \mathbf{u}_+, \mathbf{u}_-] \begin{bmatrix} \lambda_r & 0 & 0 \\ 0 & \lambda_+ & 0 \\ 0 & 0 & \lambda_- \end{bmatrix} [\mathbf{u}_r, \mathbf{u}_+, \mathbf{u}_-]^{-1}, \quad (2.41)$$

where $\lambda_{\pm} = \lambda_{cr} + i\lambda_{ci}$ are the complex eigenvalues, λ_r is the real eigenvalue and \mathbf{u}_r , \mathbf{u}_+ , and \mathbf{u}_- are the corresponding complex eigenvectors. The magnitude of the swirling strength can be measured by the imaginary part of the complex eigenvalue, λ_{ci} . In the case of rigid rotation, the swirling period is $T = 2\pi/\lambda_{ci}$.

The eigenvectors encode information about the orientation and direction of rotation of the vortex. The real eigenvector \mathbf{u}_r determines the direction of the axis of the vortex, while the direction of rotation depends on the handedness of the basis formed by the eigenvectors. In case of a left-handed basis, the rotation with respect to \mathbf{u}_r is counter-clockwise,

while it is clockwise for a right-handed basis (Canivete Cuissa and Steiner 2020). The basis can be forced to be left-handed by multiplying \mathbf{u}_r by -1 if the basis is right-handed. The flow is then always counter-clockwise with respect to the axis determined by \mathbf{u}_r and the orientation of the rotation can be inferred from the sign of \mathbf{u}_r . The shear part of the vorticity is given by $\omega_{\text{shear}} = \omega - 2\lambda_{\text{ci}}$ (Moll et al. 2011). The distribution of the transverse velocity, the vorticity, the swirling strength and the shear part of the vorticity for a slice at 2 Mm for the high resolution run are shown in Fig. 2.5. The swirling strength criterion detects the smallest vortices present. To detect larger structures with this technique, the velocity field needs to be downsampled. Following the procedure described in Yadav et al. (2020b), the velocity field is convolved with a Gaussian kernel in three dimensions. The effect of the downsampling procedure is demonstrated in Fig. 2.6, which shows the velocity orthogonal to the loop axis, the swirling strength computed from the velocity field at the original resolution and the swirling strength computed from the smoothed velocity field for a large-scale rotating structure. This structure is studied in detail in chapter 4. The computation of the swirling strength was performed in post-processing. I implemented the computation of the swirling strength using Python. The computation of the eigenvalues of the velocity gradient tensor was performed using NumPy's linalg submodule.

2.4.3 Synthetic spectral profiles

In order to compute synthetic spectral profiles, we synthesize the emission in each grid-point under the assumption of ionization equilibrium. The tabulated radiative losses for the investigated optically thin spectral lines are taken from CHIANTI version 10 (Dere et al. 1997, Del Zanna et al. 2021). The computation of the spectral profiles was done using pre-existing IDL routines and tabulated loss functions compiled with CHIANTI. Note that the calculation of optically thin losses in the current version of MURaM and the emissivities calculated in the postprocessing step differ slightly, while the optically thin loss function implemented in MURaM assume a constant ratio of electron to hydrogen density, this ratio is determined from the local value of the temperature in CHIANTI. This issue should be addressed in the future.

The spectral profiles are computed following the procedure in Peter et al. (2004, 2006). The particles within a resolution element undergo random thermal motions that lead to thermal broadening of the emission line due to the Doppler shift caused by the particle motion. The line profile at each gridpoint is assumed to have a Gaussian shape. The profile is assigned a Gaussian width given by the thermal width. The thermal width is given by

$$w_{\text{th}} = \left(\frac{2k_{\text{B}}T}{m_{\text{ion}}} \right)^{1/2}. \quad (2.42)$$

The line profile is shifted according to the LOS velocity at the respective grid point. The line profile at each grid point is then given by:

$$I_{\nu} = I_{\text{Peak}} \exp - \frac{(v - v_{\nu})^2}{w_{\text{th}}^2}. \quad (2.43)$$

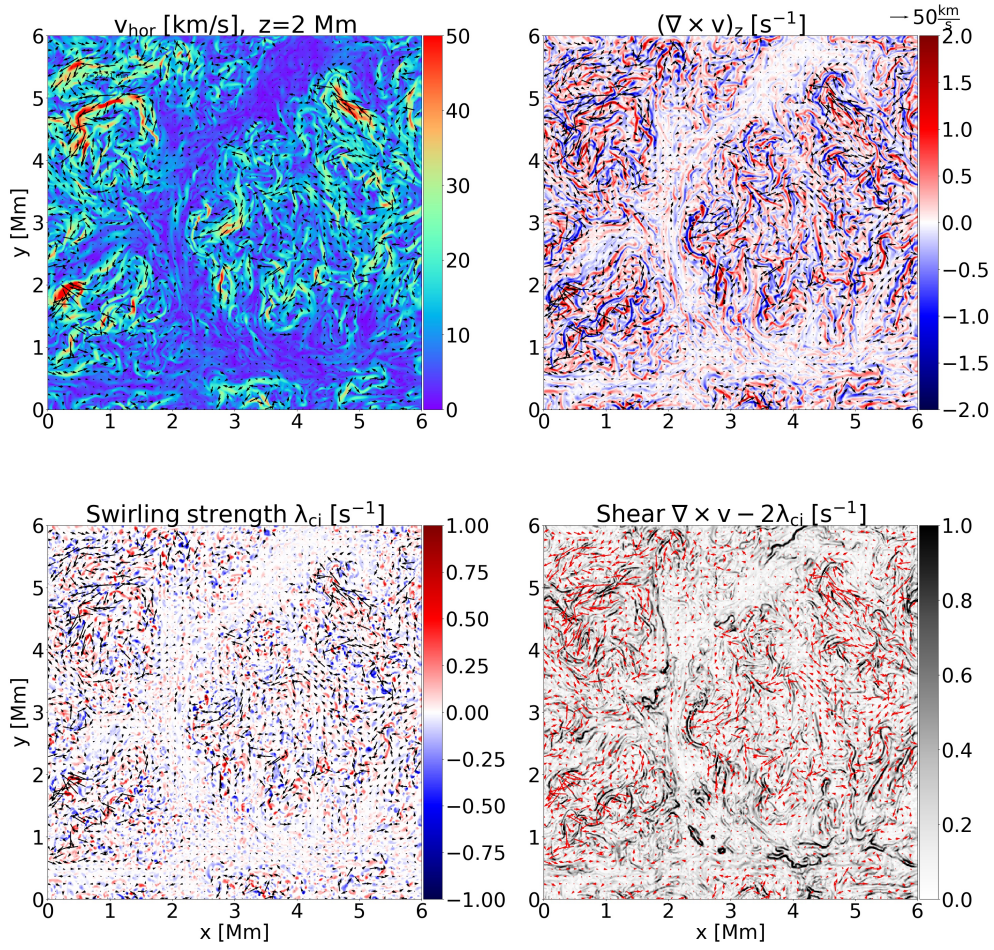


Figure 2.5: Velocity perpendicular to the magnetic field, axial component of vorticity, axial component of the swirling strength and shear part of vorticity on a cut at a height of 2 Mm above the photosphere for a resolution of 12 km at time 22.21 min.

The relationship between the peak intensity and the total intensity given by the emissivity in a gridpoint is

$$I_{\text{Peak}} = \frac{I_{\text{tot}}}{\sqrt{\pi}w_{\text{th}}}. \quad (2.44)$$

Integrating along the LOS yields the spectral profile

$$I_{\text{v}}^{\text{synth}} = \int_{\text{LOS}} I_{\text{v}} dl. \quad (2.45)$$

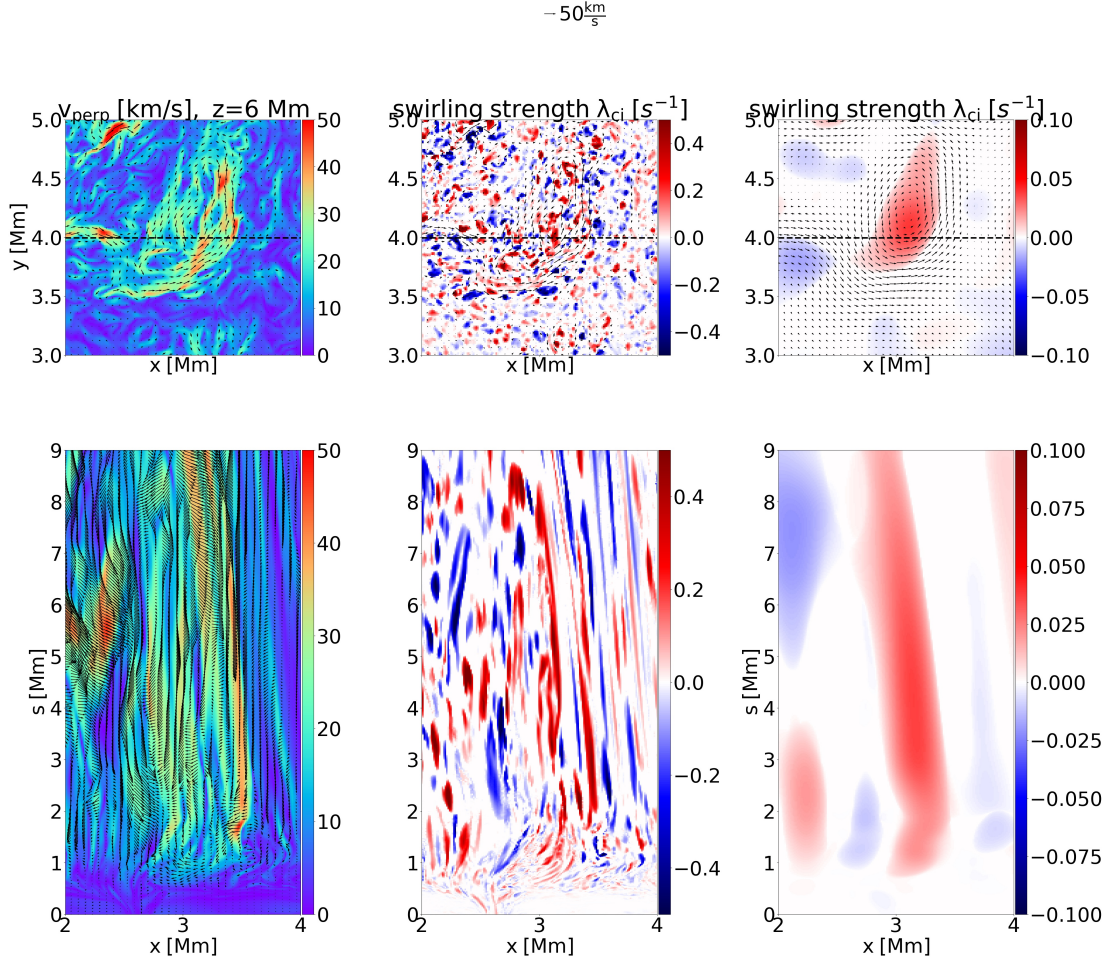


Figure 2.6: Perpendicular and axial cuts through the simulation domain for the high resolution run with $\Delta x = 12$ km at time $T=2.23$ min. The perpendicular cuts are taken at a height of 6 Mm, while the axial cuts are taken at $y=4$ Mm. From left to right: Velocity perpendicular to the loop axis, axial component of the swirling strength computed from the velocity field at the original spatial resolution of 12 km, axial component of the swirling strength computed from the velocity field at an effective resolution of 500 km. The dashed black line in the top panels marks the position of the axial cut.

Integrated intensity, shift and width are computed from the 0th, 1st and 2nd moment of the integrated spectral line profile:

$$I^{\text{synth}} = \int I_v^{\text{synth}} dv, \quad (2.46)$$

$$v^{\text{synth}} = \frac{1}{I^{\text{synth}}} \int v I_v^{\text{synth}} dv, \quad (2.47)$$

$$w^{\text{synth}} = \left(\frac{2 \int (v - v^{\text{synth}})^2 I_v^{\text{synth}} dv}{I^{\text{synth}}} \right)^{1/2}. \quad (2.48)$$

To compute the nonthermal line width, the thermal line width is subtracted, assuming a thermal width corresponding to the line formation temperature T_{line} . This yields for the nonthermal line width:

$$w_{\text{int}}^{\text{synth}} = \left(w_{\text{synth}}^2 - \frac{2k_{\text{B}}T_{\text{line}}}{m_i} \right)^{1/2}. \quad (2.49)$$

3 A solar coronal loop in a box: Energy generation and heating

The content of this chapter was published in Astronomy & Astrophysics.

Credit: C. Breu, H. Peter, R. Cameron, S.K. Solanki, D. Przybylski, M. Rempel and L.P. Chitta, A&A 658 A45, 2022, DOI: 10.1051/0004-6361/202141451, reproduced with permission © ESO

Contributions to the paper: I performed the simulations, analyzed the data, and wrote the first draft of the manuscript; all authors contributed to the ideas behind the study and to the final form of the paper.

Abstract

Coronal loops are the basic building block of the upper solar atmosphere as seen in the extreme UV and X-rays. Comprehending how these are energized, structured, and evolve is key to understanding stellar coronae. Here we investigate how the energy to heat the loop is generated by photospheric magneto-convection, transported into the upper atmosphere, and how the internal structure of a coronal magnetic loop forms. In a 3D magnetohydrodynamics (MHD) model, we study an isolated coronal loop rooted with both footpoints in a shallow layer within the convection zone using the MURaM code. To resolve its internal structure, we limited the computational domain to a rectangular box containing a single coronal loop as a straightened magnetic flux tube. Field-aligned heat conduction, gray radiative transfer in the photosphere and chromosphere, and optically thin radiative losses in the corona were taken into account. The footpoints were allowed to interact self-consistently with the granulation surrounding them. The loop is heated by a Poynting flux that is self-consistently generated through small-scale motions within individual magnetic concentrations in the photosphere. Turbulence develops in the upper layers of the atmosphere as a response to the footpoint motions. We see little sign of heating by large-scale braiding of magnetic flux tubes from different photospheric concentrations at a given footpoint. The synthesized emission, as it would be observed by the Atmospheric Imaging Assembly (AIA) or the X-ray Telescope (XRT), reveals transient bright strands that form in response to the heating events. Overall, our model roughly reproduces the properties and evolution of the plasma as observed within (the substructures of) coronal loops. With this model we can build a coherent picture of how the energy flux to heat the upper atmosphere is generated near the solar surface and how this process drives and governs the heating and dynamics of a coronal loop.

3.1 Introduction

Solar coronal loops are bright structures of hot plasma confined by the magnetic field, observable in X-ray and extreme ultraviolet (EUV) light (Reale 2014). Coronal loops can be found in the quiet sun as well as in active regions. The plasma temperatures in the coronal loops range from 1 to about 10 MK. The heating mechanism that sustains coronal loops is subject to active discussions. Proposed models include wave heating (Alfvén 1947, van Ballegoijen et al. 2011, Parnell and De Moortel 2012, van Ballegoijen et al. 2014, Shi et al. 2021) and the braiding of the magnetic field lines by photospheric motions (Parker 1972, 1983, 1988, Priest et al. 2002, Rappazzo et al. 2008).

In the direct current (DC) model, small-scale horizontal photospheric motions at the loop footpoints lead to tangling of the magnetic field lines. The reconnection of braided field lines is thought to lead to small, impulsive heating events with energies of 10^{24} erg, the so-called nanoflares (Parker 1972, 1983, 1988). Many such heating events could be capable of heating the corona to the observed temperatures. The necessary energy inflow into the corona estimated from observations is $F = 10^7$ erg cm⁻² s⁻¹ above an active region (Withbroe and Noyes 1977), which leads to an estimate for the average heating rate of $Q = 4 \times 10^{-3}$ erg cm⁻³ s⁻¹ (van Ballegoijen et al. 2011).

How energy injection and dissipation determines the internal structure of a loop is the subject of active research. Energy and mass transport predominantly occurs along the magnetic field. Instead of being a monolithic isolated structure, a loop potentially consists of a bundle of multithermal thinner flux tubes (Cargill 1994). Imaging instruments such as the High-resolution Coronal Imager (Hi-C; Cirtain et al. 2013, Rachmeler et al. 2019) have yielded observations of fine threads in the loops. It has been suggested that the interior of coronal loops is dynamic and has a substructure at scales below the instrumental resolution (Gomez et al. 1993). Theoretical considerations suggest that the individual threads could have widths down to 10 to 100 km (Beveridge et al. 2003, Cargill and Klimchuk 2004, Vekstein 2009). So far, Hi-C has provided the highest resolution in coronal observations and provided evidence of strands being as thin as 200 km (Brooks et al. 2013, Williams et al. 2020b). Thick monolithic loops, however, have also been found in Hi-C observations, which do not show evidence for any substructure below 1.5 Mm (Peter et al. 2013).

The spatial resolution that can be achieved with numerical simulations based on magnetohydrodynamics (MHD) models covering a full active region is insufficient to fully take the internal driving inside a flux tube due to computational limitations into account. With grid spacings on the order of hundreds of kilometers, coronal structures are resolved by only a few grid points across their diameter (Bingert and Peter 2011, Rempel 2017, Warnecke and Peter 2019), leading to less structured loops and potentially less energy input. High resolution simulations are required to resolve the internal loop structure and study the heating mechanism in more detail.

Therefore, we simplify the loop geometry and straighten the coronal loop to fit into a Cartesian box. The coronal loop is modeled as a magnetic flux tube between two photospheric layers evolving independently. This is possible if the loop diameter is small compared to the radius of curvature of the loop, which is comparable to the loop length. In straightened loop simulations, coronal loops are represented as straightened magnetic flux bundles anchored in a layer within the convection zone at each footpoint. In simula-

tions of a curved loop with a single photosphere, the actual loop to be modeled will fill only a small fraction of the coronal volume. This makes simulations with high resolution and long time-duration very costly in terms of computational time compared to our approach of a straightened loop in a box. This general type of stretched-loop model goes back to the seminal work of Galsgaard and Nordlund (1996).

Models of magnetic braiding and MHD turbulence in a straightened-out coronal loop in a rectangular box have been employed in a number of works. Many of these impose a photospheric driver and then investigate its influence on the coronal structure and heating. This is usually done by prescribing a velocity field driving the magnetic field line braiding at the boundary of the simulation domain. Rappazzo et al. (2008, 2010, 2013) study braiding models in reduced MHD with a prescribed velocity driver to mimic photospheric flows. MHD turbulence is found to be responsible for the transport of energy to small scales (Rappazzo et al. 2008, Buchlin and Velli 2007) where it is dissipated. These studies propose a complex relation between driving motions and resulting turbulent flows.

The first study of a straightened loop in full MHD was conducted by Galsgaard and Nordlund (1996) and investigated the response of an initially homogeneous magnetic field to shearing motions at two boundaries. This has been complemented by including stratification in a 2D simulation (Galsgaard and Rousev 2002).

Instead of the energy transport into the corona, several studies of straightened loops focus on the energy transfer from the magnetic field to the plasma and investigate the turbulent relaxation of a braided initial magnetic field (Wilmot-Smith et al. 2010, 2011, Pontin and Hornig 2015, Pontin et al. 2016, 2017). Local instabilities in flux tubes can trigger energy release by magnetic avalanches if the unstable flux tube disrupts neighboring threads (Hood et al. 2016, Reid et al. 2018, 2020).

The realism of the photospheric driving in previous stretched-loop studies ranges from a simple shearing motion as employed in Galsgaard and Nordlund (1996), to superposition of pulses recreating the observed coronal power spectrum used in Pagano and De Moortel (2019). Both shearing and twisting motions are studied. In Reale et al. (2016) the magnetic field is braided by random rotational motions. In these simulations of straightened loops, photospheric footpoint motions are assumed to occur on the length scale of granulation. van Ballegooijen et al. (2011) instead consider transverse motions within a magnetic concentration on a length scale smaller than the flux element to be responsible for coronal heating by Alfvén wave turbulence. De Moortel and Galsgaard (2006a,b) look at the interaction between two flux tubes subjected to rotating and spinning motions, whereas van Ballegooijen et al. (2011) consider only a single flux concentration. Thus it does not take the splitting up and merging of flux elements that might play an important role for the energy supply into account.

The cancellation of small-scale magnetic flux elements with a dominant main polarity and reconnection at the loop footpoints could play an important role for the energization and mass supply of coronal loops (Chitta et al. 2017, Priest et al. 2018), but has not been considered in any of these models. In particular, none of these models consider a realistic boundary condition at the photosphere, where magnetoconvection self-consistently drives the energization of the loop above. In previous straightened-loop studies, the boundary of the simulation domain is located in the lower corona or chromosphere, not including the physics of the photosphere or convection zone where the actual driving takes place. Additionally, mass transport between photosphere, chromosphere, and corona and the

interaction of magnetic elements and flux emergence at the surface is not considered.

We aim to study the internal structure of a loop and its connection to the photosphere, while having a self-consistent energy input into the corona arising from granular motion. Here we carry out simulations in full 3D MHD. A large fraction of previous studies of straightened coronal loops employ reduced MHD, which is not valid if the perturbation of the magnetic field becomes as strong as the guide field, which is the case if turbulence develops in the loop. In the framework of reduced MHD, the magnetic field is assumed to be a superposition of a strong magnetic guide field and a small perturbation perpendicular to the guide field. In contrast to reduced MHD, we solve the complete nonlinear system of MHD equations unrestricted by the assumption that the perpendicular component of the magnetic field is small compared to the guide field (Oughton et al. 2017).

Our model includes the photosphere and near-surface convection zone. Including the upper layers of the convection zone in the simulation domain self-consistently leads to heating of the chromosphere and corona due to changing magnetic structures at the loop foot-points. In contrast to more idealized experiments studying one process in isolation, with a realistic driver for the magnetic field multiple heating processes are instead excited simultaneously. Observations point to coronal loops having a substructure below the instrument resolution, which cannot be resolved in models of a full active region. Such models can resolve only a few 100 km (Warnecke and Peter 2019).

The structure of the paper is as follows. We describe the methods and our loop model in detail in Sect. 3.2, analyze heat generation, transport, dissipation, and loop structure in Sect. 3.4, discuss our results in Sect. 3.5, and present conclusions in Sect. 3.6.

3.2 Coronal loop model

In this section we describe our loop model, the code used to conduct the numerical experiments, the simulation setup, and employed initial conditions. In addition, we discuss the driving at the photosphere and the synthesis of the EUV and X-ray emission expected from the model. The loop is modeled in a simplified geometry as a straightened flux tube in a Cartesian box spanning the space between two shallow convection zone layers at its footpoints.

3.2.1 Equations and loop model

Radiative 3D MHD simulations are performed with the MURaM code (Vögler et al. 2005), using the extension of the code for coronal simulations by Rempel (2017). We solve the system of radiative magneto-hydrodynamic equations on a Cartesian grid in the

form (Rempel 2014, 2017):

$$\frac{\partial \rho}{\partial t} = -\nabla \cdot (\rho \mathbf{v}), \quad (3.1)$$

$$\begin{aligned} \frac{\partial \rho \mathbf{v}}{\partial t} &= -\nabla \cdot (\rho \mathbf{v} \mathbf{v}) - \nabla P + \rho g_s(z) \hat{\mathbf{z}} + \mathbf{F}_L + \nabla \cdot \boldsymbol{\tau} \\ &+ \mathbf{F}_{\text{SR}}, \end{aligned} \quad (3.2)$$

$$\begin{aligned} \frac{\partial E_{\text{HD}}}{\partial t} &= -\nabla \cdot [\mathbf{v}(E_{\text{HD}} + P + q\mathbf{B}/|\mathbf{B}|)] + \rho \mathbf{v} \cdot (g_s(z) \hat{\mathbf{z}}) \\ &+ \mathbf{v} \cdot \mathbf{F}_L + \mathbf{v} \cdot \mathbf{F}_{\text{SR}} + Q_{\text{rad}} + Q_{\text{thin}} \\ &+ Q_{\text{num,res}} + \nabla \cdot (\boldsymbol{\tau} \cdot \mathbf{v}), \end{aligned} \quad (3.3)$$

$$\frac{\partial \mathbf{B}}{\partial t} = \nabla \times (\mathbf{v} \times \mathbf{B}) + \mathbf{D}_{\text{num,res}}, \quad (3.4)$$

$$\frac{\partial q}{\partial t} = \frac{1}{\tau_{\text{cond}}} (-f_{\text{Sat}} \sigma T^{5/2} \mathbf{B}/|\mathbf{B}| \cdot \nabla T - q). \quad (3.5)$$

The system of equations that is being solved consists of the equations for the conservation of mass, momentum, and energy as well as the induction equation and the equation for heat conduction. ρ , \mathbf{v} , P and \mathbf{B} are mass density, velocity, pressure, and magnetic field, respectively. See Sect. 3.2.2 for a definition of the gravitational acceleration $g_s(z)$ and discussion of the loop model. \mathbf{F}_{SR} is a semi-relativistic correction term limiting the Alfvén velocity in order to alleviate constraints on the timestep by using an artificially reduced speed of light (see Rempel 2017). The Lorentz force \mathbf{F}_L is computed as $\mathbf{F}_L = \frac{f_A}{4\pi} \nabla \cdot (\mathbf{B}\mathbf{B} - \frac{1}{2}I\mathbf{B}^2) + (1 - f_A) \frac{1}{4\pi} (\nabla \times \mathbf{B} \times \mathbf{B})$. I is the identity matrix and the prefactor $f_A = 1/\sqrt{1 + (\frac{v_A}{c})^2}$ determines the transition between different treatments of the Lorentz force for high- and low beta regions to avoid spurious field-aligned components of the Lorentz force. Instead of the total energy that would include also the magnetic energy, the plasma energy E_{HD} is used, which is the sum of internal and kinetic energy: $E_{\text{HD}} = E_{\text{int}} + 0.5\rho v^2$. In order to maintain the $\nabla \cdot \mathbf{B} = 0$ condition, the code uses hyperbolic divergence cleaning (Dedner et al. 2002).

The model includes gray local thermodynamic equilibrium (LTE) radiative transfer in the photospheric and chromospheric layers as well as Spitzer heat conduction along the magnetic field and optically thin radiative losses in the corona. Q_{rad} is the radiative heating or cooling computed from LTE radiative transfer, while Q_{thin} denotes the optically thin radiative losses of the form $Q_{\text{thin}} = -n_e n_H \Lambda(T)$, where n_e is the electron density, n_H the number density of hydrogen nuclei, and $\Lambda(T)$ is a tabulated loss function (Rempel 2017). $q \cdot \mathbf{B}/|\mathbf{B}|$ is the field-aligned conductive heat flux. $\boldsymbol{\tau}$ is the strain-rate tensor. The viscous force $\nabla \cdot \boldsymbol{\tau}$ arising from nonzero viscosity is added in the momentum equation. The work done by the viscous term also leads to a contribution in the energy equation of $\mathbf{v} \cdot (\nabla \cdot \boldsymbol{\tau}) = \nabla \cdot (\boldsymbol{\tau} \cdot \mathbf{v}) - \boldsymbol{\tau} : (\nabla \mathbf{v})$, where the second term on the right-hand-side is the energy taken out of the kinetic energy reservoir and added to the internal energy by viscous heating. Since the numerical scheme is conservative for the sum of kinetic and internal energy, the viscous heating term is not explicitly included in the energy equation. The energy removed from the kinetic energy reservoir by viscous heating is added to the internal energy reservoir and thus does not lead to a net change in the sum $E_{\text{int}} + E_{\text{kin}}$.

Instead of explicit viscosity and a constant magnetic resistivity, only numerical resistivity and viscosity are taken into account in the simulations. The resistive heating is computed from the numerical fluxes at the cell interfaces for the magnetic field components. Instead of evaluating the strain-rate tensor, the viscous terms are calculated in a similar fashion from the fluxes for the velocity components. The numerical fluxes are calculated from a slope-limited diffusion scheme using a piecewise-linear reconstruction of the variables at the cell interfaces (for details on the diffusion scheme see Rempel 2014, 2017). The behavior of the diffusion is controlled by the parameter h , which, set to zero, will lead to a second order Lax-Friedrichs scheme, higher values concentrate the diffusion around monotonicity changes. Thus, the diffusivity of the scheme decreases with increasing h . For the h parameter a value of $h=2.0$ was used in the convection zone and photosphere. In the corona, a value of $h=1.25$ was employed for the diffusion of mass, energy and momentum. A value of $h=5.0$ was used for the magnetic field. For a value of $h > 1$ the diffusivity is switched off in sufficiently smooth regions and only kicks in around discontinuities in the solution (Rempel 2014, 2017). This leads to a nonuniform resistivity in the simulation box. The resistive heating term $Q_{\text{num,res}}$ is then added in the energy equation to account for conservation of energy. The viscous heating is computed only for diagnostic purposes. However, there is an energy flux due to numerical effective viscous force, which is nonzero but very small compared to the other terms. This viscous energy flux is added in the energy equation for consistency. The values we chose for the free parameter h correspond to the high Prandtl number setting in Rempel (2017). As a consequence, the viscous heating dominates over the resistive heating, especially in the chromosphere and low corona. In the coronal part, the viscous heating rate is roughly a factor of three higher than the resistive heating rate. To close the system of equations, we use an equilibrium ionization equation of state (Rempel 2017).

In order to avoid time step constraints from the numerical treatment of the heat conduction and to speed up the simulation, hyperbolic heat conduction as described in Rempel (2017) is used to limit the maximum signal propagation speed. q is the field-aligned heat flux, the parameter f_{sat} is a factor taking into account the saturation of the conductive heat flux and σ is the constant of the Spitzer heat conductivity, for which we use a value of $\sigma = 10^{-6} \text{ erg cm}^{-1} \text{ s}^{-1} \text{ K}^{-1}$. τ_{cond} is a parameter chosen to determine the maximum propagation speed of the heat front.

Likewise, we use the Boris correction in order to limit the Alfvén speed to 3000 km/s to avoid very small timesteps (Rempel 2017). The Boris correction makes use of a semi-relativistic treatment of the MHD equations with an artificially reduced speed of light, leading to an asymptotic limit of the Alfvén velocity.

The simulation box spans the solar atmosphere from the upper convection zone through the photosphere to the hot corona. The simulation domain is periodic in the x - and y -direction and has a horizontal extent of $6 \text{ Mm} \times 6 \text{ Mm}$. At both ends of the simulation box in the s -direction, there is a photosphere and shallow convection zone driving the plasma evolution in the loop. The depth of the convection zone layer at each footpoint is 3.5 Mm and the extent of the box along the loop axis is 57 Mm , leading to an effective loop length of 50 Mm . Due to its length, it can be assumed that footpoints of the loop at both ends are far apart (about 30 Mm in case of a semi-circular loop of the same length). The simulation domain is covered by $100 \times 100 \times 950$ gridpoints, giving a spatial resolution of 60 km . The grid is equidistant. The current version of MURaM does not allow

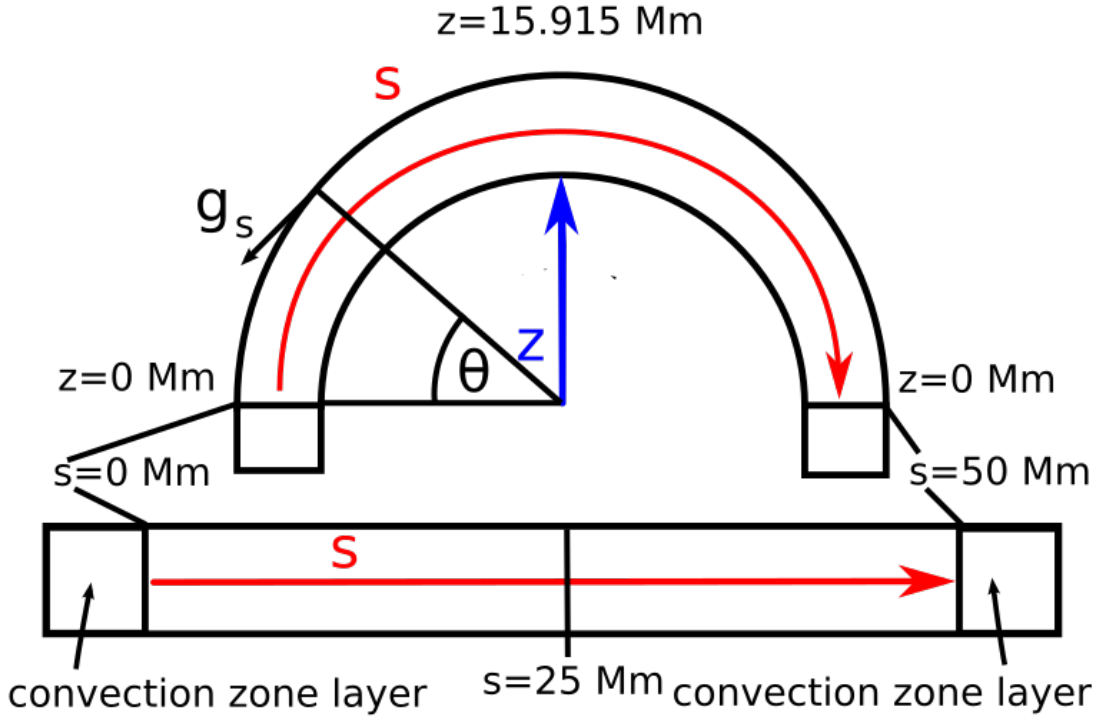


Figure 3.1: Sketch to illustrate the loop geometry.

for mesh refinement to better resolve the transition region or photosphere. In later studies this resolution will be significantly increased.

3.2.2 Loop geometry

The MURaM code was modified to allow for a simplified loop geometry. Here we define z as the geometrical height above the photosphere and s as the coordinate along the loop axis. The gravitational acceleration was modified above the photospheric layer to account for the curved geometry of the loop assuming a semicircular shape. Only the component along the loop axis, here in the s -direction was considered,

$$g_s(z) = g \cdot \cos\left(\pi \frac{s(z) - h_{\text{photo}}}{s_{\text{max}} - 2 \cdot h_{\text{photo}}}\right). \quad (3.6)$$

Here we assumed a semi-circular loop with straight vertical ends. The gravitational acceleration was modified above the photosphere, below the solar surface a constant value was assumed. Here, while h_{photo} is the height of the photosphere measured from the bottom boundary of the simulation box, which we set to 3.5 Mm. The coordinate $s(z) = \theta \times (\pi/180 \cdot R)$ is the arclength of the loop with R being the loop radius. With a height of the convection zone layer of 3.5 Mm and a loop length of 50 Mm, we have a loop radius of ca. 15.915 Mm.

s_{max} is the total extent of the simulation box in the direction along the loop axis, which is

57 Mm in our case. The setup and the relation between the height z and the coordinate s along the loop axis are illustrated in Fig. 3.1. The component of the gravitational force perpendicular to the loop axis can be neglected if the gravitational force is negligible compared to the Lorentz force. This condition is fulfilled for regions with low plasma-beta, defined as the ratio of gas pressure to magnetic pressure $\beta = \frac{p_{\text{gas}}}{p_{\text{mag}}}$. The condition $\beta \ll 1$ is fulfilled for the coronal part of the simulation box.

Both boundaries at the loop footpoints are located in the near-surface convection zone about 3.5 Mm below optical depth unity. At these boundaries we allow for mass flux across the boundary layer so that the shallow convection zone can develop below the surface. The simulated layers of the bottom of these shallow convection zone layers at both ends of the loop are open for outflows (downward directed). The entropy and pressure of the inflows through the bottom boundaries is prescribed in order to fix the mass contained in the box and the brightness of the solar surface.

Further adjustments were made to the radiative transfer computation. The optical depth was integrated from both sides of the loop from the boundary in the convection zone upward in the direction of the loop apex. The incoming radiation from each side was set to zero in the midplane at the loop apex to ensure that the radiation coming from the photosphere on one side does not heat the opposite photospheric layer. In the coronal part of the computational domain, only optically thin radiative losses play a role and the plasma is not affected by the incoming radiation from both footpoints.

3.3 Initial conditions

As a first step toward an initial condition we used a stratified atmosphere in hydrostatic equilibrium. We started from a shallow convection simulation without a corona, which extends only 1 Mm above the surface. We define the location of the photosphere as the height at which the horizontally averaged optical depth is unity. The shallow simulation box was evolved without a magnetic field until convection reaches a statistically steady state. Subsequently, a uniform axial magnetic field of 30 G was added and the box was evolved for an hour. This corresponds to many convective turnover times and several Alfvén crossing times. This should ensure that the solution becomes independent of the initial condition. During this time, the magnetic field is advected into the intergranular lanes due to convective motions. The magnetic field is concentrated in flux tubes of kilogauss strength. The average unsigned surface magnetic field is amplified by the convection to roughly 70 G, which corresponds to a weak plage region.

To get the initial condition for the coronal loop model, we took a shallow box of near-surface magnetoconvection, duplicated it, flipped the polarity, and stitched these two boxes together with a long coronal part. The shallow rectangular box formed the loop footpoints at both boundaries and a hot corona was added between the two photospheric layers. Before that, a small random velocity was added to each gridpoint for one of the shallow boxes to ensure an independent evolution of the plasma in the box and therefore of the magnetic field at each footpoint. As initial condition in the coronal part, we chose a plane parallel atmosphere. We prescribed an initial temperature profile following a hyperbolic tangent in each loop leg with a maximum temperature of 1 MK at the loop apex. The temperature profile is symmetric to the loop midplane. Density and pressure were

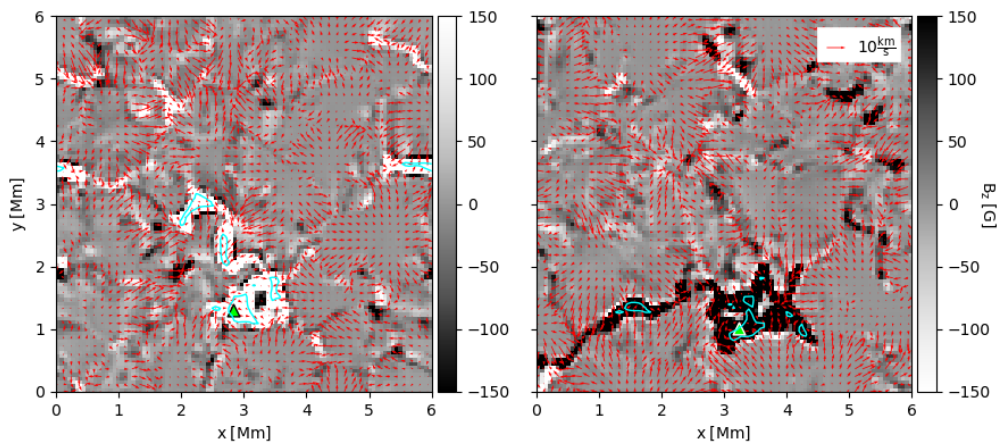


Figure 3.2: Vertical magnetic field at the photosphere at both loop footpoints at the depth where $\langle \tau \rangle = 1$. The snapshot was taken at $t = 24.34$ min. The red arrows show the magnitude of the horizontal velocity at the photospheric level (see legend at top right). The blue contours indicate regions with $|B_z| > 1000$ G. The green triangles mark the footpoints of the field line investigated in Sect. 3.4.2.2. For a discussion of the initial condition for the magnetic field see Sect. 3.3. A movie is available online.

then calculated from the temperature profile under the assumption of hydrostatic equilibrium. The setup was evolved for another hour in order to become independent of the initial condition.

Some important effects have been neglected in this setup, such as the expansion of the loop with height above the chromosphere. A study of the effect of loop geometry on heating is conducted for 1D models in Mikić et al. (2013). For loop models with nonuniform cross-section, the authors find a higher density at the apex and a higher pressure at the coronal base, which leads to an increased emission in EUV compared to the model with a uniform cross-section. This is due to an increased maximum heat flux into the loop for the nonuniform cross-section models leading to larger radiative losses in the transition region. Since the temperature at the apex is roughly the same for both the uniform and the nonuniform area models, the density at the apex is enhanced for the expanding loop models. Therefore, we expect our model to underestimate the loop density and hence the coronal emission.

3.3.1 Magnetoconvection in the bottom layers

The simulation is driven by magnetoconvection. Fig. 3.2 shows the vertical magnetic field B_z at unity optical depth at 500 nm, $\langle \tau \rangle = 1$, for both photospheric layers at each footpoint of the coronal loop. Magnetoconvection concentrates the magnetic field in flux tubes at the vortices of granular downflow lanes (Rempel 2014). These magnetic elements

with kilogauss field strengths have widths of several tens to hundreds of kilometers. Blue contours in Fig. 3.2 highlight several flux tubes with $|B_z| > 1000 G$.

In addition to displacement of the flux concentrations by convective motions, transverse motions occur within flux elements on length scales smaller than the flux element (van Ballegoijen et al. 2011, Moll et al. 2012, Yadav et al. 2020b, 2021). Observations do point to such internal motions (Chitta et al. 2012). This is possible because the flux tubes are surrounded by turbulent convective downflows. Flux elements are not only displaced as in the flux tube tectonics model by Priest et al. (2002), but also deformed and field lines rooted within them are intermixed. Fig. 3.2 is supplemented with a movie showing the time evolution of the photospheric magnetic field. Small-scale footpoint motions within the kG flux tubes have an rms velocity around 2 km s^{-1} . The rms velocity of photospheric motions away from flux concentrations is larger, about 3 km s^{-1} . The internal motions within a flux tube are comparable to the setup by van Ballegoijen et al. (2011). Instead of being prescribed at the boundaries, the driving of each loop footpoint at the coronal base thus arises self-consistently from magnetoconvection.

3.3.2 Synthetic emission

In order to compare our loop model to observational data, we computed synthetic observations as would be seen in EUV and X-ray emission. To characterize emission from the corona around 1 to 2 MK we synthesized the EUV channels of the Atmospheric Imaging Assembly (AIA; Lemen et al. 2012). For the synthesis of X-ray emission we used the response for the Al-Poly filter of the X-Ray Telescope for the Hinode Mission (XRT; Golub et al. 2007). The emission is dominated by collisionally excited lines. In case of XRT there is also a contribution from the X-ray continuum. Thus the emission is proportional to the product of electron and hydrogen number density and the energy loss per time and unit volume is given as

$$\varepsilon = n_e n_H K(T), \quad (3.7)$$

where $K(T)$ is a kernel given by the contribution function of the lines and continua in the bandpass accounting for the effective area of the instrument. These kernels for AIA are given in Boerner et al. (2012), and Lemen et al. (2012). For XRT, the kernels for the different filters are given in Golub et al. (2007). Here we used these kernels as they are provided through the SolarSoft¹ package for AIA and XRT. We computed the emission from the temperature and density in each gridpoint of the output data. The synthetic observations were then obtained by integrating along the line of sight perpendicular to the loop axis:

$$F = \int n_e n_H K(T) dx. \quad (3.8)$$

3.4 Results

In the following sections, we discuss the general properties and time evolution of the loop, the injection of energy into the upper atmosphere, its dissipation, and the resulting overall

¹<https://www.lmsal.com/solarsoft/>

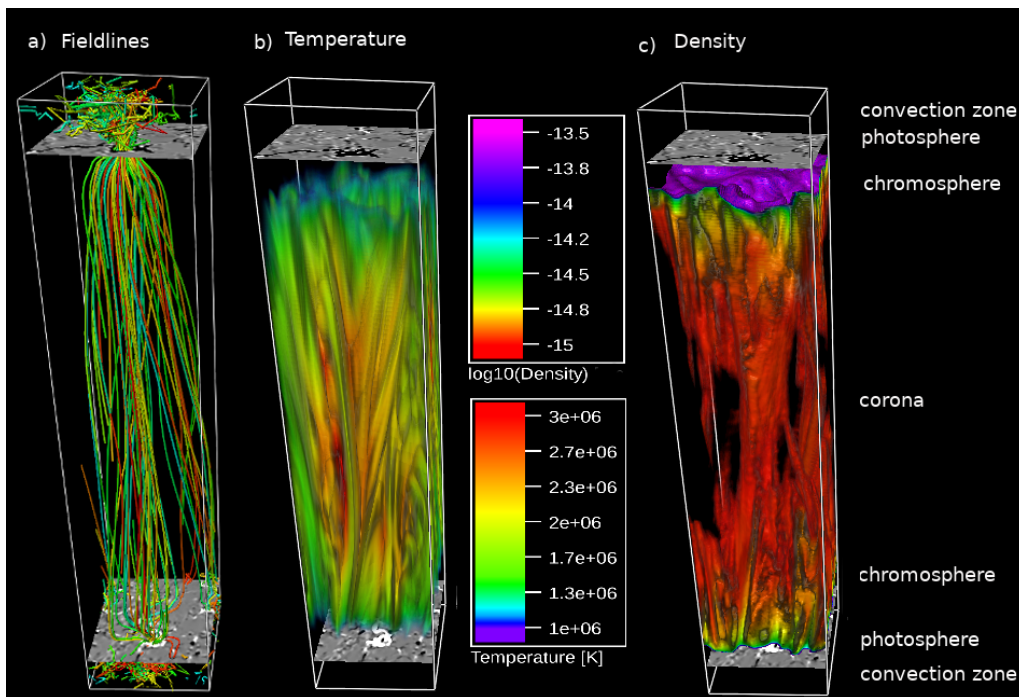


Figure 3.3: Simulation setup. (a) Example magnetic field lines in the simulation box traced from locations with strong magnetic field. The vertical magnetic field is plotted on a horizontal cut at the average photospheric height. (b) Volume rendering of the loop temperature in K. (c) Volume rendering of the loop density in gcm^{-3} . The s-axis (along the loop) has been compressed by a factor of two for better visibility.

structure and dynamics of the loop. We also synthesize observables from the simulation data.

3.4.1 Overall behavior

The simulation setup is illustrated in Fig. 3.3. The snapshot displayed is the same as in Fig. 3.2. The vertical component of the magnetic field is plotted in two cuts at the heights of each photosphere. Magnetic field lines were traced from the location of strong photospheric magnetic field. The field line bundles reveal an internal twist of the loop caused by photospheric motions. Panels (b) and (c) show a volume rendering of density and temperature, respectively. A contiguous substructure with locally enhanced temperature and density develops in the coronal part of the simulation box and is aligned with the magnetic field. A close-up of the loop footpoints is shown in Fig 3.4. The field lines were traced from locations with increased magnetic field in the lower corona to the photosphere. The magnetic field is mainly rooted in a few strong magnetic elements. At both footpoints, the magnetic field lines show signs of internal twisting and braiding within a single magnetic concentration.

The time evolution of the averages of coronal temperature, electron density, and heating rate is displayed in Fig. 3.5. All quantities were averaged over the coronal part of the computational domain, which is defined here as the part of the simulation domain

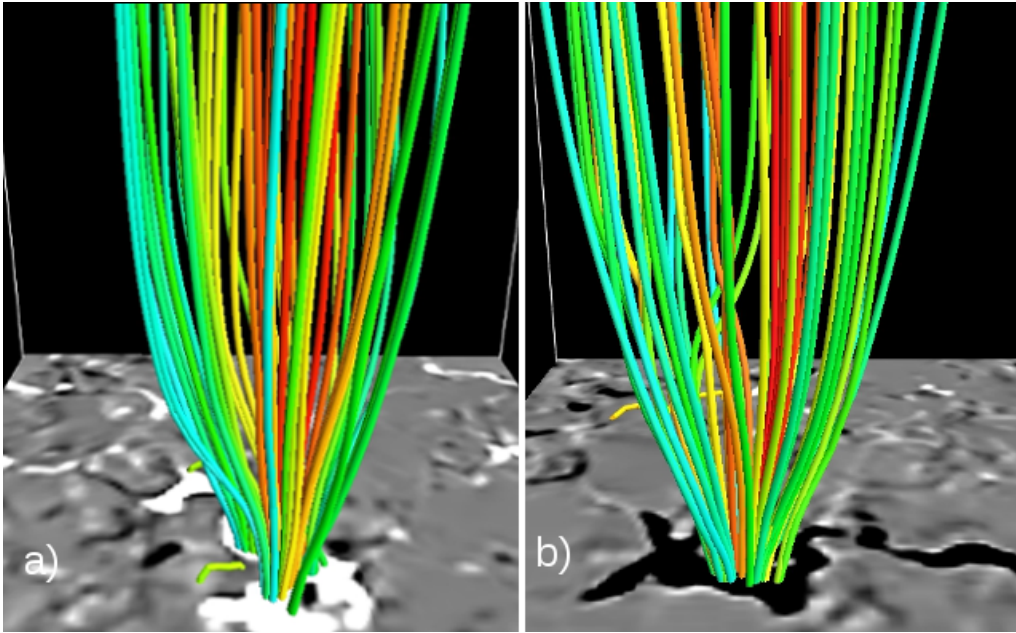


Figure 3.4: Close-up of the footpoints of the loop shown in Fig. 3.3. Magnetic field lines are traced from regions of enhanced magnetic field at a height of 2 Mm above the photosphere. The colors show the field line seed index.

with densities below 10^{-12} g/cm³ or particle densities below 5.98×10^{11} cm⁻³. All quantities show oscillatory behavior with periods of several minutes. The total heating rate, which is the sum of viscous and resistive heating, shows several strong heating events at 37.7 min, 62.2 min and 65.3 min. The heating rate is intermittent, energy is injected in pulses of varying duration. Longer heating events with lifetimes of five to ten minutes are superposed with short spikes of a duration on the order of seconds to minutes.

This is qualitatively consistent with the results of Bingert and Peter (2013) for a global active region simulation, where they find heating transient in time and space with pulses having a duration of a few minutes up to half an hour. Their study, however, is conducted with a lower resolution of 390 km in the x- and y-direction and 240 km in the z-direction.

Bursty heating, which occurs on shorter timescales than the temperature evolution, is also found by Reid et al. (2020) for a simulation of an MHD avalanche in three twisted magnetic field threads triggered by a local instability. Once the system reaches a continuously driven state, it continues to generate short bursts of heating superposed on a continuous background heating rate.

Over a simulation time of one hour, the mean temperature varies from 1.3 to 1.8 MK. We find mean electron densities on the order of 5×10^9 cm⁻³ in the corona. After the heating events at 37.7 min and 62.2 min, the coronal temperature shows a steep increase. Between 60 min and 70 min the electron density increases roughly by a factor of 1.5, reaching a peak with a delay of five minutes after the temperature peak at 62.2 min. The mean temperature reaches its maximum value at 38 min and decreases to a local minimum value over a timescale of a quarter of an hour.

In response to an increase in temperature and density, the loop brightens in EUV and

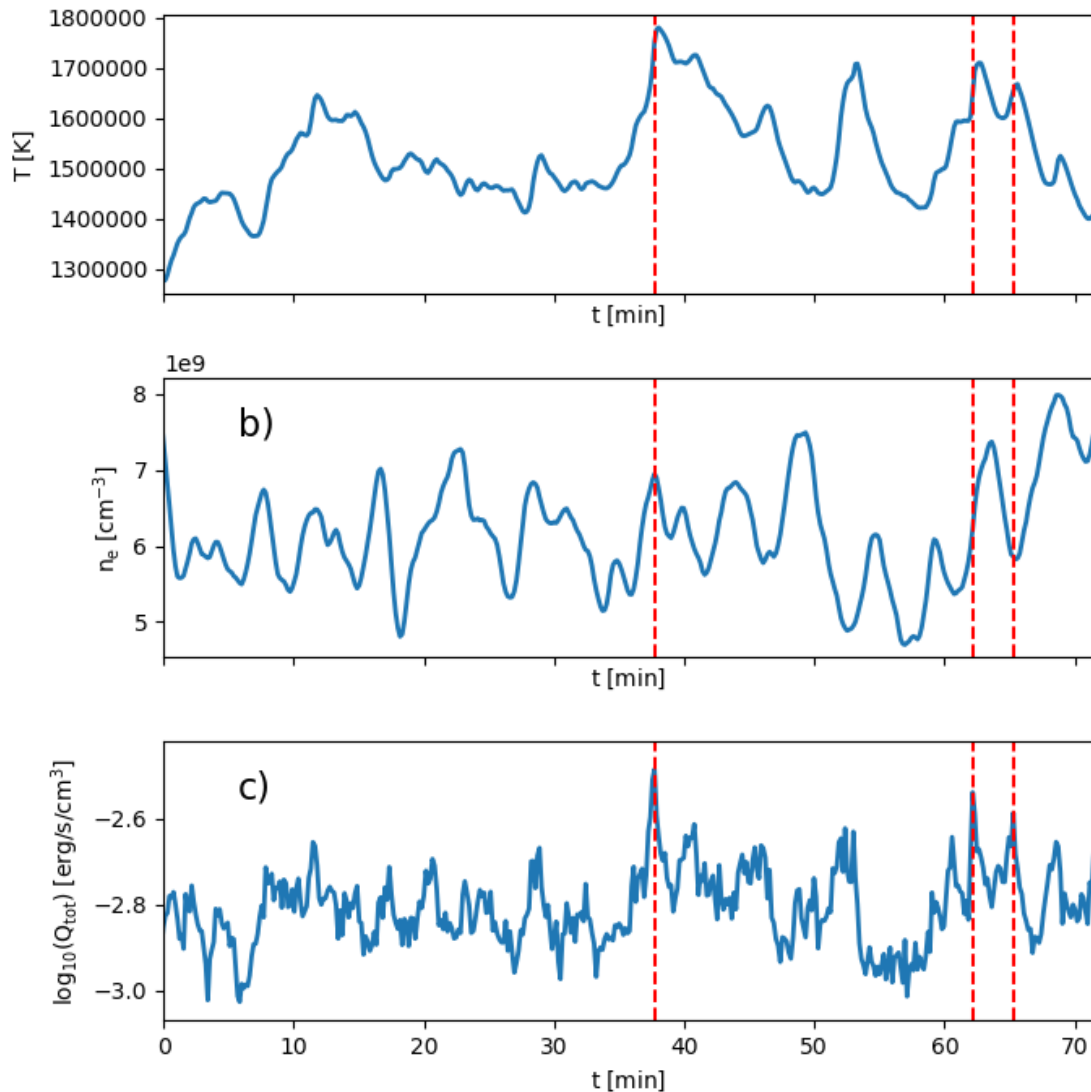


Figure 3.5: Averaged quantities in the coronal part of the simulation domain as a function of time. We define $t=0$ s as the time when we start collecting snapshots after the simulation extended to the coronal part has run for an hour of solar time. Panel (a) shows the temperature, panel (b) the electron density and panel (c) the sum of viscous and resistive heating. All quantities have been averaged over regions with densities below 10^{-12} g/cm³. The vertical dashed lines highlight several strong heating events. For a discussion of the time evolution see Sect. 3.4.1 and 3.5.1.

X-ray wavelengths. A time evolution of the normalized emission in the coronal part of the loop in the 171, 193, and 211 Å bands as well as in the Al-poly filter of XRT is shown in Fig. 3.6. After the heating event at 37.7 min, the loop brightens up in the X-ray band first. As the loop cools, the increase in X-ray emission is followed by peaks in the 211, the 193, and the 171 Å channel, which are sensitive to emission from plasma at subsequently lower temperatures. Further peaks in the emission appear after the heating

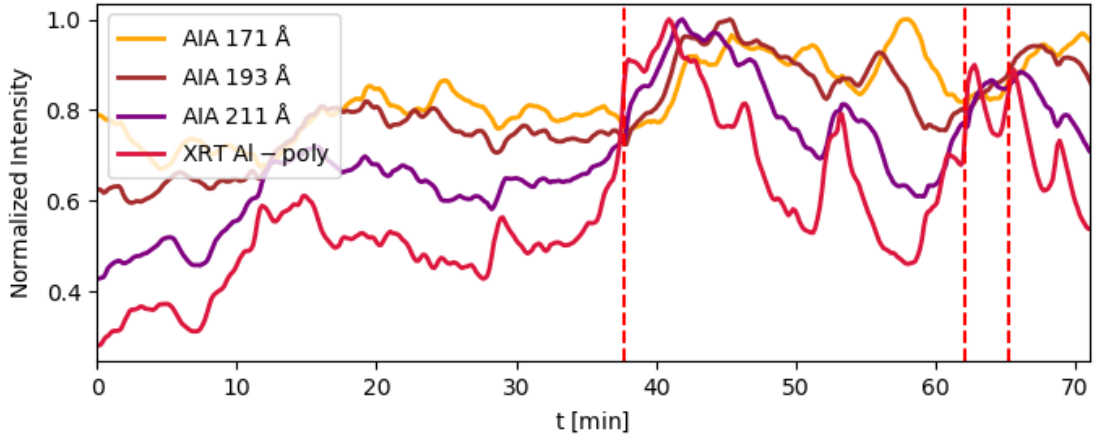


Figure 3.6: Normalized intensity integrated over the coronal part of the simulation domain as a function of time. The vertical dashed lines highlight the same strong heating events as in Fig. 3.5. For a discussion of the time evolution see Sect. 3.4.1 and 3.5.1.

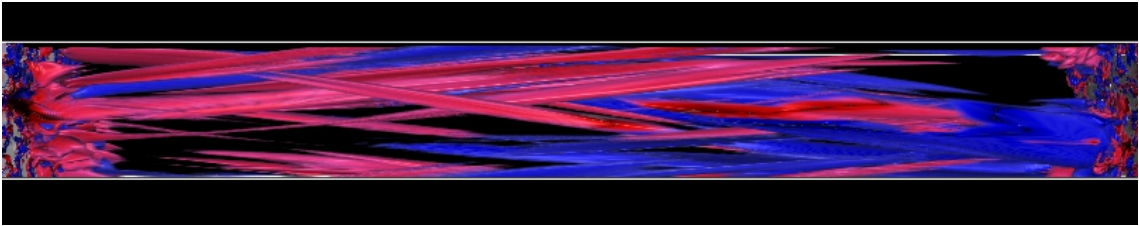


Figure 3.7: Volume rendering of the axial component of the Poynting flux in the Solar atmosphere in a given snapshot at time 24.34 min. The Poynting flux directed in the positive s -direction (that is, from left to right in this figure) is shown in red and the Poynting flux directed in the negative s -direction is shown in blue. The s -axis is defined as the coordinate along the loop axis. The range of the color scale is -1×10^8 to $+1 \times 10^8$ erg cm² s⁻¹. The figure shows the volume encompassing chromosphere and corona between the two photospheres, one at each footpoint. See Sect. 3.4.3.

events at 52 min, 62.2 min, and 65.3 min.

3.4.2 Poynting flux and heating

In this section we discuss the energy input and heating. We start with briefly outlining the field line tracing method and follow this with a discussion of energy injection as well as dissipation along an individual field line in time. We then present a description of the spatial distribution of the injection of Poynting flux into the loop, the resulting loop structure and the development of current sheets.

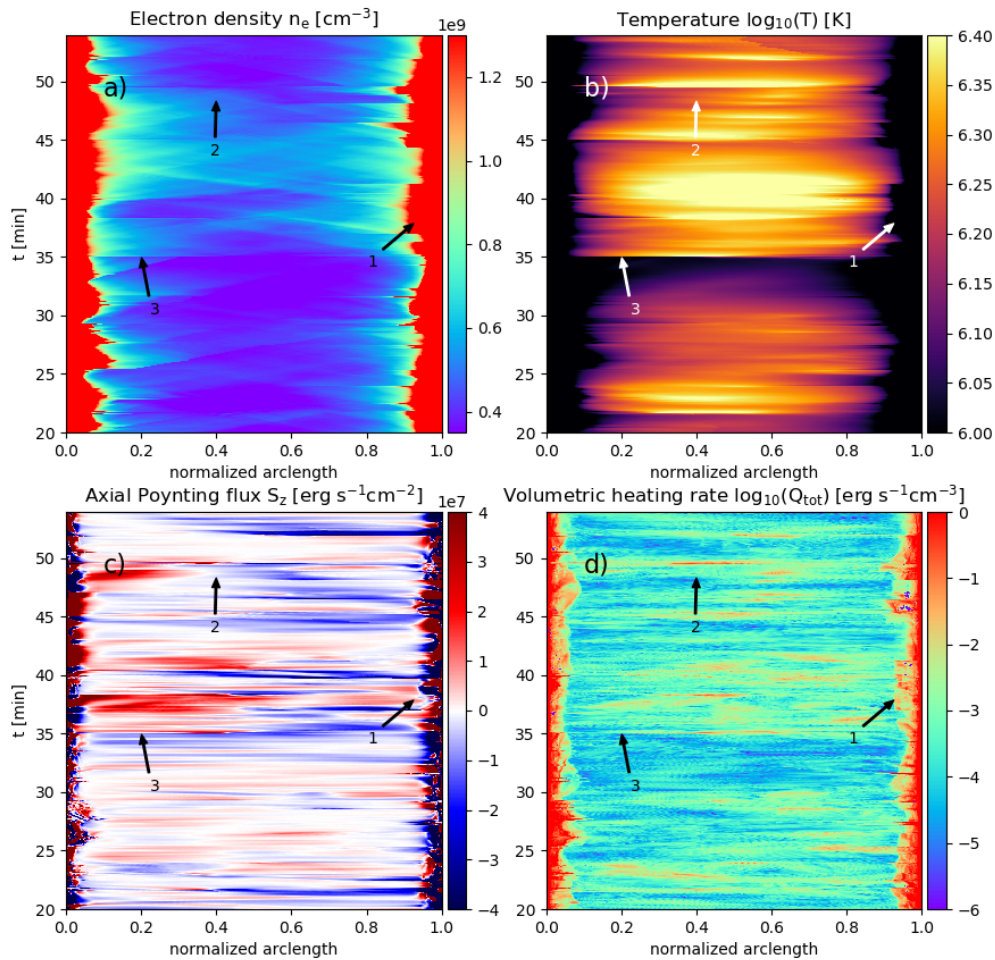


Figure 3.8: Spatio-temporal evolution along a field line with the arclength of the field line on the abscissa and time on the ordinate. The quantities shown are electron density (a), temperature (b), axial component of the Poynting flux (c), and total heating rate (d). Temperature and heating rate are scaled logarithmically. Positive Poynting flux (red) indicates energy propagating in the direction of increasing arc length (to the right), negative Poynting flux (blue) is in the opposite direction. The seed point from which the field line is traced is advected in time with the plasma velocity. The arrows mark locations of Poynting flux reaching the opposite chromosphere (1), dissipation (2), and reconnection (3), see Sect. 3.4.2.2. For clarity, only the part of the time series containing the strongest heating event at 37.7 min depicted in Fig. 3.5 is shown.

3.4.2.1 Field line tracing

In order to relate heating events to energy influx from the photosphere, we followed a set of magnetic field lines in time and space. The field lines were integrated in space from

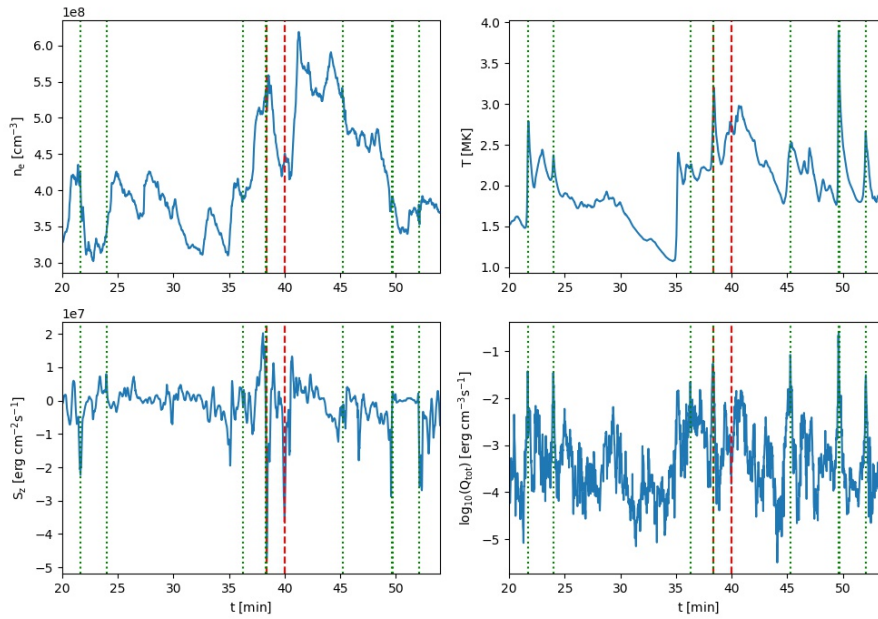


Figure 3.9: Time evolution of various quantities at the intersection of the field line shown in Fig. 3.8 with the loop apex. The red dashed lines mark the two strongest Poynting flux events, while the green dotted lines mark the six strongest heating events, see Sect. 3.4.2.2. For clarity, only part of the time series containing the strongest heating event at 37.7 min depicted in Fig. 3.5 is shown.

randomly chosen seed points at the apex using a 4th order Runge-Kutta algorithm. We followed each field line in time by assuming that the magnetic field and the plasma are frozen together because of the high electric conductivity. The seed point chosen to lie on the midplane of the loop (that is, the loop apex) was advected with the velocity field of the plasma. The updated field line at the next time step was traced from the updated location of the seed point, then the intersection of the new field line with the midplane of the simulation box was used as the new seed point to be advected in the subsequent timestep. To show results for one sample field line, we selected an individual field line connected to plasma reaching a temperature of several million Kelvin at the loop apex. This field line was found to be anchored in the kilogauss magnetic concentrations at each loop footpoint.

3.4.2.2 Behavior of an individual field line

We now investigate one selected field line to illustrate the changes along field lines in time. The temperature at the apex of this field line reaches values of up to 4.0 MK, thus the selected field line is connected to one of the hottest strands within the loop. The Poynting flux to heat this strand originates from both footpoints. The preferred direction of the Poynting flux at each footpoint is upward into the loop (red on the left side, blue on the right side in Fig. 3.7). The values of various coronal quantities interpolated along the selected field line in form of a spacetime diagram as a function of arclength along the

field line and time over a time range of 35 minutes are displayed in Fig. 3.8.

The Poynting flux in the loop shows periodic behavior. While this period is difficult to see by eye in Fig 8c, or in Fig 9, a Fourier analysis of the (mean) axial Poynting flux shows a clear enhancement of power for periods between 30 s and 50 s. This timescale corresponds to the Alfvén crossing time through the coronal part of the loop. The spacetime diagram shows bursty intermittent heating distributed along the field line as a response to the energy influx. Between $t = 35$ min and $t = 55$ min a number of strong short-lived heating events occur, which cause the field line to heat up. A clear increase in temperature is seen in panel (b) after $t = 35$ min. Following the onset of the heating, the electron density shows filling of the loop with plasma.

The evolution of the same quantities at the apex of the selected field line is shown in Fig. 3.9. The Poynting flux in the selected time range stems predominantly from the left footpoint. While the temperature reaches its maximum between 17 and 20 minutes and subsequently decreases, the electron density continues to rise in response to the up-flows from the footpoints. The two strongest Poynting flux events are associated with a dip in the electron density and subsequent increase. Both are closely followed by spikes in the total heating rate. While especially longer heating events lead to higher temperatures, some strong but short events are not associated with an increase in temperature, for example the first event marked by a vertical line in Fig. 3.9.

It is not straightforward to determine a preferred location of energy deposition in the corona. Regions of the highest level of volumetric heating are concentrated mainly near the footpoints in the chromospheric parts of the loop. The coronal part of the field line shows several strong isolated heating events, but moderate heating occurs along the whole length of the field line. Overall, there seems to be no preferred spatial location for heating in the corona apart from a slight increase in the number of strong localized heating peaks in the upper parts of the loop, which is consistent with Reid et al. (2020).

We find instances at which the Poynting flux injected at one footpoint reaches the chromospheric layer at the other footpoint of the loop, for example at $t = 38$ min (see arrow 1 in Fig. 3.8), but at the same time find evidence for the Poynting flux being dissipated in the atmosphere before reaching the opposite footpoint of the loop, thereby heating the plasma. One example is shown at $t = 48$ min where Poynting flux is injected into the loop from both sides and dissipated near the loop apex, leading to a strong heating event (see arrow 2). Reflection of Poynting flux at the opposite transition region due to the steep gradient of the Alfvén velocity in the lower atmosphere cannot be excluded. We do not see possible reflection events every time the Poynting flux reaches the chromosphere at the opposite side of the loop, instead the Poynting flux seems to be absorbed by the denser material in the lower atmosphere in most cases.

Several reconnection events take place along the field line during the time covered in Fig. 3.8. In the time range from $t = 35$ min to 50 min, when the highest temperatures and the strongest Poynting flux input along the field lines are observed, the field line is connected to the interior or the edges of the kilogauss flux tubes where plasma is pushed into the downflow lanes at least at one footpoint. The largest Poynting flux is seen for a combination of the field line being connected to a region with high magnetic field and strong horizontal flows at the photospheric level.

It is not trivial to follow the field lines in time because they do not retain their identity over a long time range. Similar to the simulation of Reid et al. (2018), the field line

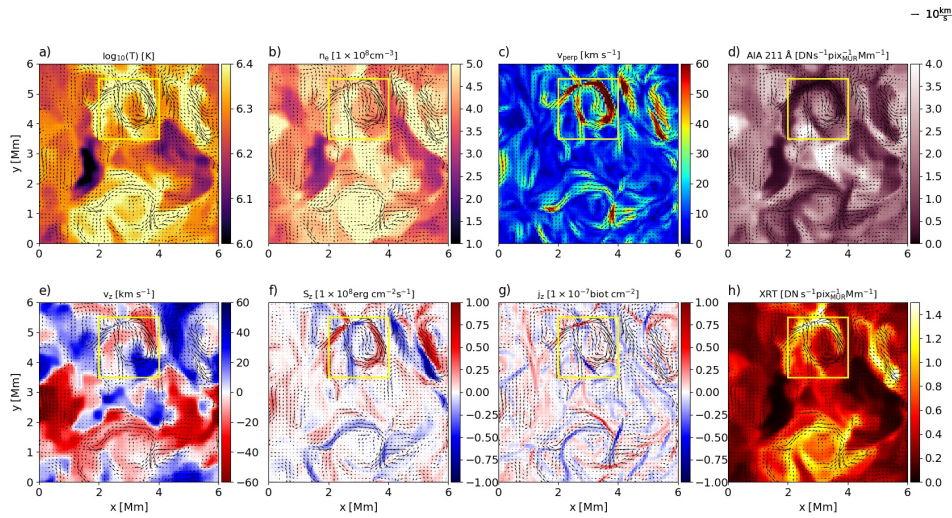


Figure 3.10: Cut through the loop at the apex (cross section perpendicular to the loop axis). (a) Temperature; (b) Electron density; (c) Magnitude of the velocity perpendicular to the loop axis; (d) emission in the 211 Å channel of AIA, (e) Axial component of the velocity; (f) Axial component of the Poynting flux; (g) Axial component of the current density, (h) emission as seen with the Al-poly filter of XRT. The black arrows illustrate the horizontal velocity field. The yellow box highlights the location of a vortex with enhanced temperature and density. The snapshot was taken at $t = 41.02$ min. See Sect. 3.4.3.

undergoes frequent reconnection events with neighboring field lines. Furthermore, in the numerical model the frozen-in condition is not strictly fulfilled due to a finite resistivity, so that the field line can slip through the plasma. Due to numerical inaccuracies, the field line tracing algorithm can jump to a neighboring field line. The algorithm becomes structurally unstable near reconnection regions, where field lines cannot be clearly defined. The arrow (3) in Fig. 3.8 at time $t=35.1$ min indicates a possible reconnection event identified by discontinuities in density and a strong increase in heating rate along the field line.

3.4.3 Loop structure

The magnetoconvection at the solar surface distorts the magnetic field. Photospheric motions such as divergence, shear, and rotation tangle the magnetic field lines. This leads to a Poynting flux into the upper Solar atmosphere. Figure 3.7 shows a volume rendering of the axial component of the Poynting flux entering the loop from the photospheric layer at each footpoint. The resulting Poynting flux has a complex structure of oppositely directed strands in close proximity. The Poynting flux varies on short timescales. In our model we find that the axial component of the Poynting flux associated with transverse flows dominates over the contribution by vertical motions carrying the horizontal magnetic field. The entanglement of strands of Poynting flux suggests braiding of the magnetic field.

The distribution of temperature and density across the loop is highly inhomogeneous.

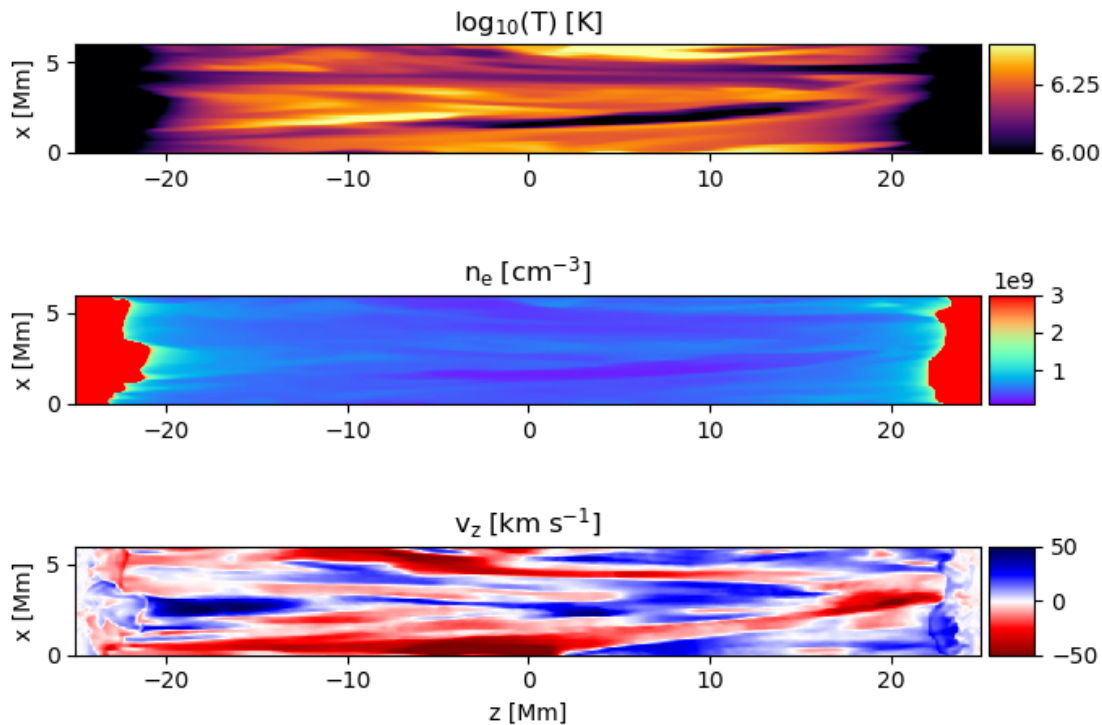


Figure 3.11: Axial cut through the simulation box. From top to bottom: Temperature, electron density, axial component of the velocity. For a discussion see 3.4.3.

Fig. 3.10 and Fig. 3.11 show cuts through the simulation box. Fig. 3.10 reveals a complex structure of the loop cross-section at the loop apex.

Several regions of enhanced Poynting flux are visible in panel (f) of Fig. 3.10. A complex structure of strong thin current sheets has formed in the loop² This is consistent with the well-known scaling relations (for example Rosner et al. 1978) that predict higher temperature and density in the case of increased energy flux into the loop (for example Eqs. 3 and 4 of Peter et al. 2012). Tracing back magnetic field lines from the loop apex shows that the hottest regions are connected to the interior of magnetic concentrations.

In our model, we find the loop to form numerous strands all along the loop, creating clearly discernible substructures. This is in contrast to Reale et al. (2016) who find only one smooth homogeneous hot and dense structure in their numerical model. Instead, in our model the loop consists of individual filaments exhibiting a wide range of temperatures in the midplane from 0.9-4 MK and electron densities from $1 \times 10^8 \text{ cm}^{-3}$ to $5 \times 10^8 \text{ cm}^{-3}$. The top panel of Fig. 3.11 shows that the temperature is enhanced in numerous strands spanning the entire loop length. Likewise, the electron density is increased

²The unit abampere per square centimeter (biot cm^{-2}) corresponds to $1 \times 10^5 \text{ A m}^{-2}$ in SI units and to $c \text{ stA cm}^{-2}$ in the CGS-ESU system, with c being the speed of light. (see panel (g)) in Fig. 3.10). The regions with increased Poynting flux show enhanced temperature. The location of the hottest plasma filaments does not exactly coincide with the highest plasma densities, but the hot regions show enhanced densities.

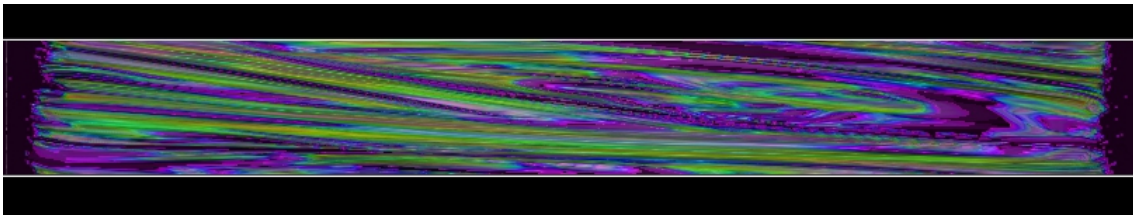


Figure 3.12: Volume rendering of the current density squared in the computational box. The range of the color scale is from 4.8×10^{-24} to 8×10^{-17} $\text{biot}^2 \text{cm}^{-4}$. See Sect. 3.4.3.1.

in structures with a width of several hundred kilometers in the coronal part of the loop. We speculate that we find substructures in our simulation because of the significantly lower diffusivity of our numerical model compared to Reale et al. (2016). Alternatively, it might be that Reale et al. (2016) do not find substructures in the loop because they apply a smooth driving at the footpoints.

Up- and downflows occur within the loop structure at the same time along different strands within the loop. Figure 3.10 e) shows two regions with oppositely-directed flows in the midplane, seen clearly as patches colored in red and blue. In each region the plasma is moving predominantly in one direction along the loop axis. As illustrated in Fig. 3.11, we find cool and dense upflows with a temperature around 10^4 K into the corona with a width of several hundred kilometers and velocities of 10 to 30 km s^{-1} while low-density plasma in the coronal part of the loop at temperatures at and above 1 MK can reach axial velocities of over 50 km s^{-1} . Structures of cool plasma extend up to several megameters above the solar surface. These jets, however, are too slow to be type II spicules (de Pontieu et al. 2007). The upflow velocity, however, is compatible with typical speeds of type I spicules of 10-20 km s^{-1} . We do not expect to accurately simulate Type II spicules due to the low resolution of the chromosphere and transition region. Additional physics may also be required; for example, ambipolar diffusion is necessary to generate spicules in simulations with the Bifrost code (Martínez-Sykora et al. 2017).

3.4.3.1 Current sheets and heating rate

The current sheets resulting from the footpoint motions are elongated along the loop axis (see Fig. 3.12). Many of the current sheets are stretched all along the loop, roughly aligned with the magnetic field. This is similar to the current sheets in the straightened-loop simulations by Rappazzo et al. (2017) and the simulation of a stable active region by (Bingert and Peter 2011). Due to the approximate alignment with the magnetic field, the inclination of the current sheets points to field line braiding. In agreement with findings of those earlier studies, we see that the temperature profile follows predominantly the concentrations of the current.

The relation between the heating rate arising from numerical diffusivity and current sheets is nontrivial. A comparison between the numerical heating and the current sheets computed from the magnetic field is shown in Fig. 3.13. The cuts through the x-y-plane in panels (a) and (b) show that clearly the temperature is enhanced where most energy is deposited. The energy dissipation term is numerical and tailored to act only in

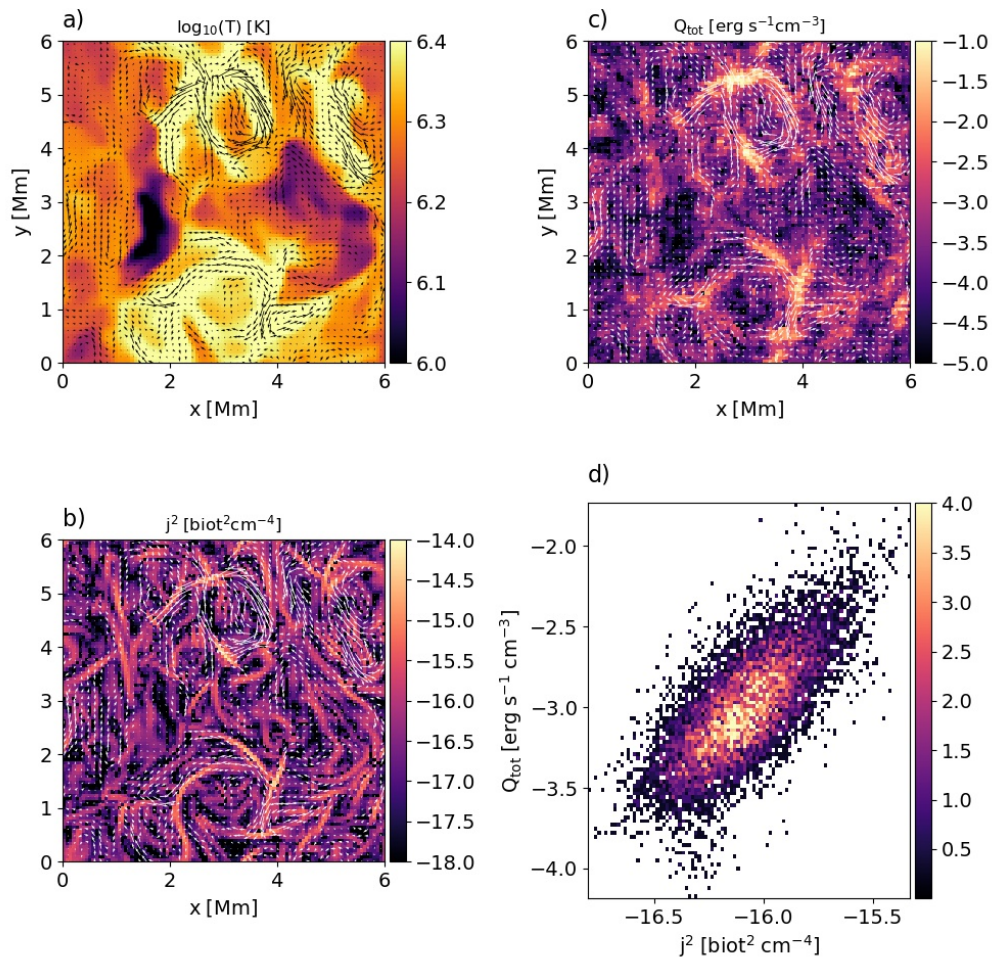


Figure 3.13: Cut through the loop at the apex (cross section perpendicular to the loop axis). (a) Temperature; (b) Sum of viscous and resistive heating; (c) Squared current density; (d) 2D histogram of the total numerical heating rate vs. the squared current density.

locations with the largest gradients, as we pointed out in Sect. 2.1 and as described in more detail by Rempel (2017). Here we show the total (numerical) heating rate, that is, viscous plus resistive. The spatial distribution of these two components is very similar, with (for this snapshot) the viscous heating being about a factor of 5.4 stronger than the resistive term in the coronal part. With the heating being defined through a numerical procedure, we cannot expect an exact one-to-one correlation to the currents, or more precisely the currents squared. Still, comparing panels (b) and (c) we see that mostly threads of enhanced currents and enhanced (numerical) heating rate coincide. This is underlined by panel (d) that shows that there is a correlation between the two quantities, albeit with significant scatter.

The evolution of the loop is dynamic, current sheets continuously form and dissipate. Variations can be seen on a timescale down to seconds, though not shown in Fig. 3.5.

While the current sheets evolve on a short timescale, the evolution of the heated plasma filaments occurs at a slower rate. The evolution of the temperature of individual heated filaments occurs on time scales ≥ 5 min because of the longer cooling time scales through heat conduction and radiation.

The location of the current sheets is associated with strong horizontal flows as can be seen in panels (c) and (f) of Fig. 3.10. We find the formation of multiple small-scale current sheets, which are continuously formed and fragment into smaller parts. The observed range of scales of the current sheets extends down to the dissipation scale, indicating turbulent behavior (Hood et al. 2016).

The substructure of the loop is often organized in swirls. These are best seen through the velocity component perpendicular to the loop. In Fig. 3.10 c we show a cut at the loop apex that shows one prominent swirl (highlighted by the box). Swirling motions in the lower atmosphere due to rotational motions at the solar photosphere have been reported in observations and simulations. They have been related to heating in locations of shear flows (e.g., Wedemeyer-Böhm et al. 2012, Wedemeyer and Steiner 2014, Moll et al. 2011, 2012, Yadav et al. 2021). Here we now see such swirls to extend all the way into the corona where they can still be found at the apex of a coronal loop at a height above the photosphere of 16 Mm. A detailed analysis of these structures will be presented in a subsequent paper.

Likewise, we find these swirls to show an increased temperature as illustrated in Fig. 3.10 a which shows a rotating structure with a width of 2 Mm in the loop midplane (see yellow box). Current density, temperature, and Poynting flux are all enhanced at the outer edge of the swirl (panels (a), (e), (g)). Currents building up at the edges of flux tubes due to the shear caused by the velocity gradient were studied before in De Moortel and Galsgaard (2006a), but in our model these swirls are driven self-consistently by the near-surface magnetoconvection. The rotating swirl is also clearly visible in the EUV emission at 211 Å and in X-rays (see Fig. 3.10d and h). While it appears bright in X-rays, in the EUV it is darker than the surrounding loop. This is also the case for the other swirls in the loop cross-section. This is because in this swirl the temperature exceeds 2 MK (Fig 8a) and it thus is too hot to emit in the 211 Å channel of AIA. With X-rays being sensitive to higher temperatures, these then show a significant brightening. The role these vortices play for coronal loop heating will be subject to a separate study.

Motions perpendicular to the magnetic field are mainly responsible for carrying energy upward into the corona. In our model we find that this s -component of the Poynting flux (along the loop axis) dominates the contribution by vertical motions carrying the horizontal magnetic field (in the x and y directions). Rotating motions that extend upward in nearly vertical vortices are common in the intergranular lanes, but other driving motions such as shear motions are equally possible. Figure 3.14 shows a 2D histogram of the temperature, total heating rate, and squared current density at the loop apex as a function of the velocity perpendicular to the loop axis. This is generally in agreement with Yadav et al. (2020b, 2021), although their simulations do not reach into the corona. The total heating rate is the sum of resistive and viscous heating. An increase of the heat input results in an immediate temperature increase and thus an increase of coronal emission. Consequently, we find a positive correlation between the coronal emission and the velocities perpendicular to the loop. We find that increased heating rates, current densities, and plasma temperatures are clearly associated with higher perpendicular velocities. The

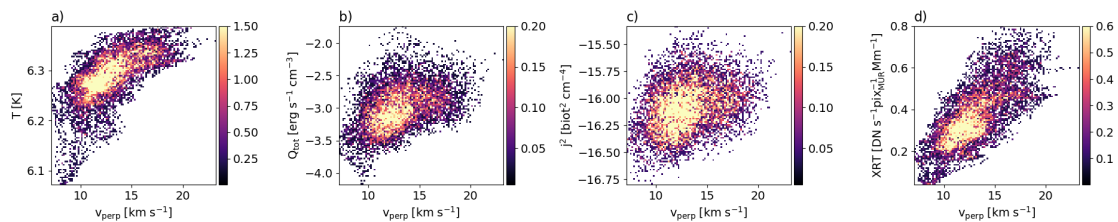


Figure 3.14: 2D histograms of the temperature, total heating, squared current density, and X-ray emission at the apex vs. the velocity perpendicular to the loop axis. The X-ray emission has been computed to correspond to what XRT on Hinode would measure. The quantities have been averaged over a time range of 15 minutes. See Sect. 3.4.3.1.

temperature is enhanced at the location of current sheets created by velocity shear. What one has to keep in mind is that due to the low plasma beta of 7×10^{-3} the Lorentz force will dominate over the gas pressure and the plasma dynamics in the corona are driven by the magnetic field, which follows vortical photospheric flows, not the other way around. The correlation we find between emission and LOS-velocity (panel (d)) in Fig. 3.14 is consistent with the observed correlation between line intensity and nonthermal broadening (e.g., Peter 2000, De Pontieu et al. 2015). We do not see an instantaneous correlation between a peak in the heating rate and the density (Figs. 3.8 and Fig. 3.9). A temperature increase, however, leads to chromospheric evaporation and thus a delayed increase of the loop density. The data have been averaged over 15 minutes of solar time before computing the histograms, so that delayed effects of the heating are also taken into account. The parts of the loop with increased heating are eventually filled with higher-density plasma and brighten in the X-ray band.

3.4.3.2 Isotropy of the velocity amplitude

The velocity components perpendicular to the loop axis have different properties compared to the velocity parallel to the loop axis. The perpendicular velocity is structured on small scales like the currents and is driven by the turbulent motions of the magnetic field. The parallel velocity is structured on larger scales and driven in response to the evaporation of plasma along the guide field due to heating. The distribution of the magnitude of the velocity components, however, is nearly isotropic. We find velocities in the corona perpendicular to the loop axis with an amplitude of up to 80 km s^{-1} . The flows along the loop axis have a similar amplitude. However, comparing the spatial structuring of the perpendicular and the axial flows (Fig. 3.10c and e reveals that in general the axial flows are organized on larger spatial scales (across the loop) ranging from several hundred kilometers up to 2 Mm.

This is in contrast to Pontin et al. (2020), whose loop models lack the dynamics along the guide field because they do not include the interaction with the chromosphere and thus evaporation of plasma that drives the parallel flows. Hence, Pontin et al. (2020) find a strong deviation from isotropy with the axial speeds being much smaller than the flow speeds perpendicular to the loop axis.

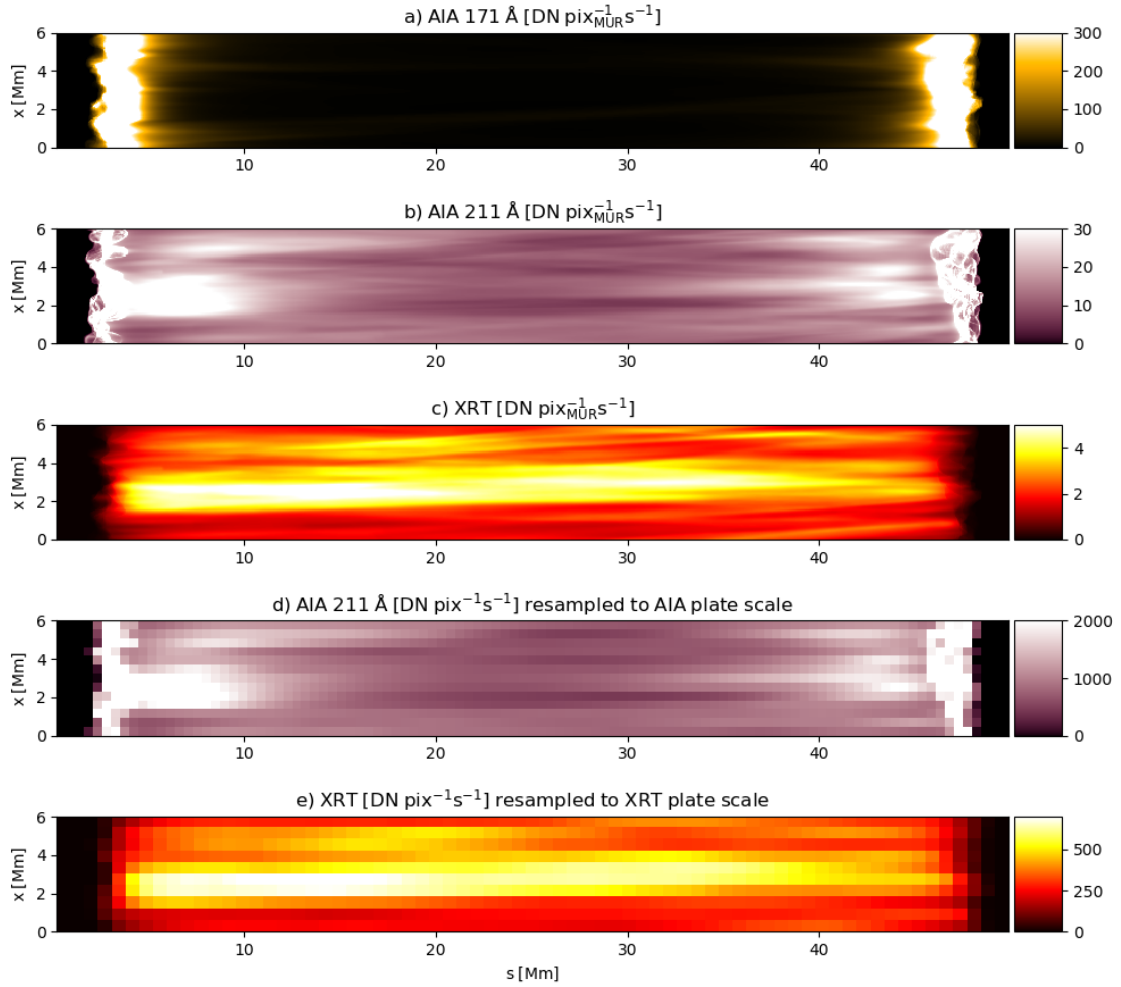


Figure 3.15: View of the simulated loop from the side as seen in EUV and X-ray observations. Panels (a) to (c) show the view at the original resolution of the numerical model, panels (d) and (e) the images downsampled to the plate scale of the instruments. From top to bottom: Synthetic emission for the 171 Å and 211 Å AIA bands integrated along the y -axis, emission as would be measured with the Al-poly filter of XRT, degraded synthetic emission in the 211 Å band taking into account the pixel size of the AIA instrument of 0.6'', degraded emission for XRT with a pixel size of $\sim 1''$. The synthetic emission has been integrated along the line of sight perpendicular to the loop axis. See Sect. 3.4.4.

3.4.4 Synthesized emission

To compare our loop model directly to actual observations by, for example, AIA or XRT we derived the emission from the model as these instruments would observe it. For this we employed the procedure described in Sect. 3.3.2. The average loop temperature ranges from 1.3 MK to 1.8 MK as can be seen in Fig. 3.5. Consequently, the emission corresponding to the AIA 171 Å channel is very much concentrated at the footpoints, with negligible emission in the upper part of the loop compared to the footpoints as shown in panel (a) of Fig. 3.15. This is very similar to the moss emission observed at the footpoints

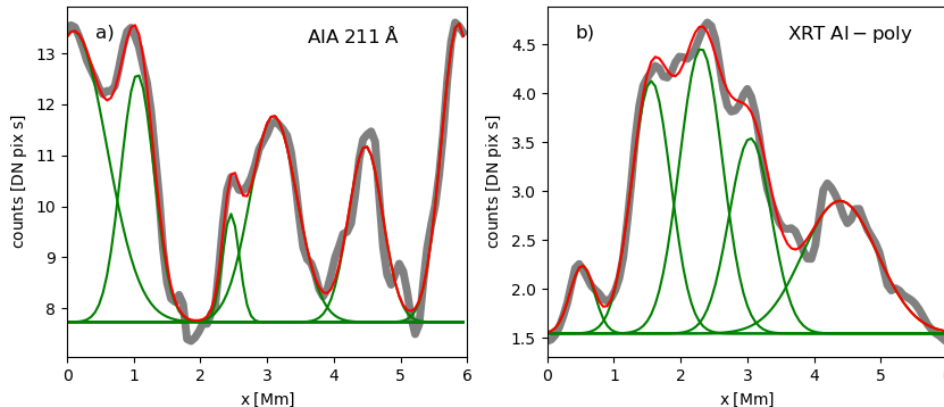


Figure 3.16: Cross-sectional cut of the loop in coronal emission. The gray thick lines show cuts at the apex of the loop as displayed in Fig. 3.15 for AIA 211 Å and XRT at the original resolution. To quantify these cross-sectional cuts we show multi-Gaussian fits with a constant background in each case. The individual Gaussians of the fit are shown in green, the sum of all Gaussians in red. See Sect. 3.4.4.

of hot loops (e.g., de Pontieu et al. 1999, Berger et al. 1999). In this sense the loop we study here represents a hot loop with moss emission at its footpoints. Consequently, to investigate the substructure of the loop in the corona we employed an AIA channel showing hotter plasma and X-rays. For the AIA instrument we chose to focus on the 211 Å band, which is sensitive to emission from plasma with a temperature near 2 MK.

The plasma in our simulation reaches temperatures of three million Kelvin or more in the coronal part of the simulation domain, with the peak temperature being 5.2 MK. Plasma at these temperatures emits mainly in the X-ray part of the spectrum. The synthesized emission for the 211 Å band and the X-ray emission is shown in Fig. 3.15b and c, respectively. The emission in both wavelength bands displays a clear substructure with several bright slender strands running almost from footpoint to footpoint.

The emission computed in the AIA bands is significantly stronger near the footpoints where the plasma is colder and denser than in the upper atmosphere. The AIA 211 Å emission near the footpoints shows multiple bright thin features that show heated dense low-lying plasma. A future study will have to show to what extent these are low-lying features separate from the coronal part of the loop, or if these are actually a signature of small-scale heating events in the low part of the loop that contribute (significantly) to the energization of the corona as a whole.

Discrete strands are visible both in the 211 Å channel and in X-ray. To illustrate the fine structure of the loop emission, Fig. 3.16 shows a cut through the line of sight integrated emission for both filters. We applied a multi-Gaussian fit to the cross-sectional cuts to determine the full width at half maximum (FWHM) of the strands. This FWHM in the range of of 290 to 1200 km for the strands in the 211 Å channel and 370 to 1300 km for the strands in X-ray emission. This is consistent with typical strand widths observed by Hi-C (e.g., Brooks et al. 2013, Williams et al. 2020b). Also, the finding that the structures appear broader at higher temperature is consistent with observations that show structures

at higher temperatures to become more fuzzy (e.g., Tripathi et al. 2009). The lifetime of the strands is 3 to 20 minutes. When comparing the artificial emission to observations, we need to take into account the pixel sizes of the instruments, which differ from the pixel size of our simulation. The AIA instrument has a plate scale of 0.6'' per pixel (and a resolution of about 1.4''). On the Sun near disk center this corresponds to a pixel size of 450 km. For XRT the plate scale is 1'' per pixel (corresponding to 725 km) at a resolution of about 2''. We resampled the synthesized emission to the instrument plate scale. For simplicity we did not convolve with the point spread function, which should be sufficient here for illustrative purposes. The count rates for a patch of neighboring pixels of the numerical model, which correspond to the instrument plate scale, were summed up. While individual strands are still visible in parts of the loop for AIA, discerning different strands is more difficult for XRT which has a coarser resolution. The resampled synthesized emission is displayed in panels (d) and (e) of Fig. 3.15. For XRT the emission shows two main structures, a bright wide strand and a dimmer narrow strand. For the decreased resolution, only the widest strand is clearly distinguished from the background, while the dimmer strand is only visible in parts of the loop and appears to be partially merged with the larger strand. For the emission in the 211 Å channel, the four main strands that appear in the undegraded emission are still distinguishable, although not along the whole length of the loop. The substructure on scales of a few hundred kilometers that is shown in the perpendicular cut in Fig. 3.10, is not resolved.

3.5 Discussion

In this section we cover the source of the energy injection into the corona in our simulation, the formation of current sheets in the loop, the relation between the photospheric driver and flows in the hot corona, energy input by global loop oscillations, and, finally, predictions for observation of the simulated loop with AIA and XRT. We compare our results to previous models of straightened loops and observations.

3.5.1 Poynting flux and heating

Convective motions lead to the deformation of magnetic concentrations that twist and shear the magnetic field. As the main source of the heating we find photospheric motions within elements of strong magnetic flux concentrated in the intergranular downflow lanes, rather than braiding due to horizontal motions of magnetic features relative to each other. We observe rotational motions of the plasma within the magnetic concentrations that lead to rotation and twisting of traced magnetic field lines. The small-scale horizontal motions within the magnetic patches and the deformation of the patches lead to an upward directed Poynting flux into the loop. The magnetic field lines connected to hot patches in the corona are mainly anchored in parts of the intergranular downflow lanes which show both strong magnetic fields and increased horizontal flows (see, for instance, the footpoint of field line in Fig. 3.2). Rotational motions have also been found in simulations by Wedemeyer-Böhm et al. (2012), Moll et al. (2012), Shelyag et al. (2013), Yadav et al. (2020a), Battaglia et al. (2021). The Poynting flux is injected into the coronal loop from both footpoints. It is dissipated throughout the corona without a preferred location in the

coronal loop.

We find a "bursty" heating profile along individual field lines that strongly varies on short timescales and small spatial scales (see Sect. 3.4.2.1). Heating events are of short duration and distributed throughout the atmosphere. While heating can occur along the full length of a field line, strong heating events appear to be more localized. Both Poynting flux and heating rate fluctuate strongly in space and time. We find that strong Poynting flux events at a point along the field line (here chosen to be the apex) are associated with or closely followed by an increase in the heating rate and a delayed increase in density along the studied field line, consistent with chromospheric evaporation (see Fig. 3.9).

Peaks in the total heating rate are superimposed on continuous background heating. Bingert and Peter (2011) investigate energy input and heating along individual field lines in their 3D active region simulation. They find heating predominantly near the footpoints for field lines connecting the main polarities of the spots in the simulated active region to network due to the higher velocity shear at the footpoints located in weaker magnetic field concentrations, but also find field lines that show strong heating events at the loop top consisting of several short small-scale events. In our simulation, we find no clear concentration of the heating near the footpoints. Bingert and Peter (2013) investigate the temporal statistics of heating events and find short spikes below a minute imposed on slower variations in individual gridpoints, which is consistent with our results. Kanella and Gudiksen (2017) also studied the size distribution of the heating events and found that large energy release events are favored, which is in contrast to our findings, which show many small events. Their algorithm used to identify heating events, however, cannot resolve clusters of small heating events that are closely packed, thus the number of small heating events might be underestimated in their analysis.

3.5.2 Current sheets

The structure of the current density in our model qualitatively resembles the current sheets found by Reid et al. (2018) as a result of a magnetic avalanche. Reid et al. (2018) study the disruption of three magnetic threads after undergoing an initial instability. The end state of the simulation after the onset of the Kink instability and the magnetic avalanche is a braided system that undergoes continuous dissipation. The current sheets then form a network of small complex structures enabling reconnection of magnetic field lines and subsequent heating (Reid et al. 2020).

The resistivity in numerical simulations is several orders of magnitude higher than on the real sun. This leads to an onset of reconnection at smaller misalignment angles between magnetic field lines than would occur in the plasma on the sun. This problem is avoided in relaxation studies by starting from a prescribed braided flux tube with large misalignment angles of the field lines as initial condition. In contrast to relaxation models such as the simulations conducted by Wilmot-Smith et al. (2010) and Pontin et al. (2011), we do not start with an artificially braided field as an initial condition that undergoes an instability and relaxes to a new equilibrium. Instead, the system is in a continuously driven state due to photospheric motions.

Rappazzo et al. (2008) conducted simulations of a coronal loop in Cartesian coordinates in which slow photospheric motions drive a Poynting flux, leading to a turbulent cascade of energy from the scale of convective motions to small scales where the energy

is dissipated. They find that the field lines are barely entangled, current sheets still form and are continuously dissipated. This is similar to the situation we find in our simulations. The original Parker model predicts angles of 20° between braided field lines, which is not observed (van Ballegoijen et al. 2011). We find an inclination angle of the magnetic field in the range of $0 - 70^\circ$ in the coronal part of the loop with a mean value of 5.4° . This is consistent with previous simulations. Thus, reconnecting field lines in the coronal part of the computational domain are almost parallel. These angles are much smaller than the value of 30° predicted by nanoflare theories and not compatible with the large misalignment angles required for the secondary instability to set in (Dahlburg et al. 2005).

3.5.3 Atmospheric coupling

An unanswered question is how the magnetic structure at the loop footpoints affects the internal structure of the loop. One possibility is that the topology of the photospheric driver strongly influences the dynamics of the loop (Rappazzo et al. 2010). Electric currents should develop along field lines with footpoints that are subject to shear motion. The magnetic field would then be a mapping of the velocity pattern driving the field line tangling. As found in Rappazzo et al. (2007) and Rappazzo et al. (2008, 2010) the magnetic field lines have a topology mostly independent of the photospheric velocities. Rappazzo et al. (2008, 2010) argue that the formation and dissipation of current sheets arises from the nonlinear nature of the system and does not require complex footpoint motions of the magnetic field lines. Ritchie et al. (2016), however, argue that the nature of the energy release does depend on the complexity of the photospheric driver, with coherent motions leading to a smaller number of large events and more complex drivers causing frequent small heating events. We find both imprints of the photospheric motions such as vortices in our simulations as well as turbulent flows not directly related to footpoint motions. Therefore, both statements are not mutually exclusive.

Although temperature and density are generally enhanced in the region of the simulation box above the strongest magnetic field concentrations in the photosphere, in our model the distribution of temperatures in the corona does not follow directly the distribution of the magnetic field at the photosphere. Instead, the photospheric driving leads to a braided state showing aspects of turbulent behavior. The key role that MHD turbulence plays here is that it transports energy to smaller scales where it is dissipated (Rappazzo et al. 2008), for example by creating small-scale local field reversals (Jafari et al. 2020).

Care has to be taken when following individual field lines in a turbulent flow. The algorithm can jump between different field lines due to numerical errors and becomes structurally unstable in the vicinity of reconnection regions. It is therefore not possible without a doubt to distinguish between field line jumps due to physical reconnection events and jumps due to numerical inaccuracies. As illustrated in Fig. 3.8, changes of identity of a field line can be identified by a sudden change of plasma parameters. In between those events, however, tracing of a field line is reasonably reliable, although the output of the field line tracing algorithm should be checked manually.

3.5.4 Emission

In agreement with Pontin et al. (2017), we find that the synthesized emission does not necessarily show a braided appearance despite the braided state of the magnetic field. The bright strands in the 211 Å channel have a smooth appearance and do not show clear indications of overlapping strands. This is not necessarily a sign, however, that no braiding of loop strands occurs (Pontin et al. 2017). Especially in the hot part of the loop, evidence for the crossing of strands is visible in some snapshots in the X-ray emission.

The discrete strands visible in the emission are in contrast to the simulation by Reale et al. (2016) which yields a loop that appears monolithic. The appearance of a substructure might be due to the significantly lower diffusivity of our numerical model. We find an effective resistive diffusivity of $2.4 \times 10^{12} \text{ cm}^2\text{s}^{-1}$ in the corona (see Sect. 3.3).

The width and lifetime of the strands that we see in the synthesized observations is compatible with observed threads in coronal loops (Brooks et al. 2013, Williams et al. 2020b,a). Strand widths range from 250 to 1400 km FWHM for the AIA 211 Å channel and 600 to 1500 km FWHM for the XRT channel. Brooks et al. (2013) examine a set of 91 loops observed by Hi-C and find strand widths from 212 km FWHM to 1665 km FWHM, thus the strand widths we find in our simulation are within the observed range for both channels. Williams et al. (2020a) find that most of the strands have widths between 200-760 km FWHM observed by Hi-C 2.1. The lifetimes that we find for individual coronal loop strands is on the order of minutes, which is consistent with observed temporal variability of loop emission, although observed loops (in which, most probably, the strands are not resolved) usually remain bright as a whole for several hours (Reale 2014).

If the synthesized emission is degraded to the instrument resolution of AIA and XRT, the loop has a mostly smooth appearance. To detect the substructure, a higher resolution would be needed. The Hi-C instrument (Kobayashi et al. 2014) and the EUI instrument (Rochus et al. 2020) on Solar Orbiter have a high enough spatial resolution to detect strands of the width found in our simulations. The emission in the 211 Å channel exhibits more fine structuring than the emission from hotter plasma in X-ray which has a smoother appearance, consistent with observations (Tripathi et al. 2009).

A cut perpendicular to the axial direction, as shown in Fig. 3.10, reveals a highly complex structure of the density and temperature distribution throughout the loop cross-section, the strands seen in the emission after integration along the line of sight might therefore in part be caused by projection effects. Pontin et al. (2017) also find a nonzero angle between magnetic field lines and bright strands in regions exhibiting frequent reconnection events which cause changes of the connectivity on a timescale on the order of the timescale of heat conduction parallel to the field lines.

3.6 Conclusions

In this paper we investigated how the energy to heat a coronal loop is generated in the photosphere, injected along the magnetic field, and finally dissipated. We tailored the 3D computational domain to contain a single coronal loop. Essentially, this is a straightened loop, with gravity pointing downward on both ends and decreasing to zero at the apex of the loop. This setup allows us to study the details within the loop on scales not achievable in a 3D model covering a whole active region. What distinguishes our model from pre-

vious setups that have been similar in geometry (e.g., Reale et al. 2016, Rappazzo et al. 2008) is the realistic treatment of the bottom boundary at the solar surface (at each of the ends of the loop). Here we fully account for the near-surface magneto-convection that self-consistently drives the evolution of the photosphere where the loop is rooted. With this model setup, we can investigate the formation and evolution of (sub)structures within the loop and how they are driven by the motions of magnetic patches at the surface. As a response to the driving, a complex fine structure of small-scale current sheets and flows develops in the loop. In its coronal part, the loop plasma exhibits turbulent behavior, for instance, visualized through the spatial structures of the current and the velocity in cuts across the loop. The temperature distribution higher up in the loop, however, does not directly follow the magnetic field distribution at the photosphere in a simple fashion. Energy is supplied to the upper atmosphere via the Poynting flux originating from the photospheric layer, and we can follow the Poynting flux as it propagates along individual field lines. At the same time, we see frequent reconnection of field lines, illustrated through sudden changes of, for example, density. The energy input, intermittent in both space and time, results in a substructure of the loop seen in synthesized EUV and X-ray emission.

In our study we showed the power of loop-in-a-box models with a realistic photosphere driven by magneto-convection. After having proven the concept, one of our next steps will be to conduct a detailed analysis of the (magnetic) coupling from the photosphere to the hot corona, and of the photospheric roots of the individual strands seen in emission. Another topic will be an in-depth analysis of the (an)isotropy of the velocity field that would be uncovered in real observations through an analysis of emission line widths. We find indications for oscillations and waves in the simulations, which we also plan to study more closely. With these types of studies we will be able to improve the quantification of contributions of different heating mechanisms, such as field-line braiding, wave heating, or low-lying reconnection. Future tests of our model simulations may be expected from the Solar Orbiter mission (Müller et al. 2020), in particular from the High Resolution Imager of the Extreme Ultraviolet Imager (EUI, Rochus et al. (2020)) combined with the magnetic field measurements made by the High Resolution Telescope of the Polarimetric and Helioseismic Imager (PHI, Solanki et al. (2020)).

Improved future simulations would profit from a significantly smaller grid size. Also, the current simulations suffer from the treatment of radiation in the chromosphere in LTE. This shortcoming will eventually be addressed by using the new version of MURaM (Przybylski et al. 2021).

4 Swirls in the solar corona

This chapter is the manuscript for a paper to be submitted to Astronomy & Astrophysics by C. Breu, H. Peter, R. Cameron and S.K. Solanki.

Contributions to the paper: I performed the simulations, analyzed the data, and wrote the first draft of the manuscript; all authors contributed to the ideas behind the study.

Abstract

Vortex flows have been found in the photosphere, chromosphere and low corona in observations and simulations. It has been suggested that vortices play an important role for channelling energy and plasma into the corona, but the impact of vortex flows on the corona has not directly been studied in a realistic setup. We investigate the role vortices play for coronal heating using high resolution simulations of coronal loops. We perform 3D resistive MHD simulations with the MURaM code. Studying an isolated coronal loop in a Cartesian geometry allows us to resolve the structure of the loop interior. We conduct a statistical analysis to determine vortex properties as a function of height from the chromosphere into the corona. We find that the energy injected into the loop is generated by internal coherent motions within strong magnetic elements. A significant part of the resulting Poynting flux is channelled through the chromosphere in vortex tubes forming a magnetic connection between the photosphere and corona. Vortices can form contiguous structures that reach up to coronal heights, but in the corona itself the vortex tubes get deformed and eventually lose their identity with increasing height. Vortices show increased upward directed Poynting flux and heating rate both in the chromosphere and corona, but their effect becomes less pronounced with increasing height. While vortices play an important role for the energy transport and structuring in the chromosphere and low corona, their importance decreases higher up in the atmosphere. Vortex tubes reaching the corona show a complex relationship with the coronal emission.

4.1 Introduction

Vortex flows driven by magnetoconvection have been proposed as a possible energy channel from the convection zone to the upper solar atmosphere (Wedemeyer-Böhm et al. 2012). Rotating structures have been detected in the photosphere and chromosphere in high resolution observations (Bonet et al. 2008, Wedemeyer-Böhm and Rouppe van der Voort 2009) and simulations (Carlsson et al. 2010, Shelyag et al. 2011, Moll et al. 2011, Kitiashvili et al. 2011, Moll et al. 2012, Steiner and Rezaei 2012, Kitiashvili et al.

2012a,b). The photospheric vortices have sizes of the order of the width of the downflow lanes or smaller (Moll et al. 2011). It is not yet known what drives the formation of these small-scale vortices. Stein and Nordlund (1998) find regions of enhanced vorticity in downflow regions in the intergranular lanes and suggest that vorticity is produced at granule edges and in downdrafts by a misalignment of pressure and density gradients and then concentrated in the intergranular lanes by advection. The conservation of the angular momentum of the inflows results in the bathtub effect, amplifying the rotational motion in the narrow downflow lanes (Nordlund 1985). In contrast to this, Kitiashvili et al. (2012a) propose that instead vorticity is generated by convective granular instability or the Kelvin-Helmholtz instability developing between shearing flows in the intergranular lanes.

The rotating downflows wind up the magnetic field in the photosphere because the magnetic field lines are frozen into the plasma. The twisting of the magnetic field potentially helps to confine magnetic flux tubes by the pinch effect (Stenflo 1975).

In the chromosphere, swirls have been observed as dark structures in the Ca II 8542 Å line (Wedemeyer-Böhm and Rouppe van der Voort 2009). Multiwavelength observations of chromospheric swirls co-located with magnetic bright points have shown that vortices reach from the photosphere into the low corona (Wedemeyer-Böhm and Rouppe van der Voort 2009, Wedemeyer-Böhm et al. 2012). An imprint of rapidly rotating magnetic structures has been detected in transition region and coronal emission in the 304 and 171 Å channels of AIA corresponding to hot coronal plasma (Wedemeyer-Böhm et al. 2012). A persistent vortex flow reaching the low corona was also reported by Tziotziou et al. (2018). In contrast to Wedemeyer-Böhm et al. (2012), Tziotziou et al. (2018) find a decrease in intensity in the 171 Å channel and no signal in the 193 or 211 Å channel. The vortices are also seen as absorbing structures in Wedemeyer-Böhm et al. (2012), but the authors noted higher intensities in some AIA channels at the edges of the vortex flows.

The observed enhanced emission in coronal spectral lines points to heating of the swirls. Heating at the location of vortices has been found in simulations in the upper photospheric layers due to viscosity (Moll et al. 2012) and in the chromosphere, for example in Kitiashvili et al. (2012b), Yadav et al. (2020a, 2021). The main contribution to the Poynting flux in the atmosphere was suggested to stem from horizontal motions acting on the strong predominantly vertical magnetic field (Shelyag et al. 2012). Yadav et al. (2020a) found that vortices contribute a significant fraction of the Poynting flux in the chromosphere. An increased Poynting flux associated with vortex locations was also reported by Battaglia et al. (2021). Vortex motions could thus be partially responsible for heating the solar chromosphere.

In addition to acting as an energy channel, vortices could also be associated with the transport of matter. Wedemeyer-Böhm and Rouppe van der Voort (2009) found that the chromospheric swirls were blue-shifted, which they interpreted as plasma moving upward along a twisted magnetic field. Tziotziou et al. (2018) also detected upflows within the observed swirling structure. Vortices could be related to the ejection of jets and spicules which have been observed to be spinning (Wedemeyer-Böhm and Rouppe van der Voort 2009, De Pontieu et al. 2012). Kitiashvili et al. (2012b, 2013) find that the vortices in their simulation are associated with quasi-periodic upflows at the vortex edge driven by the Lorentz force arising from current sheets in the atmosphere and by the pressure gradient in the subsurface layers, while at the same time a helical downflow is present in

the vortex core. Iijima and Yokoyama (2017) showed that the twisted magnetic field in a vertical vortex can drive chromospheric jets via the Lorentz force.

Vortices could launch Alfvén waves that propagate into the corona. Shelyag et al. (2013) interpret vortices not as continuous rotational flows, but instead as torsional Alfvén waves propagating along the guide field excited by oscillatory motions of the plasma in magnetic concentrations. This view has been challenged by Battaglia et al. (2021), who instead find unidirectional upward propagating pulses that could contribute to chromospheric and coronal heating. Various wave modes in a long-lived vortex structure have been observed by Tziotziou et al. (2020).

Common to existing simulations is that they have an upper boundary located in the chromosphere, transition region or low corona. The solar surface convection simulations of Moll et al. (2011) reach heights of 500 to 600 km above the $\langle \tau \rangle = 1$ layer, the simulations studied in Moll et al. (2012) and Shelyag et al. (2013) reach 800 km above the photosphere. The simulation analysed in Yadav et al. (2020a, 2021) has an upper boundary set in the upper chromosphere at 2.5 Mm. Kitiashvili et al. (2013) used an upper boundary in the chromosphere that extends to 1 Mm above the photosphere. The study including the largest coronal part is the simulation by Iijima and Yokoyama (2017) with an upper boundary at a height of 8 Mm in an open field setup. This study, however, did not investigate the Poynting flux transport and dissipation inside the structure.

The choice of the top boundary conditions can affect the behavior of the thermodynamic quantities, for example an increased diffusivity near the boundary (Moll et al. 2012, Yadav et al. 2020b, 2021).

The evolution of the swirling structures in higher layers of the atmosphere, and their contribution to the energy transport and the impact of the energy and mass transfer in the chromosphere has not yet been studied in detail. Including a corona makes it possible to study the propagation of perturbations as well as the effects of heating events in higher atmospheric layers on the cooler chromospheric plasma, such as chromospheric evaporation.

The aim of this chapter is to investigate the role the vortex flows play for the energy and mass transport between the photosphere and the corona in coronal loops and their influence on coronal loop structure. The paper is structured as follows: Section 4.2 describes the numerical setup and analysis methods. The results are presented in Section 4.3 and subsequently discussed in Section 4.4. A conclusion is given in Section 4.5.

4.2 Methods

4.2.1 Numerical setup

We model an isolated coronal loop in a Cartesian box using the MURaM code with the coronal extension (Vögler et al. 2005, Rempel 2017). The setup is similar to the loop model described in Breu et al. (2022)¹. The coronal loop is modelled as a straightened magnetic flux tube with a shallow convection zone included at the loop footpoints at each end of the box. The simulation domain includes the convection zone, the photosphere,

¹Chapter 3 in this thesis.

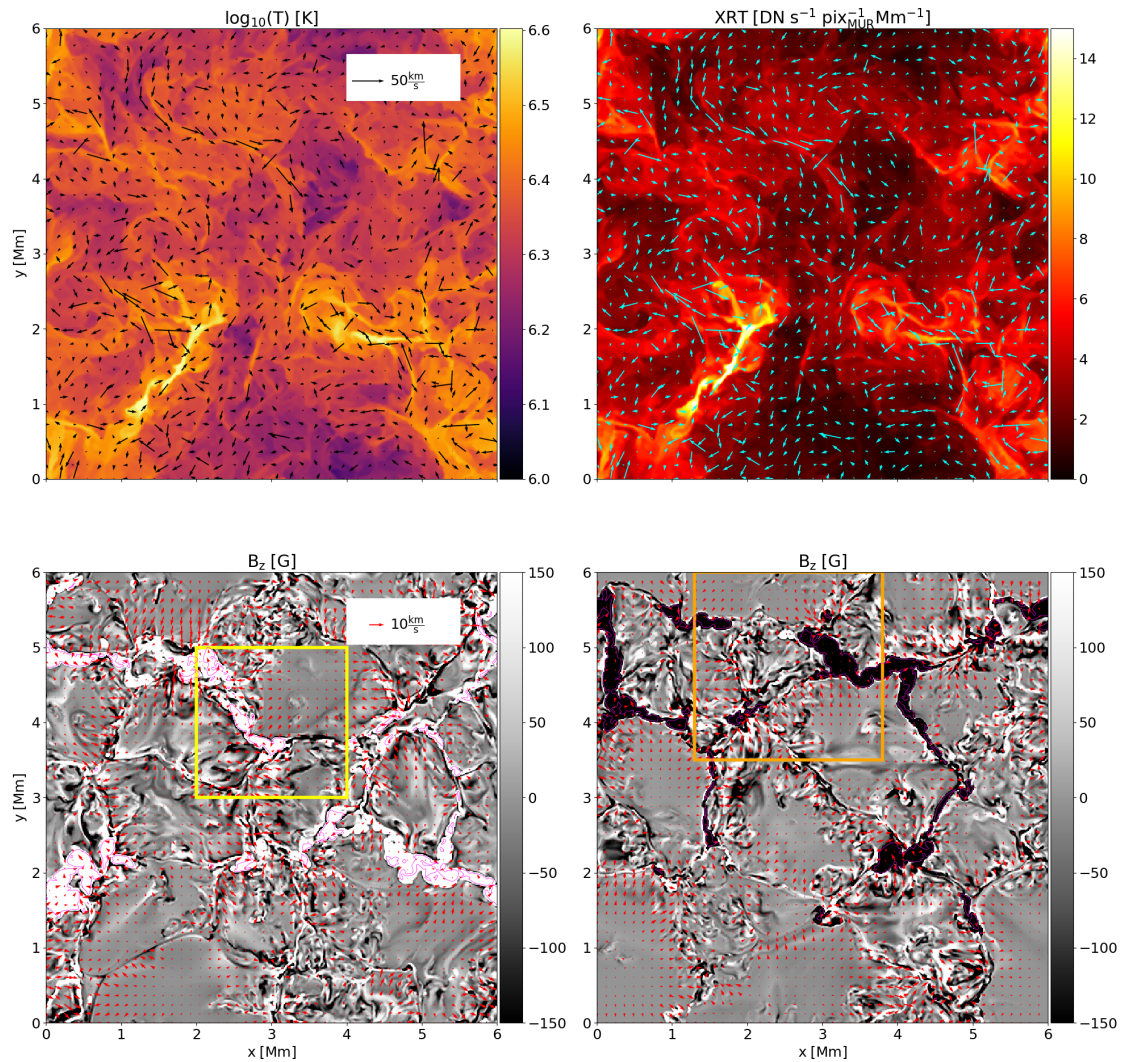


Figure 4.1: Overview over the simulation box. Top row: Temperature distribution (left) and the emission as it would be seen with the Al-poly filter of the Hinode/XRT X-ray imager at the loop apex. Bottom row: Vertical magnetic field at the $\langle \tau \rangle = 1$ layer at both loop footpoints. The arrows show magnitude and direction of the velocity field perpendicular to the loop axis. The yellow and orange rectangles mark the position of the closeups of the footpoints shown in Fig. 4.2. The magenta contours outline magnetic field concentrations with $|B_z| \geq 1000$ G. The snapshot was taken at $T=2.23$ min. See Sect. 4.2.

an LTE chromosphere and a corona spanning between the footpoints. The coronal part is heated self-consistently by magnetoconvection at the loop footpoints. The magnetic field configuration at the footpoints and temperature as well as resulting X-ray emission are shown in Fig. 4.1. We solve the compressible MHD equations by conducting 3D resistive MHD simulations including the effects of field-aligned heat conduction, optically thick grey radiative transfer in the photosphere and chromosphere and optically thin losses in

the corona. To close the system of equations, we use a non-ideal equation of state. The effective loop length is 50 Mm and the photosphere is located at an average height of 3.5 Mm above the bottom boundary. The horizontal extent of the simulation box is 6×6 Mm. The spatial resolution is $\Delta x = 12$ km in both the horizontal and vertical direction. We limit the Alfvén speed to $v_A = 6000$ km s⁻¹ to avoid strict limits on the time step.

The initial condition for the magnetic field is a uniform vertical field of 60 G. The high resolution simulation used in this study is interpolated from a snapshot of a corresponding simulation with a lower resolution of 60 km. The simulation is run for 30 minutes with the new resolution to let initial transients subside.

4.2.2 Vortex detection

Identifying vortices in a systematic way is not straightforward. We use the swirling strength criterion by Zhou et al. (1999) to detect vortices in the simulation. The swirling strength criterion is more reliable in the detection of vortices than an increased vorticity alone, since the vorticity is not only enhanced in rotational flows but also in shear flows without rotation (Moll et al. 2012).

The velocity gradient tensor $U_{ij} = (\partial_j v_i)$ can have all real eigenvalues, or one real eigenvalue and two complex conjugate eigenvalues (Chong et al. 1990). According to the swirling strength criterion, a grid cell is part of a vortex if the velocity gradient tensor has a complex-conjugated pair of eigenvalues. The eigenvector corresponding to the real eigenvalue λ_r is identified as the direction of the vortex. The swirling strength is then defined as the unsigned imaginary part λ_{ci} of the complex eigenvalue. The sign of the swirling strength determines whether the vortex rotates clockwise or counterclockwise. The shear part of the vorticity can be computed as $\omega_{\text{shear}} = \omega - 2\lambda_{ci}$.

Since this criterion selects the smallest vortices present in the simulation domain, we follow the approach by Yadav et al. (2020b) and smooth the velocity field with a Gaussian kernel with a FWHM of 500 km before applying the swirling strength criterion in order to capture larger rotating structures.

4.3 Results

4.3.1 Atmospheric coupling

Our simulations show an abundance of vortex flows in all layers of the solar atmosphere. We have traced magnetic field lines from a prominent vortex flow in order to determine how the rotating flows in the coronal part of the simulation are magnetically connected to the solar surface. The swirling structure in the low corona and the footpoints of magnetic field lines connected to the structure are shown in Fig. 4.2. The field lines were traced from a region of enhanced swirling strength at a distance of $s=6$ Mm to the solar surface (corresponding to a height of 5.86 Mm) to the photospheric layers at both footpoints of the loop. Here we use the swirling strength computed from the smoothed velocity field. The threshold for the swirling strength was set to 0.002 s⁻¹, corresponding to a rotation period of less than 50 minutes.

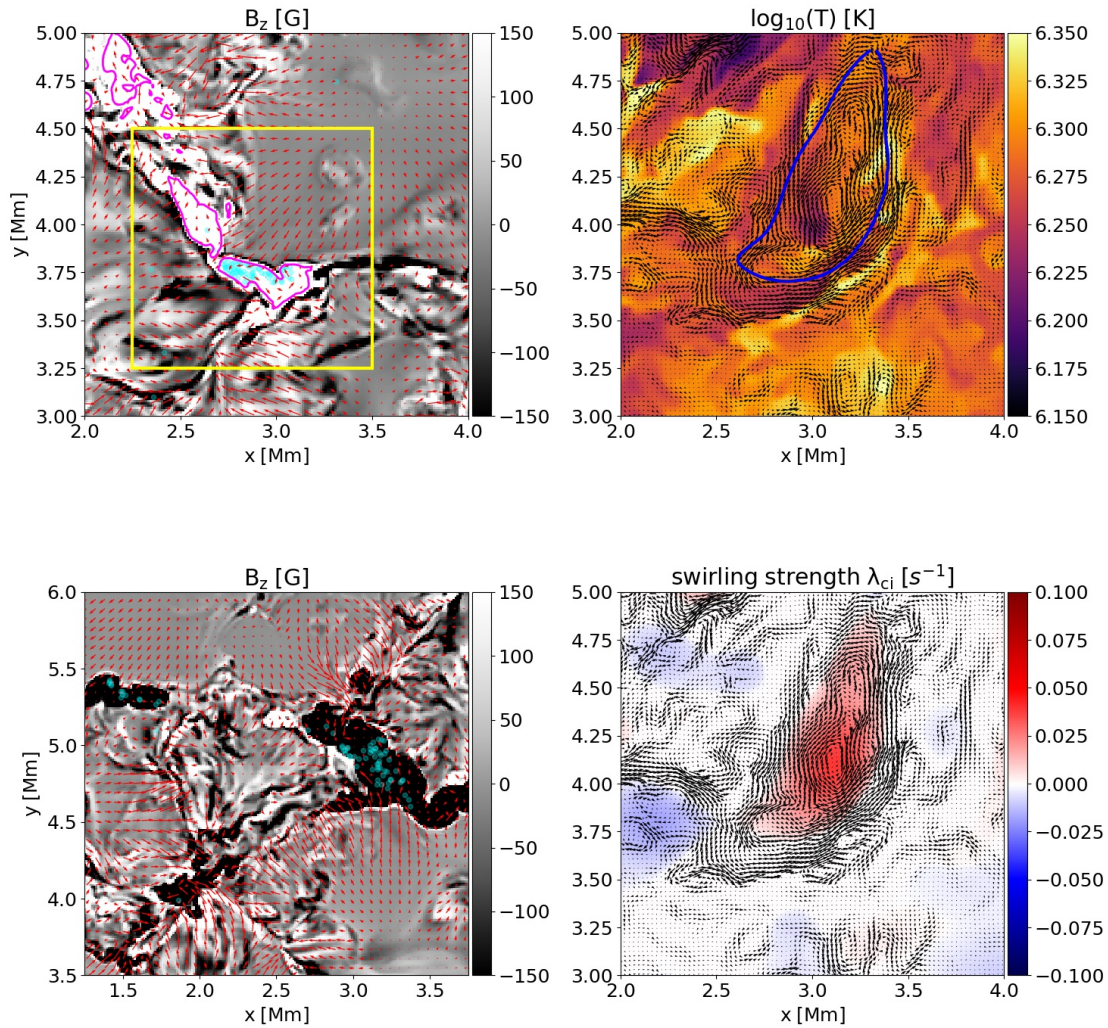


Figure 4.2: Swirling strength, temperature and connection to the footpoints. Left column: Cuts at the photospheric level showing the vertical magnetic field component at both footpoints. The cut shown in the top left panel is located at a height of 0 Mm, the cut shown in the bottom left panel at an arclength of 50 Mm at the other footpoint. Upper right panel: Temperature at an arclength of 6 Mm. The blue contour is outlining a patch of enhanced swirling strength ($|\lambda_{ci}| = 0.002 \text{ s}^{-1}$ for an effective resolution of 500 km after smoothing the velocity field to bring out the larger structures). The swirling strength calculated from the smoothed flow field is shown in the bottom right panel at an arclength of 6 Mm. The light blue circles in the left column show the intersection of the magnetic field lines traced from the region outlined in blue in the upper right panel with the photospheric layer. The magenta contours outline kilogauss magnetic field concentrations. The field of view of the closeup in Fig. 4.3 is indicated by the yellow square. The arrows show direction and magnitude of the velocity field perpendicular to the loop axis. See Sects. 4.3.1 and 4.4.3.

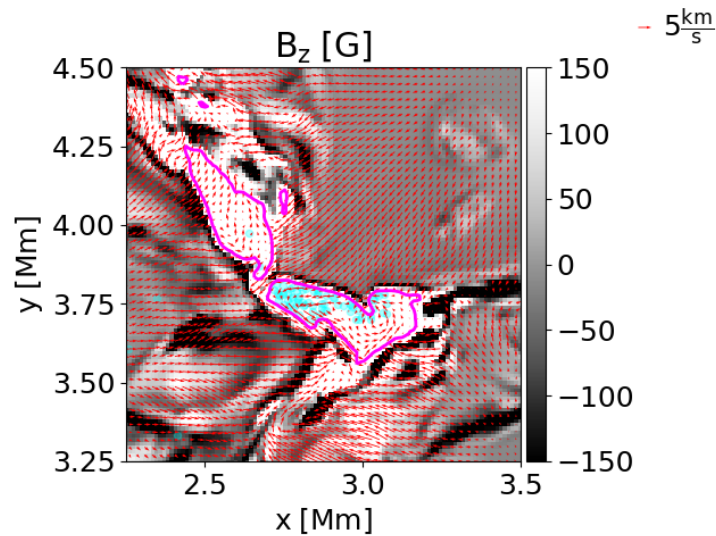


Figure 4.3: Closeup of the footpoint of the swirl shown in Fig. 4.2. The field of view corresponds to the region within the yellow rectangle in Fig. 4.2. Contours in magenta mark regions with $|B_z| \geq 1000$ G. The red arrows show the magnitude and direction of the velocity field at the $\langle \tau \rangle = 1$ surface. The light blue markers correspond to the intersections of the field lines traced from the swirl under consideration with the photospheric layer. See Sect. 4.3.1.

The right column shows the temperature and the swirling strength computed from the smoothed flow field. The vertical magnetic field at the magnetic footpoints of the structure is shown in the left column. The temperature shows an enhancement along the edge of the rotating structure on the right side.

At the footpoint closer to the swirl, the magnetic field lines are connected to a region displaying rotational motions in a magnetic concentration with kilogauss magnetic field strength located in the intergranular lanes. A closeup of the region corresponding to the yellow square is depicted in Fig. 4.3. The bundle of field lines traced from the swirl seen in the low corona splits into two bundles of field lines at a distance along the loop arc of about 16 Mm and ends in two different magnetic concentrations with kilogauss strength at the other loop footpoint. The geometry of the field lines is illustrated in Fig. 4.7. Due to the strong guide field and consequently large Alfvén speed, the magnetic field is only weakly twisted in the upper atmospheric layers. The field lines are twisted around each other at the footpoint where the swirl is located. While the field lines are almost vertical above the chromosphere, the streamlines of the velocity field show a helical structure. At the other loop footpoint, the field line footpoints are less concentrated in space and are not rooted in a particular flow structure, as can be seen in the bottom left panel of Fig. 4.2.

From 81 traced field lines, 58 field lines are rooted in the large kilogauss concentration centered at $[x,y]=[3.25,4.75]$ Mm, while 19 field lines are rooted in the smaller concentration at $[x,y]=[1.6,5.4]$ Mm. The axial Poynting flux interpolated along the two bundles of field lines is illustrated in Fig. 4.8. While the Poynting flux on each individual field

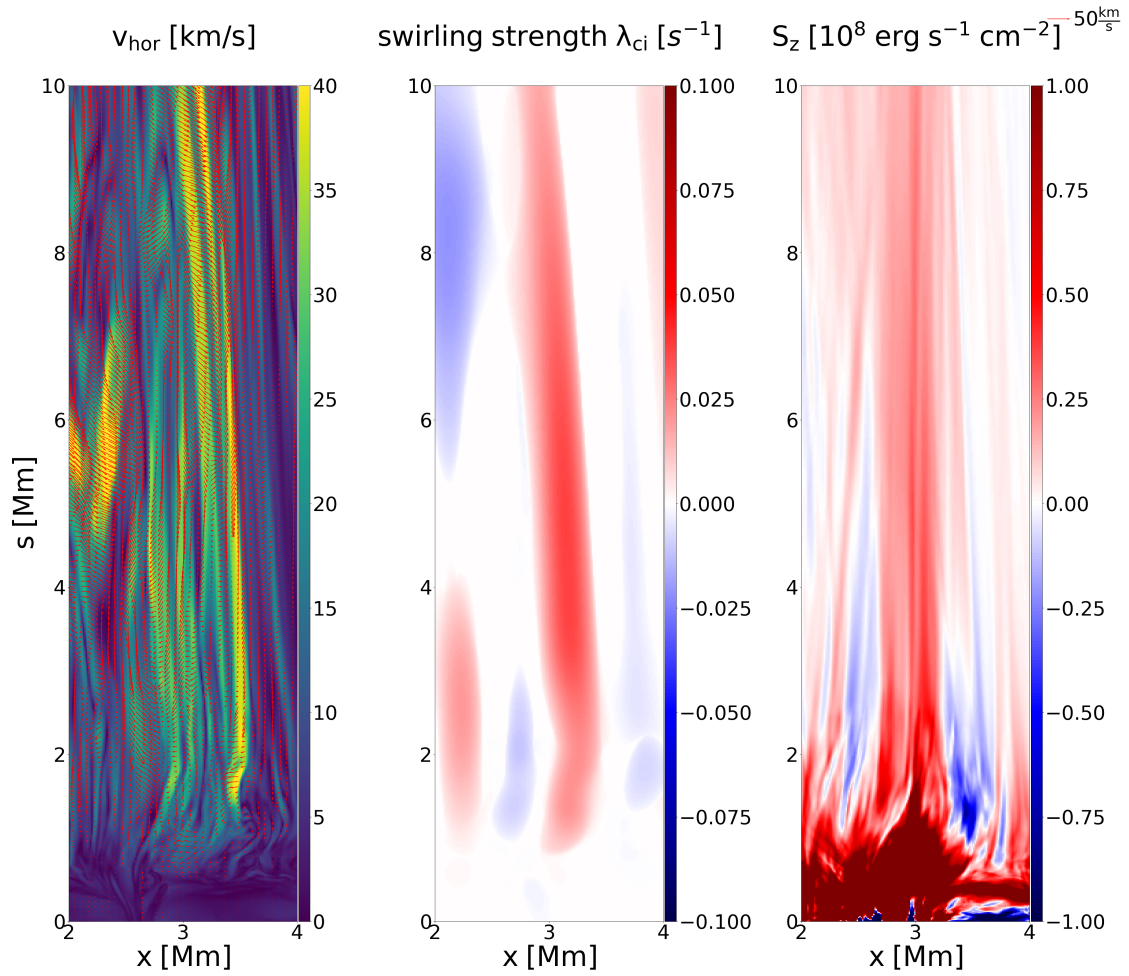


Figure 4.4: Axial cut through the loop at $y=4$ Mm. From left to right: Velocity transverse to the guide field, Swirling strength computed after smoothing the velocity field with a Gaussian with an FWHM of 500 km, axial component of the Poynting flux averaged over a slab between $y=3.5$ Mm and $y=5$ Mm centered on the swirling structure. The red arrows illustrate the velocity field projected onto the plane of the axial cut. For a discussion, see Sect. 4.3.1.

line strongly varies, the Poynting flux averaged over all the traced field lines indicated by the dashed black line is positive through almost the whole domain.

Transverse velocity and swirling strength are organised in elongated structures aligned with the magnetic field. The velocity perpendicular to the guide field in a cut along the loop is shown in the left panel of Fig. 4.4. An elongated structure with increased transverse velocity can be seen with its axis located at roughly $x=3$ Mm. The middle panel shows the swirling strength computed from the velocity field smoothed with a Gaussian with a width of 0.5 Mm. Small-scale swirls are abundant both inside and outside the larger rotating structure. After smoothing, the vortex is visible as a single contiguous structure with enhanced swirling strength reaching coronal heights. Note that for the lower effective resolution, the vortex appears to begin at a height of 1 Mm. This is due to the strong

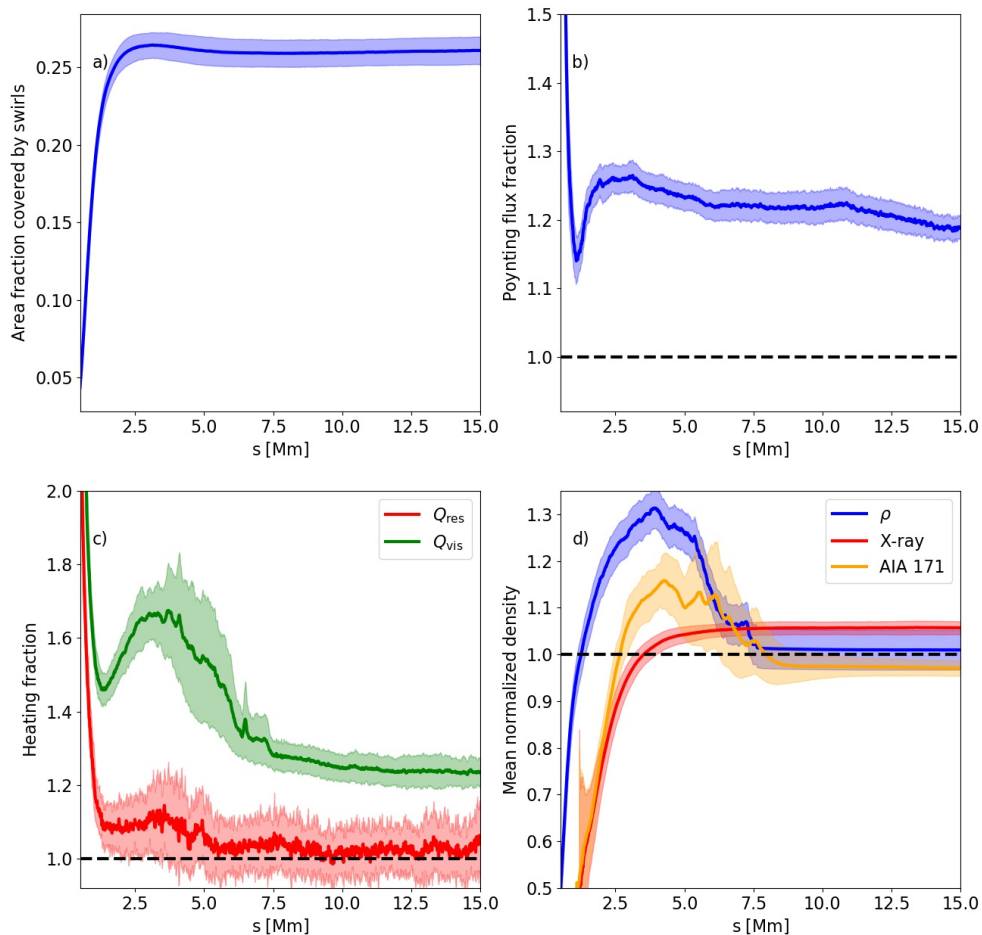


Figure 4.5: Dependence of swirl properties on the axial coordinate along the loop. (a) Area fraction covered by vortices, (b) Poynting flux over vortices normalized by the Poynting flux averaged over the loop cross section at the same distance along the loop, (c) normalized viscous (green) and resistive (red) heating fraction over vortices, (d) normalized density and emission in the X-ray and the 171 Å bands. The shaded areas refer to the standard deviation of the depicted quantities at any given arclength along the loop due to variation in time. See Sects. 4.3.2 and 4.4.2.

increase of the swirling strength in the corona and the horizontal expansion of structures, so that slower, smaller vortices in the chromosphere are not accurately captured.

The rightmost panel of Fig. 4.4 shows the Poynting flux averaged over a slab centered on the vortex location. The average was performed between $y=3.5$ Mm and $y=5$ Mm. The Poynting flux is enhanced at the location of the vortex. The enhancement of the Poynting flux is still present far into the coronal part of the loop. The Poynting flux stems from

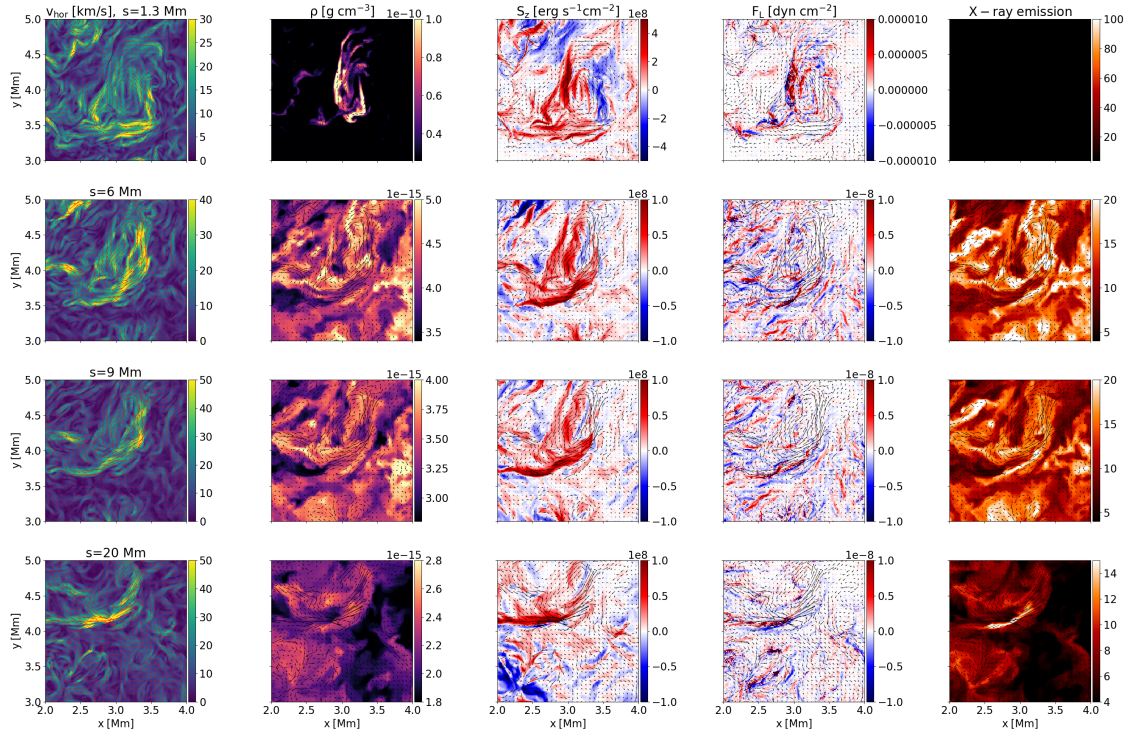


Figure 4.6: Cuts perpendicular to the loop axis at different distances to the photospheric layer through the structure shown in Fig. 4.2. From left to right: Velocity perpendicular to the loop axis, density, axial component of the Poynting flux, axial component of the Lorentz force, X-ray emission. From the top to the bottom row, cuts are shown at values of the axial coordinate s of 1.3 Mm, 6 Mm, 10 Mm and 20 Mm. The arrows show direction and magnitude of the velocity field. The units of the X-ray emission are $\text{DN s}^{-1} \text{pix}_{\text{MUR}}^{-1} \text{Mm}^{-1}$. For a discussion, see Sects. 4.3.1 and 4.4.1.

the footpoint at which the vortex originates and the field is twisted by the photospheric motion. There is only a weak upwards directed Poynting flux at the two footpoints on the opposite side.

The vortex evolves with height as it propagates into the atmosphere. The height evolution of the vortex is shown in Fig. 4.6. Regions of increased transverse velocity and Poynting flux appear at all four heights shown in the figure. The vortex shows increased elongation with height and is eventually deformed into a crescent shaped flow at $s=20$ Mm.

While we find an increased upwards directed Lorentz force at the edge of the vortex in the low chromosphere, there is no clear enhancement at the vortex location in the corona. The Lorentz force is concentrated in many oppositely directed patches at greater heights and does not seem to lead to a large-scale acceleration of material.

In the chromosphere, the vortex contains a structure denser than the surrounding plasma. At coronal heights, the density contrast is much lower and the area with the highest density in the field of view is located outside the vortex. Generally, the X-ray emission follows the density distribution. For the lowest height of 1.3 Mm, no X-ray emission is present since the plasma is too cool to emit in this wavelength range. With increasing height, the

X-ray emission begins to show a bright elongated structure at the edge of the vortex that becomes the brightest structure in the field of view at $s=20$ Mm.

4.3.2 Swirl properties

To investigate general properties of swirls across a large range of atmospheric heights, we conducted a statistical study of swirl properties analogous to the study in Yadav et al. (2020a) and Yadav et al. (2021). To study how swirls influence quantities such as Poynting flux, heating rate, and density, we compute the averaged quantities over swirls and then normalize by dividing by the horizontal average over a cross section with fixed coordinate s . In order to compare our results to Yadav et al. (2021), we choose a threshold of 0.0628 rad/s for the swirling strength. This is equivalent to a rotation period under $\tau = 100$ s if the swirls were rotating uniformly. Due to the steep decrease in density, the rms velocity and thus the swirling strength strongly increase with height in the chromosphere and transition region. We nevertheless chose a fixed value for the swirling strength threshold for simplicity since any choice of threshold would introduce a bias to the results. The average swirling strength for the small-scale swirls in the coronal part of the loop is roughly 0.05 s^{-1} , vortices with a swirling strength above our threshold are thus above the average swirling strength in the loop cross-section. The profiles were averaged over 34 snapshots taken over a time range of 34.9 minutes.

The swirl properties as a function of height are displayed in Fig. 4.5. The filling factor or area fraction covered by swirls as a function of height is shown in panel (a). The area coverage is low at the base of the chromosphere with less than 5 %, reaches a maximum in the transition region with about 26 %, then decreases slightly and remains roughly constant in the corona since the magnetic field cannot expand due to the limitations of our setup.

The Poynting flux shown in Fig. 4.5 panel (b) is increased above vortices in the lower chromosphere. The contribution from vortices strongly decreases in the upper layers of the chromosphere. After a local minimum at 1.15 Mm, it reaches a local maximum of an increase of 26 % at about 2.5 Mm. Subsequently, the normalized Poynting flux decreases and levels off at an enhancement of roughly 20 % in the corona, then decreasing further with increasing height. We checked the different components of the Poynting flux and found that the Poynting flux due to perpendicular flows is increased, while the flux due to vertical motions is even decreased in the swirls compared to the average.

Likewise, the viscous heating shown in panel (c) of Fig. 4.5 is increased by about 20 % over small-scale vortices in the corona. The enhancement reaches values of more than 60 % in the chromosphere and transition region after a local minimum between 1-2 Mm. The resistive heating is not enhanced in vortices above about 5 Mm. In the high Prandtl number setting that we are using, the energy dissipation occurs mostly due to viscous dissipation of flows. The total heating therefore closely follows the behaviour of the viscous heating.

The vortices are evacuated up to a height of about 1 Mm above the photosphere. The density is decreased by about 50 % in the lower chromosphere and increased in the upper chromosphere by about 30 %. In the corona, the density of the vortices does not differ significantly from the background density.

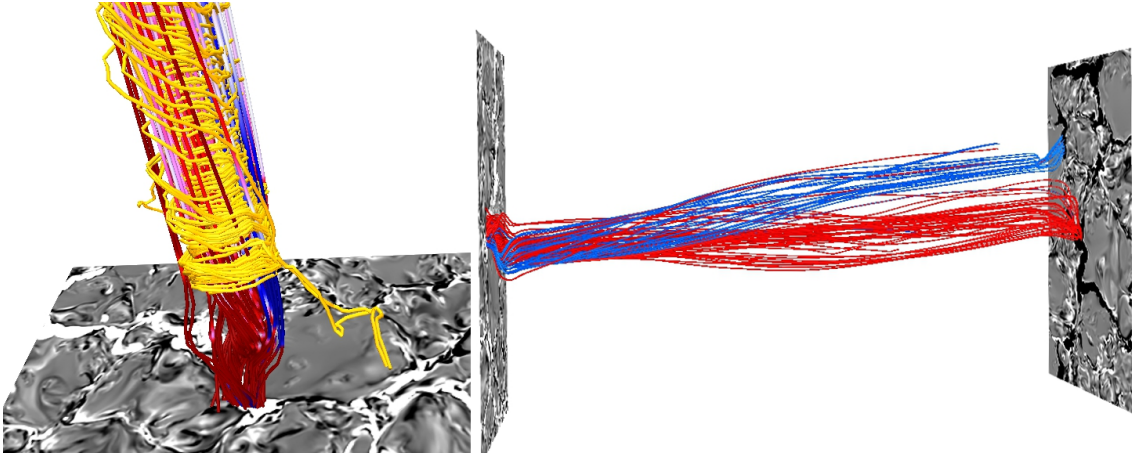


Figure 4.7: 3D rendering of the magnetic field lines connected to the region with enhanced swirling strength shown in Fig. 4.2. Left panel: Closeup of the footpoint rooted in the swirl shown in Fig. 4.2. The field lines are color-coded with the axial component of the Poynting flux. Red corresponds to upward directed Poynting flux, while blue corresponds to downward directed Poynting flux. The range of the color scale is from -5×10^7 to 5×10^7 erg cm²s⁻¹. The vertical magnetic field is plotted on a cut at the height of the $\langle \tau \rangle = 1$ surface. The range of the color scale of the magnetic field is from -150 to 150 G. The orange lines illustrate the streamlines of the velocity field traced from the swirl. Right panel: Magnetic topology of the structure rooted in the swirl. The field line bundles are colored red and blue, respectively, depending on which magnetic concentration they are rooted in at the second footpoint. The probes show the vertical component of the magnetic field at the $\langle \tau \rangle = 1$ surface at each footpoint. In the right panel, the simulation box has been compressed by a factor of five in the axial direction for better visibility. The horizontal periodicity of the magnetic field lines has been neglected. See Sect. 4.3.1.

The increase in density leads to enhanced emission in the 171 Å channel of AIA. The emission is increased by about 15 % at a height of 4 Mm. At 8 Mm, the emission over vortices drops to values below the mean value. In contrast to the emission in the 171 Å channel, the X-ray emission is only increased by about 5 % in the corona compared to the average emission at a certain height. In both wavelength ranges, the emission is decreased in the chromosphere.

4.3.3 Additional events

We have identified several more swirling events that reach up into the upper chromosphere and low corona. Two such events are presented in Fig. 4.10 and Fig. 4.11. Similar to Battaglia et al. (2021), we frequently find events consisting of superpositions of swirls, especially with increasing distance to the photosphere. The swirl we have analysed in this chapter is rooted in a relatively simple and isolated footpoint that shows a clear anti-clockwise rotational motion (see Fig. 4.3). Most magnetic patches have a more complex structure and show a combination of rotation- and shearing motions. A superposition of events originating from a large magnetic footpoint containing several magnetic flux con-

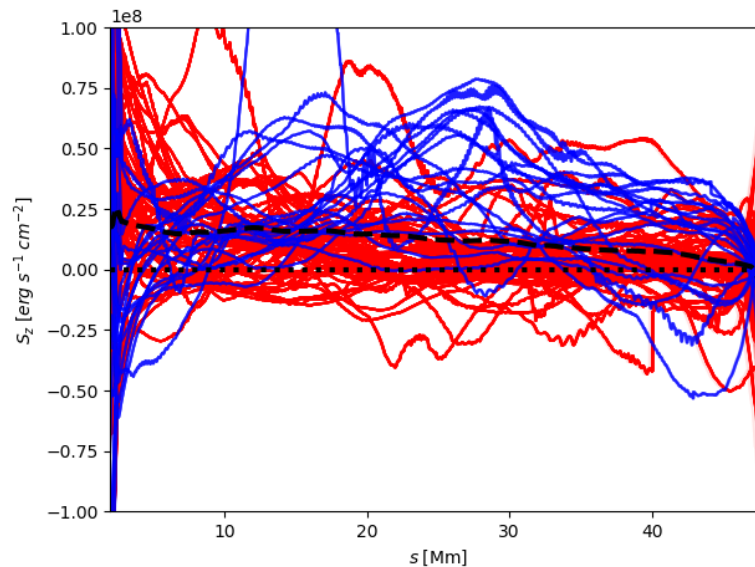


Figure 4.8: Axial Poynting flux interpolated along field lines rooted in the swirling structure shown in Fig. 4.2 traced from seed points at a height of 6 Mm. The two populations of field lines are colored in red and blue depending on the magnetic field patch in which they are rooted at the opposite loop footpoint. The color-coding is the same as in Fig. 4.7. The dotted black line is drawn at a constant value of zero. The dashed black line shows the average taken over all traced field lines. For a discussion, see Sects. 4.3.1 and 4.4.3.

centrations of kilogauss strength is shown in Fig. 4.9. This footpoint is connected to the regions with the highest emissivity in X-rays within the simulation domain. While several separate rotating regions are recognizable at a height of 1.3 Mm, the flow field does not show a clear swirling pattern above that height. Instead, bright X-ray emission is present at the location of strong shear flows.

4.4 Discussion

4.4.1 Atmospheric coupling

The rotating structure seen at coronal heights is magnetically connected to the chromosphere. Strong vortices are mainly found in regions above strong magnetic concentrations. These regions show increased transverse motions and as a consequence heightened Poynting flux, since the magnetic field communicates the photospheric motions upward due to the Lorentz force.

Vortices twisting the magnetic field lines have been found to be important for the transport of Poynting flux in the chromosphere (Yadav et al. 2020a,b), but so far it has been unclear whether they transport Poynting flux beyond the transition region or if most of the Poynting flux is either dissipated in the chromosphere or reflected at the transition region. We find a contiguous structure with enhanced Poynting flux extending high into the atmosphere. The Poynting flux strongly drops at a height of 1-2 Mm, but the enhance-

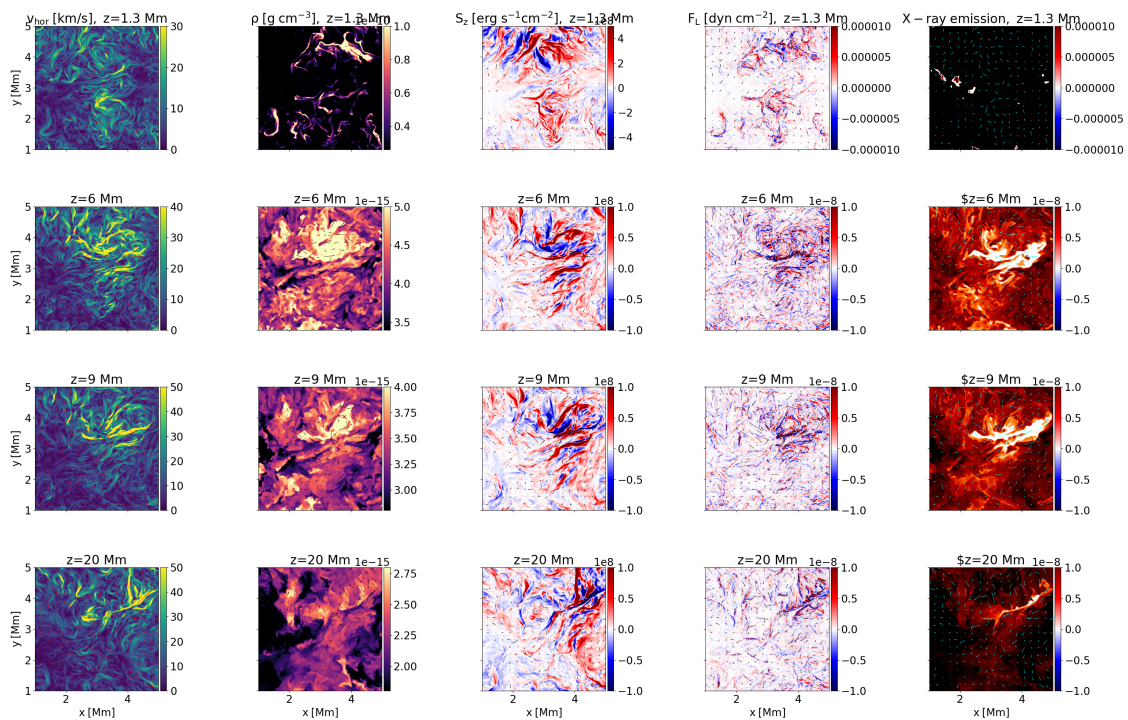


Figure 4.9: Perpendicular cuts at different distances to the photospheric layer for the complex magnetic footpoint located at $[x,y]=[0.5,1.5]$ Mm. From left to right: (a) Transverse velocity, (b) density, (c) Axial component of the Poynting flux, (d) axial component of the Lorentz force, (e) X-ray emission. From the top to the bottom row, cuts are shown at values of the axial coordinate s of 1.3 Mm, 6 Mm, 10 Mm and 20 Mm. The arrows show direction and magnitude of the velocity field. The field of view has been centered on the footpoint assuming periodic boundary conditions. The domain has been shifted by 3 Mm in the x - and y direction. The units of the X-ray emission are $\text{DN s}^{-1} \text{pix}_{\text{MUR}}^{-1} \text{Mm}^{-1}$.

ment reaches far into the coronal part of the loop. Therefore, even though dissipation and possibly reflection do take place at the transition region, a large fraction of the Poynting flux still escapes into the atmosphere.

The structure under consideration has one footpoint rooted in the swirl and two footpoints on the other end of the simulation box. Poynting flux can be injected both by internal motions within magnetic flux concentrations that twist the magnetic field or by relative motions of magnetic field concentrations that lead to the magnetic flux tubes being wrapped around each other. In this case, the Poynting flux averaged over the traced magnetic field lines is positive throughout most of the length of the box, indicating that the majority of the injected Poynting flux is indeed coming from the twisting motion that is imposed upon the flux tube by the vortical motion inside the magnetic flux concentration. It has been a longstanding debate what the exact mechanism is that transports energy into the atmosphere and subsequently releases it. The original idea by Parker of field lines braided by random motions at the boundaries (Parker 1972, 1983) has been further developed into the fluxtube tectonics model. In this model, heating occurs at the boundaries of

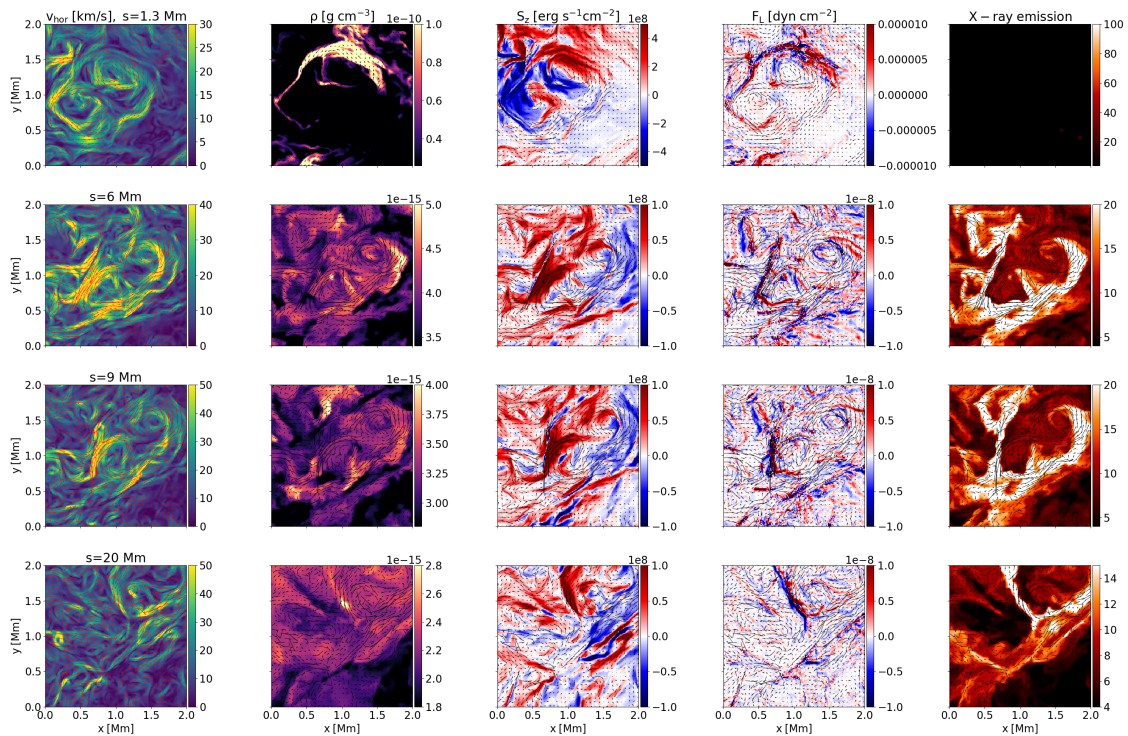


Figure 4.10: Same as Fig. 4.6, but for a different case at a time of 5.17 min. Cuts perpendicular to the loop axis at different distances to the photospheric layer along the loop arclength. From left to right: Velocity perpendicular to the loop axis, density, axial component of the Poynting flux, axial component of the Lorentz force, X-ray emission. From the top to the bottom row, cuts are shown at values of the axial coordinate s of 1.3 Mm, 6 Mm, 10 Mm and 20 Mm. The arrows show direction and magnitude of the velocity field. The units of the X-ray emission are $\text{DN s}^{-1} \text{pix}_{\text{MUR}}^{-1} \text{Mm}^{-1}$.

flux tubes that are braided by photospheric motions (Priest et al. 2002). In the concept of "dynamic braiding", introduced by van Ballegoijen et al. (2011), internal motions within a magnetic flux element launch packets of Alfvén waves that generate turbulence in the corona. While an extensive study of the relative contributions of braiding of magnetic field by external or internal footpoint motions is out of the scope of this work, the rotating motions inject sufficient Poynting flux into the atmosphere that is transmitted past the transition region to heat a strand to several million Kelvin. Internal footpoint motions could therefore be sufficient to heat loops of a few million Kelvin, while very hot loops might be heated by a different mechanism. Our scenario is similar to the Alfvén pulses found by Battaglia et al. (2021) since we do not see an oscillatory motion. The swirl lasts for roughly three minutes, instead of an oscillatory motion in the photosphere, it arises from coherent internal motion within a flux element.

In addition to energy transport, vortices could play a role for the transport of mass. Distorted magnetic field lines can lead to an upwards directed Lorentz force (Iijima and Yokoyama 2017). In hydrodynamic equilibrium, the gravitational force acting on the

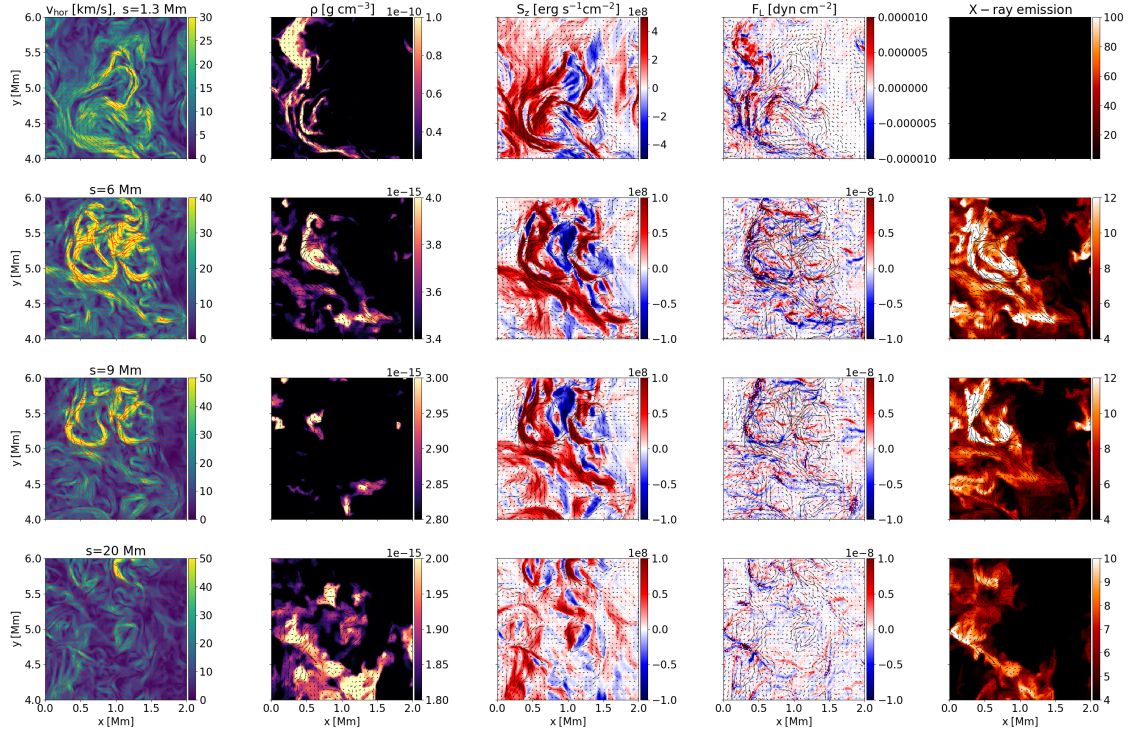


Figure 4.11: Same as Fig. 4.6, but for a different case at a time of 13.3 min. Cuts perpendicular to the loop axis at different distances to the photospheric layer through the structure shown in Fig. 4.2. From left to right: Velocity perpendicular to the loop axis, density, axial component of the Poynting flux, axial component of the Lorentz force, X-ray emission. From the top to the bottom row, cuts are shown at values of the axial coordinate s of 1.3 Mm, 6 Mm, 10 Mm and 20 Mm. The arrows show direction and magnitude of the velocity field. The units of the X-ray emission are $\text{DN s}^{-1} \text{pix}_{\text{MUR}}^{-1} \text{Mm}^{-1}$.

plasma is balanced by the pressure gradient. We find that the upward directed Lorentz force is of the same order as the force caused by the pressure gradient. The resulting dense structure in the chromosphere shown in the second column of Fig. 4.6 is roughly 500 km wide and 1 Mm long at a height of 1.3 Mm, consistent with the dark structures observed by Wedemeyer-Böhm and Rouppe van der Voort (2009). Another possible effect that could lead to the increased density in vortices in the lower atmosphere is downflowing plasma being trapped in magnetic flux tubes. The increase in Lorentz force is not equally distributed over the rotating structure but enhanced at the leftmost edge. Wedemeyer-Böhm et al. (2012) found that the highest Doppler shifts were found in the outer part of the ring-like structures where the centrifugal forces are largest, which is consistent with our simulations.

Various types of motion occur within magnetic concentrations at the photosphere. In addition to rotational motions, shearing of field lines occurs and magnetic concentrations merge and split up again. Vortices might act to transport Poynting flux into the upper atmosphere, but this does not automatically mean that the energy is dissipated. While we do find increased heating of the vortices, the relation between vortices and bright strands

is more complicated. Instead of a hot, dense, and bright loop that is clearly distinct from its environment we find that the emission has a complex structure similar to the coronal veil picture in Malanushenko et al. (2021). There is no one-to-one correspondence between a bright strand and a vortex. Instead, we find a picture similar to Antolin et al. (2014). In their simulation, strands arise from velocity sheared regions with enhanced emissivity. The vortices are generated from the Kelvin-Helmholtz instability in response to transverse oscillations of the entire magnetic flux tube. Yadav et al. (2021) interpret small-scale vortices as the result of vorticity cascading down from large scale flows to smaller scales. It is not straightforward to determine whether individual small-scale vortices in our simulation are driven directly by rotating magnetic flux tubes or if they are created by instabilities affecting larger structures. Individual large-scale swirls, at least, can be traced back to corresponding rotating motions in the photosphere.

4.4.2 Swirl properties

Several simulations have shown that vortex flows could contribute to chromospheric heating and transport Poynting flux into the corona. Yadav et al. (2021) have studied the statistical properties of vortices.

In agreement with their study, we find that the area fraction covered by vortices increases with height due to the expansion of the magnetic flux tubes.

The vortices are predominantly located in the intergranular lanes and thus evacuated due to the strong magnetic fields in the downflow lanes. In addition, a contribution from the dynamical pressure created by the centrifugal force to the total pressure further lowers the gas pressure inside the vortices (Moll et al. 2011). This is consistent with our findings. From a height of 1 Mm on, this behavior reverses and the vortices are instead overdense. Increased density associated with vortices in the low chromosphere was also found by Yadav et al. (2021), and by Kitiashvili et al. (2012b), where the vortex forms a dense ring-like structure. A possible cause for this increase in density is the tangling of field lines, leading to a Lorentz force that lifts up dense plasma from the lower atmosphere, as can be seen in Fig. 4.6.

An increased Poynting flux over vortices due to the twisting of the magnetic field in the chromosphere has also been found by Yadav et al. (2020b), Battaglia et al. (2021). The local minimum at and the subsequent sharp rise of the Poynting flux above the transition region is possible because the signed Poynting flux is used. At the transition region height, a larger fraction of the upward directed Poynting flux is balanced by downward directed flux, possibly from the submergence of low lying loops or reflection at the transition region. In response to the increased influx of energy, the vortices show an increased heating rate compared to the surroundings, consistent with (Yadav et al. 2021). Since the magnitude of the viscous heating depends on density, the strong increase in the heating fraction in the chromosphere is due to the increased density over chromospheric vortices. The resistive heating is also increased, but only by about 10 % in the chromosphere while not showing an increase compared to the background at coronal heights. This is likely due to the more complex field geometry in the chromosphere compared to the corona. Yadav et al. (2021) find strong current sheets at the interfaces of vortices in the chromosphere and an enhancement of currents over vortices. In Carlsson et al. (2010), the heating is seen mainly at the edges of magnetic flux concentrations and is Ohmic in nature. Moll

et al. (2012) associate vortices with increased viscous dissipation and Ohmic dissipation with the edges of magnetic flux concentrations. The ratio of viscous to resistive heating in simulations depends on the magnetic Prandtl number (Brandenburg 2014, Rempel 2016). The temperature over vortices is lower in the upper photosphere and lower chromosphere compared to the averaged temperature at the same geometrical height, consistent with the location of the vortices in the cooler intergranular lanes (Moll et al. 2012). In contrast to Yadav et al. (2021), who find that the temperature is increased in vortices at all heights above the base of the chromosphere, the temperature over vortices in our simulation is lower than average in the chromospheric layers and slightly increased in the corona. This could be due to the cooler material at higher densities trapped in the vortices at chromospheric heights. In the corona, the temperature is increased by about 1-2 % despite a 20 % increase in the heating rate. This is not surprising if we take a look at the RTV scaling laws (Rosner et al. 1978). For an increase in the heating rate of 20 %, we would only expect an increase of the temperature by 5 %. We find an even smaller temperature increase, but the RTV scaling laws assume a 1D atmosphere in thermal equilibrium, which is not the case in a realistic time-dependent 3D simulation.

In the corona, where the magnetic field is uniform, the effect of vortices on the density is negligible. The regions with the highest densities are not associated with vortex flows, despite the increased heating rate in vortices. This behavior can be understood considering the timescales involved. The density reacts to increases in the temperature with a delay. Typical axial velocities in the simulation are of the order of 50-100 km/s, therefore it takes several minutes to transport material through the loop. This is on the order of the typical lifetimes of small-scale vortices. The cooling timescale for a coronal loop is on the order of half an hour, therefore the loop remains hot after the actual heating event has ceased. The initial increase in density in the chromosphere is consistent with Yadav et al. (2021), though since the upper boundary in their simulation is at a height of 2.5 Mm, they do not see the subsequent decline in overdensity of the swirls in the corona.

In observations, chromospheric vortices appear as dark features (Wedemeyer-Böhm and Rouppe van der Voort 2009). This is compatible with the presence of elevated, dense and cool material that we find in the vortices in the upper photosphere and chromosphere. Despite the increased density and heating rate for the low corona up to 7.5 Mm, the X-ray emission is only increased by about 4-5 percent. The emission follows mainly the density distribution that is not significantly enhanced in swirls above a height of 8 Mm. At chromospheric heights, both the emission in the 171 Å channel and in X-rays is lower than the average emission at the same perpendicular slice. This could be due to cool material reaching larger heights in the vortices, so that the swirls are overdense in the chromosphere and low corona, but slightly cooler than the surroundings and thus too cool for being bright in X-ray emission or in the 171 Å channel.

The emission in the 171 Å channel, which is sensitive to temperatures around 600000 K, is increased by about 10 % in the low corona and its behavior qualitatively follows the density distribution from a height of 2.5 Mm on. At coronal heights, the swirls are darker in the 171 Å channel than the surroundings. This is due to the high temperatures in the corona that rise way above 600000 K. The X-ray emission is enhanced in the hottest parts of the corona.

The brightest areas do not coincide with the highest swirling strength and the brightness contrast is small compared to other parts of the loop cross section. Heating occurs at

strong gradients in either the magnetic or velocity field. This is the case in regions with strong shear flows such as the edge of a vortex or regions where vortices interact. This is similar to Reale et al. (2016), where the current first increases at the location of shear between the twisted and untwisted regions. Other types of motion, however, such as relative motion of flux tubes or pure shear motions can also lead to gradients in the velocity and magnetic field and thus to viscous and resistive dissipation. The strand of bright X-ray emission in the right column of Fig. 4.6 corresponds to such a dissipation region caused by the vortex flow, but since the vortex edge falls below the swirling strength threshold and the emission is not necessarily increased within the swirls themselves, this relation between vortices and bright areas is not accurately captured in the statistics. The swirling strength criterion, when applied to the smoothed velocity field, does not capture the rotating structure in its entirety. An arbitrary threshold needs to be selected to define the vortex boundary. Different vortex identification methods should be investigated and compared.

4.4.3 Implications for coronal heating

While the original Parker model considered random motions on an infinitely conducting plate as the driver for the braiding of field lines, the model has since been extended to more realistic scenarios and the term is often used to refer to large-scale braiding of magnetic structures. Most loops, however, do not show evidence for braiding on observable scales (van Ballegoijen et al. 2011). They instead suggest that the heating is due to motions inside magnetic concentrations. De Moortel and Galsgaard (2006b) compare coronal heating due to rotational and spinning footpoint motions. In the first case, the sources of two flux tubes are rotating around each other, entangling the flux tubes. In the second case, the footpoints do not undergo a bulk motion, instead the field lines inside the flux tubes are tangled by internal spinning motions. The authors find that in the presence of a background field, the small-scale spinning motions are more efficient at dissipating energy for the same misalignment angle as rotational motions. Our findings are more in line with the original Parker braiding model that also includes reconnection due to torsion within aligned flux tubes (Parker 1982) than with the flux tube tectonics model in which heating arises from the relative motion of flux tubes (Priest et al. 2002). It was found before that swirls can provide a significant amount of the energy flux to heat the chromosphere and corona (Wedemeyer-Böhm et al. 2012, Battaglia et al. 2021). The average vertical Poynting flux at a height of 6 Mm above the swirling structure outlined by the contour in panel of Fig. 4.2 is 5.1 kWm^{-2} . At height of 2 Mm the average Poynting flux is still 18.4 kWm^{-2} and at a height of 1 Mm above the photosphere even 127.8 kWm^{-2} . Large-scale swirls with a swirling strength above a threshold of 0.002 s^{-1} , cover about 30 % of the simulation domain at a height of 1 Mm, while roughly 40 % of the Poynting flux is channeled through them. The amount of Poynting flux available at the transition region is compatible with the requirement of 10 kWm^{-2} to heat coronal plasma to several million Kelvin. A significant fraction of the Poynting flux is transmitted through the transition region. In order to dissipate the injected energy, gradients in the magnetic field or in the velocity field need to form. As Fig. 4.8 shows, the average axial Poynting flux along a set of sample field lines is positive almost through the entire length of the loop. A small fraction of the Poynting flux thus does not get dissipated and reaches the opposite transition region. The strongest dissipation occurs along the outer edge of the vortex structure along

a strong velocity gradient. The heating rate is higher above the complex footpoint seen in the lower left quadrant. A superposition of swirls creates more small-scale structure that allows for dissipation.

4.5 Conclusion

In simulations, vortices have been found both in the photosphere and in the chromosphere. These structures are not distinct, but the chromospheric vortices are rooted in their photospheric counterparts. While vortices have been observed in the low corona and it has been suggested that vortices play an important role for channelling energy and plasma into the corona (Wedemeyer-Böhm et al. 2012), the continuation of these structures beyond the transition region has never been studied in detail in simulations.

Using high resolution simulations of the solar surface, chromosphere, and corona, we find that vortices do not only extend into the chromosphere, but form contiguous structures that connect the photosphere with the corona. Consistent with previous studies, vortices are energetically important especially in the upper chromosphere, showing increased Poynting flux and heating rates. Upward acceleration of chromospheric plasma leads to a higher density at vortex locations in the chromosphere and low corona. While vortices play an important role for energy transport and transverse density structuring of the chromosphere and low corona, their role becomes less clear with increasing height. Poynting flux and heating rate are still increased at coronal heights, but less so than in the chromosphere, and the effect on the density is small. There is a complex relationship between coronal emission and vortices. Regions with enhanced emissivity at vortex edges could potentially appear as loop strands. The influence of different criteria for the identification of vortices and their boundaries needs to be investigated.

5 Nonthermal broadening of coronal lines in a 3D MHD loop model

This chapter is the manuscript for a paper to be submitted to Astronomy & Astrophysics by C. Breu, H. Peter, R. Cameron and S.K. Solanki.

Contributions to the paper: I performed the simulations, analyzed the data, and wrote the first draft of the manuscript; all authors contributed to the ideas behind the study.

Abstract

Observed spectral profiles of emission lines from the corona are found to have widths exceeding the thermal line width. To investigate the physical mechanism behind this, we run a 3D MHD model of a single loop in which we partially resolve the turbulent motions within the loop and the substructures that form self-consistently in response to the driving by magneto-convection in the photosphere. The loop is modelled as a straightened-out magnetic flux tube with a shallow, self-consistently evolving convection zone layer at each end. From the model we synthesize spectral profiles of emission lines forming at temperatures around and above 1 MK, representing a typical active region loop. Our model includes the mass exchange between corona and chromosphere, for example through chromospheric evaporation and localised downflows, and thus we can also capture flows parallel to the loop axis in our model. Most synthesized line profiles have a single Gaussian shape, but we also find locations where the line profile has enhanced wings or double peaks, sometimes associated with bi-directional flows. We find that the spectral lines show a nonthermal line broadening roughly consistent with observations for a viewing angle perpendicular to the guide field, albeit at the low end of observed values. The broadening through field-parallel flows is comparable to the broadening due to turbulent-like motions that develop mostly perpendicular to the (guide) field, although slightly smaller. The line broadening increases with higher resolution of the simulations. Our study shows that the resolution of the model needs to be sufficiently high to capture the turbulent-like motions causing the non-thermal broadening. We find the nonthermal motions to be roughly isotropic, even though different in nature in the parallel and perpendicular directions to the magnetic (guide) field. We can directly connect the nonthermal line broadening to heating events and flows in the coronal loop.

5.1 Introduction

In observations of the solar corona, emission lines in the extreme ultraviolet show broadening that exceeds the effects of the thermal line width and instrumental broadening. The amount of nonthermal line broadening depends on the observed region. Different values are found for the quiet Sun, active regions or coronal holes. It is largest in the quiet Sun with values up to 30 km s^{-1} (Chae et al. 1998). Typical values for the observed nonthermal broadening of emission lines in active regions from plasma above 1 MK are in the range of $15\text{-}20 \text{ km s}^{-1}$ (Hara and Ichimoto 1999, Brooks and Warren 2016). A correlation of intensity and nonthermal line broadening was found for lines emitted in the low transition region for temperatures in the range up to 10^5 K (Dere et al. 1984). For hotter plasma in active regions or coronal loops, there is only a weak correlation between the intensity and the nonthermal line broadening (Chae et al. 1998).

The observed nonthermal broadening is independent of the instrument resolution (De Pontieu et al. 2015, Testa et al. 2016).

Different processes can cause the broadening of emission lines. In thermodynamic equilibrium, the particles in a plasma move according to a Maxwellian velocity distribution with a width determined by the temperature. The motion of the emitting particles results in a broadening of emission lines, the thermal broadening. Unresolved motions within a resolution element of the observing instrument and along the line of sight lead to nonthermal broadening of spectral lines. Potential processes to explain these unresolved motions are turbulence, quasi-periodic upflows, nanoflares, shocks or waves (De Pontieu et al. 2015, Pontin et al. 2020). It follows from the independence of nonthermal line broadening of the resolution of the observing instrument that the process responsible for line broadening must operate along the line of sight or on scales below the highest currently available instrument resolution of $0.35''$, or below about 250 km. Otherwise one would expect that the nonthermal broadening increases with decreasing instrument resolution.

Due to the frozen-in condition, the movement of plasma in the corona is strongly impeded in the direction perpendicular to the magnetic field. Therefore, nonthermal velocities along and across the magnetic field are likely to arise from different processes. The correlation between line width and intensity has been linked to shocks for an LOS parallel to the magnetic field, while for the perpendicular direction, small-scale twist could explain the correlation (De Pontieu et al. 2015).

The shapes of the spectral line profiles can provide information about heating mechanisms and mass flows in the corona. If a structure is observed at the limb, motions perpendicular to the magnetic field are expected to produce the dominant contribution to the nonthermal line broadening, while line widths measured in on-disk observations contain components from motions along the magnetic field. The center-to-limb variation of the observed nonthermal broadening can therefore help to disentangle contributions from flows along and perpendicular to the magnetic guide field.

Observed line profiles of transition region lines in the quiet Sun have several components consisting of a narrow core and a broad second component that could be related to flows in the footpoint regions of large loops (Peter 2000). While Chae et al. (1998) did not find a significant center-to-limb variation of the nonthermal broadening for lines from plasma at temperatures between 10^4 K and $2 \times 10^6 \text{ K}$, Hara et al. (2008) find that nonthermal velocities observed at the footpoints of an active region in the Fe XIV and Fe XV lines

decrease towards the limb. They interpret deviations from a Gaussian profile in the blue line wing as strong unresolved upflows and conclude that the enhanced line broadening at loop footpoints in the disk observations is due to field-aligned flows. Li and Peter (2019) interpret the blue wing of spectra measured at the footpoint of a cool, low-lying loop as plasma injection into the loop. Peter (2010) also find blueshifted components in the profiles of the Fe XV line in the footpoint regions of an active region. Erdelyi et al. (1998) observe a broadening of the line profiles of chromospheric and transition region lines towards the limb and interpret this as signatures of Alfvén waves.

Nonthermal line broadening can arise both from the heating process itself, for example from unresolved wave motions, and from the response of the plasma to the heating. The line width is often taken as a measure for the root-mean-square velocity and thus the energy flux carried into the corona by various types of waves (McIntosh and De Pontieu 2012, Pant et al. 2019). In this case the nonthermal line broadening arises from the mechanism that carries energy into the corona and thus from the cause of the heating.

Not only wave motions may lead to increased line broadening, the nanoflare model of coronal heating can also cause nonthermal broadening. Reconnection of magnetic field lines in the atmosphere can drive bidirectional reconnection jets that lead to spectral line profiles with separate components in the wings (Dere and Mason 1993, Innes et al. 1997, Antolin et al. 2021).

Energy release in the corona due to reconnection could also lead to nonthermal broadening by chromospheric evaporation (Peter 2010), as was suggested by Patsourakos and Klimchuk (2006). Peter (2010), however, find that the velocities at the footpoints are too low. Furthermore, the line broadening higher up in the loop was stronger than at the loop footpoints. This scenario would be more compatible with transverse Alfvén waves.

The nonthermal line broadening is underestimated in numerical simulations of active regions compared to observations for transition region lines (Peter et al. 2006), although the values are closer to observations for lines formed at coronal temperatures. A possible reason is that the resolution in those models is not high enough. With a higher resolution, small-scale flows with potentially higher velocities could be resolved (Peter et al. 2006, Pontin et al. 2020).

Several aspects of the observed characteristics of nonthermal line broadening have been successfully reproduced in a simulation of the turbulent relaxation of a magnetic braid by Pontin et al. (2020), including the typical observed values, independence of the field of view and excess emission in the line wings, which is interpreted as a signature of turbulent motion.

This chapter is organized as follows. First the simulation setup and the calculation of synthetic spectra is described in Sect. 5.2, then the results for the nonthermal line width are presented for different resolutions and spectral lines in Sect. 5.3 and discussed with respect to coronal heating and flows triggered by heating events in Sect. 5.4. We present conclusions in Sect. 5.5.

5.2 Methods

5.2.1 The loop model

We solve the compressible, resistive MHD equations with the MURaM code. The coronal loop is modelled as a straightened-out magnetic flux tube with a coronal part spanning between two footpoints. The simulation domain includes the chromosphere, corona and a shallow convection zone at each loop footpoint. The heating of the coronal loop is driven self-consistently by magnetoconvection at the footpoints. The simulation setup is described in detail in Breu et al. (2022)¹. As an initial condition for the magnetic field configuration, we choose a uniform magnetic field strength of 60 G, corresponding to a weak plage region. In order to study the effect of grid resolution on the line profiles, we run the simulation at three different grid resolutions, 60 km, 24 km and 12 km. In the coronal part of the simulation domain, the radiative losses are modelled using an optically thin loss function, while radiative transfer in the grey approximation in the photosphere and chromosphere is included. The chromosphere is assumed to be in local thermodynamic equilibrium (LTE).

5.2.2 Synthesizing line profiles

In a first step, we compute the emissivity at each gridpoint assuming ionization equilibrium. We synthesize the emission for the Fe XV 284.163 Å and Fe XII 195.119 Å lines that correspond to a plasma temperature of about 2.2 MK and 1.5 MK, respectively. The plasma in the coronal part of the loop has a temperature of several million Kelvin and is thus bright in Fe XV. To also capture the broadening arising from motions of cooler plasma especially at the footpoints, we also synthesize emission in the Fe XII line. Both lines are commonly used in solar extreme-UV spectroscopy. To compute the spectral line profiles, we assign a Gaussian line profile to each gridpoint. The width of the Gaussian is given by the thermal width

$$w_{\text{th}} = \sqrt{\frac{2k_{\text{B}}T}{m_{\text{Fe}}}} \quad (5.1)$$

that arises from the thermal motion of the particles in the plasma. The thermal width is computed from the temperature in the each grid cell and the mass of the Fe atom. The Gaussian profile is then shifted according to the LOS velocity at each gridpoint. Subsequently, we integrate the line profiles along the line of sight. For an equidistant grid, we approximate the integral as a sum over the line profiles from each gridpoint along the line of sight. The spectra can be calculated in this way because the coronal lines under consideration are optically thin and full radiative transfer calculations are not necessary.

5.2.3 Nonthermal velocities

We compute the width w_{obs} by calculating the second moment of the line profile, thus mimicking an observation. In order to obtain the nonthermal line width w_{ntlw} , we need to

¹Chapter 3 in this thesis

subtract the thermal width:

$$w_{\text{nth}} = \sqrt{w_{\text{obs}}^2 - w_{\text{th}}^2}. \quad (5.2)$$

We assume a thermal width w_{th} computed using the peak formation temperature of the respective emission line. This is the same way as observations define the nonthermal width. One has to remember, however, that the coronal part of the simulation domain does not have a homogeneous temperature. Instead, a large range of temperatures can be present along the line of sight.

Assuming a constant thermal line width can lead to unphysical values for the nonthermal broadening such as negative nonthermal line widths. This can occur in cool areas with plasma temperatures below the line formation temperature, where the broadening by velocity fluctuations along the line of sight is smaller than the assumed thermal line width. In the majority of the simulation domain, however, this is not a problem. We perform a comparison between the nonthermal line broadening computed assuming a constant line width and the nonthermal width using the actual plasma temperature in Sect. 5.3.3.

5.3 Results

In response to the photospheric driving, turbulent-like behavior develops in the coronal loop. Multiple small current sheets form at length scales below the resolution limit of current instruments. A cross section of velocities and current densities at the loop apex is shown in Fig. 5.1. The transverse velocity components show a complex small-scale structure, while the velocity parallel to the guide field is organized on larger length scales. The magnetic field distribution at the footpoints and the distribution of temperature and emission in the Fe XV line at the apex are shown in Fig. 5.2. The temperature in the loop cross section ranges from 1.6 MK to 7.3 MK. Since a significant amount of plasma is above the line formation temperature and the emission depends quadratically on the density, the distribution of the emission in Fe XV deviates from the temperature distribution. It also shows that over only 6 Mm across the loop, a large variation in temperature can occur. This has consequences for the interpretation of the obtained spectra. In the following sections, we discuss the properties of the line profiles obtained from forward modelling, their dependence on the grid resolution of the simulation runs and the resolution of synthetic observations as well as their connection to heating events and resulting plasma flows.

5.3.1 Nonthermal broadening perpendicular to guide field

The maps obtained from an LOS-integration along the x- and y-direction correspond to a loop seen from the side above the limb, with only motions transverse to the magnetic field contributing to the line broadening. LOS-integrated emission, Doppler shift and nonthermal broadening for the high resolution run are shown in Fig. 5.3 for an integration along the x-direction and in Fig. 5.4 for an integration along the y-direction. The nonthermal line width reaches values up to and above 30 km s^{-1} which is consistent with observations. Emission, Doppler shift and nonthermal line broadening exhibit elongated structures aligned with the guide field.

The brightest regions do not coincide with the largest line widths or Doppler shift. Near

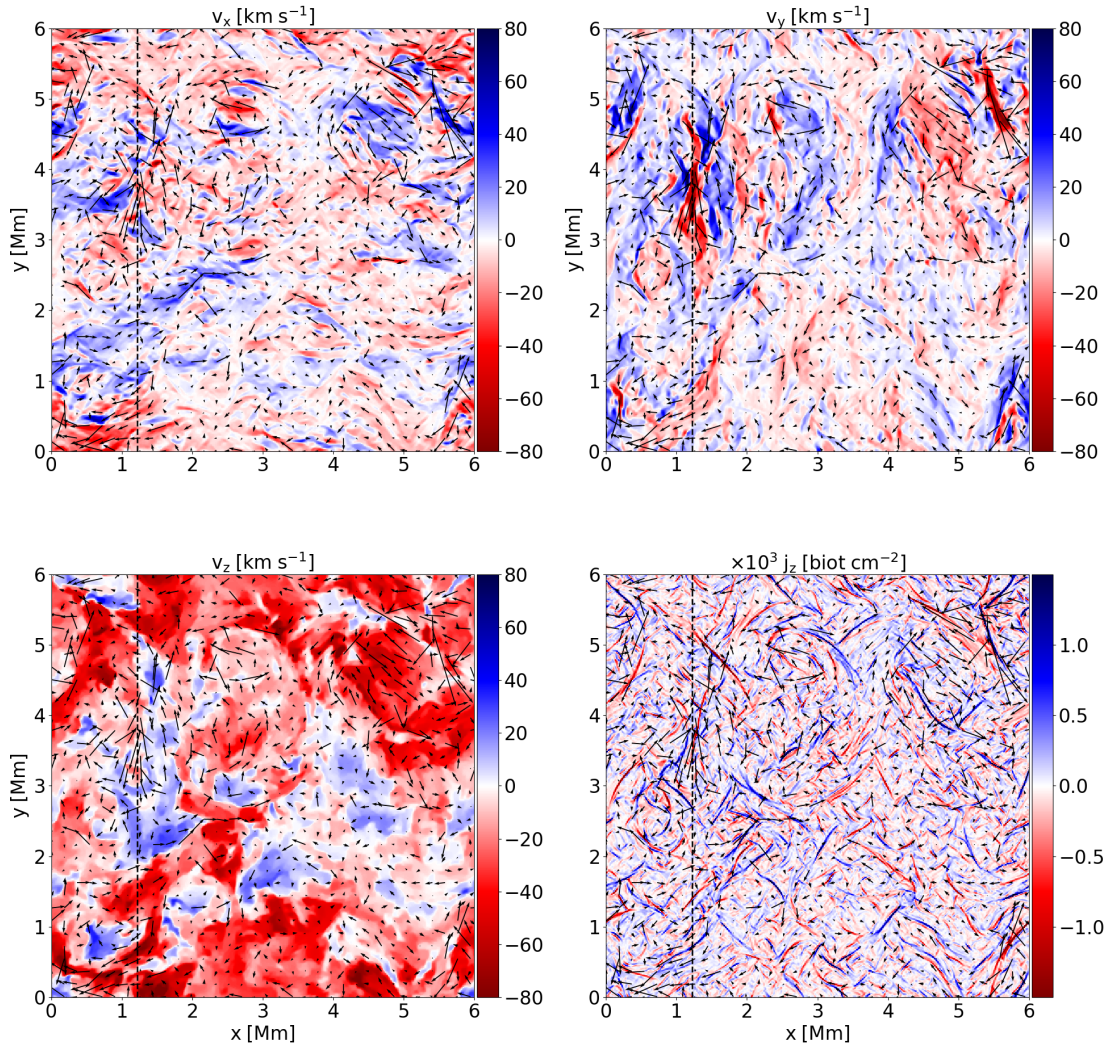


Figure 5.1: Cross-section through the loop apex for the high resolution run with $\Delta x = 12$ km at time 22.21 min. Top row: Velocity components perpendicular to the guide field. Bottom row: Velocity and current density parallel to the guide field. The vertical black line marks the position of the line profile shown in Sect. 5.3.4. The arrows illustrate direction and magnitude of the transverse velocity field. See Sect. 5.3.

the loop apex, the highest Doppler shifts and values for the line broadening appear in the dark regions. The correlation between nonthermal line widths and intensity is very weak or even moderately negative for some snapshots for Fe XV and moderately negative for Fe XII for the high resolution run. While areas showing a large Doppler shift also to a large part exhibit increased nonthermal broadening, increased line broadening is also present in regions with a low Doppler shift. The correlation between the magnitude of the Doppler shift and the nonthermal line broadening is weak for both Fe XV and Fe XII.

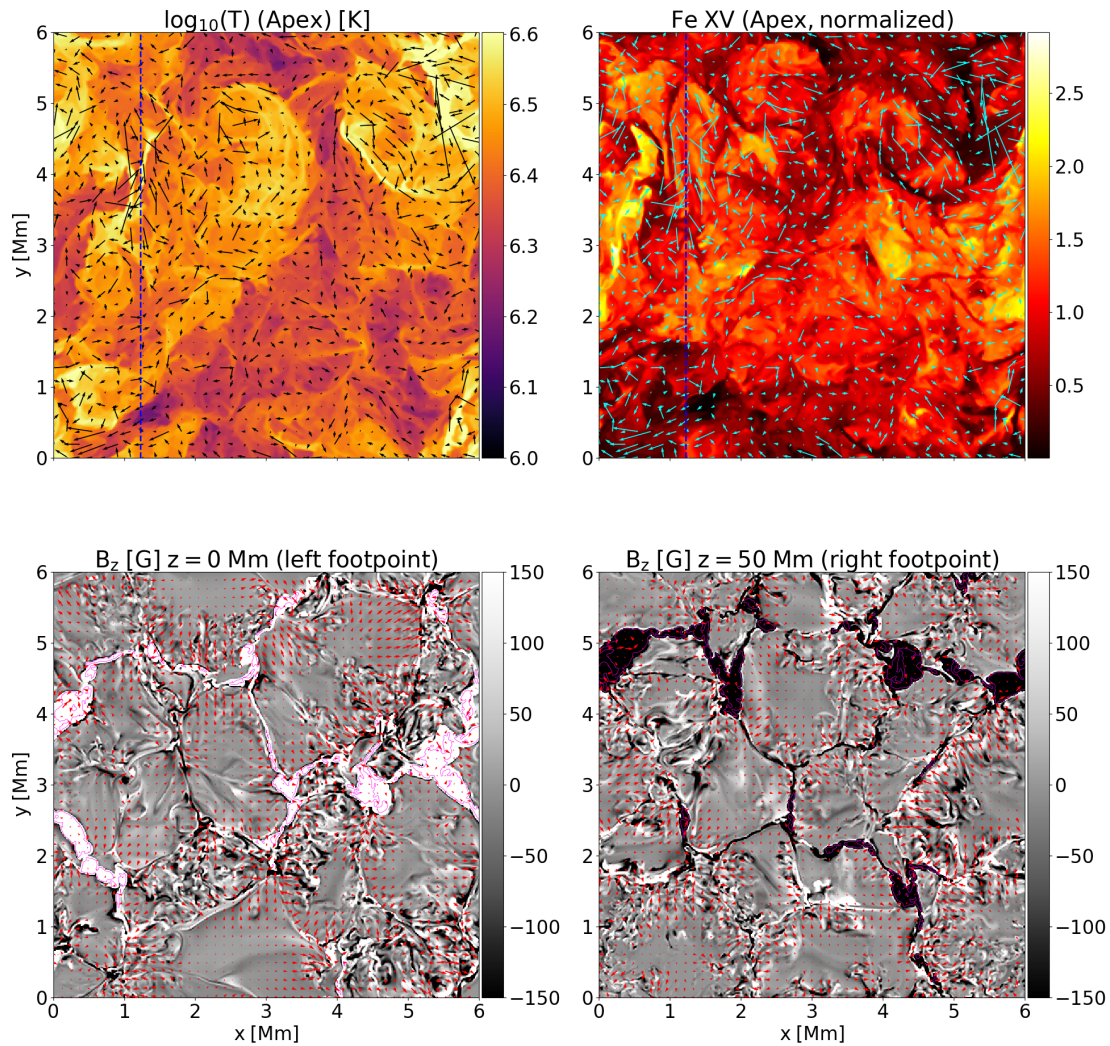


Figure 5.2: Overview over the simulation box for the high resolution run with $\Delta x = 12\text{km}$ at time 22.21 min. Top row: Temperature and emission in the Fe XV line at the loop apex (right). The vertical blue line marks the position of the line profile shown in Sect. 5.3.4. Bottom row: Vertical magnetic field at the photospheric layer. The pink contours mark the outlines of kilogauss concentrations with $|B_z| > 1000\text{ G}$. The arrows illustrate direction and magnitude of the transverse velocity field. The units of the emission are $[\text{DN pix}_{\text{MURS}}^{-1}\text{Mm}^{-1}]$. See Sect. 5.3.

We find fine-structure in intensity, Doppler shift and line broadening. A one-dimensional cut through intensity, Doppler shift and nonthermal line broadening for the Fe XV line and the high resolution run is shown in Fig. 5.7. Not only are fine strands present in the emission, but also in the Doppler shift and nonthermal line broadening. Various parts of the loop move independently. Doppler shift and nonthermal broadening show more fine structure than the intensity. The cut shows a peak in Doppler shift and nonthermal line

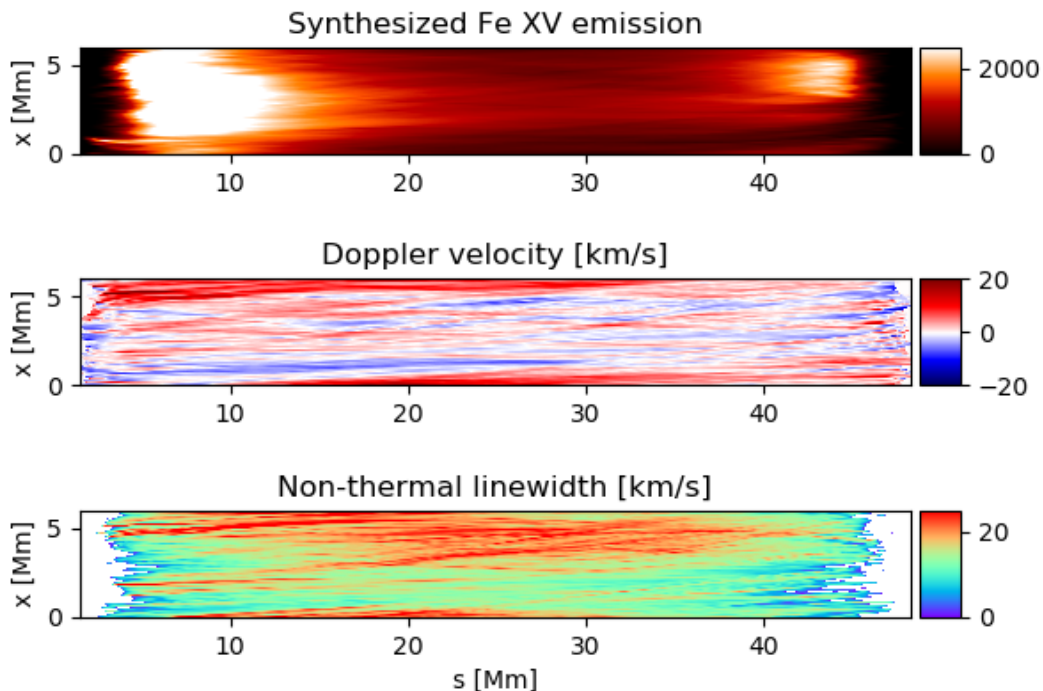


Figure 5.3: From top to bottom: Intensity of the emission in the Fe XV line, Doppler shift, and nonthermal line broadening seen perpendicular to the guide field for the high resolution run at time 22.21 min. The line of sight integration was performed along the x-axis. In the white areas, imaginary values for the nonthermal line broadening would be obtained due to low plasma temperatures. The integrated emission has the units $[\text{DN pix}_{\text{MUR}}^{-1} \text{s}^{-1}]$.

broadening at the location of the strong heating event located at $x,y=[1.2,4]$ Mm.

The statistical properties of the nonthermal line broadening for simulations with different resolutions are shown in Fig. 5.5 and Fig. 5.6. Since the nonthermal line broadening varies with changing temperature and velocities in the loop, we have computed normalized histograms for a range of snapshots and then averaged the histograms in time. Data for line-of-site integration in both the x- and the y-direction was included in the distribution. The areas with imaginary nonthermal line width were excluded. For the low resolution, 50 snapshots covering a timerange of one hour were used. For the medium resolution, 25 snapshots over the range of 40 minutes were used and for the high resolution simulation 10 snapshots over 25 minutes.

We find higher peak and mean values for the nonthermal broadening for the medium and high resolution run. For the Fe XV emission, the peak of the distribution is at 9.9 km s^{-1} for the lowest resolution of 60 km, 13.1 km s^{-1} for the medium resolution and 14.1 km s^{-1} for the highest resolution run. The mean values for the distribution are 10.3 km s^{-1} , 13.3

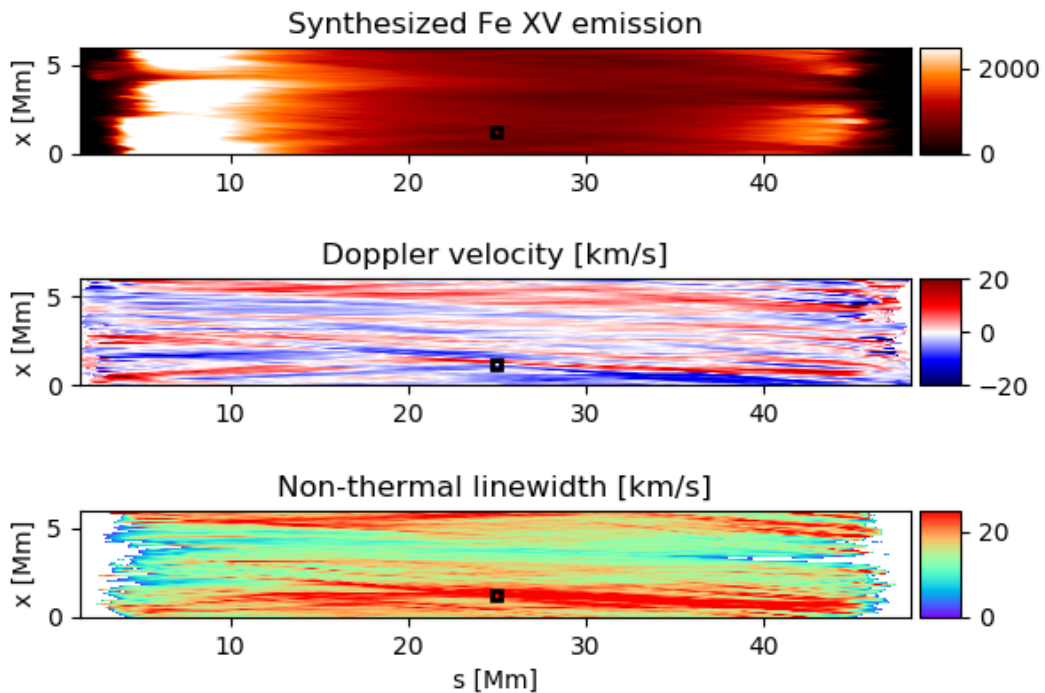


Figure 5.4: From top to bottom: Intensity of the emission in the Fe XV line, Doppler shift, and non-thermal line broadening seen perpendicular to the guide field for the high resolution run at time 22.21 min. The line of sight integration was performed along the y-axis. In the white areas, imaginary values for the nonthermal line broadening would be obtained due to low plasma temperatures. The black square marks the field of view used for the line profile in Fig. 5.19. The integrated emission has the units $[\text{DN pix}_{\text{MUR}}^{-1} \text{s}^{-1}]$. For a discussion see Sect. 5.3.1.

km s^{-1} and 14 km s^{-1} , respectively.

For the emission in the Fe XII line, the peaks of the histograms are at slightly higher values of 11 km s^{-1} , 13.4 km s^{-1} , and 14.8 km s^{-1} . We find average nonthermal line widths of 11.1 km s^{-1} , 14 km s^{-1} , and 15.2 km s^{-1} for the three different resolutions. For both emission lines, the difference between the 24 km run and the 12 km run is smaller than the difference between the 60 km run and the 24 km run.

5.3.2 Nonthermal broadening parallel to guide field

In order to simulate an observation of the loop footpoints close to disk center, we integrate the line profiles along an LOS parallel to the guide field. Since an observer would not look down from the apex along the curved magnetic field to the footpoints, but only see part of the loop leg, we limit the range of integration to $s \in [0, 10] \text{ Mm}$. This captures the footpoint region of the 50 Mm long semi-circular loop quite well.

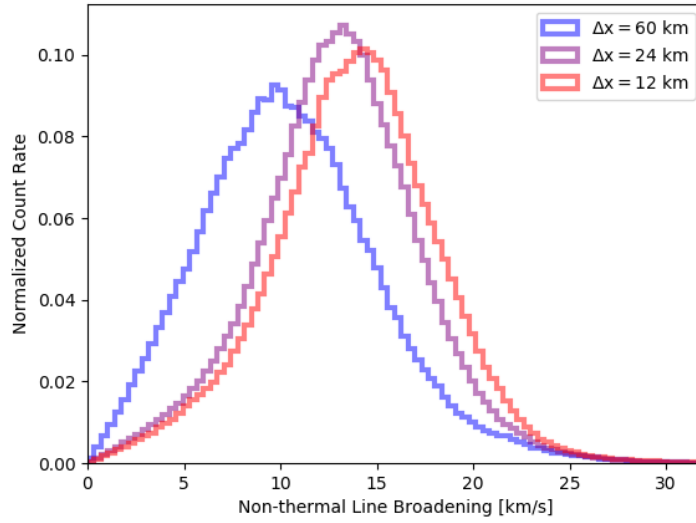


Figure 5.5: Time-averaged normalized histograms for the nonthermal line width in Fe XV seen perpendicular to the guide field. We show the histograms for three different grid resolutions of 60 km, 24 km and 12 km, respectively. See Sect. 5.3.1.

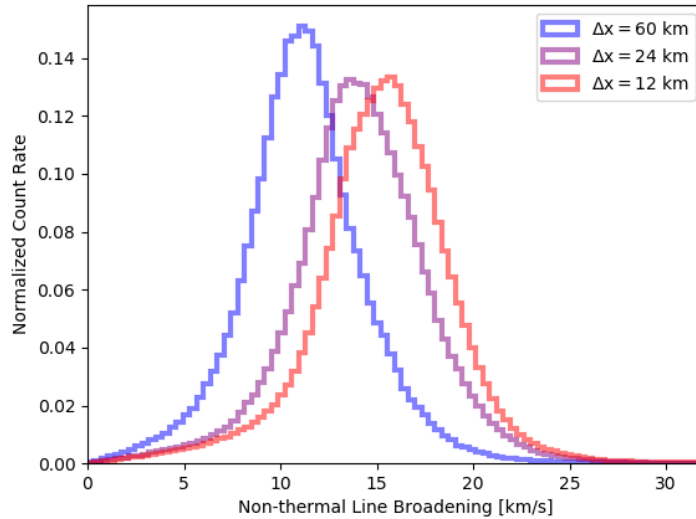


Figure 5.6: Time-averaged normalized histograms for the nonthermal line width in Fe XII perpendicular to the guide field. We show the histograms for three different grid resolutions of 60 km, 24 km and 12 km, respectively. See Sect. 5.3.1.

The emission in the Fe XII line, Doppler shift and nonthermal broadening for the left loop footpoint are shown in Fig. 5.8. The nonthermal broadening is organized in patches. Peak and average values of the distribution of nonthermal line widths are slightly lower

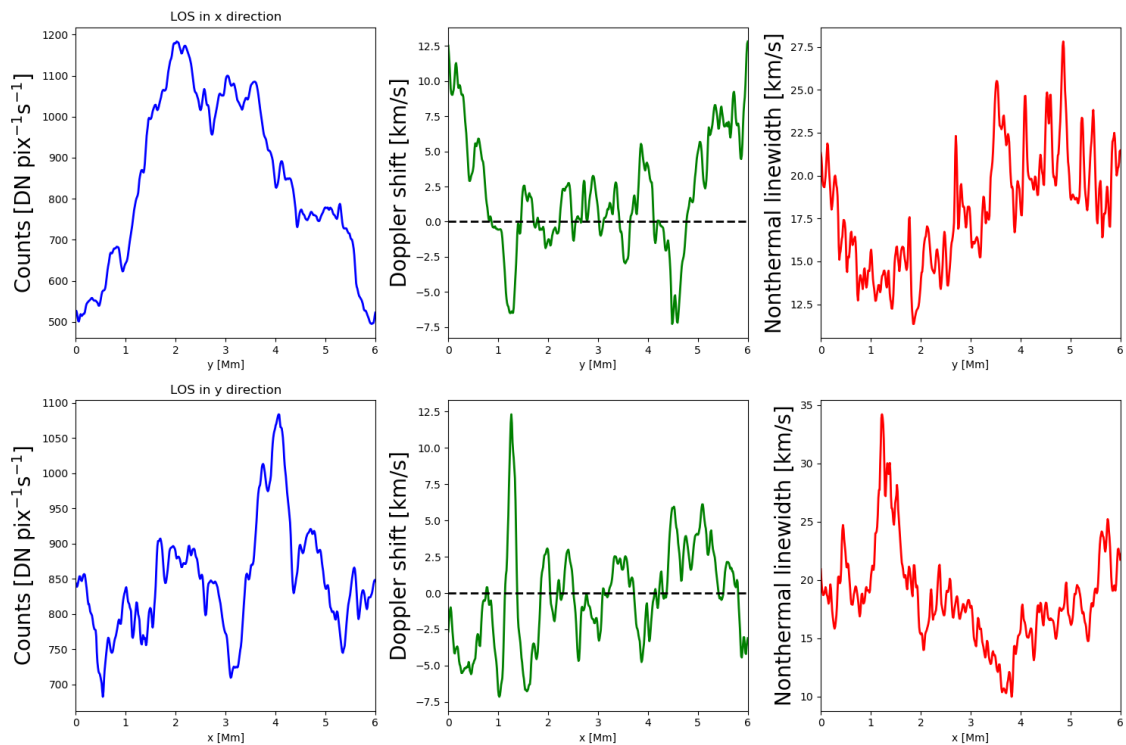


Figure 5.7: Cross-sectional cut through the loop apex for the high resolution run. Top row: The LOS lies in the x-direction. Bottom row: The LOS lies in the y-direction. From left to right: Intensity for the Fe XV emission, Doppler shift and nonthermal broadening. The dashed black line in the middle panel marks the location of zero Doppler shift. See Sect. 5.3.1

than for the view perpendicular to the guide field. The distribution of the nonthermal broadening is shown in Fig. 5.9 and Fig. 5.10 for the Fe XV and the Fe XII emission, respectively. The average nonthermal line broadening at the footpoints in the Fe XV line is 9.4, 11.7 and 11.5 km s⁻¹ and the peaks are at 6.7, 8.5 and 7.8 km s⁻¹ in the Fe XV emission. The histogram peak values for the Fe XII emission are at 6, 8.1 and 9.2 km s⁻¹ and the average values are 7.8, 11.1 and 12 km s⁻¹, respectively.

While there is a significant difference between the low and the medium resolution run, the difference between the medium and high resolution run is very small. For the Fe XV emission, peak and average values for the high resolution run are even slightly smaller than for the medium resolution run. Similar to the LOS perpendicular to the guide field, the correlation between nonthermal broadening and Doppler shift is weak for both the Fe XV and the Fe XII line. The correlation between nonthermal velocities and intensity is negligible, but not negative as in the perpendicular case.

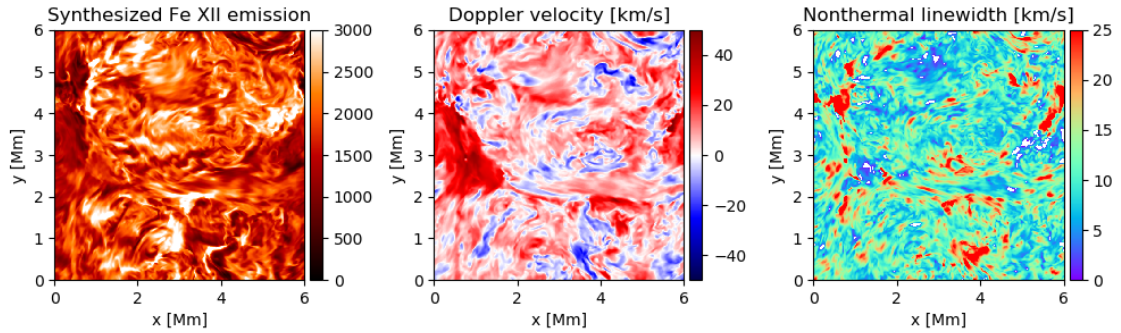


Figure 5.8: From left to right: Intensity of the emission in the Fe XII line integrated along the line of sight over the range $s \in [0, 10]$ Mm, Doppler shift and nonthermal line broadening seen parallel to the guide field for the left loop footpoint and the high resolution run. The integrated emission has the units $[\text{DN pix}_{\text{MUR}}^{-1} \text{s}^{-1}]$. For a discussion, see Sect. 5.3.2.

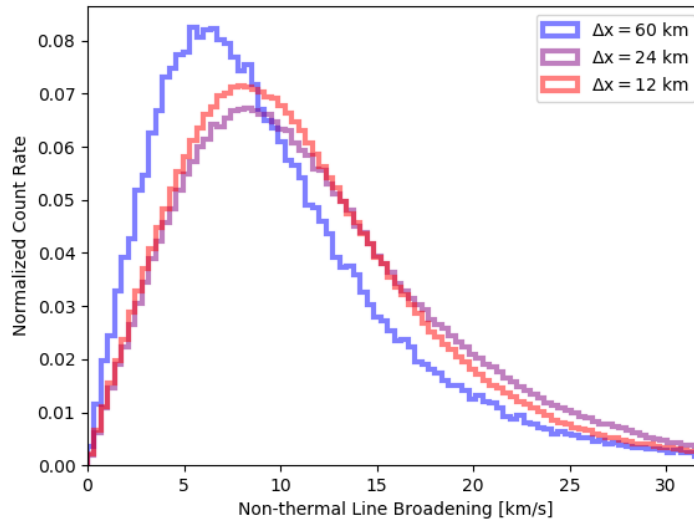


Figure 5.9: Time-averaged normalized histograms for the nonthermal line width in the Fe XV line emission parallel to the guide field. We show the histograms for three different grid resolutions of 60 km, 24 km and 12 km, respectively. See Sect. 5.3.2.

5.3.3 Nonthermal broadening and heating

The nonthermal line width varies in time. We constructed a timeseries of the loop-averaged nonthermal broadening for the $\Delta x = 60$ km resolution run. The time evolution of the coronal averages of various quantities is shown in Fig. 5.11. The coronal part of the simulation domain is here defined as the region with a density below $10^{-12} \text{ g cm}^{-3}$. The

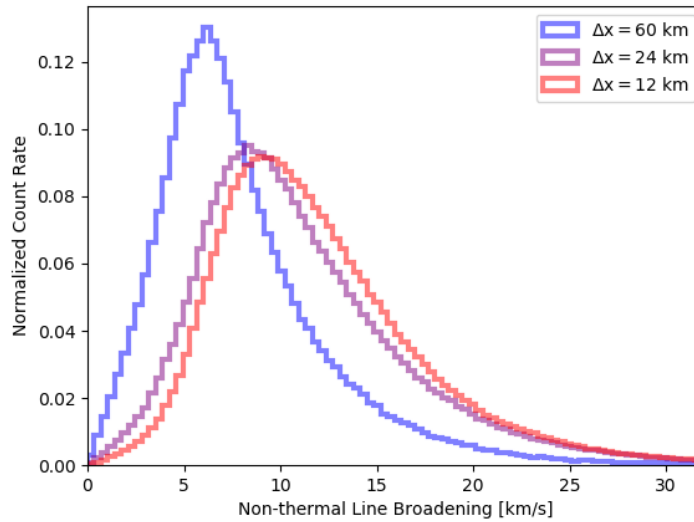


Figure 5.10: Time-averaged normalized histogram for the nonthermal line width in the Fe XII line emission parallel to the guide field. We show the histograms for three different grid resolutions of 60 km, 24 km and 12 km, respectively. See Sect. 5.3.2.

temperature shows several peaks, with the strongest event at 17.9 min, and subsequent cooling. The emission increases in response to the increased temperature. The peaks in the emission show a delay of several minutes with respect to the temperature peaks.

All the temperature maxima are preceded by peaks in the heating rate. The second panel shows the time evolution of the heating rate. The strongest peak is located at time 17.9 min. The blue curve is the magnetic energy density arising from the transverse field components alone. For the stratified loop setup with an initially uniform, axial magnetic field that we use in our simulation, the potential magnetic field is close to axial in the coronal part of the loop. Thus the magnetic energy density associated with the transverse field components is an approximation for the available free magnetic energy. The magnetic energy density drops shortly before the first and second strong heating event. The third heating event is associated with an initial increase in magnetic energy density, followed by several smaller dips.

The time development of the line width seen perpendicular to the loop axis follows the time evolution of the heating rate, with the largest line width associated with the strongest peak in the heating rate. Panel (c) of Fig. 5.11 shows the spectral line width averaged over the entire domain as a function of time. The total line width was calculated as the second moment of the integrated line profile. The increase in line width can be due to both line broadening in response to increased velocities in the loop or caused by higher local thermal line broadening due to elevated temperatures. To check whether the peaks in the line broadening arise from increased velocity fluctuations in the loop or from increased plasma temperature, we compute the line profiles for the timeseries with the Doppler shift set to zero. The red curve in panel (c) of Fig. 5.11 shows the line width that arises from thermal broadening alone. While the evolution of the thermal line width roughly follows

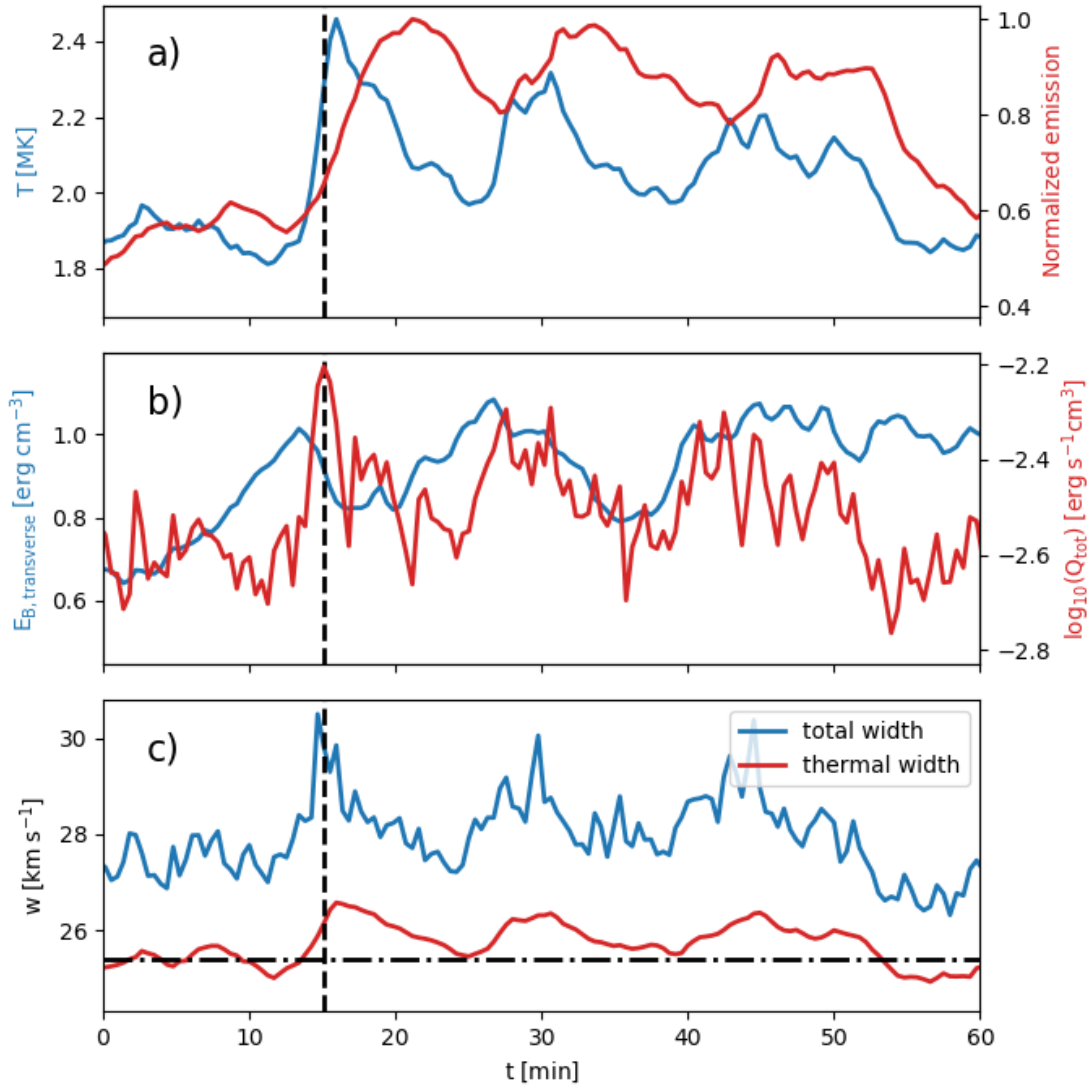


Figure 5.11: Time evolution of the coronal loop for the low resolution run. Panel (a) shows the temperature (blue) and normalized emission in the Fe XV line (red) averaged over the coronal part of the loop. Panel (b) shows the sum of viscous and resistive heating rate (red) and the magnetic energy density computed from the transverse components of the magnetic field (blue), and panel (c) shows the total spectral line width measured for an LOS along the y-axis and a field of view corresponding to the whole coronal part of the simulation box. The solid red line shows the evolution of the thermal line width integrated over the simulation box. The vertical dashed line marks the location of the strongest heating event in the time series. The dash-dotted horizontal line denotes the thermal line width of 25.4 km s^{-1} at the peak formation temperature of Fe XV of 2.2 MK. See Sect. 5.3.3.

the evolution of the temperature, the thermal width depends on the square root of the temperature. Even for a steep increase in temperature, the thermal width increases only by a

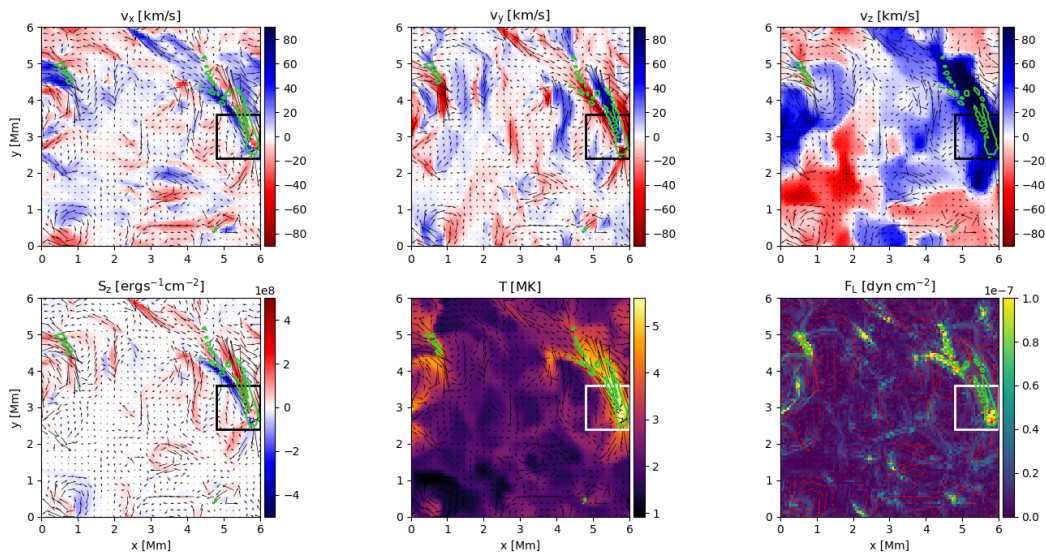


Figure 5.12: Cross-section through the strongest heating event in the timeseries shown in Fig. 5.11 at time 17.9 min and a height of 11.26 Mm. Top row from left to right: Transverse velocity components v_x , v_y and field-aligned velocity v_z . Bottom row from left to right: Axial component of the Poynting flux, temperature, and transverse component of the Lorentz force. The green contour outlines the regions with a total heating rate above a threshold value of $0.1 \text{ erg s}^{-1}\text{cm}^{-3}$. The black arrows illustrate direction and magnitude of the velocity field. The white and black rectangles mark the location of the $1.2 \times 1.2 \times 1.2$ Mm box containing the strongest heating event. For a discussion see Sect. 5.3.3.

maximum of 1.5 km s^{-1} above the thermal width at line formation temperature. We find that the effect from the small-scale motions dominates and the increase in nonthermal line broadening still persists after subtracting the thermal line width. The line width always exceeds the thermal width during the simulation time.

To study the relation between nonthermal broadening, the velocity field and heating events in more detail, we have a closer look at the origin of the strongest peak in the heating rate. We divide the simulation domain into $1.2 \times 1.2 \times 1.2$ Mm subdomains and determine the cube containing the strongest heating event. The region containing the strongest heating is centered on the point $x,y,z=[5.4,3,11.26]$ Mm. A cross-section through the strongest heating event is shown in Fig. 5.12. The heating occurs at the location of a strong shear flow. The green contour outlines the location of the heating event, with a threshold of $Q_{\text{tot}} = 0.1 \text{ erg s}^{-1}\text{cm}^{-3}$. Axial Poynting flux, viscous and resistive heating rate are increased. In response to the heating, temperatures exceeding five MK are achieved. The heating event is located over a strong gradient in the x- and y- components of the velocity. The event occurs at the location of several misaligned magnetic field strands as illustrated in Fig. 5.15. Intensity, Doppler shift and nonthermal line width at the time of the strongest heating event in the low resolution run are shown in Fig. 5.16 and Fig. 5.17. A strong upward flow is present in the parallel component of the velocity at the location of the heating event. The horizontal component of the Lorentz force is increased at the heating site, leading to the acceleration of flows. This structure is similar to the one visible in the

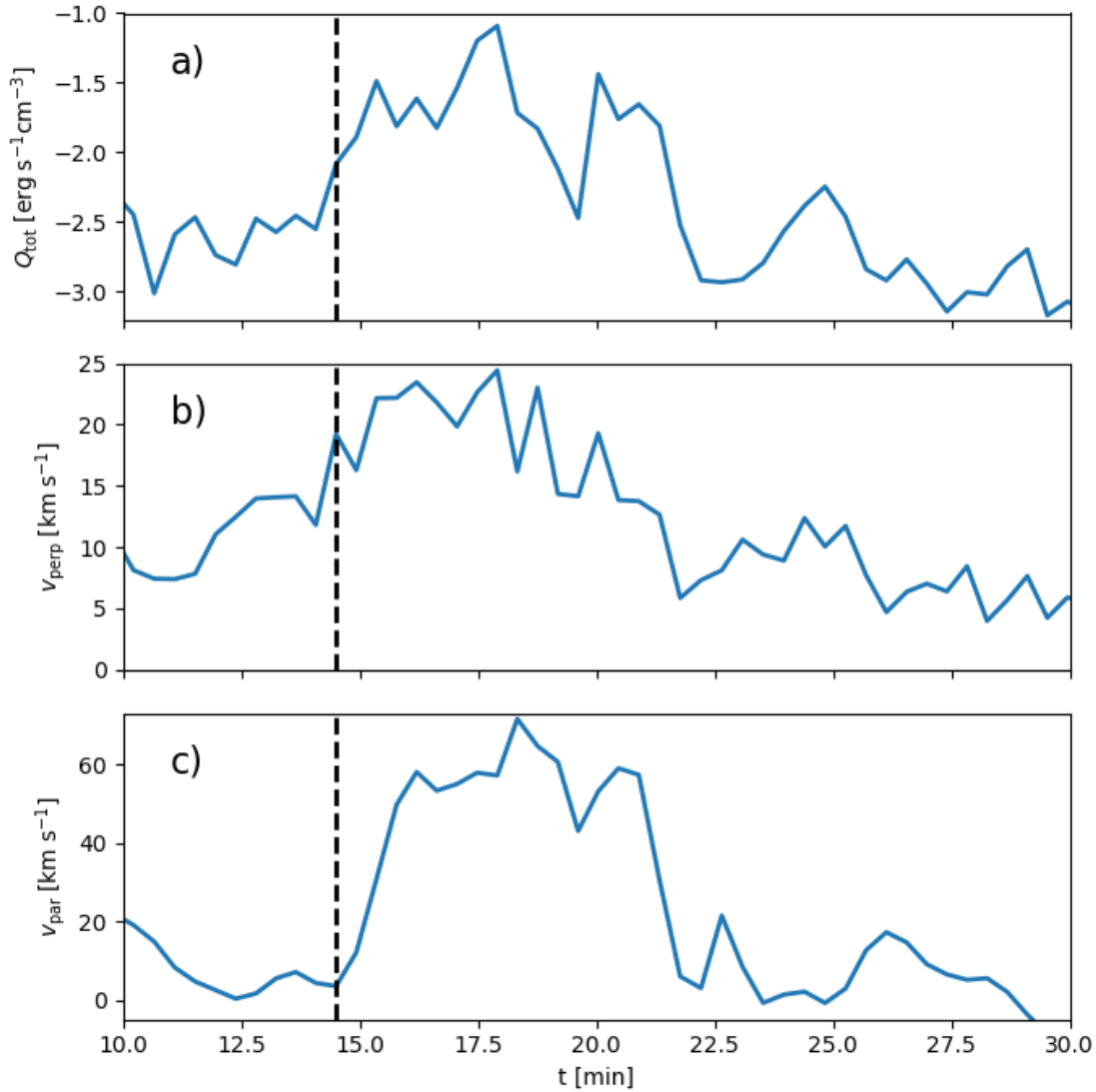


Figure 5.13: Time evolution of the total heating rate (a) and perpendicular (b) and parallel velocity components averaged over a $1.2 \times 1.2 \times 1.2$ Mm box centered on the strongest heating event at 17.9 min. To guide the eye, the dashed black line marks roughly the midpoint between the heating baseline and the first peak in the heating rate. See Sect. 5.3.3.

high resolution simulation at the loop apex. Due to the lower numerical diffusivity in the high resolution run, the current sheet is narrower.

To investigate whether the increase of the different velocity components at the heating site are a cause of or a response to the heating event in Fig. 5.13, we plot the time evolution of the total heating rate, the perpendicular and the parallel velocity in the previously determined region of size 1.2×1.2 Mm for a time range of 20 minutes around the strongest heating event in the time series for the 60 km run. The black dashed line marks a position roughly halfway between the baseline heating and the first local peak associated with

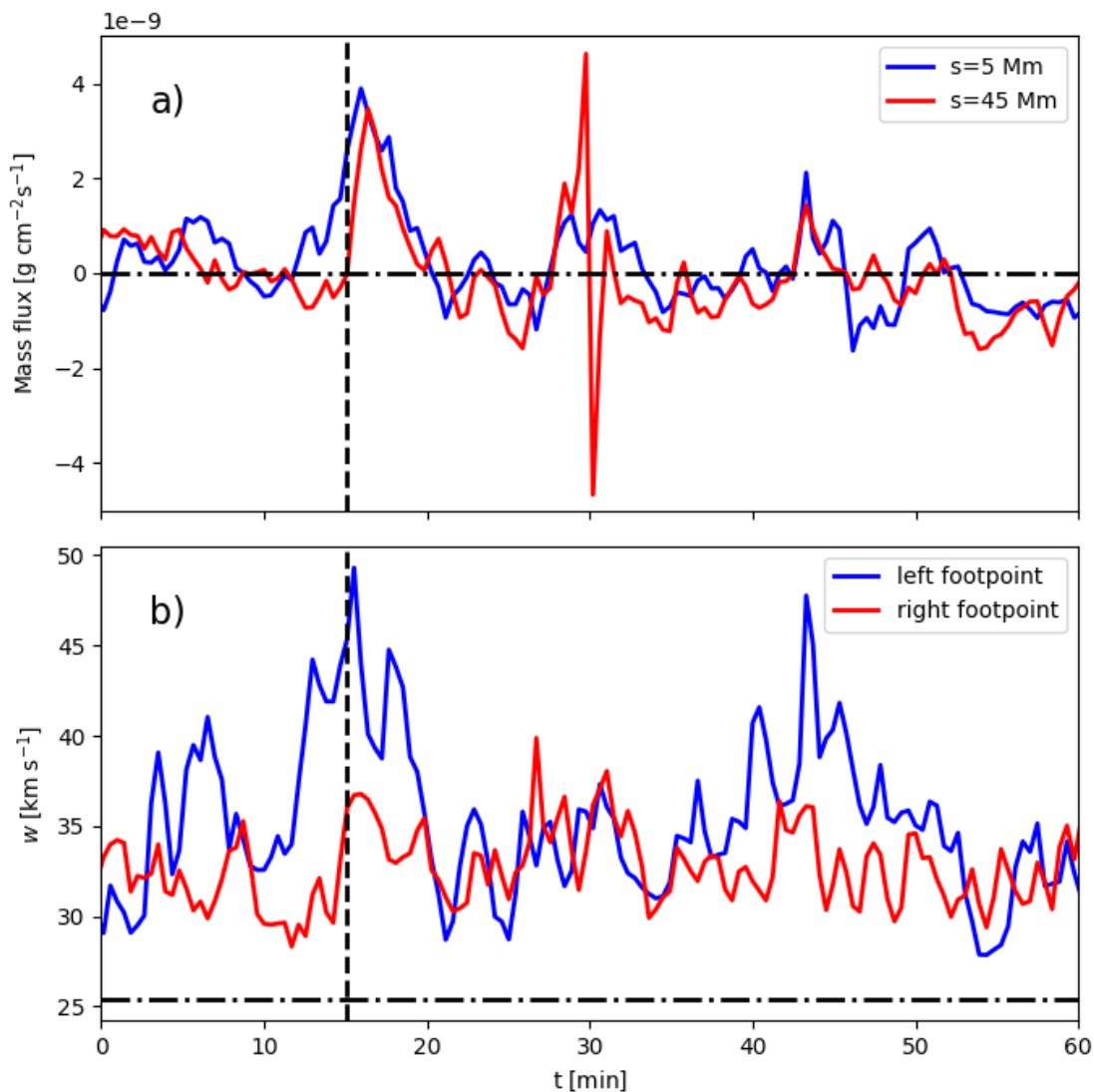


Figure 5.14: Time evolution of mass flux through a cross-section at height 5 Mm above each loop footpoint (panel (a)) and spectral linewidth seen parallel to the guide field for the emission in the Fe XV line integrated over the loop cross-section for each footpoint. The vertical dashed line marks the location of the strongest heating event, while the dash-dotted horizontal line denotes the thermal line width of 25.4 km at the peak formation temperature of Fe XV of 2.2 MK. See Sect. 5.3.3.

the heating event. The velocity perpendicular to the guide field rises prior to the step increase in heating rate, while the rise in the velocity component parallel to the guide field occurs with a delay of about one minute. While the transverse velocity reaches peak values of about 25 km s^{-1} , the parallel flow is much stronger with speeds of over 60 km s^{-1} . Since the transverse velocity starts to increase shortly before the heating rate and the axial velocity shortly after the onset of the heating event, it can be assumed that the heating is due to the shear flow shown in Fig. 5.12 and the increase in the axial component is a

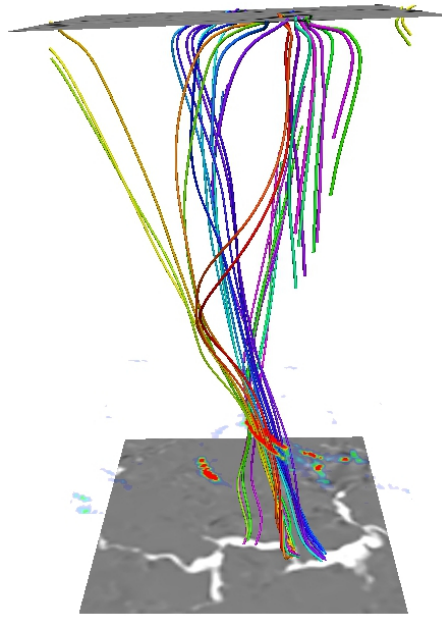


Figure 5.15: Magnetic field lines connected to the strongest heating event at time 17.9 min for the low resolution run. The shading on the plane at 11.26 Mm shows the viscous heating rate. The axial direction has been compressed by a factor of five in the axial direction for better visibility. The visualization was made with VAPOR. The domain is assumed to be periodic in the horizontal directions.

reaction to the heating event.

The presence of the strong upflow indicates that there should also be an increase in the line width at the loop footpoint closest to the heating event for the LOS parallel to the guide magnetic field. The time evolution of the nonthermal broadening parallel to the guide field integrated over the entire loop cross-section and the mass flow through a slice located in the low corona at 5 Mm above the photosphere is shown in Fig. 5.14. For both footpoints, the heating event is followed by an increase in the mass flow with a delay of about one minute. The heating event is also accompanied by a strong peak in the nonthermal line broadening for the footpoint closest to the heating event, while the other footpoint does not show a clear peak. For maps for the integrated intensity, Doppler shift and nonthermal line broadening perpendicular and parallel to the guide field at the time of the strongest heating event see Fig. 5.16 and Fig. 5.10.

There is a weak to moderate correlation between the nonthermal line width and the LOS-integrated total heating rate for the emission perpendicular to the guide field. Since the viscous heating dominates over the resistive heating in the coronal part, the total heating rate follows the behavior of the viscous heating. A 2D histogram for the relation between nonthermal line broadening and LOS-averaged heating rate is shown in Fig. 5.18. For the snapshot shown in Fig. 5.4, Spearman's rank coefficient is 0.43 for an LOS along the x-direction and 0.42 for an LOS along the y-direction. The average over all snapshots and LOS is 0.37. A similar moderate correlation exists between the nonther-

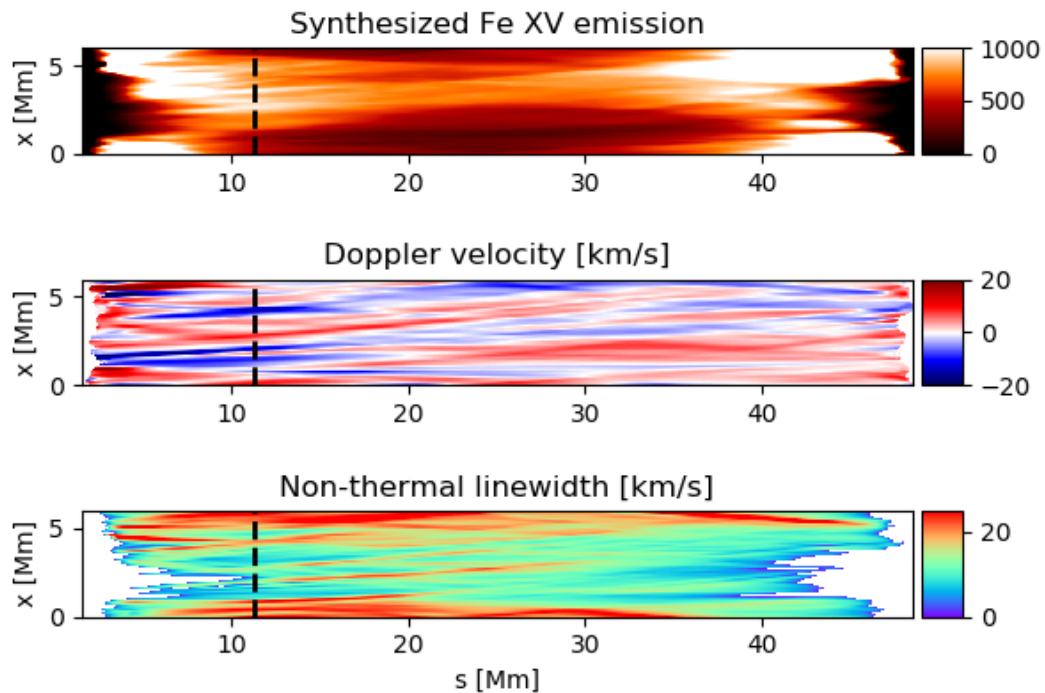


Figure 5.16: From top to bottom: Intensity of the emission in the Fe XV line, Doppler shift, non-thermal line broadening seen perpendicular to the guide field for the low resolution run with a resolution of $\Delta x = 60$ km. Line-of-sight integration was performed along the y-direction. The black dashed line shows the location of the cut shown in Fig. 5.12. The integrated emission has the units $[\text{DN pix}_{\text{MUR}}^{-1} \text{s}^{-1}]$.

mal line width and the unsigned Poynting flux. For the snapshot under consideration, the Spearman's rank coefficient is slightly higher with 0.53 for an LOS in the x-direction and 0.69 for an LOS in the y-direction for Fe XV and coefficients of 0.49 and 0.63 for Fe XII. The average Spearman's rank coefficient for all snapshots under consideration is 0.48 for the Fe XV emission.

To check if the correlation between the nonthermal line width and the heating rate is not solely due to an increased thermal width in response to the heating, we isolate the effect of velocity fluctuations on the line width. To this end, we calculate the line broadening for the same snapshot with a fixed thermal line width of 25.4 km s^{-1} corresponding to the formation temperature, which is then subtracted, leaving only the contribution from velocity fluctuations. The correlation still holds with Spearman's rank coefficients of 0.44 and 0.38.

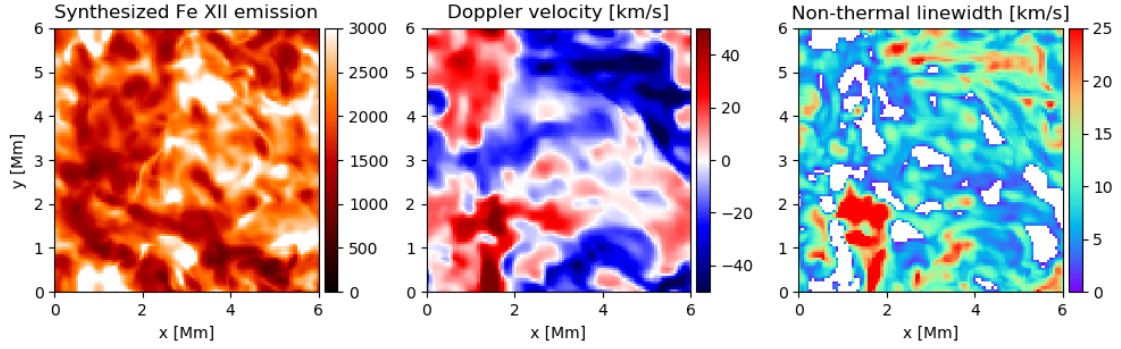


Figure 5.17: From left to right: Intensity of the emission in the Fe XII line integrated along the line of sight over the range $s \in [0, 10]$ Mm, Doppler shift and nonthermal line broadening seen parallel to the guide field for the left loop footpoint of the low resolution run with a resolution of $\Delta x = 60$ km. The integrated emission has the units $[\text{DN pix}_{\text{MUR}}^{-1} \text{s}^{-1}]$.

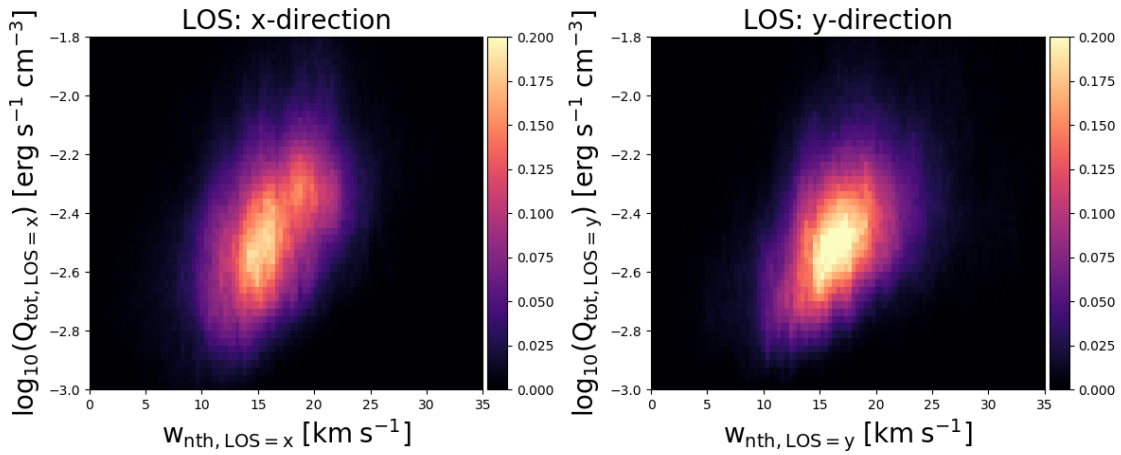


Figure 5.18: 2D histograms relating the LOS-averaged total heating rate to the nonthermal line broadening for the snapshot shown in Fig. 5.4. The nonthermal broadening was calculated for emission in the Fe XV line. Shown here is the histogram for an LOS along the x-direction (left panel) and y-direction (right panel). The histogram was computed for the coronal part of the domain between 3 and 47 Mm. See Sect. 5.3.3.

5.3.4 Line profiles

Line profiles in observations often show a non-Gaussian shape with enhanced power in the line wings.

Pontin et al. (2020) found that some of the line profiles have enhanced wings and cannot be properly fitted by a Gaussian function. The enhanced wings stem from the underlying velocity distribution. An example for a line profile averaged over a region of

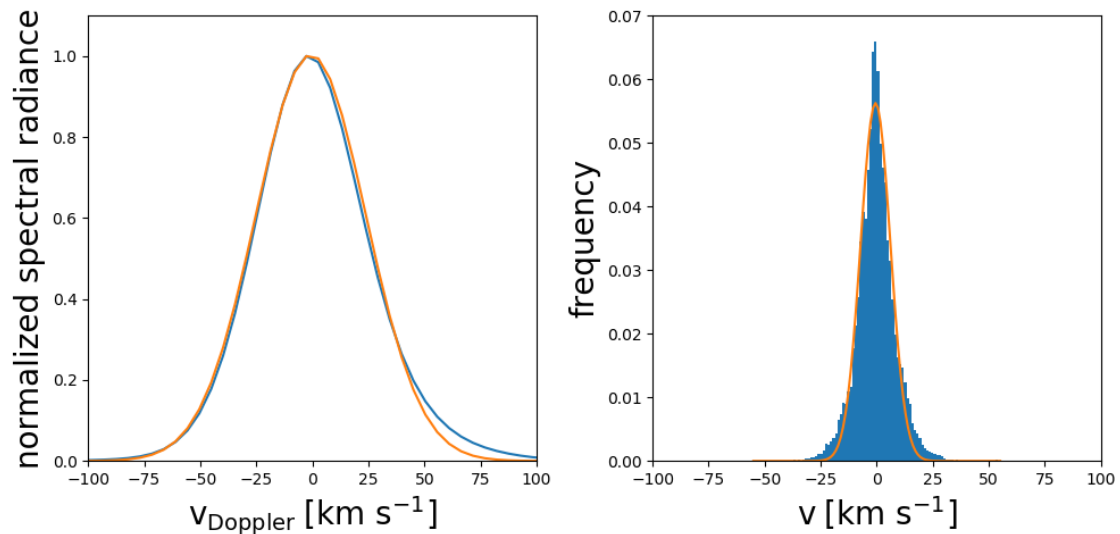


Figure 5.19: Synthesized line profile and velocity distribution for a field of view of 0.5×0.5 Mm at location highlighted by the black rectangle in Fig. 5.4. Left panel: Line profile of Fe XV with wavelength in Doppler units. The orange line shows a Gaussian fit to the profile. Right panel: Histogram of LOS-velocity in the field of view. The histogram has been normalized so that the area under the curve is unity. The orange line shows a single Gaussian fit to the distribution. See Sect. 5.3.4.

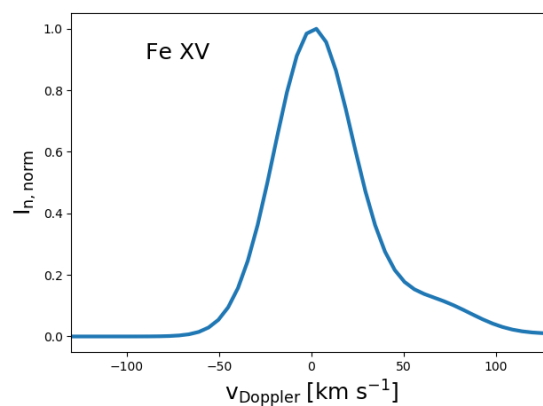


Figure 5.20: Example for an asymmetric line profile seen in Fe XV for an LOS along the y -direction at time 22.21 min for a single grid point. The LOS is shown in Fig. 5.1 as a vertical black line. The normalized spectral radiance is shown as a function of Doppler velocity. See Sect. 5.3.4.

large line-broadening marked by the black rectangle in Fig. 5.4 is shown in Fig. 5.19. While the velocity distribution shows enhancements in the wings, the resulting line profile can be well fitted by a Gaussian, although the profile does show an excess in the red wing. The velocity distribution shown in the right panel shows a slight enhancement in

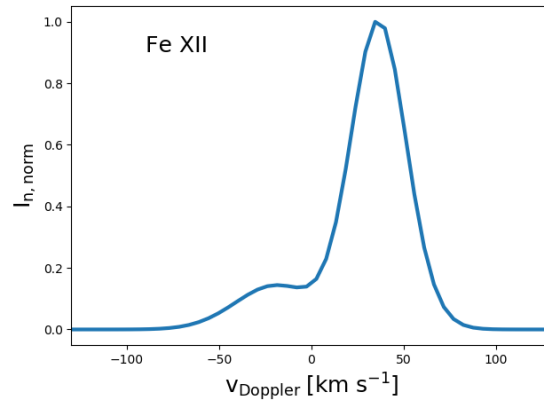


Figure 5.21: Example for a line profile with excess emission in the line wings seen in Fe XII for an LOS along the guide field for the high resolution run at time 5.2 min for a single grid point. The normalized spectral radiance is shown as a function of Doppler velocity. See Sect. 5.3.4.

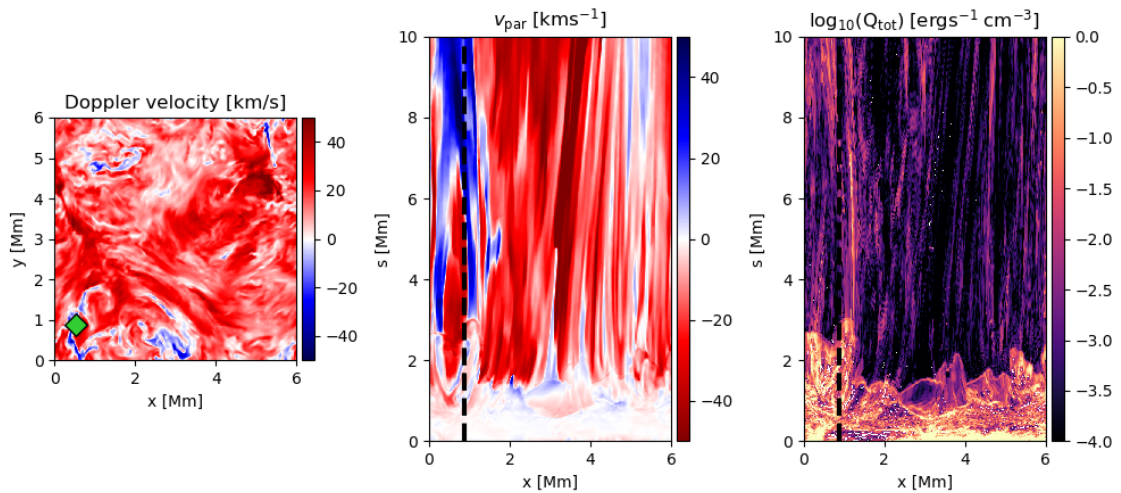


Figure 5.22: Left panel: Doppler velocity at the left loop footpoint at time 5.2 min for the high resolution run. The green diamond marks the location of the line profile shown in Fig. 5.21. Middle panel: Velocity parallel to the guide field on a cut along the y -axis through the location marked by the green diamond. The line of sight is marked by the dashed black line. Right panel: Logarithmic total heating rate on a cut along the y -axis through the location marked by the green diamond. The line of sight is marked by the dashed black line.

both wings. The wing excess of the line profile is just 2.3 percent.

When computing the resulting profile over a field of view of 0.5×0.5 Mm, the contributions from the different grid points are weighted by the intensity at each gridpoint. Fig.

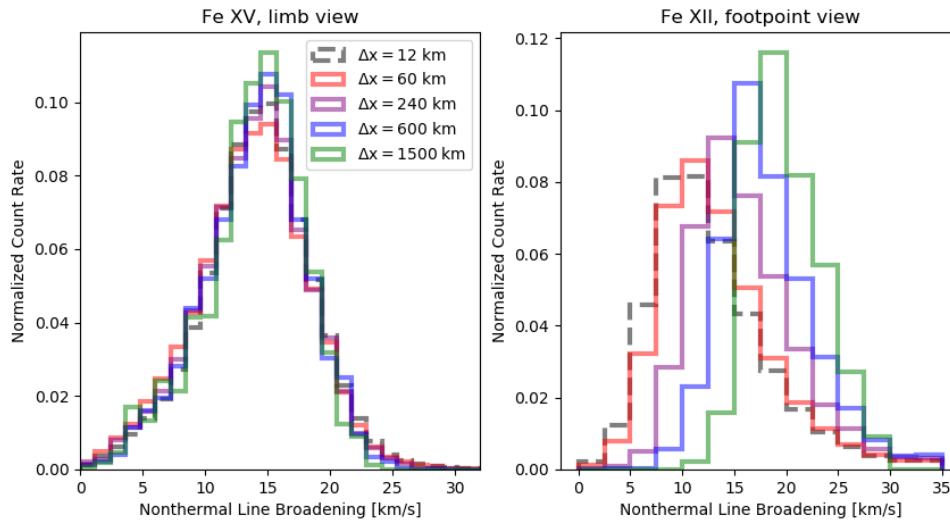


Figure 5.23: Distribution of nonthermal line widths for different binning factors and line of sights. Left panel: Effective line widths for Fe XV and an LOS perpendicular to the guide field in the x-direction. The behavior for the y-direction is similar. We chose the Fe XV line for the perpendicular view since a large part of the plasma in the loop is at temperatures in the range of 2-3 MK. Right panel: Effective line width for Fe XII and an LOS parallel to the guide field for $s \in [0,10]$ Mm. For the footpoints we have used the Fe XII line to account for the cooler plasma there. A lower number of bins is used for the footpoints since the loop cross-section is covered by a smaller number of pixels than the side view. See Sect. 5.3.5.

5.2 shows that the plasma at the location of the heating event contained in the field of view (FOV) is very hot, it is not the brightest region since the temperature lies above the line formation temperature of Fe XV. The line profile is thus dominated by emission from cooler regions with lower velocities.

Most line profiles have a roughly Gaussian shape, but we also find asymmetric profiles with excess emission in the wings. An example profile for an asymmetric line profile seen perpendicular to the axial direction with a broad minor component is shown in Fig. 5.20. This profile arises from a line of sight crossing a strong heating event with outflows close to 100 km s^{-1} . The line of sight is marked by the dashed black line in Fig. 5.2. An example profile for an asymmetric profile seen along a line of sight parallel to the magnetic guide field is shown in Fig. 5.21. In addition to the redshifted major component, there is a blueshifted minor component corresponding to an upflow into the loop associated with a region of increased heating rate. The Doppler shift, the axial component of the velocity and the heating rate on axial cuts through the location of the upflow are shown in Fig. 5.22.

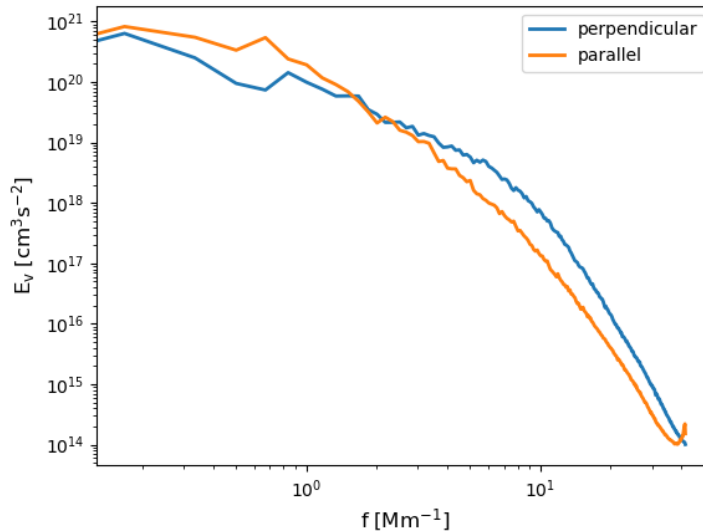


Figure 5.24: Velocity power spectra of the velocity components perpendicular and parallel to the magnetic guide field averaged over a slab with 1 Mm thickness centered on the loop apex for the high resolution run at 22.21 min. For a discussion see Sect. 5.3.5.

5.3.5 Dependence on resolution

While in Sect. 5.3.1 and 5.3.2 we find higher values for the nonthermal line broadening for an increased grid resolution, observed nonthermal line widths have been found to be independent of the resolution of the instrument (De Pontieu et al. 2015). In order to investigate the dependence on the spatial scales of observations, we apply different levels of spatial binning to the synthesized spectra before calculating the profile moments. For this study, the simulation run with the highest resolution of $\Delta x = 12$ km was employed. The rebinning was performed by summing up the line profiles over a square with a side length of different multiples of the grid spacing. We show a time-averaged histogram for the nonthermal line widths for different effective resolutions ranging from the original resolution of $\Delta x = 12$ km to $\Delta x = 1500$ km in Fig. 5.23.

The non-thermal line width does not depend strongly on resolution for a limb view of the loop. For the line of sight parallel to the magnetic field at the loop footpoints, however, we find that the line broadening increases for a larger rebinning factor. For the nonthermal line broadening perpendicular to the guide field, the position of the peak of the distribution lies at roughly 15 km s^{-1} , independently of the chosen field of view. For the LOS parallel to the guide field, the peak is shifted towards larger line widths, from about 11.2 km s^{-1} for the original resolution of 12 km and at roughly 18.5 km s^{-1} for the lowest effective resolution of 1500 km. The histograms for the footpoint view have to be treated with caution due the limited width of the box of just six by six megameters. For the lowest resolution regarded here, the loop cross section is only covered by 16 pixels for one timestep.

A Fourier transform of the different velocity components in a plane at the loop apex as depicted in Fig. 5.24 confirms that the transverse components have more power at small

scales than the longitudinal component.

We checked the dependence of the nonthermal line width on exposure time for a five minute time sequence of the low resolution run with a cadence of 5 s. We used the Fe XV emission line and a line of sight perpendicular to the guide field. We used four different exposure times, 300 s, 150 s, 125 s and 15 s. We did not find a significant dependence of the nonthermal line broadening on the exposure time.

5.4 Discussion

5.4.1 Perpendicular and parallel broadening

For the line of sight perpendicular to the guide field, in the medium and high resolution run we roughly reproduce the peak of the distribution of non-thermal line widths at 15 km s^{-1} from Testa et al. (2016) seen for the Fe XII 1349.4 Å line for both the emission in Fe XV and Fe XII, but not the tail they see at large nonthermal velocities. Instead, our distribution for the perpendicular line of sight is approximately symmetrical. For this reason, we find similar values for the peak of the distribution but lower average values for the line broadening than in their simulation. The non-thermal line widths for the line of sight along the guide field peak at lower velocities.

In reality, the coronal loop would be seen from a variety of angles, not just perpendicular or parallel to the guide field. To isolate the footpoint region, we have integrated the spectra for the footpoints up to a distance along the loop of $s=10 \text{ Mm}$. For the perpendicular line of sight, we integrate over a range of just six Mm. On the Sun, a loop would never be observed in isolation, more plasma would be present along the LOS below and above the loop and contribute to the broadening. Another possible explanation for our synthesized nonthermal line broadening values being at the low end of observed values is that we have a setup with a strong uniform guide field. Effects such as large-scale flux emergence or interaction of several loop systems are not taken into account. These events might lead to a stronger acceleration of plasma. In our simulation, the nonthermal broadening stems from small-scale velocity fluctuations along the LOS.

While some observations report larger nonthermal line widths for on-disk observations (Testa et al. 2016), other studies find higher nonthermal velocities at the limb (Erdelyi et al. 1998, Rao et al. 2022). The nonthermal broadening perpendicular to the magnetic field has been interpreted as resulting from small-scale twist (De Pontieu et al. 2015, Rao et al. 2022). We find for the high resolution run that there is a moderate correlation between the nonthermal line broadening for Fe XV and the LOS-averaged unsigned axial vorticity. Despite being lower than in observations, the nonthermal velocities seen along the guide field at the footpoints are larger than those seen in previous stretched loop models. Pontin et al. (2020) study the turbulence induced by the relaxation of an entangled magnetic field braid. Since the magnetic Reynolds numbers that can be reached in numerical simulations are way below the values estimated for the solar atmosphere, it is expected that the magnetic field lines in simulations do not reach the same degree of tangling that they would in the corona. Starting with an already braided magnetic field as in Pontin et al. (2020) allows for larger misalignment angles before the onset of reconnection than can be produced in simulations. In their study, reconnection leads to turbulent relaxation

of the magnetic field, driving flows perpendicular to the guide field. The perpendicular velocity fluctuations are significantly larger than the fluctuations aligned with the field. The model of Pontin et al. (2020) does not include a chromosphere that could serve as mass reservoir for upflows induced by coronal heating. Instead, closed boundaries are employed at the loop footpoints and the magnetic field is line-tied. The nonthermal line widths in the parallel direction are thus significantly smaller than in our model. Coupling a stretched loop simulation to a realistic lower atmosphere, as we do here, allows for chromospheric evaporation in response to heating events and thus leads to larger field-aligned velocities. Fig. 5.13 shows that the vertical velocity starts to increase with a delay after the rise in the heating rate. A similar behavior is seen for the mass flux shown in Fig. 5.14. The mass flux in the low corona reaches a peak approximately one minute after the occurrence of the strongest heating event. This points to chromospheric evaporation in response to heating events as a cause for strong field-aligned flows.

The loop-averaged line widths we find for a line of sight parallel to the guide field reach larger values than seen in the perpendicular direction. This is in contrast to the statistical distributions, which yield smaller average nonthermal line widths parallel to the loop axis. This can be explained by the different relation between intensity and nonthermal line width for the different lines of sight. The line formation temperature for Fe XV is roughly 2 MK, but the hottest plasma in the regions with the strongest heating and highest velocities reaches temperatures of more than four MK. Thus, the hottest regions with the largest line broadening are not the brightest regions. When computing the loop-averaged line broadening by summing up the line profiles and extracting the nonthermal line widths, the cooler regions of the loop are weighted more strongly. We find slightly larger values of the nonthermal broadening for the Fe XII emission, which is due to the smaller thermal broadening subtracted from the line width.

With increasing rebinning factor, the tail at large nonthermal velocities disappears, but the peak moves to higher values (Testa et al. 2016). For the LOS perpendicular to the magnetic field, we find a more symmetrical distribution.

5.4.2 Line profiles

Line profiles with excess emission in the wings (Peter 2010). In Pontin et al. (2020) enhanced wings in the velocity distribution are interpreted as a sign for turbulence. While we find complex motions on various scales in the loop interior, the motions are less violent than in the case of Pontin et al. (2020) where the untwisting braid leads to large velocities. Instead, the magnetic field in our simulation is continuously driven by magnetoconvection. We therefore do not have large-scale unbraiding events driving strong flows. The small wing excess is similar to the braid relaxation simulation at later times in the simulation when the initial turbulent state has already partially decayed. The line profile is also determined by the interplay of velocities in the FOV and emissivities. Bright regions with small velocities could dominate the line profile. Fe XV is emitted by plasma around 2 MK. The hottest plasma in our simulation, however, is a factor two to three larger than that and is not the brightest in Fe XV.

5.4.3 Heating

The averaged heating rate is characterized by a background heating rate with superposed strong heating events. The increase in density in response to the elevated temperature is delayed because material needs time to reach the corona through chromospheric evaporation. The time evolution of the nonthermal velocities shows similarities and differences to the evolution of the braid in Pontin et al. (2020). The nonthermal line broadening is often used as a proxy for the heating of the corona. In the timeseries, the nonthermal velocities seen perpendicular to the guide field and partially the nonthermal velocities parallel to the guide field follow the time evolution of the heating rate. Since we do not start with a pre-braided magnetic field, reconnection in our simulation usually happens between almost parallel field lines.

The magnetic energy in the study by Pontin et al. (2020) drops continuously as the braid relaxes. Likewise, we find that peaks in the line width are often preceded by a drop in the magnetic energy associated with the transverse field components. This is most pronounced for the first two large heating events at 17.9 min and 30 min. Unwinding and reconnection of the magnetic field could thus cause the first two heating events. The excess magnetic energy, however, is replenished by shuffling of the magnetic field due to magnetoconvection. With the untangling of the braid, the turbulence in the model by Pontin et al. (2020) eventually decays and the line width of the synthesized profiles approaches the thermal line width. In contrast to Pontin et al. (2020), in our simulation the line width is always significantly above the thermal line width, which is because of the continuous driving in the photosphere.

Pontin et al. (2020) also find oscillatory behavior in the time evolution of the nonthermal line width corresponding to Alfvén waves bouncing back and forth through the loop. In our simulation, the time evolution is dominated by several large spikes corresponding to strong heating events. As in Pontin et al. (2020), the peaks in emission appear with a delay of several minutes after the heating peaks, the observed line widths would therefore lie below the maximum widths occurring in the time evolution.

At the time of largest broadening in the low resolution timeseries, we find several reconnection events heating the plasma and leading to outflows. We can directly attribute the largest peak in heating and nonthermal line width to a reconnection event accelerating plasma which is shown in Fig. 5.12. The heating event occurs at the location of shearing of several misaligned bundles of magnetic field lines (see Fig. 5.15). In addition to an enhanced transverse velocity, a strong upflow is present. The strongest heating, however, occurs in the interior of the upflow and not at this edges, therefore we conclude that the heating stems mostly from the shear in the transverse velocity components and that the field parallel component is mainly a consequence of the heating event and not the cause. The delay between the steep gradient in the heating rate and the rise in the field-aligned velocity indicates that the heat deposited at the reconnection site drives chromospheric evaporation that leads to increased line broadening parallel to the magnetic field.

A similar event occurs in the high resolution simulation at $x,y=[1.2,4]$ Mm, also leading to an increase in line broadening as can be seen from the asymmetric profile shown in Fig. 5.20.

For the examined heating event in the low resolution time series, we find that a rise in the transverse velocity precedes the sharp increase in the heating rate. The increase in

transverse velocity could thus be associated with both an increased Poynting flux that is partially dissipated in the heating event, as well as a response to the heating event due to outflows from the reconnection site.

For the high resolution case, we find a weak to moderate correlation between nonthermal broadening and both Poynting flux and heating rate. Nonthermal line broadening has been interpreted as both an indication for Alfvén waves as well as flows developing in response to nanoflare heating (Patsourakos and Klimchuk 2006). While we find bursty heating events associated with reconnection after the buildup of magnetic energy over timescales of the order of ten minutes, this does not exclude that waves are also present. Fyfe et al. (2021) compare synthesized spectra for simulations driven by different characteristic timescales associated with DC and AC heating, respectively. They find no observable difference between AC and DC runs for the location of the energy release. Both DC and AC heating leads to line broadening, but they find larger line broadening for the DC simulation since the DC driving leads to higher temperatures.

5.4.4 Dependence on resolution

The behavior of the broadening in the perpendicular direction for different effective instrument resolutions is consistent with the invariance to spatial rebinning in De Pontieu et al. (2015). The independence of the line broadening perpendicular to the guide field and the slight dependence for the line broadening parallel to the guide field can be explained by the different sizes of structures in the transverse and field aligned velocity components. As shown in the cut through the loop cross-section in Fig. 5.1, the transverse velocity components have a complex small-scale structure while structures in the field-aligned velocity are larger. A Fourier transform of the unsigned velocity components at the loop apex confirms that the the field-aligned velocity has more power on larger scales above roughly 200 km and falls off faster than the power spectra for the transverse velocity components below this value. On smaller scales, the power spectrum drops faster than the power spectrum of the transverse velocity components.

For an effective resolution of 60 km, the field of view is still smaller than typical structure sizes in the field-aligned velocity. For resolutions below 240 km, it is more likely that one pixel in the synthetic observation covers several structures with different velocities along the LOS. For the LOS perpendicular to the guide field, the LOS-integration over the width of the simulation box of six Mm alone thus leads to broadening due to small-scale velocity components along the LOS even for a field of view comprised of just one grid cell with a side length of 12 km. For the parallel velocity component, structures are elongated along the line of sight and show less fluctuations. Integration over a field of view larger than the grid cells thus does lead to increased broadening. Even with significantly increased resolution, instruments would likely not see a large difference in the nonthermal line broadening due to the LOS-integration. The dependence of the parallel broadening on the FOV is difficult to test since normally the magnetic field would not align perfectly with the line of sight. This effect could possibly be observed in moss regions where the field is mostly vertical.

5.5 Conclusion

We find values for the non-thermal line broadening both perpendicular and parallel to the guide field that are compatible with observations, albeit at the lower end of the observed range. We include proper treatment of the mass transfer between the chromosphere and corona. The treatment of the coupling between the different atmospheric layers is necessary to properly model field-aligned flows. Thus we arrive at more realistic values for the non-thermal line broadening in the field-parallel direction along the loop axis than previous studies in a similar geometry. Including a shallow convection zone also ensures that the non-thermal line broadening is sustained throughout the lifetime of the loop by continuous driving and exceeds the thermal width. The line broadening measured perpendicular and parallel to the loop axis is of similar order of magnitude, but arises from different causes. For an LOS perpendicular to the loop axis the spectral line profiles are broadened due to the formation of small-scale flows perpendicular to the guide field, including outflows from heating events. For an LOS parallel to the guide field, we find the largest values for the nonthermal broadening in response to upflows developing in response to heating events. The nonthermal line broadening follows the time evolution of the heating rate. For a single snapshot in time, there is a weak to moderate correlation between heating rate and nonthermal line broadening. We can directly relate the largest values of nonthermal line broadening to strong heating events and resulting outflows. Consistent with observations, the nonthermal line broadening is independent of effective resolution for the line of sight perpendicular to the guide field. For the line of sight parallel to the guide field, the nonthermal line broadening increases with effective resolution.

6 Discussion and conclusions

In this work we present a self-consistent model of an isolated coronal loop modelled by adapting a box-in-a-star code for a straightened loop simulation. In **chapter 3**, we describe the model and the general evolution of bulk quantities in the coronal loop. In response to the driving, a complex structure of small-scale flows and current sheets develops in the loop cross-section. Despite the absence of compact bright structures that are well distinguished from their environment, line of sight integration of synthesized emission yields strands with widths compatible with observations. This model allows us to follow energy in the form of Poynting flux injected into the upper atmosphere from the solar surface where it is generated up into the corona where it is dissipated. We resolve both the photospheric motions responsible for the energy injection and the loop fine structure. We find little evidence of braiding on large scales, instead the Poynting flux is generated by small-scale motions at the solar surface. Magnetic field lines are twisted and sheared by motions within magnetic concentrations. We identify vortex tubes reaching from the solar surface into the corona as structures associated with energy transport and dissipation.

In **chapter 4**, we use the high resolution run to study these structures and the magnetic coupling to the photosphere in more detail. In agreement with observations and previous simulations, we find an abundance of vortex motions on a wide range of scales in all layers of the solar atmosphere. In agreement with previous findings, small-scale vortices carry a significant part of the Poynting flux in the lower atmosphere. Previous studies usually focus on the chromospheric part of the solar atmosphere. We study the energy input, the magnetic field structure and the relation to coronal emission at the example of a single isolated vortex tube that originates in a vortex within a magnetic concentration at the solar surface and reaches coronal heights. In the chromosphere, the vortex is associated with twisted magnetic field lines contributing to the acceleration of upflows due to an upwards directed Lorentz force. The Poynting flux associated with the vortex reaches coronal heights and is sufficient to heat a strand to coronal temperatures. In addition, we perform statistics on regions with enhanced swirling strength and find that swirls are associated with enhanced Poynting flux and heating rate up into coronal heights, although their contribution to the total Poynting flux and heating rate decreases with increasing height. In the height range from the chromosphere to the low corona, vortices in the velocity field are overdense and thus influence the structure of the atmosphere. While carrying a large Poynting flux, vortices are on average just a few percent brighter than their surroundings in X-ray emission. This can be explained by the timescales involved and the strong density dependence of the optically thin emission. A local heating event will cause the temperature along the field lines it is connected to to increase due to the high thermal conductivity along the magnetic field. A density increase in response to the heating will occur with a delay. Therefore, while we do find increased heating rates in

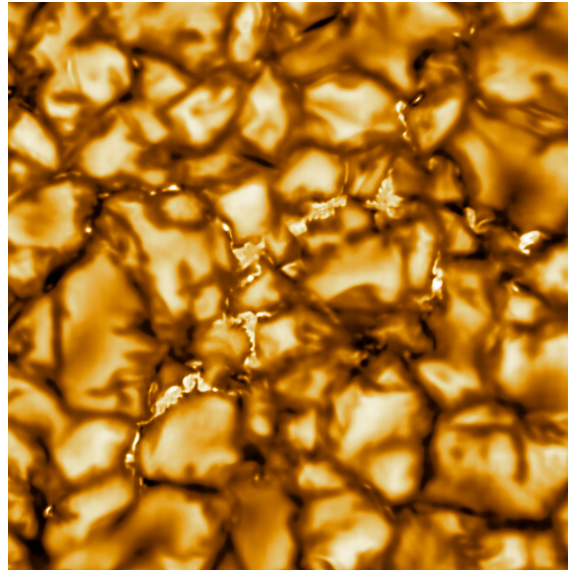


Figure 6.1: Image of the solar photosphere taken by the DKIST telescope at 789 nm. Credit: NSO/AURA/NSF

vortices, there is no one-to-one correspondence of rotating structures to bright strands.

In general, we find that magnetic footpoints contain a superposition of rotation and shear motions in addition to deformation and bulk motion of the footpoints. An isolated vortex launching a Poynting flux into the atmosphere is therefore a special case of complex motions within magnetic concentrations at the footpoints that lead to an energy flux into the atmosphere.

Eventually, we investigate the resulting observational signatures in **chapter 5**. We find that the small-scale motions perpendicular to the magnetic field and field aligned flows lead to nonthermal line broadening with a similar order of magnitude. The small-scale motions perpendicular to the magnetic field give rise to values for the nonthermal line widths at the low end of the range of observed values. For the direction perpendicular to the magnetic field, we also reproduce the independence of the nonthermal line broadening of the resolution of the observing instrument and conclude that in our case this is due to the velocity fluctuations occurring on scales well below the observing capacity of current instruments.

Ongoing missions such as the Solar Orbiter mission and ground-based telescopes such as the Daniel K. Inouye Telescope (DKIST) will provide high resolution observations of photospheric and coronal structures in the next few years. An image of the photosphere taken by DKIST is shown in Fig. 6.1. DKIST can resolve structures in the photosphere with a resolution of 30 km and high cadence. This study has shown that internal coherent motions within magnetic concentrations play an important role for the energy flux into the upper atmosphere. All in all, we built a comprehensive model of a coronal loop that allows to connect observables with energy injection at the footpoints.

7 Outlook

In this work, we have introduced a loop-in-a-box model with a realistic photosphere. This model opens possibilities for further studies, especially for the generation and propagation of waves in a gravitationally stratified, realistic solar atmosphere and the role played by different types of footpoint motions. In its current form, the loop model discussed in this work has several shortcomings and would benefit from further refinement. Steps to increase the realism of the loop model are, for example, the coronal expansion of the loop and improved treatment of the chromosphere. This would lead to a more accurate profile of quantities such as magnetic field strength, pressure, density and heating rate along the coronal loop and would make it possible to compute more realistic synthetic observations.

The magnetic field is currently initialized as a uniform field along the loop axis. An expanding loop would lead to a decrease in magnetic field strength towards the apex. This would likely also cause a decrease in current density and thus of the heating rate, which is almost constant in the coronal part of the loop for the model in its current state. The inclusion of magnetic field expansion could be achieved by a larger domain size combined with pinning of magnetic field lines at the domain boundary at each footpoint. This would allow the field to expand radially into the surrounding atmosphere. An alternate solution is the use of a nonuniform, non-Cartesian coordinate system in the coronal part of the loop.

The loop model spans from the convection zone to the corona, traversing layers of the Sun with different physical processes important in each layer. Connecting the photosphere and the corona, the chromosphere plays a crucial role for the exchange of mass and energy between different atmospheric layers. Due to the low collision rates and densities in the chromosphere, the assumption of local thermodynamic equilibrium (LTE) for the radiative transfer is not justified. Ionized hydrogen and helium have recombination timescales exceeding dynamical timescales, therefore the chromosphere cannot be treated in statistical equilibrium. To accurately model this layer of the solar atmosphere, nonequilibrium and multifluid effects need to be taken into account. An extension of the MURaM code into the chromosphere has been developed by Przybylski et al. (2021).

The relative contribution of different heating mechanisms to the energization of coronal loops is still an open question. Loops of different sizes and temperatures might be heated by different processes. Motions on a wide range of timescales contribute to coronal heating and cannot easily be divided into contributions from different heating mechanisms such as braiding or wave heating (Rempel 2017).

The original general braiding model by Parker has developed into different models. The flux tube tectonics model focuses on the displacement of long-lived flux elements as a whole (Priest et al. 2002), while other models have studied heating by MHD turbulence

or "dynamic braiding" from motions within magnetic concentrations (van Ballegoijen et al. 2011). More work needs to be done to cleanly separate the bulk motion of magnetic concentrations in the photosphere from effects of deformation and internal small-scale motions within the magnetic concentrations. This could be done by tracking the location of magnetic patches in time and decompose the flows into the motion of the center of mass of the magnetic patches superposed with the internal motions inside a magnetic concentration. Another approach would be to extract the photospheric velocity field, apply spatial and temporal filtering and use it as a boundary condition for another straightened-loop simulation. The domain size of this model of 6×6 Mm might be too small to properly take into account the build-up of large-scale magnetic stresses. Therefore, the model needs to be additionally compared to large-scale simulations.

We have found that complex small-scale structures develop across the loop cross-section, but it would be interesting to investigate whether MHD turbulence develops in the strict mathematical sense. Preliminary results from investigating a possible turbulent cascade are presented in appendix B.

Ubiquitous transverse and longitudinal wave-like motions can be observed in the simulation domain. Motions on short timescales appear to carry a significant fraction of the energy (see appendix A). Wave propagation and heating has been studied extensively in idealized setups omitting the lower atmosphere. Studying properties of Alfvénic perturbations and the location and extent of their dissipation would yield more information on the contribution of waves to energy transport. The loop model presented in this work could be used to study the generation, propagation and dissipation of excited by a self-consistent convection zone layer in a stratified atmosphere including effects from the coupling of different atmospheric layers, such as chromospheric evaporation in response to heating and magnetic fields with a complex topology. This setup easily allows to vary field strength, loop length and the magnetic configurations at the footpoints and could also be used to test estimates of loop properties from coronal seismology. The model could also be extended to stellar coronal loops by varying the boundary conditions at the footpoints.

Bibliography

- Alfvén, H.: 1942, *Nature* **150(3805)**, 405
- Alfvén, H.: 1947, *MNRAS* **107**, 211
- Antolin, P., Pagano, P., Testa, P., Petralia, A., and Reale, F.: 2021, *Nature Astronomy* **5**, 54
- Antolin, P., Yokoyama, T., and Van Doorselaere, T.: 2014, *ApJ* **787(2)**, L22
- Battaglia, A. F., Canivete Cuissa, J. R., Calvo, F., Bossart, A. A., and Steiner, O.: 2021, *A&A* **649**, A121
- Berger, T. E., de Pontieu, B., Fletcher, L., Schrijver, C. J., Tarbell, T. D., and Title, A. M.: 1999, *Sol. Phys.* **190**, 409
- Beveridge, C., Longcope, D. W., and Priest, E. R.: 2003, *Sol. Phys.* **216(1)**, 27
- Bingert, S. and Peter, H.: 2011, *A&A* **530**, A112
- Bingert, S. and Peter, H.: 2013, *A&A* **550**, A30
- Boerner, P., Edwards, C., Lemen, J., Rausch, A., Schrijver, C., Shine, R., Shing, L., Stern, R., Tarbell, T., Title, A., Wolfson, C. J., Soufli, R., Spiller, E., Gullikson, E., McKenzie, D., Windt, D., Golub, L., Podgorski, W., Testa, P., and Weber, M.: 2012, *Sol. Phys.* **275(1-2)**, 41
- Bonet, J. A., Márquez, I., Sánchez Almeida, J., Cabello, I., and Domingo, V.: 2008, *ApJ* **687(2)**, L131
- Bonet, J. A., Márquez, I., Sánchez Almeida, J., Palacios, J., Martínez Pillet, V., Solanki, S. K., del Toro Iniesta, J. C., Domingo, V., Berkefeld, T., Schmidt, W., Gandorfer, A., Barthol, P., and Knölker, M.: 2010, *ApJ* **723(2)**, L139
- Boris, J. P. and Mariska, J. T.: 1982, *ApJ* **258**, L49
- Bourdin, P. A., Bingert, S., and Peter, H.: 2013, *A&A* **555**, A123
- Bradshaw, S. J. and Cargill, P. J.: 2013, *ApJ* **770(1)**, 12
- Brandenburg, A.: 2014, *ApJ* **791(1)**, 12

- Brandt, P. N., Scharmer, G. B., Ferguson, S., Shine, R. A., Tarbell, T. D., and Title, A. M.: 1988, *Nature* **335(6187)**, 238
- Breu, C., Peter, H., Cameron, R., Solanki, S. K., Przybylski, D., Rempel, M., and Chitta, L. P.: 2022, *A&A* **658**, A45
- Brooks, D. H. and Warren, H. P.: 2016, *ApJ* **820(1)**, 63
- Brooks, D. H., Warren, H. P., Ugarte-Urra, I., and Winebarger, A. R.: 2013, *ApJ* **772(2)**, L19
- Buchlin, E. and Velli, M.: 2007, *ApJ* **662(1)**, 701
- Canivete Cuissa, J. R. and Steiner, O.: 2020, *A&A* **639**, A118
- Cargill, P. J.: 1994, *ApJ* **422**, 381
- Cargill, P. J. and Klimchuk, J. A.: 2004, *ApJ* **605(2)**, 911
- Carlsson, M., Hansteen, V. H., and Gudiksen, B. V.: 2010, *Mem. Soc. Astron. Italiana* **81**, 582
- Chae, J., Schühle, U., and Lemaire, P.: 1998, *ApJ* **505(2)**, 957
- Chen, F., Peter, H., Bingert, S., and Cheung, M. C. M.: 2014, *A&A* **564**, A12
- Chen, F., Rempel, M., and Fan, Y.: 2021, *arXiv e-prints* p. arXiv:2106.14055
- Cheung, M. C. M., Rempel, M., Chintzoglou, G., Chen, F., Testa, P., Martínez-Sykora, J., Sainz Dalda, A., DeRosa, M. L., Malanushenko, A., Hansteen, V., De Pontieu, B., Carlsson, M., Gudiksen, B., and McIntosh, S. W.: 2019, *Nature Astronomy* **3**, 160
- Chitta, L. P., Peter, H., Priest, E. R., and Solanki, S. K.: 2020, *A&A* **644**, A130
- Chitta, L. P., Peter, H., and Solanki, S. K.: 2018, *A&A* **615**, L9
- Chitta, L. P., Peter, H., Solanki, S. K., Barthol, P., Gandorfer, A., Gizon, L., Hirzberger, J., Riethmüller, T. L., van Noort, M., Blanco Rodríguez, J., Del Toro Iniesta, J. C., Orozco Suárez, D., Schmidt, W., Martínez Pillet, V., and Knölker, M.: 2017, *ApJS* **229(1)**, 4
- Chitta, L. P., van Ballegoijen, A. A., Rouppe van der Voort, L., DeLuca, E. E., and Kariyappa, R.: 2012, *ApJ* **752(1)**, 48
- Chong, M. S., Perry, A. E., and Cantwell, B. J.: 1990, *Physics of Fluids A* **2(5)**, 765
- Cirtain, J. W., Golub, L., Winebarger, A. R., de Pontieu, B., Kobayashi, K., Moore, R. L., Walsh, R. W., Korreck, K. E., Weber, M., McCauley, P., Title, A., Kuzin, S., and Deforest, C. E.: 2013, *Nature* **493(7433)**, 501
- Cowie, L. L. and McKee, C. F.: 1977, *ApJ* **211**, 135
- Dahlburg, R. B., Klimchuk, J. A., and Antiochos, S. K.: 2005, *ApJ* **622(2)**, 1191

- De Moortel, I. and Galsgaard, K.: 2006a, *A&A* **451(3)**, 1101
- De Moortel, I. and Galsgaard, K.: 2006b, *A&A* **459(2)**, 627
- de Pontieu, B., Berger, T. E., Schrijver, C. J., and Title, A. M.: 1999, *Sol. Phys.* **190**, 419
- De Pontieu, B., Carlsson, M., Rouppe van der Voort, L. H. M., Rutten, R. J., Hansteen, V. H., and Watanabe, H.: 2012, *ApJ* **752(1)**, L12
- de Pontieu, B., McIntosh, S., Hansteen, V. H., Carlsson, M., Schrijver, C. J., Tarbell, T. D., Title, A. M., Shine, R. A., Suematsu, Y., Tsuneta, S., Katsukawa, Y., Ichimoto, K., Shimizu, T., and Nagata, S.: 2007, *PASJ* **59**, S655
- De Pontieu, B., McIntosh, S., Martinez-Sykora, J., Peter, H., and Pereira, T. M. D.: 2015, *ApJ* **799(1)**, L12
- Dedner, A., Kemm, F., Kröner, D., Munz, C. D., Schnitzer, T., and Wesenberg, M.: 2002, *Journal of Computational Physics* **175(2)**, 645
- Del Zanna, G., Dere, K. P., Young, P. R., and Landi, E.: 2021, *ApJ* **909(1)**, 38
- Dere, K. P., Bartoe, J. D. F., and Brueckner, G. E.: 1984, *ApJ* **281**, 870
- Dere, K. P., Landi, E., Mason, H. E., Monsignori Fossi, B. C., and Young, P. R.: 1997, *A&AS* **125**, 149
- Dere, K. P. and Mason, H. E.: 1993, *Sol. Phys.* **144(2)**, 217
- Edlén, B.: 1943, *ZAp* **22**, 30
- Erdelyi, R., Doyle, J. G., Perez, M. E., and Wilhelm, K.: 1998, *A&A* **337**, 287
- Fedun, V., Shelyag, S., Verth, G., Mathioudakis, M., and Erdélyi, R.: 2011, *Annales Geophysicae* **29(6)**, 1029
- Fisher, G. H., Canfield, R. C., and McClymont, A. N.: 1985, *ApJ* **289**, 414
- Fyfe, L. E., Howson, T. A., and De Moortel, I.: 2021, *A&A* **656**, A120
- Galsgaard, K. and Nordlund, Å.: 1996, *J. Geophys. Res.* **101(A6)**, 13445
- Galsgaard, K. and Rousev, I.: 2002, *A&A* **383**, 685
- Golub, L., Deluca, E., Austin, G., Bookbinder, J., Caldwell, D., Cheimets, P., Cirtain, J., Cosmo, M., Reid, P., Sette, A., Weber, M., Sakao, T., Kano, R., Shibasaki, K., Hara, H., Tsuneta, S., Kumagai, K., Tamura, T., Shimojo, M., McCracken, J., Carpenter, J., Haight, H., Siler, R., Wright, E., Tucker, J., Rutledge, H., Barbera, M., Peres, G., and Varisco, S.: 2007, *Sol. Phys.* **243(1)**, 63
- Gombosi, T. I., Tóth, G., De Zeeuw, D. L., Hansen, K. C., Kabin, K., and Powell, K. G.: 2002, *Journal of Computational Physics* **177(1)**, 176
- Gomez, D. O., Martens, P. C. H., and Golub, L.: 1993, *ApJ* **405**, 767

- Grottrian, W.: 1939, *Naturwissenschaften* **27(13)**, 214
- Güdel, M.: 2004, *A&A Rev.* **12(2-3)**, 71
- Gudiksen, B. V., Carlsson, M., Hansteen, V. H., Hayek, W., Leenaarts, J., and Martínez-Sykora, J.: 2011, *A&A* **531**, A154
- Gudiksen, B. V. and Nordlund, Å.: 2002, *ApJ* **572(1)**, L113
- Gudiksen, B. V. and Nordlund, Å.: 2005a, *ApJ* **618(2)**, 1031
- Gudiksen, B. V. and Nordlund, Å.: 2005b, *ApJ* **618(2)**, 1020
- Guo, Y., Erdélyi, R., Srivastava, A. K., Hao, Q., Cheng, X., Chen, P. F., Ding, M. D., and Dwivedi, B. N.: 2015, *ApJ* **799(2)**, 151
- Gustafsson, B., Bell, R. A., Eriksson, K., and Nordlund, A.: 1975, *A&A* **500**, 67
- Hansteen, V.: 1993, *ApJ* **402**, 741
- Hansteen, V., Guerreiro, N., De Pontieu, B., and Carlsson, M.: 2015, *ApJ* **811(2)**, 106
- Hara, H. and Ichimoto, K.: 1999, *ApJ* **513(2)**, 969
- Hara, H., Watanabe, T., Harra, L. K., Culhane, J. L., Young, P. R., Mariska, J. T., and Doschek, G. A.: 2008, *ApJ* **678(1)**, L67
- Heyvaerts, J. and Priest, E. R.: 1983, *A&A* **117**, 220
- Hollweg, J. V.: 1984, *ApJ* **277**, 392
- Hood, A. W., Cargill, P. J., Browning, P. K., and Tam, K. V.: 2016, *ApJ* **817(1)**, 5
- Iijima, H. and Yokoyama, T.: 2017, *ApJ* **848(1)**, 38
- Innes, D. E., Inhester, B., Axford, W. I., and Wilhelm, K.: 1997, *Nature* **386(6627)**, 811
- Ionson, J. A.: 1978, *ApJ* **226**, 650
- Iroshnikov, P. S.: 1964, *Soviet Ast.* **7**, 566
- Jafari, A., Vishniac, E., and Xu, S.: 2020, *arXiv e-prints* p. arXiv:2004.06186
- Jameson, A.: 2017, *AIAA Journal* **55(5)**, 1487
- Kanella, C. and Gudiksen, B. V.: 2017, *A&A* **603**, A83
- Kitiashvili, I. N., Kosovichev, A. G., Lele, S. K., Mansour, N. N., and Wray, A. A.: 2013, *ApJ* **770(1)**, 37
- Kitiashvili, I. N., Kosovichev, A. G., Mansour, N. N., Lele, S. K., and Wray, A. A.: 2012a, *Phys. Scr* **86(1)**, 018403

- Kitiashvili, I. N., Kosovichev, A. G., Mansour, N. N., and Wray, A. A.: 2011, *ApJ* **727(2)**, L50
- Kitiashvili, I. N., Kosovichev, A. G., Mansour, N. N., and Wray, A. A.: 2012b, *ApJ* **751(1)**, L21
- Klimchuk, J. A.: 2006, *Sol. Phys.* **234(1)**, 41
- Kobayashi, K., Cirtain, J., Winebarger, A. R., Korreck, K., Golub, L., Walsh, R. W., De Pontieu, B., DeForest, C., Title, A., Kuzin, S., Savage, S., Beabout, D., Beabout, B., Podgorski, W., Caldwell, D., McCracken, K., Ordway, M., Bergner, H., Gates, R., McKillop, S., Cheimets, P., Platt, S., Mitchell, N., and Windt, D.: 2014, *Sol. Phys.* **289(11)**, 4393
- Kraichnan, R. H.: 1965, *Physics of Fluids* **8(7)**, 1385
- Kunasz, P. and Auer, L. H.: 1988, *J. Quant. Spec. Radiat. Transf.* **39**, 67
- Landau, L. D. and Lifshitz, E. M.: 1987, *Fluid Mechanics*
- Landi, E., Del Zanna, G., Young, P. R., Dere, K. P., and Mason, H. E.: 2012, *ApJ* **744(2)**, 99
- Lemen, J. R., Title, A. M., Akin, D. J., Boerner, P. F., Chou, C., Drake, J. F., Duncan, D. W., Edwards, C. G., Friedlaender, F. M., Heyman, G. F., Hurlburt, N. E., Katz, N. L., Kushner, G. D., Levay, M., Lindgren, R. W., Mathur, D. P., McFeaters, E. L., Mitchell, S., Rehse, R. A., Schrijver, C. J., Springer, L. A., Stern, R. A., Tarbell, T. D., Wuelser, J.-P., Wolfson, C. J., Yanari, C., Bookbinder, J. A., Cheimets, P. N., Caldwell, D., Deluca, E. E., Gates, R., Golub, L., Park, S., Podgorski, W. A., Bush, R. I., Scherrer, P. H., Gummin, M. A., Smith, P., Auken, G., Jerram, P., Pool, P., Soufli, R., Windt, D. L., Beardsley, S., Clapp, M., Lang, J., and Waltham, N.: 2012, *Sol. Phys.* **275(1-2)**, 17
- Li, L. P. and Peter, H.: 2019, *A&A* **626**, A98
- Malanushenko, A., Cheung, M. C. M., DeForest, C. E., Klimchuk, J. A., and Rempel, M.: 2021, *arXiv e-prints* p. arXiv:2106.14877
- Mariska, J. T. and Boris, J. P.: 1983, *ApJ* **267**, 409
- Martínez-Sykora, J., De Pontieu, B., Hansteen, V. H., Rouppe van der Voort, L., Carlsson, M., and Pereira, T. M. D.: 2017, *Science* **356(6344)**, 1269
- McIntosh, S. W. and De Pontieu, B.: 2012, *ApJ* **761(2)**, 138
- Meyer, C. D., Balsara, D. S., and Aslam, T. D.: 2012, *MNRAS* **422(3)**, 2102
- Mikić, Z., Lionello, R., Mok, Y., Linker, J. A., and Winebarger, A. R.: 2013, *ApJ* **773(2)**, 94
- Mikic, Z., Schnack, D. D., and van Hoven, G.: 1989, *ApJ* **338**, 1148

- Mikic, Z., Schnack, D. D., and van Hoven, G.: 1990, *ApJ* **361**, 690
- Moll, R., Cameron, R. H., and Schüssler, M.: 2011, *A&A* **533**, A126
- Moll, R., Cameron, R. H., and Schüssler, M.: 2012, *A&A* **541**, A68
- Moriyasu, S., Kudoh, T., Yokoyama, T., and Shibata, K.: 2004, *ApJ* **601(1)**, L107
- Müller, D., Nicula, B., Felix, S., Verstringe, F., Bourgoignie, B., Csillaghy, A., Berghmans, D., Jiggins, P., García-Ortiz, J. P., Ireland, J., Zahniy, S., and Fleck, B.: 2017, *A&A* **606**, A10
- Müller, D., St. Cyr, O. C., Zouganelis, I., Gilbert, H. R., Marsden, R., Nieves-Chinchilla, T., Antonucci, E., Auchère, F., Berghmans, D., Horbury, T. S., Howard, R. A., Krucker, S., Maksimovic, M., Owen, C. J., Rochus, P., Rodriguez-Pacheco, J., Romoli, M., Solanki, S. K., Bruno, R., Carlsson, M., Fludra, A., Harra, L., Hassler, D. M., Livi, S., Louarn, P., Peter, H., Schühle, U., Teriaca, L., del Toro Iniesta, J. C., Wimmer-Schweingruber, R. F., Marsch, E., Velli, M., De Groof, A., Walsh, A., and Williams, D.: 2020, *A&A* **642**, A1
- Nakariakov, V. M. and Ofman, L.: 2001, *A&A* **372**, L53
- Nordlund, A.: 1985, *Sol. Phys.* **100**, 209
- Oughton, S., Matthaeus, W. H., and Dmitruk, P.: 2017, *ApJ* **839(1)**, 2
- Pagano, P. and De Moortel, I.: 2019, *A&A* **623**, A37
- Pant, V., Magyar, N., Van Doorselaere, T., and Morton, R. J.: 2019, *ApJ* **881(2)**, 95
- Parker, E. N.: 1972, *ApJ* **174**, 499
- Parker, E. N.: 1982, *Geophysical and Astrophysical Fluid Dynamics* **22(3)**, 195
- Parker, E. N.: 1983, *ApJ* **264**, 642
- Parker, E. N.: 1988, *ApJ* **330**, 474
- Parnell, C. E. and De Moortel, I.: 2012, *Philosophical Transactions of the Royal Society of London Series A* **370(1970)**, 3217
- Patsourakos, S. and Klimchuk, J. A.: 2006, *ApJ* **647(2)**, 1452
- Peter, H.: 2000, *A&A* **360**, 761
- Peter, H.: 2010, *A&A* **521**, A51
- Peter, H.: 2015, *Philosophical Transactions of the Royal Society of London Series A* **373(2042)**, 20150055
- Peter, H., Bingert, S., and Kamio, S.: 2012, *A&A* **537**, A152

- Peter, H., Bingert, S., Klimchuk, J. A., de Forest, C., Cirtain, J. W., Golub, L., Winebarger, A. R., Kobayashi, K., and Korreck, K. E.: 2013, *A&A* **556**, A104
- Peter, H. and Dwivedi, B. N.: 2014, *Frontiers in Astronomy and Space Sciences* **1**, 2
- Peter, H., Gudiksen, B. V., and Nordlund, Å.: 2004, *ApJ* **617(1)**, L85
- Peter, H., Gudiksen, B. V., and Nordlund, Å.: 2006, *ApJ* **638(2)**, 1086
- Petschek, H. E.: 1964, in *NASA Special Publication*, Vol. 50, p. 425
- Pontin, D. I., Candelaresi, S., Russell, A. J. B., and Hornig, G.: 2016, *Plasma Physics and Controlled Fusion* **58(5)**, 054008
- Pontin, D. I. and Hornig, G.: 2015, *ApJ* **805(1)**, 47
- Pontin, D. I. and Hornig, G.: 2020, *Living Reviews in Solar Physics* **17(1)**, 5
- Pontin, D. I., Janvier, M., Tiwari, S. K., Galsgaard, K., Winebarger, A. R., and Cirtain, J. W.: 2017, *ApJ* **837(2)**, 108
- Pontin, D. I., Peter, H., and Chitta, L. P.: 2020, *A&A* **639**, A21
- Pontin, D. I., Wilmot-Smith, A. L., Hornig, G., and Galsgaard, K.: 2011, *A&A* **525**, A57
- Priest, E.: 2014, *Magnetohydrodynamics of the Sun*, Cambridge University Press
- Priest, E. R., Chitta, L. P., and Syntelis, P.: 2018, *ApJ* **862(2)**, L24
- Priest, E. R., Heyvaerts, J. F., and Title, A. M.: 2002, *ApJ* **576(1)**, 533
- Przybylski, D., Cameron, R., Solanki, S. K., Rempel, M., Leenarts, J., Anusha, L. S., Witzke, V., and Shapiro, A. L.: 2021, *A&A*, Submitted.
- Rachmeler, L. A., Winebarger, A. R., Savage, S. L., Golub, L., Kobayashi, K., Vigil, G. D., Brooks, D. H., Cirtain, J. W., De Pontieu, B., McKenzie, D. E., Morton, R. J., Peter, H., Testa, P., Tiwari, S. K., Walsh, R. W., Warren, H. P., Alexander, C., Ansell, D., Beabout, B. L., Beabout, D. L., Bethge, C. W., Champey, P. R., Cheimets, P. N., Cooper, M. A., Creel, H. K., Gates, R., Gomez, C., Guillory, A., Haight, H., Hogue, W. D., Holloway, T., Hyde, D. W., Kenyon, R., Marshall, J. N., McCracken, J. E., McCracken, K., Mitchell, K. O., Ordway, M., Owen, T., Ranganathan, J., Robertson, B. A., Payne, M. J., Podgorski, W., Pryor, J., Samra, J., Sloan, M. D., Soohoo, H. A., Steele, D. B., Thompson, F. V., Thornton, G. S., Watkinson, B., and Windt, D.: 2019, *Sol. Phys.* **294(12)**, 174
- Rao, Y. K., Del Zanna, G., and Mason, H. E.: 2022, *arXiv e-prints* p. arXiv:2201.07290
- Rappazzo, A. F., Matthaeus, W. H., Ruffolo, D., Velli, M., and Servidio, S.: 2017, *ApJ* **844(1)**, 87
- Rappazzo, A. F. and Velli, M.: 2011, *Phys. Rev. E* **83(6)**, 065401

- Rappazzo, A. F., Velli, M., Dahlburg, R. B., and Einaudi, G.: 2019, *ApJ* **883**(2), 148
- Rappazzo, A. F., Velli, M., and Einaudi, G.: 2010, *The Astrophysical Journal* **722**(1), 65–78
- Rappazzo, A. F., Velli, M., and Einaudi, G.: 2013, *The Astrophysical Journal* **771**(2), 76
- Rappazzo, A. F., Velli, M., Einaudi, G., and Dahlburg, R. B.: 2007, *ApJ* **657**(1), L47
- Rappazzo, A. F., Velli, M., Einaudi, G., and Dahlburg, R. B.: 2008, *The Astrophysical Journal* **677**(2), 1348–1366
- Reale, F.: 2014, *Living Reviews in Solar Physics* **11**(1), 4
- Reale, F., Orlando, S., Guarrasi, M., Mignone, A., Peres, G., Hood, A. W., and Priest, E. R.: 2016, *ApJ* **830**(1), 21
- Reid, J., Cargill, P. J., Hood, A. W., Parnell, C. E., and Arber, T. D.: 2020, *A&A* **633**, A158
- Reid, J., Hood, A. W., Parnell, C. E., Browning, P. K., and Cargill, P. J.: 2018, *A&A* **615**, A84
- Rempel, M.: 2014, *ApJ* **789**(2), 132
- Rempel, M.: 2016, *The Astrophysical Journal* **834**(1), 10
- Rempel, M.: 2017, *ApJ* **834**(1), 10
- Rempel, M.: 2018, *ApJ* **859**(2), 161
- Ritchie, M. L., Wilmot-Smith, A. L., and Hornig, G.: 2016, *The Astrophysical Journal* **824**(1), 19
- Rochus, P., Auchère, F., Berghmans, D., Harra, L., Schmutz, W., Schühle, U., Addison, P., Appourchaux, T., Aznar Cuadrado, R., Baker, D., Barbay, J., Bates, D., BenMoussa, A., Bergmann, M., Beurthe, C., Borgo, B., Bonte, K., Bouzit, M., Bradley, L., Büchel, V., Buchlin, E., Büchner, J., Cabé, F., Cadiergues, L., Chaigneau, M., Chares, B., Choque Cortez, C., Coker, P., Condamin, M., Coumar, S., Curdt, W., Cutler, J., Davies, D., Davison, G., Defise, J. M., Del Zanna, G., Delmotte, F., Delouille, V., Dolla, L., Dumesnil, C., Dürig, F., Enge, R., François, S., Fourmond, J. J., Gillis, J. M., Giordanengo, B., Gissot, S., Green, L. M., Guerreiro, N., Guilbaud, A., Gyo, M., Haberreiter, M., Hafiz, A., Hailey, M., Halain, J. P., Hansotte, J., Hecquet, C., Heerlein, K., Hellin, M. L., Hemsley, S., Hermans, A., Hervier, V., Hochedez, J. F., Houbrechts, Y., Ihsan, K., Jacques, L., Jérôme, A., Jones, J., Kahle, M., Kennedy, T., Klaproth, M., Kolleck, M., Koller, S., Kotsialos, E., Kraaikamp, E., Langer, P., Lawrenson, A., Le Clech', J. C., Lenaerts, C., Liebecq, S., Linder, D., Long, D. M., Mampaey, B., Markiewicz-Innes, D., Marquet, B., Marsch, E., Matthews, S., Mazy, E., Mazzoli, A., Meining, S., Meltchakov, E., Mercier, R., Meyer, S., Monecke, M., Monfort, F., Morinaud, G., Moron, F., Mountney, L., Müller, R., Nicula, B., Parenti, S., Peter, H., Pfiffner, D.,

- Philippon, A., Phillips, I., Plessier, J. Y., Pylyser, E., Rabecki, F., Ravet-Krill, M. F., Rebellato, J., Renotte, E., Rodriguez, L., Roose, S., Rosin, J., Rossi, L., Roth, P., Rouesnel, F., Roulliy, M., Rousseau, A., Ruane, K., Scanlan, J., Schlatter, P., Seaton, D. B., Silliman, K., Smit, S., Smith, P. J., Solanki, S. K., Spescha, M., Spencer, A., Stegen, K., Stockman, Y., Szwec, N., Tamiatto, C., Tandy, J., Teriaca, L., Theobald, C., Tychon, I., van Driel-Gesztelyi, L., Verbeeck, C., Vial, J. C., Werner, S., West, M. J., Westwood, D., Wiegmann, T., Willis, G., Winter, B., Zerr, A., Zhang, X., and Zhukov, A. N.: 2020, *A&A* **642**, A8
- Rogers, F. J. and Iglesias, C. A.: 1996, in *American Astronomical Society Meeting Abstracts #188*, Vol. 188 of *American Astronomical Society Meeting Abstracts*, p. 58.04
- Rosner, R., Tucker, W. H., and Vaiana, G. S.: 1978, *ApJ* **220**, 643
- Schindler, K., Hesse, M., and Birn, J.: 1988, *J. Geophys. Res.* **93(A6)**, 5547
- Schrijver, C. J., Title, A. M., Harvey, K. L., Sheeley, N. R., Wang, Y. M., van den Oord, G. H. J., Shine, R. A., Tarbell, T. D., and Hurlburt, N. E.: 1998, *Nature* **394(6689)**, 152
- Serio, S., Peres, G., Vaiana, G. S., Golub, L., and Rosner, R.: 1981, *ApJ* **243**, 288
- Shelyag, S., Cally, P. S., Reid, A., and Mathioudakis, M.: 2013, *ApJ* **776(1)**, L4
- Shelyag, S., Keys, P., Mathioudakis, M., and Keenan, F. P.: 2011, *A&A* **526**, A5
- Shelyag, S., Mathioudakis, M., and Keenan, F. P.: 2012, *ApJ* **753(1)**, L22
- Shi, M., Van Doorsselaere, T., Guo, M., Karamelas, K., Li, B., and Antolin, P.: 2021, *ApJ* **908(2)**, 233
- Silva, S. S. A., Fedun, V., Verth, G., Rempel, E. L., and Shelyag, S.: 2020, *ApJ* **898(2)**, 137
- Snodin, A. P., Brandenburg, A., Mee, A. J., and Shukurov, A.: 2006, *MNRAS* **373(2)**, 643
- Solanki, S. K., del Toro Iniesta, J. C., Woch, J., Gandorfer, A., Hirzberger, J., Alvarez-Herrero, A., Appourchaux, T., Martínez Pillet, V., Pérez-Grande, I., Sanchis Kilders, E., Schmidt, W., Gómez Cama, J. M., Michalik, H., Deutsch, W., Fernandez-Rico, G., Grauf, B., Gizon, L., Heerlein, K., Kolleck, M., Lagg, A., Meller, R., Müller, R., Schühle, U., Staub, J., Albert, K., Alvarez Copano, M., Beckmann, U., Bischoff, J., Busse, D., Enge, R., Frahm, S., Germerott, D., Guerrero, L., Löptien, B., Meierdierks, T., Oberdorfer, D., Papagiannaki, I., Ramanath, S., Schou, J., Werner, S., Yang, D., Zerr, A., Bergmann, M., Bochmann, J., Heinrichs, J., Meyer, S., Monecke, M., Müller, M. F., Sperling, M., Álvarez García, D., Aparicio, B., Balaguer Jiménez, M., Bellot Rubio, L. R., Cobos Carracosa, J. P., Girela, F., Hernández Expósito, D., Herranz, M., Labrousse, P., López Jiménez, A., Orozco Suárez, D., Ramos, J. L., Barandiarán, J., Bastide, L., Campuzano, C., Cebollero, M., Dávila, B., Fernández-Medina, A., García Parejo, P., Garranzo-García, D., Laguna, H., Martín, J. A., Navarro, R., Núñez Peral, A., Royo, M., Sánchez, A., Silva-López, M., Vera, I., Villanueva, J., Fourmond, J. J., de Galarreta, C. R., Bouzit, M., Hervier, V., Le Clec'h, J. C., Szwec, N., Chaigneau, M.,

- Buttice, V., Dominguez-Tagle, C., Philippon, A., Boumier, P., Le Cocguen, R., Baranjuk, G., Bell, A., Berkefeld, T., Baumgartner, J., Heidecke, F., Maue, T., Nakai, E., Scheiffelen, T., Sigwarth, M., Soltau, D., Volkmer, R., Blanco Rodríguez, J., Domingo, V., Ferreres Sabater, A., Gasent Blesa, J. L., Rodríguez Martínez, P., Osorno Caudel, D., Bosch, J., Casas, A., Carmona, M., Herms, A., Roma, D., Alonso, G., Gómez-Sanjuan, A., Piqueras, J., Torralbo, I., Fiethe, B., Guan, Y., Lange, T., Michel, H., Bonet, J. A., Fahmy, S., Müller, D., and Zouganelis, I.: 2020, *A&A* **642**, A11
- Spitzer, L.: 1962, *Physics of Fully Ionized Gases*
- Stein, R. F. and Nordlund, Å.: 1998, *ApJ* **499(2)**, 914
- Steiner, O. and Rezaei, R.: 2012, in L. Golub, I. De Moortel, and T. Shimizu (eds.), *Fifth Hinode Science Meeting*, Vol. 456 of *Astronomical Society of the Pacific Conference Series*, p. 3
- Stenflo, J. O.: 1975, *Sol. Phys.* **42(1)**, 79
- Stix, M.: 2004, *The sun : an introduction*
- Strauss, H. R.: 1976, *Physics of Fluids* **19(1)**, 134
- Sweet, P. A.: 1958, in B. Lehnert (ed.), *Electromagnetic Phenomena in Cosmical Physics*, Vol. 6, p. 123
- Syntelis, P., Priest, E. R., and Chitta, L. P.: 2019, *ApJ* **872(1)**, 32
- Testa, P., De Pontieu, B., and Hansteen, V.: 2016, *ApJ* **827(2)**, 99
- Tian, H., McIntosh, S. W., Wang, T., Ofman, L., De Pontieu, B., Innes, D. E., and Peter, H.: 2012, *ApJ* **759(2)**, 144
- Tomczyk, S. and McIntosh, S. W.: 2009, *ApJ* **697(2)**, 1384
- Tripathi, D., Mason, H. E., Dwivedi, B. N., del Zanna, G., and Young, P. R.: 2009, *ApJ* **694(2)**, 1256
- Tziotziou, K., Tsiropoula, G., and Kontogiannis, I.: 2020, *A&A* **643**, A166
- Tziotziou, K., Tsiropoula, G., Kontogiannis, I., Scullion, E., and Doyle, J. G.: 2018, *A&A* **618**, A51
- van Ballegooijen, A. A., Asgari-Targhi, M., and Berger, M. A.: 2014, *ApJ* **787(1)**, 87
- van Ballegooijen, A. A., Asgari-Targhi, M., Cranmer, S. R., and DeLuca, E. E.: 2011, *The Astrophysical Journal* **736(1)**, 3
- van Ballegooijen, A. A., Asgari-Targhi, M., and Voss, A.: 2017, *ApJ* **849(1)**, 46
- Vekstein, G.: 2009, *A&A* **499(1)**, L5
- Verwichte, E., Van Doorselaere, T., Foullon, C., and White, R. S.: 2013, *ApJ* **767(1)**, 16

- Vögler, A.: 2003, *Ph.D. thesis*, University of Göttingen, Germany
- Vögler, A., Shelyag, S., Schüssler, M., Cattaneo, F., Emonet, T., and Linde, T.: 2005, *A&A* **429**, 335
- Warnecke, J. and Peter, H.: 2019, *A&A* **624**, L12
- Wedemeyer, S. and Steiner, O.: 2014, *PASJ* **66**, S10
- Wedemeyer-Böhm, S. and Rouppe van der Voort, L.: 2009, *A&A* **507(1)**, L9
- Wedemeyer-Böhm, S., Scullion, E., Steiner, O., Rouppe van der Voort, L., de La Cruz Rodriguez, J., Fedun, V., and Erdélyi, R.: 2012, *Nature* **486(7404)**, 505
- Williams, T., Walsh, R. W., Peter, H., and Winebarger, A. R.: 2020a, *ApJ* **902(2)**, 90
- Williams, T., Walsh, R. W., Winebarger, A. R., Brooks, D. H., Cirtain, J. W., De Pontieu, B., Golub, L., Kobayashi, K., McKenzie, D. E., Morton, R. J., Peter, H., Rachmeler, L. A., Savage, S. L., Testa, P., Tiwari, S. K., Warren, H. P., and Watkinson, B. J.: 2020b, *ApJ* **892(2)**, 134
- Wilmot-Smith, A. L., Hornig, G., and Pontin, D. I.: 2009a, *ApJ* **696(2)**, 1339
- Wilmot-Smith, A. L., Hornig, G., and Pontin, D. I.: 2009b, *ApJ* **704(2)**, 1288
- Wilmot-Smith, A. L., Pontin, D. I., and Hornig, G.: 2010, *A&A* **516**, A5
- Wilmot-Smith, A. L., Pontin, D. I., Yeates, A. R., and Hornig, G.: 2011, *A&A* **536**, A67
- Withbroe, G. L. and Noyes, R. W.: 1977, *ARA&A* **15**, 363
- Yadav, N., Cameron, R. H., and Solanki, S. K.: 2020a, *arXiv e-prints* p. arXiv:2004.13996
- Yadav, N., Cameron, R. H., and Solanki, S. K.: 2020b, *ApJ* **894(2)**, L17
- Yadav, N., Cameron, R. H., and Solanki, S. K.: 2021, *A&A* **645**, A3
- Yadav, N., Keppens, R., and Popescu Braileanu, B.: 2022, *arXiv e-prints* p. arXiv:2201.09704
- Zhou, J., Adrian, R. J., Balachandar, S., and Kendall, T. M.: 1999, *Journal of Fluid Mechanics* **387(1)**, 353

A Timescales of the energy transport

DC and AC models for coronal loop heating differ mainly in the timescales of velocities driving the magnetic field evolution and the timescales of the coronal response to the driver. If the driving occurs on timescales much larger than the Alfvén travel time through the coronal structure, the corona responds quasi-statically to the driving. If the timescales are shorter than the Alfvén travel time, the corona responds dynamically.

We perform an analysis similar to Rempel (2017) and compare the time-averaged Poynting flux $\langle \mathbf{B} \times (\mathbf{v} \times \mathbf{B}) \rangle / 4\pi$ to the Poynting flux computed from the time-averaged magnetic and velocity field $\langle \mathbf{B} \rangle \times (\langle \mathbf{v} \rangle \times \langle \mathbf{B} \rangle) / 4\pi$. Using different averaging windows, we can filter out contributions from short timescales. The remaining Poynting flux fraction after the temporal averaging as a function of the averaging time window is shown in Fig. A.1. The Poynting flux computed from the averaged velocity and magnetic fields is normalized by the averaged value of the Poynting flux computed from the instantaneous fields for each respective averaging window.

Similar to Rempel (2017), we find a continuum of timescales.

At photospheric heights, approximately half of the Poynting flux is lost after integrating over more than 1.1 minutes. These timescales are even shorter for chromospheric and transition region heights at 1.3 Mm and 3 Mm. From low coronal heights on, the timescale slightly increases again to 1.3 minutes and continues to increase with height up to 1.7 minutes at 15 Mm. The remaining Poynting flux drops to less than half of the reference value at timescales of less than two minutes, considerably less than the lifetime of a granule of approximately ten minutes. The Alfvén travel time between a height of 500 km in the low chromosphere and a distance of 15 Mm along its loop is of the order of 100 s, the heating can therefore neither clearly be classified as DC nor as AC heating.

Rempel (2017) find that for their simulations the characteristic timescale of energy transport increases with height. The higher the magnetic field reaches into the corona, the larger is the footpoint separation of the magnetic field lines and the longer the timescales of motions involved. At lower heights, the characteristic timescale corresponds to the lifetime of a granule. In contrast to this, we find more Poynting flux from motions on shorter timescales also for larger heights. Since our box has horizontal dimensions of only 6×6 Mm and thus covers only a small region, motions on longer timescales are likely not reproduced. The periodic boundary conditions in the horizontal directions technically allow for motions on long timescales to stretch the field, but this would lead to large misalignment angles between field lines in the simulation box that cannot be reached due to the high values of the numerical diffusivities that will lead to reconnection before the field line can be sufficiently stretched to traverse the box several times.

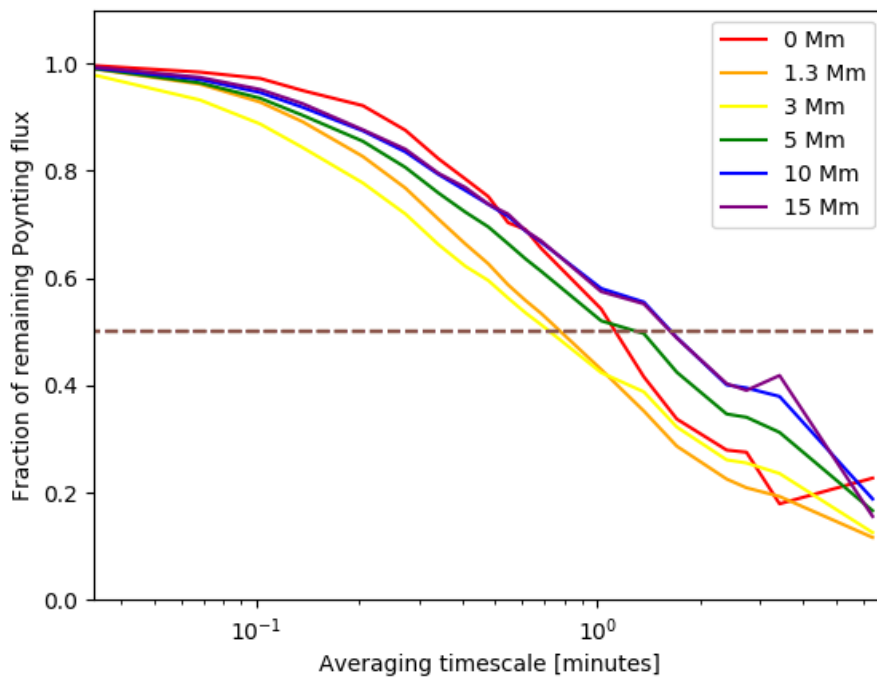


Figure A.1: Fraction of remaining Poynting flux after temporal averaging of the magnetic and velocity field for different averaging timescales. The line colors correspond to different slices at the axial coordinate s for the high resolution run. The dashed line marks the timescale at which 50 percent of the Poynting flux is lost.

B Is there a turbulent cascade in the coronal loop?

B.1 Aim

A complex structure of small-scale current sheets and plasma motions develops perpendicular to the direction of the magnetic guide field in all our simulation runs. It is, however, unclear whether this behavior constitutes a turbulent cascade of energy and momentum from large to small scales. In order to answer this question, we investigate the spectral energy transfer in the corona. In this section we present preliminary results of this study for the low resolution run.

B.2 Methods

In order to investigate the transfer of energy between different energy reservoirs and spatial scales, the spectral energy transfer functions were calculated in the form described in Rempel (2014).

The spectral energy transfer functions for the transfer to the magnetic energy reservoir obtained from the time evolution of the magnetic energy in Fourier space are:

$$T_{\text{KBA}}(k) = -\frac{1}{8\pi} \hat{\mathbf{B}}(k) [\mathbf{v} \cdot \widehat{\nabla \mathbf{B}}]^*(k) + cc, \quad (\text{B.1})$$

$$T_{\text{KBT}}(k) = \frac{1}{8\pi} \hat{\mathbf{B}}(k) [\widehat{\mathbf{B}} \cdot \widehat{\nabla \mathbf{v}}]^*(k) + cc, \quad (\text{B.2})$$

$$T_{\text{KBP}}(k) = -\frac{1}{8\pi} \hat{\mathbf{B}}(k) [\widehat{\mathbf{B}} \widehat{\nabla} \cdot \mathbf{v}]^*(k) + cc, \quad (\text{B.3})$$

where cc is the complex conjugate. The spectral energy transfer functions to the kinetic energy reservoir are:

$$T_{\text{KKA}} = -\frac{1}{2} [\widehat{\sqrt{\rho \mathbf{v}}}(k) \cdot \left[\frac{\widehat{\nabla(\rho \mathbf{v} \mathbf{v})}}{\sqrt{\rho}} \right]^*] - \frac{1}{4} [\widehat{\sqrt{\rho \mathbf{v}}}(k) \cdot \left[\frac{\mathbf{v} \widehat{\nabla} \cdot (\rho \mathbf{v})}{\sqrt{\rho}} \right]^*] (k) + cc, \quad (\text{B.4})$$

$$T_{\text{IKP}} = \frac{1}{2} [\widehat{\rho \mathbf{v}}(k) \cdot \left[\frac{-\widehat{\nabla P} + \rho \widehat{\mathbf{g}}}{\sqrt{\rho}} \right]^*] (k) + cc, \quad (\text{B.5})$$

$$T_{\text{BKL}} = \frac{1}{8\pi} [\widehat{\sqrt{\rho \mathbf{v}}}(k) \cdot \left[\frac{\widehat{\nabla \cdot (\mathbf{B} \mathbf{B})}}{\sqrt{\rho}} \right]^*] (k) - \frac{1}{8\pi} [\widehat{\sqrt{\rho \mathbf{v}}}(k) \cdot \left[\frac{\widehat{\nabla B^2}}{2\sqrt{\rho}} \right]^*] (k) + cc. \quad (\text{B.6})$$

B.3 Results

B.3.1 Transfer Functions

Energy is transferred between the kinetic, magnetic and internal energy reservoir. The energy transfer functions as a function of spatial wave number in Fourier space are shown in Fig. B.1 and B.2 for the convection zone and corona, respectively. Solid lines refer to positive energy transfer, dashed lines to negative energy transfer. Energy is transported from the kinetic to the magnetic energy reservoir by stretching (T_{KBT} , red), advection (T_{KBA} , blue) and compression (T_{KBP} , split between stretching and advection). The magnetic field can drive flows via the Lorentz force (T_{BKL} , green), enhancing the kinetic energy. The kinetic energy is reduced if work is done against the Lorentz force. Energy is transferred from the kinetic and magnetic to the internal reservoir by viscous (T_{NUMV} , purple) and resistive (T_{NUMB} , pink) dissipation, respectively.

Energy is transported from the internal to the kinetic reservoir due to pressure and buoyancy forces (T_{IKP} , black). Energy can also be transferred to smaller scales by advection within a reservoir, such as in the momentum cascade (T_{KKA} , yellow).

B.3.2 Convection zone

In the shallow convection zone layer below the photosphere, the energy transfer functions shown in Fig. B.1 resemble the small-scale dynamo setup during the saturation phase in Rempel (2014), although the grid spacing is much coarser in our runs with $\Delta x = 60$ km. The dominant term is the pressure/buoyancy term, which is balanced at large scales by the advection of kinetic energy to small scales. At small scales, the kinetic energy is dissipated due to numerical viscosity. The energy transfer from kinetic to magnetic energy by stretching of the magnetic field is positive on all scales. At large scales, this term is balanced by advection of magnetic energy to small scales which is then dissipated by numerical resistivity. While the energy transfer function from magnetic to internal energy due to dissipation is negative at all scales, the energy transfer due to viscous dissipation is positive at large scales. This likely corresponds to the broadening of structures in the velocity field due to viscous dissipation. At large scales, work is done against the Lorentz force. At small scales, however, the kinetic energy is enhanced due to the contribution of the Lorentz force.

B.3.3 Chromosphere and corona

Higher up in the corona, as shown in Fig. B.2, the buoyancy term and the momentum cascade are even less important. The dominant term over a large range of scales is now the Lorentz force contribution to kinetic energy. Overall, at small scales, the Lorentz force, advection of magnetic energy and viscous dissipation of the associated flows dominate the energy exchange between different reservoirs. The buoyancy term and the momentum cascade are now several orders of magnitude smaller than the contributions from the other terms.

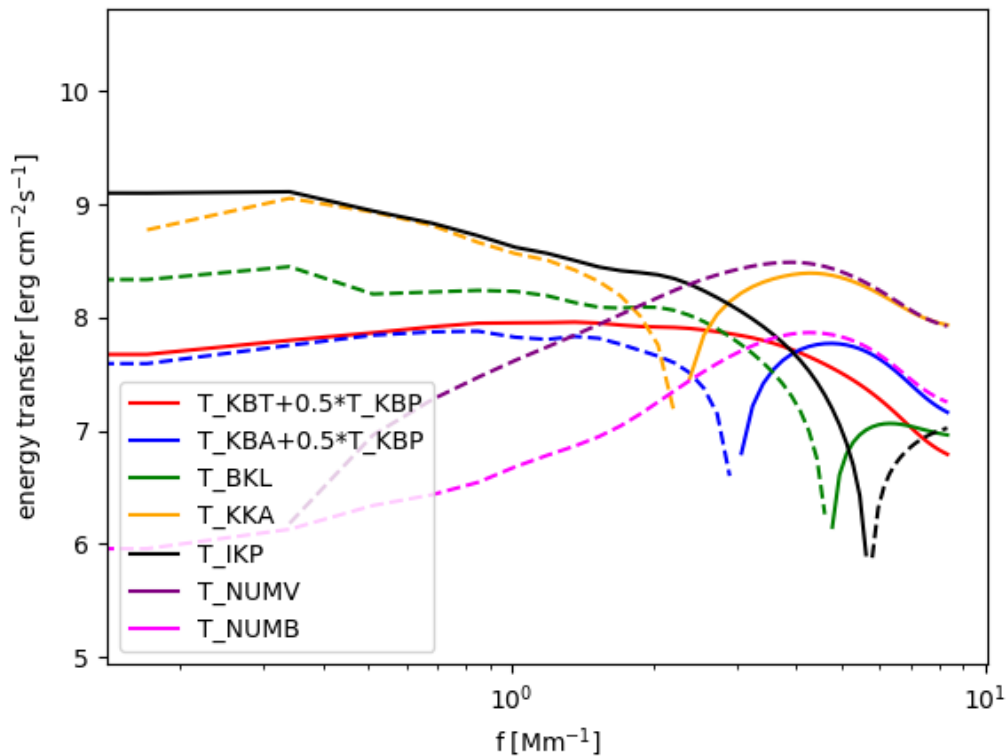


Figure B.1: Energy transfer functions in the convection zone layer for the low resolution run, averaged over a slab centered on a depth of 800 km beneath the photosphere. The average was performed over ten gridpoints (600 km). The transfer functions were averaged over six snapshots taken over an hour of solar time. The transfer functions have been smoothed to suppress noise.

B.4 Discussion

The transfer functions in the convection zone layer show signs of a turbulent cascade. Magnetic and kinetic energy is removed at large scales and advected towards small scales, where it is dissipated.

In the coronal part, however, the momentum cascade becomes less and less important with increasing height. Advection of magnetic field to small scales and the Lorentz force term are dominant at small scales.

This behavior of the different terms of the energy transfer functions is similar to the findings of Rappazzo and Velli (2011). Due to the low plasma beta in the corona, the magnetic field governs the coronal dynamics.

A possible interpretation of this behaviour is a scenario in which the turbulence is essentially two-dimensional, the cascade to small scales occurs in the chromosphere and is communicated upward by the magnetic field. In the coronal part, the magnetic field drives flows on intermediate and small scales, which are then dissipated.

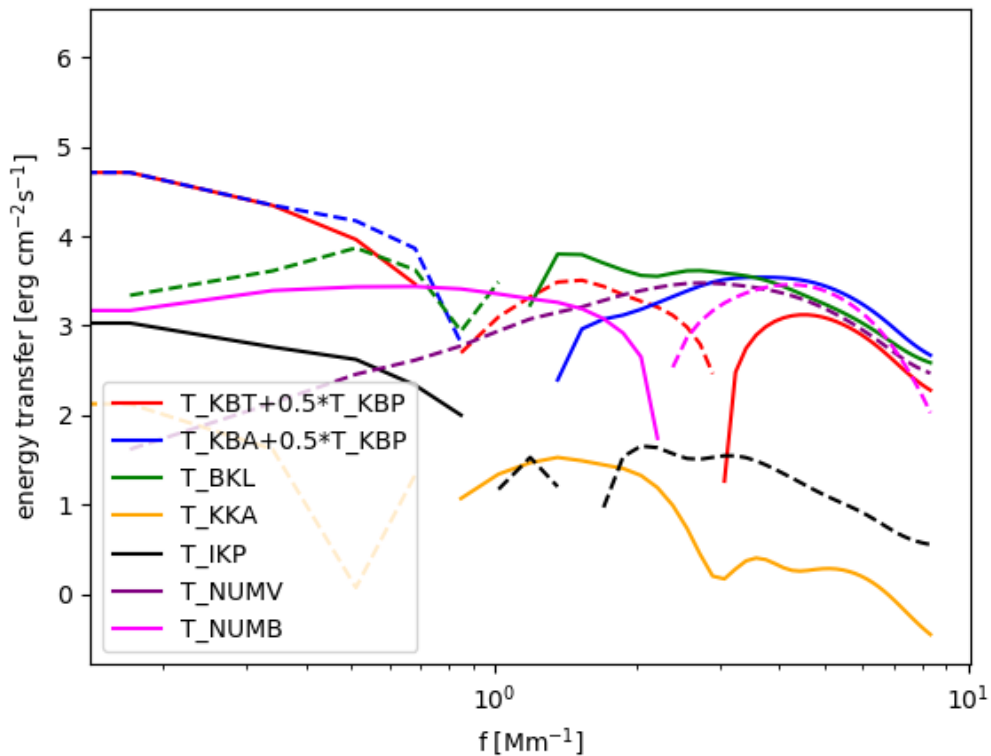


Figure B.2: Energy transfer functions in the loop leg, averaged over a slab centered at an arclength of 10 Mm, corresponding to a height of 9.4 Mm. An average was performed over a height range of 100 gridpoints (6 Mm). The transfer functions were averaged over six snapshots taken over an hour of solar time. The transfer functions have been smoothed to suppress noise.

B.5 Conclusion

We found that the energy transfer to small scales in the corona is driven by the magnetic field. The momentum cascade to small scales is negligible, which can be expected for a low plasma beta. In the future, we plan to extend this study to higher resolutions and different Prandtl number regimes.

Publications

Refereed publications

- **C. Breu**, H. Peter, R. Cameron, S.K. Solanki, D. Przybylski, M. Rempel, L.P. Chitta, *A solar coronal loop in a box: energy generation and heating*, 2022, *A&A* 658, A45
- **C. Breu** and L. Rezzolla, *Maximum mass, moment of inertia and compactness of relativistic stars*, 2016, *MNRAS* 459, 646

Conference presentations

- Energy generation, transport and dissipation in a coronal loop -iPoster
ESPM-16, Virtual meeting
- A solar coronal loop in a box: energy generation, heating and dynamics -Talk
NAM 2021, Virtual meeting
- Coronal loops in a box: 3D models of their internal structure, dynamics and heating
-Talk
238 Meeting of the AAS, Virtual meeting
- A Coronal Loop Braided by Realistic Photospheric Motions -Poster
SolFER Spring Meeting, Virtual meeting
- Coronal loops in a box: 3D models of their internal structure, dynamics and heating
-Talk
CoolStars 20.5, Virtual meeting
- The Parker Problem: A Coronal Loop Braided by Realistic Photospheric Motions
-Talk
Max Planck Princeton Center Workshop, Virtual meeting
- A Coronal Loop in a Box: Energy Generation, Heating and Dynamics -Talk
Annual Meeting of the German Astronomical Society
- A Coronal Loop in a Box: Energy Generation, Heating and Dynamics -iPoster
51st SPD Meeting, Virtual meeting

B Is there a turbulent cascade in the coronal loop?

- A coronal loop in a box: comparing the role of field line braiding and flux cancellation in a model from below the solar surface to the corona *9th Coronal Loops Workshop 2019, St. Andrews, UK*

Acknowledgements

First and foremost, I want to thank my supervisors Hardi and Robert for their guidance and support over the past few years. Going from dying to living stars, the field of solar physics was new to me in the beginning and I have greatly benefitted from getting to know different perspectives on solar physics. I want to express my gratitude to Sami for his insight and ideas for this work. Special thanks goes to Damien who has introduced me to the MURaM code and answered countless questions I kept bothering him with especially in the beginning (and the end). To Pradeep I am grateful for his inexhaustible fund of knowledge about coronal heating and pretty much everything else. Furthermore, I want to thank all the people from the Corona group and the Solar and Stellar MHD group for tea and cake meetings and discussions about various science and non-science topics. Special thanks also goes to Matthias Rempel for making it possible to visit Boulder virtually despite travel restrictions.

The last few years have been turbulent both on small and on global scales, now more than ever. I feel grateful everyone who has made life in often rainy and cloudy Göttingen a lot brighter than it would otherwise have been. Being part of the IMPRS community is something that I have very much enjoyed.

I want to thank Nina for all the coffee meetings, in person and online, and for weekend afternoons spent in the bouldering gym, Tanayveer for countless excursions hiking mountains and gorges, spontaneous Harz multiday cycling trips and late work pizza, Kok Leng for the many after-lunch caffeine-intensive coffee meetings, Bernhard, Aline, Pablo, Bastian and Chris and Stephan for all the game nights, Philipp, Juxhin and Mayukh for sharing a desk and an office and many discussions about scientific careers, life and all the rest. Many thanks also to Paula, Argiris, Jonas, and all the other IMPRS students. Many thanks also to Trenton and Zach and all the people I got to meet in Boulder.

I also want to thank the people who have supported me throughout life, even if not everyone is here anymore. Ganz besonders möchte ich mich bei meinen Eltern, Johann und Almut Breu, und meinen Schwestern Andrea und Annette für ihre Unterstützung bedanken. Vielen Dank auch an Sigrid. You have always supported me despite me sometimes having my head in the clouds.

"Sometimes you have to go a very long way to get one step forward."

This project has been funded by the European Research Council under the European Union's Horizon 2020 research and innovation programme (grant agreement No. 69507). A part of this project is based upon work supported by the National Center for Atmospheric Research, which is a major facility sponsored by the National Science Foundation under Cooperative Agreement No. 1852977.

Curriculum Vitae

Personal data

Name: Cosima Alexandra Breu

Day of birth: 31.08.1991

Place of birth: Frankfurt am Main, Germany

Education

- April 2018-March 2022: PhD
International Max Planck Research School (IMPRS) at the Max-Planck-Institute for Solar System Research and Georg-August-University of Göttingen, Germany
Supervisor: Prof. H. Peter, Dr. R. Cameron, Prof. W. Glatzel
Thesis title: 'A coronal loop in a box: From energy generation to coronal emission'
- 2015-2017: MSc in Computational Physics
Goethe University Frankfurt am Main, Germany
Supervisor: Prof. L. Rezzolla
Thesis title: 'Magnetically driven Winds from Binary Neutron Star Merger Remnants'
- 2011-2015: BSc in Physics
Goethe University Frankfurt am Main, Germany
Supervisor: Prof. L. Rezzolla
Thesis title: 'Universal Relations for the Moment of Inertia in Relativistic Stars'